LOW-ENERGY ELECTRON INTERACTIONS WITH WATER

Rhiannon Monckton

2014

School of Chemistry

University of Manchester

A thesis submitted to the University of Manchester for the degree of Doctor of Philosophy in the Faculty of Engineering and Physical Sciences

Contents

List of Tables 6

Abbreviations 7

Abstract 8

Declaration 9

Copyright statement 10

Acknowledgements 12

1. Introduction 14
   1.1. Motivation 14
   1.2. Objectives 16

2. Background and Previous Work 18
   2.1. Radiation Chemistry of Water 18
      2.1.1. Water radiolysis 18
      2.1.2. Low energy electrons 20
      2.1.3. Low-energy electron interactions with water 21
   2.2. Radiolysis of water-ice 25
      2.2.1. Amorphous solid water (ASW) 25
      2.2.2. Electron-stimulated reactions in ASW 26
   2.3. Previous studies of ice radiolysis 28
      2.3.1. Irradiation of pure water ices 28
      2.3.2. Electron-irradiation of CO:H_2O ices 31
      2.3.3. Energy transfer through water-ice 38
   2.4. Dissociative Electron Attachment (DEA) 41
      2.4.1. DEA in gas-phase H_2O 42
      2.4.2. DEA in the condensed phase of H_2O 46
      2.4.3. Cross-sections for DEA in water 48
   2.5. Previous studies of DEA to water 51
      2.5.1. Assignment of resonance forms 51
      2.5.2. Dominant dissociation pathway at each resonance 54

2.5.3. Energy partitioning in the parent and product ions 56
2.5.4. OH Production Channels in DEA to H_2O 57
2.5.5. Previous Studies of OH ($X^2\Pi$) formed by electron impact on H_2O 60

3. Laser-Induced Fluorescence (LIF) Spectroscopy of OH 62
3.1. Principles of Fluorescence 62
3.2. Laser-Induced Fluorescence (LIF) 64
3.3. Molecular Energy Levels of OH 67

4. Experimental Apparatus (Gas-phase studies) 70
4.1. Overview of the gas-phase experiment 70
4.2. High Vacuum (HV) System 71
4.2.1. Vacuum chambers 71
4.2.2. Vacuum principles 72
4.2.3. Vacuum pumps 73
4.2.4. Monitoring Pressure 75
4.2.5. Preparing the UHV chamber for surface studies 75
4.3. Molecular Beam 77
4.3.1. Molecular Beam Hardware 77
4.3.2. Principle of Molecular Beams 80
4.3.3. Alternative forms of sample introduction 82
4.4. Electron Gun 83
4.4.1. Electron Gun Design 83
4.4.2. Electron Gun Hardware 87
4.4.3. Helmholtz coils 88
4.4.4. Electron Beam Characterisation 91
4.5. Optical System 94
4.5.1. Nd:YAG Laser 94
4.5.2. Dye Laser 95
4.5.3. Excimer Laser 97
4.6. Detection Systems 99
4.6.1. Photomultiplier Tube (PMT) 99
4.6.2. Reduction of scattered light 101
4.7. Experimental Control and Signal Processing 103
4.7.1. Delay generator 103
4.7.2. Data acquisition 103

5. Experimental Methods (Condensed phase) 104
5.1. Overview of condensed phase experiments 104
5.2. Sample preparation 105
5.2.1. Surface preparation 105
5.2.2. ASW/CO ice deposition 105
5.3. Electron-stimulated desorption (ESD) 107
5.3.1. Principles of ESD 107
5.3.2. ESD Experimental Conditions 108
5.4. Temperature-programmed desorption (TPD) 110
5.4.1. Principles of TPD 110
5.4.2. TPD Experimental Conditions 111
5.5. Reflection-absorption infra-red spectroscopy (RAIRS) 113
5.5.1. Principles of RAIRS 113
5.5.2. RAIRS Experimental Conditions 114

6. Laser-induced fluorescence studies of DEA in water 116
6.1. Preliminary Experiments 116
6.2. OH LIF spectra for low pressure of precursor gas 120
6.3. Improvements in signal to noise ratio 125
6.4. Calculations of number density of OH molecules 132
6.4.1. Photo-dissociation of allyl alcohol at ~$9\times10-3$ Torr 134
6.5. Discussion 143

7. Electron-stimulated reactions of ASW/CO films 149
7.1. Experimental Results 149
7.1.1. Effect of CO on radiolysis of ASW 149
7.1.2. Decomposition of CO 152
7.1.3. Oxidation Channels 160
7.1.4. Reduction Channels 163
7.2. Sources of Error 169
7.3. Discussion 174
7.3.1. Electron-stimulated oxidation of CO 174
7.3.2. Kinetics of sequential hydrogenation of CO 180
7.3.3. Mechanism of electron energy transfer in reduction of CO 183
7.4. Monte Carlo simulations of H atom diffusion 190
7.4.1. Monte Carlo Model 190
7.4.2. Monte Carlo Simulation Results 193

8. Conclusions 199
8.1. LIF studies of low-energy electron interactions with H_2O 199
8.2. Low-energy electron interactions in ASW/CO/ASW ices 200

9. Further Work 202
9.1. LIF spectra of OH by DEA to water 202
9.2. Further studies of layered ASW/CO/ASW ices 204
9.3. Condensed phase studies of DEA in water 205

Appendix 207

References 218

Word count: 44,161

List of Tables

Table 1 - Classification of secondary electrons by energy and interaction in irradiated materials 21

Table 2 - Incident electron energy at which peak anion yield is observed/eV 42

Table 3 - Summary of cross-section measurements for H^- and O^- yields from DEA to water at each resonance 50

Table 4 - Relative intensities of vibrational levels of OH fragment at 6.5 eV 58

Table 5 - Rotational energy distribution of OH at 8.5 eV 59

Table 6 - Naming conventions for vacuum regimen 72

Table 7 - Voltage potentials applied across electron gun components during Helmholtz coil optimisation 92

Table 8 - Dissociation cross-sections and vapour pressures for OH precursors 118

Table 9 - S/N ratio for OH LIF spectra as a function of PMT voltage 126

Table 10 - S/N ratio for OH LIF spectra as a function of T_1 ($T_0 = 5.0 \times 10^{-7}$ s) 129

Table 11 - IR band and m/z peak assignment for products of ASW/CO radiolysis 156

Table 12 - Estimated % error on TPD integrals for mass fragments studied in the present work 172

Abbreviations

ASW	Amorphous solid water
DEA	Dissociative electron attachment
ESD	Electron-stimulated desorption
FTIR	Fourier Transform infra-red
ISM	Interstellar medium
LIF	Laser-induced fluorescence
ML	Mono-layer
PMT	Photomultiplier tube
RAIRS	Reflection absorption infra-red spectroscopy
TDS	Thermal desorption spectroscopy
TNI	Transient negative ion
TPD	Temperature-programmed desorption
UHV (HV)	Ultra-high vacuum (High vacuum)

Abstract

Low-energy Electron Interactions with Water

Doctor of Philosophy, The University of Manchester

Rhiannon Monckton, August 2014

Understanding the radiation chemistry of water is important in many disciplines including the nuclear industry, astrochemistry, and medicine. In recent years, low-energy electrons have been paid much greater attention, due to their abundance and reactivity in irradiated materials. Electrons with energies < 20 eV may interact via the dissociative electron attachment (DEA) mechanism, which has been found to cause single-strand breaks in DNA.

DEA in water involves the capture of a low energy electron by a neutral water molecule into an outer orbital and is generally accompanied by excitation of the H_2O molecule, causing it to dissociate. The aim of this work is to study the OH radical produced in DEA to H_2O using laser-induced fluorescence (LIF).

A high-vacuum chamber equipped with low energy electron gun, molecular beam and laser system was built for gas-phase studies of DEA in water. LIF spectra were recorded from OH formed by dissociation of gas-phase H_2O, for determination of the rotational and vibrational state distributions.

In addition to the gas-phase studies, low-energy (100 eV) electron-stimulated reactions in layered $H_2O/CO/H_2O$ ices were investigated using a combination of temperature-programmed desorption (TPD) and infrared reflection-absorption spectroscopy (IRAS).

For CO trapped within approximately 50 mono-layers of the vacuum interface both reduction and oxidation products were observed including HCO, H_2CO, H_3CO and CH_3OH, and CO_2. Concentration profiles of CO versus film thickness showed two zones in the film: a near-surface zone of preferential oxidation, and a zone of preferential reduction deeper in the film. A Monte Carlo model was developed based on diffusion of H atoms through the ice lattice, which supported the experimental results.

Declaration

No portion of the work referred to in this thesis has been submitted in support of an application for another degree or qualification of this or any other university or other institute of learning.

Copyright statement

http://www.manchester.ac.uk/library/aboutus/regulations) and in The University's policy on Presentation of Theses

Acknowledgements

First of all, I would like to thank my supervisor Dr. Sven Koehler for giving me the opportunity to pursue such a varied and interesting PhD. Thank you for your support, patience and enthusiasm over the last four years; it has been great fun working with you.

Secondly, thank you to Greg Kimmel and Nick Petrik for hosting me at PNNL. It was a great experience and I learned a lot both during my placement and from our many conversations since.

I'd also like to thank Prof. Simon Pimblott for so much help and guidance since the move to Cumbria. It has been a huge support to know that your door is always open.

To everyone at the Dalton Cumbrian Facility (DCF), thank you for making it such a great place to work and for being such good friends. Special thanks to Kevin, Ruth, Vicky, Amanda and Mark for helping me to get the lab set up and keep my experiments running. Thanks also to Howard Sims for taking an interest in my work and for many helpful conversations.

My PhD would not have been possible without the mechanical and electronic workshops in Manchester. Huge thanks to Peter, Malcolm, Chris and Terry for building and rebuilding so much of my equipment and for being such a delight to work with. Thanks also to Steve and Siraj for all your help, particularly your work on the electron gun in the midst of the move.

The electron gun was designed and built with the help of Prof. Andrew Murray and his group, for which I am extremely grateful.

This work was completed thanks to generous funding from the DCF and Nuclear Decommissioning Authority (NDA). Support from the PSI is also gratefully acknowledged.

To Logan, thanks for sharing the ups and downs of the last three years. My PhD wouldn’t have been the same without you in it.

Finally, I would like to thank my family, in particular Mum and Dad for inspiring, encouraging and supporting me every step of the way and for never letting me give up.

1. Introduction

1.1. Motivation

Understanding the interactions between water and radiation has considerable importance in a number of fields including medicine, astrochemistry, atmospheric sciences and nuclear energy. In irradiated materials, reactions of primary radiolysis products give rise to a large number of secondary electrons, which subsequently lose energy through interaction with the medium. The result is an abundance of low energy electrons, which have a much greater impact on radiation damage pathways than previously thought, and merit further investigation. Electrons with energies as low as 5 eV may continue to react within a material post-irradiation by a mechanism known as dissociative electron attachment (DEA).

DEA has been shown to cause double strand breaks in DNA, highlighting the importance of this mechanism in radiation damage.[1] Given the ubiquitous nature of water in biology, an improved understanding of the role of dissociative electron attachment to water in radiation damage to biological systems is needed to support developments in radiation therapy and nuclear medicine.

In the nuclear industry, water is used in cooling systems and is also present in waste streams and containers for long-term disposal. For safe disposal of nuclear waste, the interfacial reactions between low energy electrons, water and the solid waste-form must be understood, particularly the generation of H_2 and O_2, given the flammable and explosive nature of these gases. Although a number of studies have investigated the evolution of H_2 following irradiation, current models fail to accurately predict the H_2 yields in the waste canisters, suggesting that further research is needed.[2,3] In addition to H_2 production, the radiolysis of water also

releases radical species such as OH, O, H and HO_2, as well as H_2O_2, all of which can cause damage in water-cooled nuclear reactors.[4] In order to better understand damage pathways, it is vital to learn more about the fundamental processes involved in the irradiation of water, as well as the effect of interfacial reactions.

Radiation-stimulated reactions of water are also of interest in astrochemistry, where formation of simple hydrocarbons in the interstellar medium (ISM) occurs on icy dust grains. In this field, not only the radiolysis of water, but the combined interactions of water ice, hydrocarbons and electrons are of interest, in order to provide, for example, an explanation for the abundances of simple hydrocarbons observed in comets or dust clouds. Studies in which water ice is mixed with a second molecule such as ammonia or acetonitrile have yet to arrive at a unified picture of the fundamental processes occurring.[5,6,7] Disagreement exists about which products result from radiolysis of such mixed ices, whether the reactions are limited to ice surfaces, and, if reactions take place deeper into the ice, how the energy is transferred.

1.2. Objectives

Low-energy electrons are abundant in irradiated materials, and make a significant contribution to radiation damage. The objective of this work is to study the interaction of low energy electrons with water in both the gaseous and condensed phases.

Experiments were conducted to study the products of low energy electron irradiation of layered water and carbon monoxide ices, with the aim of building on previous studies of electron-stimulated reactions in pure water ice. In addition to the condensed-phase studies, a new experimental set-up was constructed in order to study electron-stimulated reactions of gas-phase water, for electrons with energies 0-100 eV. This will facilitate the study of the dissociative electron attachment (DEA) mechanism in water vapour.

The aim of the gas-phase work is to study the internal energy of OH radicals produced by DEA to water, which occurs in the electron energy range 5-12 eV. The main part of this work is to design and build a high vacuum (HV) chamber incorporating a low energy electron gun, molecular beam and optical system for performing laser-induced fluorescence (LIF). Following successful commissioning of this apparatus, energy distributions of the OH radical may be measured for the two lowest DEA resonances in H_2O in order to learn about the water anion transition state by which the DEA proceeds.

In the condensed phase studies, layered ices of amorphous solid water (ASW) and carbon monoxide (CO) were grown on a TiO_2 (110) or Pt (111) substrate at low temperature. Reflection absorption infra-red spectroscopy (RAIRS) was used in conjunction with temperature-programmed desorption (TPD) and electron-stimulated

desorption (ESD) to study the products of irradiation of the ices with 100 eV electrons. The purpose of these experiments is to study the mechanism of energy transfer through thick ice films.

2. Background and Previous Work

2.1. Radiation Chemistry of Water

2.1.1. Water radiolysis

Radiation is broadly divided into two types: ionising and non-ionising. Ionising radiation, such as α particles, γ rays and fast electrons (β particles) have enough energy to ionise atoms and molecules. Radical species are also created, which contain unpaired electrons and are responsible for most of the radiation damage in living organisms.[8] Ionisation releases a large number of electrons into the medium, known as secondary electrons. Non-ionising radiation generally causes electronic, vibrational and rotational excitation of molecules, which may dissociate to produce reactive radicals. Examples of non-ionising radiation include visible and infra-red radiation and low energy electrons.

The radiation-induced ionisation, dissociation and subsequent reactions of molecules in matter are known as radiolysis. In general, the products of radiolysis are termed "primary" or "secondary" products, depending on the stage at which they are formed. The primary products of liquid water radiolysis are H, OH, H_3O^+ and e^-_{aq}. Secondary products include H_2 and H_2O_2. Equations (2.1)-(2.9) show the reaction scheme for radiolysis of liquid water by ionising radiation, first summarised by M. Burton[9] and A. Allen.[10]

$$H_2O \rightsquigarrow H_2O^+ + e^-_{aq} \qquad (2.1)$$

$$H_2O + e^-_{aq} \rightarrow OH^- + H \qquad (2.2)$$

$$H_2O^+ + H_2O \rightarrow H_3O^+ + OH \qquad (2.3)$$

Primary reactions

$$H + H \rightarrow H_2 \quad (2.4)$$

$$OH + OH \rightarrow H_2O_2 \quad (2.5)$$

$$OH + H \rightarrow H_2O \quad (2.6)$$

Secondary reactions

$$H + H_2O_2 \rightarrow H_2O + OH \quad (2.7)$$

$$OH + H_2 \rightarrow H_2O + H \quad (2.8)$$

Radical propagation

Equation (2.1) shows the initial absorption of incident radiation, resulting in ionisation of the water molecule. This process releases a secondary electron in to the material, which plays an important role in the radiation damage pathway. Equations (2.2) and (2.3) describe the reactions which lead to the primary reaction products of water radiolysis: reducing species: H; and oxidising species: OH. Secondary radiolysis products H_2 (2.4) and H_2O_2 (2.5) are formed by radical recombination, rather than by reactions of H_2O^+ or e^-_{aq}, but are still often listed as primary radiolysis products due to the short timescales on which they are formed; typically H, OH, H_3O^+, e^-_{aq}, H_2O_2 and H_2 are all formed within the first few nano-seconds of high-energy irradiation. Recombination of radicals may also result in neutral, excited H_2O (2.6) along with propagation of radicals (2.7-2.8) which may then react further within the material.

Water radiolysis by non-ionising radiation includes reactions of the electronically excited water molecule, H_2O^*. As equations (2.9)-(2.11) show, dissociation of H_2O^*also contributes to the production of oxidising and reducing radical species.

$$H_2O \rightsquigarrow H_2O^* \rightarrow H + OH \quad (2.9)$$

$$H_2O^* \rightarrow 2H + O \quad (2.10)$$

$$H_2O^* \rightarrow H_2 + O \quad (2.11)$$

In addition to the products listed in equations (2.1)-(2.11), further reaction of radicals within the water leads to the creation of a wide range of species including HO_2, O_2, O_2^- and H^+, all of which contribute to radiation damage in materials.

There are a number of other radiation-induced mechanisms which may take place in water, depending upon the type and energy of the incident radiation. For low energy radiation close to the ionisation energy of the medium, some of these minor processes play a much greater role. The following chapters focus on radiation damage mechanisms in the low energy electron irradiation of water.

2.1.2. Low energy electrons

As described, secondary electrons have a range of energies (typically 0-500 eV) and may react with the surrounding atoms and molecules. Often, secondary electrons have relatively low energies (< 100 eV) and are recaptured by the parent molecule in a process called "geminate recombination", however studies show that many have sufficient energy to escape recapture and go on to ionise or excite other molecules in the medium. Approximately 4×10^4 non-thermal secondary electrons are released per MeV energy deposited following irradiation of water, of which ~20% are recaptured in the first 100 fs.[11,12] The majority of secondary electrons undergo energy loss through a number of collisions before thermalizing, resulting in an abundance of low energy electrons in irradiated materials. It is estimated that around 10-15% of the energy absorbed following irradiation of a material is dissipated by sub-excitation electrons.[13]

Table 1 lists four classifications of secondary electrons in terms of their energy (E) and interaction with the irradiated material, where E_i refers to the ionisation energy of the medium. In general, studies of secondary electrons may refer to electrons with

$E \leq 500$ eV, although increasingly studies have focused on the region $E \leq E_i$. For the purpose of this thesis, the term "low energy electrons" is used to refer to slow, sub-excitation and thermal electrons, unless otherwise stated.

Table 1 - Classification of secondary electrons by energy and interaction in irradiated materials

	Typical energy / eV	**Mode of interaction**
Fast electrons	> 100	Multiple collisions causing ionisation and electronic excitation
Slow electrons	$100 > E > E_i$	Ionisation or excitation
Sub-excitation electrons	$E_i > E > 20$	Vibrational and rotational excitation
Thermal electrons	$20 > E$	Electron attachment, vibrational and rotational excitation

This table gives a good classification scheme for low-energy electron damage to many widely-used materials, however there are one or two points to consider when applying these classifications to water. The ionisation threshold of water is ~11 eV, which means that the sub-excitation electrons as defined in Table 1 are already in the thermal electron classification.[14] Furthermore, in condensed phase water, electronic excitations are available with an onset of ~7.3 eV, making thermal electrons much more important to radiation damage of water than implied by this table.

2.1.3. Low-energy electron interactions with water

Low energy electrons in water undergo a number of different types of scattering process: elastic scattering, ionisation, electron attachment and rotational, vibrational and electronic excitation. Indirect scattering, in which the electron is temporarily

captured into a transient ion state, (e.g. dissociative electron attachment) is abundant in both the gaseous and condensed phase interactions of low energy electrons.

Thermal and sub-excitation electrons primarily interact with water molecules by accessing resonance forms. A resonance structure arises when an electron remains in close vicinity to a molecule for an extended period of time, usually described in terms of the formation of a transient negative ion (TNI), with the electron residing in a molecular orbital. In the case of water, the TNI is H_2O^-, which may be formed in a number of different states, discussed in greater detail in chapter 2.4.1. The decay channels and further reactions of the TNI, listed in equations (2.12)-(2.17), add a number of additional pathways for production of radicals and ions in radiolysis, making it important to understand the mechanisms of these low energy electrons in greater detail. As shown here, the TNI may be formed with varying degrees of electronic, vibrational or rotational excitation, indicated by H_2O^{*-} (2.29). This is not intended to be an exhaustive list; in particular, dissociation of the H_2O^{*-} anion may proceed via three different fragmentation routes with varying probabilities depending upon the energies involved. These routes are shown for the dissociation in equation 2.13 (a-c), but alternative fragmentation routes are also possible in any dissociative decay of the water TNI.

$$H_2O^- \rightarrow \quad H_2O^*(r,v) + e^- \qquad (2.12)$$

$$H_2O^*(n,r,v) + e^- \rightarrow H + OH + e^- \qquad (2.13a)$$

$$H_2O^*(n,r,v) + e^- \rightarrow H_2 + O + e^- \qquad (2.13b)$$

$$H_2O^*(n,r,v) + e^- \rightarrow H + H + O + e^- \qquad (2.13c)$$

$$H^- + OH \qquad (2.14)$$

$$H_2O^{*-} \rightarrow \quad H^- + OH^* \qquad (2.15)$$

$$H_2O^+ + 2e^- \quad (2.16)$$

$$H_2O^{*-} \rightarrow \quad H_2O^{*-} \xrightarrow{-\Delta E} H_2O^- \quad (2.17)$$

As equations (2.12) and (2.13) show, decay by ejection of the attached electron ("auto-detachment") is possible, usually leaving water in a rotationally (*r*), vibrationally (*v*) or even electronically (*n*) excited state. If the resulting excited state is dissociative, then the molecule may dissociate into neutral fragments (2.13a-c). H_2O^- may decay by dissociation into an ion and a neutral species, either with or without excitation (2.14-2.15). For this to occur, the resonance lifetime must be at least the same order of magnitude as the vibrational period of the molecule, and the H_2O^- state must be dissociative in the Franck-Condon region. In cases where the energy of the incident electron is greater than the ionisation energy of the neutral molecule, 2-electron emission is possible (2.16); the TNI decays by releasing an electron from a molecular orbital in addition to the incident electron. In equation (2.17), the TNI loses energy by transfer to another molecule, for example by collision, resulting in a stable, ionic fragment.

In summary, the major products of the low-energy (0-100 eV) electron irradiation of water include the primary products of high-energy radiation: H, OH, H_3O^+ and e^-, as well as the secondary products H_2, O, O_2, and H_2O_2. The anionic species H^- and OH^- are also produced as a direct result of H_2O^- resonance forms accessed by electrons with energies below the ionisation threshold of water.

Electron penetration depth in water

The interaction of radiation with matter can be considered in terms of a series of collisions between the radiation particles, in this case electrons, and the molecules of the medium. The distance between these collisions is known as the mean free path.[15]

In the condensed phase, the mean free path is much shorter than in gases, which means that the electrons lose energy much more quickly and therefore have much shorter lifetimes. The average distance an electron can travel before losing most of its energy and becoming thermalized is the penetration depth of the radiation into the material and affects the magnitude and the nature of radiation damage.

Munoz *et al* calculated that, for 100 eV electrons in water vapour at 0.5 Torr, a single electron may penetrate as much as 20 mm, although the peak deposition is much lower, around 2 mm. In comparison, recent simulation data for secondary electrons in condensed phase water suggest that those electrons which escape recapture by the parent ion diffuse an average of 3 nm within the material.[12] Using Monte Carlo simulations, Mankhetorn *et al* calculated the electron penetration into amorphous water-ice for a range of electron energies.[16] For the experiments described in this thesis, typical electron energies are 100 eV, with a typical penetration depth on the order of 1-10 nm, corresponding to at most 30 monolayers (ML) of water-ice.[17] The penetration depth of the initial radiation has a considerable effect on the subsequent reactions that occur. In the following discussion, thick water ices (> 30 ML) are considered, whose thickness is greater than the penetration depth of the electrons. Reactions that occur deeper in the films than the penetration depth must be initiated by some other energy carrier, which will be discussed in greater detail in later chapters.

2.2. Radiolysis of water-ice

2.2.1. Amorphous solid water (ASW)

In gas-phase water, the density of molecules is low, meaning that the density of collisions is also low and the interactions between H_2O molecules are weak. However, in order to more accurately represent the radiation-induced reactions in liquid water, denser structures which take into account hydrogen bonding must be considered. Water-ice adsorbed to a substrate at low temperature (< 120 K) has the advantage over liquid water that it may be studied under ultra-high vacuum (UHV) conditions, making it possible to probe fundamental interactions in the water. As such, water-ice has already been well studied for this purpose on a number of surfaces and will be used as the substrate in this study.

Amorphous solid water (ASW) is a form of water ice produced by low temperature deposition of H_2O under UHV conditions. At temperatures of ~120 K, H_2O molecules do not have sufficient energy to assume the most energetically favorable orientation, leading to an amorphous solid structure rather than the regular ordered structure of crystalline ice, which results from higher temperature deposition (over 140 K). Deposition of water below 100 K leads to the formation of porous ASW,[18] which has a similar disordered structure to ASW, but with larger pores which have been found to influence the ESD yields of electron-induced reactions.[19]

ASW is frequently used as a substitute for liquid water in UHV conditions, as the disordered structure has more in common with the liquid phase than crystalline ice but can be deposited on a surface. Monte Carlo simulations of electron-stimulated processes in liquid water have been found to give good agreement with similar studies of amorphous solid water.[16]

ASW on the rutile TiO_2 (110) and Pt (111) surfaces

ASW ice is generally grown on a metal or metal oxide substrate. In the work outlined in this thesis, the substrates used are TiO_2 (110) and Pt (111). A number of studies of ASW films on the Pt (111) surface point to reactions at the ASW/Pt interface as playing an important role in the reactions of thick water-ice films (up to 40 ML), which highlights the importance of an understanding of the surface interactions in studies of bulk reactions.[20] Similarly, studies of ASW adsorbed on the TiO_2 (110) surface show that OH groups on the reduced TiO_2 surface influence the reactions of the adsorbed water.[21] In the experiments which follow, a minimum thickness of 60 ML of ASW is laid on the substrate in order to discount the effect of interactions with the metal or metal oxide surface.

By convention, a single water monolayer on TiO_2 (110) is typically defined as a coverage of 5.2×10^{14} molecules cm^{-2}, which in fact corresponds to occupation of around half of the available adsorption sites. As such, some studies also refer to coverage in terms of "ice monolayers", for which 1 ML = 1.1×10^{15} molecules cm^{-2}, approximately twice the number of H_2O molecules described by the water monolayer. In the work presented in this thesis, a single ASW monolayer is defined as 1.2×10^{15} molecules cm^{-2}.

2.2.2. Electron-stimulated reactions in ASW

The major products from low-energy electron irradiation of pure ASW films have been described. The formation of these products from ASW on both the Pt (111) and the TiO_2 (110) surfaces has been monitored in previous studies using electron-stimulated desorption (ESD).[22] The yields of O_2 and H_2 were found to alter according to the temperature of the film during irradiation, the thickness of the film,

and the electron fluence. By monitoring how the yields change with these variables, it is possible to learn about the processes occurring in electron-irradiated water ice, both in the bulk film and at the interfaces.

The main electron-water reactions following irradiation of thick ASW films are the same as those described for liquid water; an incident electron may ionize, excite or attach to a water molecule, depending on the energy of the electron and the internal energy of the molecule. In the experiments described, in which thick films are irradiated with 100 eV electrons, the dominant process is likely to be excitation of the water molecule. This process is generally followed by dissociation of the water molecule, resulting in a large number of H and OH radicals in the ice, as well as H_2 and O, formed in the minor dissociation pathway. The major products of water radiolysis are listed in chapter 2.1.1. The reactions below show some of the products which may be formed by further reactions of OH and H within the ice.[23]

$$O + O \rightarrow O_2 \qquad (2.18)$$

$$OH + OH \rightarrow H_2O_2 \qquad (2.19)$$

$$H_2O_2 + OH \rightarrow HO_2 + H_2O \qquad (2.20)$$

$$H_2O_2 + H \rightarrow H_2O + OH \qquad (2.21)$$

$$HO_2 + O \rightarrow O_2 + OH \qquad (2.22)$$

Equations (2.18-2.22) are intended to show identity and origin of certain species which have been observed following low-energy irradiation of water ices. By monitoring these products it is possible to learn about the dominant reaction processes and mechanisms of energy transfer within water films. Previous studies to investigate these processes are detailed in the following chapter.

2.3. Previous studies of ice radiolysis

2.3.1. Irradiation of pure water ices

Surface-catalysed reactions of water ices have received much attention in recent years due to interest in water splitting for H_2 production. A number of studies involving ionising radiation effects on water ices have been undertaken to investigate production of hydrogen, oxygen and other species from water-ices adsorbed to a substrate. Interactions where water-ice itself is the substrate have also been the subject of investigation by the astrochemical community due to the importance of such reactions in interstellar space where a surface is often required for energy transfer.[24] It has been proposed that due to the low number density of H atoms in space, molecular hydrogen is synthesized by recombination of two H atoms at a surface such as dust grains covered in water-ice.[25] The production of H_2 and O_2 by irradiation of water is of interest in the nuclear industry, in the context of long-term disposal of low-level radioactive wastes. The effect of radiolysis on the interaction between water and metal oxides is also of importance in nuclear waste disposal, as reduction of the oxide may reduce the stability of the waste-form.[26]

Production of Hydrogen

Hydrogen production from water following gamma irradiation has been investigated for different metal oxide substrates.[27] Compared with hydrogen production from pure water, the yield of hydrogen was found to vary according to the metal oxide, with certain oxides significantly enhancing the yield of hydrogen, for example ZrO_2. This is in agreement with studies of hydrogen production in cements used in the disposal of nuclear wastes at the Hanford nuclear site, which found that much of the hydrogen

was produced by water adsorbed on solids, rather than by direct radiolysis of the liquid phase.3

Studies of electron irradiation of water-ice find that hydrogen (usually a combination of molecular and atomic hydrogen) is the primary product of radiolysis, with yields up to two orders of magnitude greater than yields of molecular oxygen. This is at least partly due to the fact that hydrogen may be produced as a direct product of water decomposition whereas molecular oxygen is formed by the reaction of precursors (e.g. OH, HO_2, H_2O_2).[28]

A similar study found that for any oxide the yield of hydrogen increases as the amount of water adsorbed decreases.[29] That is, irradiation of thinner water films leads to an increased production of molecular hydrogen, most likely due to the transfer of energy from the oxide to the water. Similar work by Petrik *et al*, to study electron-irradiation of amorphous solid water adsorbed on Pt (111), showed that for thicker films reactions may take place at the buried interface between ASW and the platinum surface. There appears to be little or no production of H_2 in the bulk of the film, however. These findings are supported by further work with layered films of D_2O and H_2O which showed that molecular hydrogen is preferentially produced at or near to the interfaces, either the ASW/vacuum interface or the ASW/Pt interface.[30] Similar experiments have been performed for water-ice adsorbed on TiO_2 (110), in which the same observations of H_2 production at interfaces were reported.[31] Further to this, it was noted in ESD that H_2 formed at the ASW/vacuum interface appears quickly and is independent of electron fluence, while production of H_2 at the ASW/TiO_2 interface starts slowly, gradually increasing to a steady state concentration with increasing electron fluence.

Following electron-induced ionisation or excitation of the water molecules, the possible outcomes may be summarised as follows:

Recombination: $H_2O^+ + e^- \rightarrow H_2O^*$ (2.23)

Hydronium ion formation: $H_2O^+ + H_2O \rightarrow H_3O^+ + OH$ (2.24)

Electron capture: $OH + e^- \rightarrow OH^-$ (2.25a)

$H_3O^+ + e^- \rightarrow H_3O^*$ (2.26b)

Electron trapping by ice $e^- \rightarrow e^-_{trap}$ (2.27)

According to Bergeld and Chakarov,[159] the large number of defects in amorphous solid water enhances the probability of creating excitons, an idea which is consistent with studies by Kimmel *et al*.[32]

Experiments using layered films appear to rule out reactions of hydroxyl radicals in H_2 production; although the presence of the OH radical does accelerate the production of H_2, this is most likely through hydroxylation of the TiO_2 surface.[33]

Production of oxygen

In comparison with hydrogen production, the formation of molecular oxygen in irradiated ASW films is a minor process, yet the two productions mechanisms have some characteristics in common. O_2 production occurs solely at the ASW/vacuum interface, rather than in the bulk, however, in contrast with H_2 production, no O_2 is produced at the buried interface. This suggests that either the mechanism for oxygen production is entirely different from hydrogen production, or else that O_2 precursors are produced in the bulk and diffuse to the surface before reacting. Experiments using isotopically-labelled water layers indicated that dissociation of water at the

buried interface does indeed contribute to O_2 production at the surface.[34] In contrast with the single step reaction to produce hydrogen by water decomposition, it appears that O_2 production requires a 2-step reaction involving OH or possibly OH^-.[23] Hydroxyl species produced at the buried interface must be transported to the surface, but not through any exciton mechanism. Instead, it is likely that migration of OH occurs via the H-bonding network.

2.3.2. Electron-irradiation of CO:H_2O ices

Due to the role of CO in the formation of simple hydrocarbons in the interstellar medium (ISM), much of the research into the reactions of CO in water-ice has been carried out by the astrochemistry community.[35] In their 2006 paper, Zheng *et al* highlight the importance of reactions at the surface of water-ice in the formation of molecular hydrogen in interstellar space.[28] Several groups have also published work supporting an ice-catalysed mechanism for the production of methanol as an explanation for observed abundances of methanol on comets and in interstellar space.[25,36,37] In 1995, Mumma *et al* published findings of ethane, methane and carbon monoxide along with water ice on the comet C/1996 B2 Hyakutake, and investigated their findings for evidence of the interstellar origin of these species.[38]

The work outlined in this thesis aims to study the electron-stimulated reactions of layered ASW/CO/ASW ices, which may proceed by both oxidation and reduction. The following is a review of recent work in this area, specifically irradiation of ices incorporating CO and other simple carbon-containing species.

Production of H_2 and O_2

L. Šiller *et al* investigated the role of trapped electrons and precursors on the oxidation pathway in CO_2 ices. In a study of electron stimulated desorption from

pure CO_2 and H-doped CO_2 films, the authors report a considerable difference between the yields of molecular oxygen (in the form of O_2^+) from pure CO_2 compared with hydrogen-doped CO_2, with the result that the presence of H_2 significantly decreases the yield of O_2^+.[39] These effects are not explained, but raise a number of questions about the nature of energy transfer in ice films, as well as the exact mechanism for oxygen production and the role of precursors. The authors argue that a two step reaction process is necessary since a direct ion-molecule reaction cannot occur below 21.5 eV. They consider atomic oxygen as the precursor but also note that OH, HO_2 or H_2O_2 may be involved.

A subsequent paper to investigate low energy (10-100 eV) electron-stimulated reaction products from pure CO_2 ices as well as D_2O/CO_2 ices suggests that trapping of precursors within pores in the CO_2 may provide an explanation for the observed yields of O_2^+.[40] In addition, production of O_2^+ in pure CO_2 ice is attributed to a second pathway, strongly influenced by low energy electrons trapped in the ice.

In electron-irradiation of ASW films capped with methanol, it was found that the presence of a methanol cap layer effectively suppresses the production of both O_2 and CO_2.[41] This is consistent with previous observations of oxidation reactions occurring primarily at the vacuum interface, and is attributed to quenching of reactions between methanol and OH radical precursors to O_2 formation. This observation is consistent with their proposed mechanism of migration of excited states or defects through the ice to the interfaces as part of the mechanism for H_2 and O_2 production in water ice[42].

Some suppression of the H_2 yield was also noted, most likely for the same reason, namely that reaction channels at one of the interfaces were essentially quenched. For

CO studies where CO is deposited as a layer within the film rather than as a capping layer this quenching effect is not expected. However, since much evidence points towards some prior reactions taking place in the bulk, it will be important to note the relative yields of reaction products for different compositions of CO/ASW ices in the current work.

Hydrogenation reactions

The hydrogenation of CO in water-ice is key to the production of simple hydrocarbons, however there has been much debate about which products are observed following irradiation. In the first of the two conflicting papers about production of formaldehyde and methanol by H-atom bombardment of pure CO films, Hiraoka *et al* observed only formaldehyde production, whereas Watanabe and Kouchi reported efficient methanol production.[43,44] In work published by researchers at the University of Leiden, results showed both formaldehyde and methanol production for several-monolayer thick films exposed to a relatively high H-atom flux ($5x10^{13}$ cm^{-2} s^{-1}). At a lower H-atom flux ($1x10^{12}$ cm^{-2} s^{-1}), formaldehyde is easily detectable, but significantly lower yields of methanol are observed. The electron fluxes in this study were chosen to reflect the different conditions of the two papers by Hiraoka *et al* and by Watanabe and Kouchi and provide a clear explanation for the discrepancy in their results. The results support a suggestion by Hidaka and co-workers that differing H-atom flux may be responsible for the difference in product yields. [45] By monitoring the yields of formaldehyde and methanol over time, it was demonstrated that the onset of methanol production occurs at the expense of formaldehyde production; this is consistent with a mechanism in which methanol is produced by hydrogenation of formaldehyde.

Although information regarding the dependence of yield on film thickness in these experiments is limited, it was noted that for films with ~4-9 ML of bulk CO, the yield of reaction products appears independent of thickness. This probably results from the fact that this film thickness is on the order of the penetration depth of electrons, meaning that the whole film receives a similar dose.

The influence of temperature on the reactions is very apparent: Figure 1 shows the yields of CO, H_2CO and CH_3OH versus H-atom fluence at four different temperatures.[46] As the temperature increases between 12 and 15 K, both the rate of production and the final yield of methanol increases, however for formaldehyde the production rate decreases at higher temperatures. This effect is attributed to differences in the reaction barriers to H + CO and HCO + H_2CO. At temperatures >15 K, changes in the sticking coefficient of H atoms to the surface along with increased production of H_2 result in lowering of the yields of both formaldehyde and methanol.

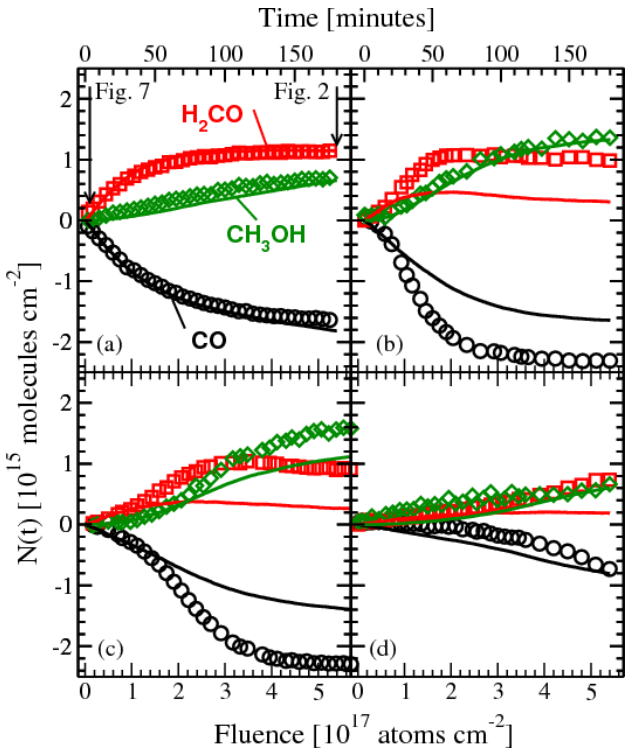

Figure 1 - Yields of CO, H_2CO and CH_3OH during H-atom bombardment of CO ice at surface temperature a) 12.0K b) 13.5 c) 15.0K and d) 16.5K. Experimental data (symbols) and Monte Carlo simulation results (lines) are shown.[46]

In contrast with these H atom experiments on pure CO ice, work by Hudson and Moore reports on the products of irradiating mixtures of CO and H_2O with 0.8 MeV protons.[47] In these experiments, in which thicker films experience much higher energy irradiation, a greater variety of products are observed: formyl radical (HCO), formaldehyde (H_2CO), formic acid (HCOOH), methanol (CH_3OH), methane (CH_4) and carbon dioxide (CO_2). Figure 2 shows the trend in product yields for these molecules versus radiation dose for a mixed H_2O:CO (5:1) film. The figure clearly shows the decline in CO, as well as the delayed onset and increasing yield of methanol with increasing dose. Once again, the trend in formaldehyde abundance is less straight-forward, but the concentration of formaldehyde no longer increases after the onset of methanol production. These trends appear to support a sequential hydrogenation scheme: $CO \rightarrow HCO \rightarrow H_2CO \rightarrow CH_3O \rightarrow CH_3OH$.

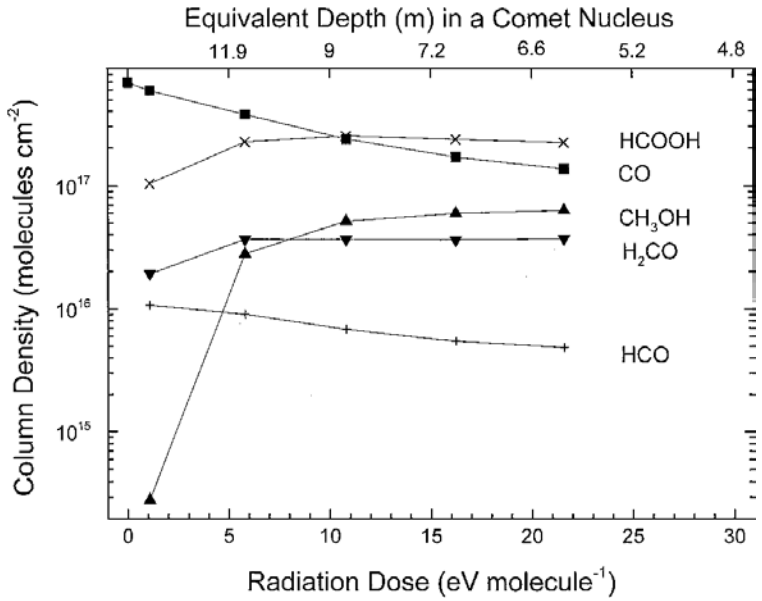

Figure 2 - Abundance of CO, HCO, HCOOH, H_2CO and CH_3OH in an H_2O:CO (5:1) ice as a function of radiation dose at 16 K [47]

Further experiments in which ASW:formaldehyde ices were irradiated add support to a sequential H-atom addition scheme, although with some uncertainty as to the identity of the radical formed by H-atom addition to H_2CO, which may be H_2COH or CH_3O.

Yoshinobu and co-workers investigated the temperature and electron energy dependence (5-50 eV) of reactions within layered ASW/CO/ASW ices.[48] The authors confirm observations of the formyl radical, formaldehyde and methanol in the reduction channel using RAIRS, however they remark on the temperature dependence of the reduction channel, finding it necessary to simultaneously heat and irradiate the sample in order to observe reduction products. This feature is explained in terms of increased excitation and freedom to change orientation, which promote the successive reactions in which the reduction products are formed. In comparison with Hudson and Moore's similar work, this study uses much lower energy irradiation, which may be sufficient to explain the discrepancy in product detection at

low temperatures. It is important to note that heating alone in these experiments is not sufficient to cause a reaction between H_2O and CO, as this would require much higher temperatures, above those at which H_2O and CO would desorb from TiO_2.

The formation of other hydrogenated molecules such as 2-carbon molecules, polymeric species, cyclic hydrocarbons, or aromatics was not observed in either of these H_2O-rich ice studies, however this is in contrast with studies where pure carbon-containing ices were irradiated. For example, in a 1992 study of proton and alpha irradiation of pure methanol ices, Kaiser and Roessler found lengthening of the carbon chain quite common, therefore it may still be possible to observe these types of products in mixed ices.[49] In addition, depending upon the timescales of the experiments, radical-radical reactions may occur, for example $CH_3O + CH_3O \rightarrow H_2CO + CH_3OH$, which offer an alternative route to production of formaldehyde and methanol.

Oxidation reactions

Following irradiation of CO/H_2O films, the only carbon-containing oxidation product is CO_2, which has been observed in many of the studies mentioned previously. Yoshinobu and co-workers used RAIRS to confirm the appearance of CO_2 by oxidation of CO.[48] They also found that with respect to electron energy, the yield of CO_2 increases rapidly above 21 eV. The authors conclude that the energy dependence is due to a number of additional excited states which become accessible. They also note the appearance of the low cross-section dipolar dissociation pathway above 16.9 eV. The authors attribute the small amounts of CO_2 produced below 20 eV to the condensed-phase dissociative electron attachment mechanism (chapter 2.4.2). Much like the formation of O_2 in pure H_2O ices, ESD traces for CO_2

production in these experiments rise slowly, indicating a requirement for the concentration of reaction precursors to build up. In fact, the formation of CO_2 shares many characteristics with O_2 formation, most likely as a result of competition between the H_2O and CO molecules for reactive OH radicals. Though it has not yet been identified, one might predict that CO_2 is produced mainly at the ASW/vacuum interface, in the same way as O_2 in pure ASW, perhaps from the same OH and HO_2 precursors.

2.3.3. Energy transfer through water-ice

Given the observations of radiolysis products in thick films, the question of the energy transfer mechanisms responsible has received much attention. Previous studies of electron-stimulated reactions in pure ASW ice attributed reaction products formed at the deeply buried ice-substrate interface to diffusion of hydronium ion defects (H_3O^+) or excitons. The following is a brief overview of the accepted knowledge concerning energy transfer mechanisms in water-ice.

Excitons

In the condensed phase, excitation of a molecule may result in the elevation of an electron in one orbital to a higher energy orbital, creating a "hole" in the lower energy orbital. This form of excitation is known as an electron-hole pair and behaves as a particle or "exciton", moving from one molecule to another.[50] In molecular solids (rather than metals or semi-conductors), the mobility of electron-hole pairs is affected by the strength of the interactions between molecules, specifically, the transition dipole moment interactions. An electric dipole transition in a molecule is accompanied by a shift of charge, which exerts a force on an adjacent molecule, which in turn shifts its charge. In this way, the electron-hole pair migrates through the structure. Strong dipole moment interaction, such as hydrogen-bonding in water-

ice, leads to highly mobile excitons, making exciton migration an effective mechanism for energy transfer through a solid.

In molecular solids, Frenkel excitons, in which the electron and hole are localised on a single water molecule and jump together to a second molecule, are most common (compared with Wannier excitons, in which the electron and hole may separate over large distances). In their 1997 paper on low energy electron irradiation of D_2O ices, Kimmel and Orlando attribute observations of certain atomic fragments (specifically the $D(^2S)$, $O(^3P_2)$ and $O(^1D_2)$ fragments) to dissociation of Frenkel excitons.[42] Frenkel excitons in water-ice have been identified at 8.6, 10.4 and 14.5 eV using optical absorption spectroscopy and attributed to the $1b_1 \rightarrow 4a_1$, $3a_1 \rightarrow 4a_1$ and $1b_2 \rightarrow 4a_1$ transitions, respectively. [51] All of these transitions are dissociative due to the anti-bonding nature of the $4a_1$ orbital, which lies in the band gap between the valence and conduction bands.

A theoretical study by Hahn *et al* of the optical absorption spectrum of cubic, hexagonal and amorphous water-ices predicted that exciton effects are 40% reduced in solid water compared with gas-phase measurements.[52]

Molecular defects

Energy transfer in ices may proceed via transfer of point defects through the lattice. There are several types of defect, but the most important in electron-irradiated ices are molecular defects and point defects (see later). In ASW, there are a greater number of defects compared with crystalline ices, as a result of the increased degree of disorder and pores formed during the low temperature deposition. Molecular defects arise when an H_2O molecule is displaced from its position within the lattice, leaving a vacancy, instead sitting in an otherwise unoccupied site, usually in one of

the voids in the lattice structure, forming an interstitial. Alternatively, other atoms and molecules formed in water radiolysis (i.e. H, OH) may form interstitials. EPR studies of water-ice suggest that H atoms sit in interstitial sites within the ice and have zero net interaction with surrounding molecules.[53] Diffusion of molecular defects fits the Arrhenius relation (2.27):

$$D = D_0 \exp\left(\frac{-E_a}{kT}\right) \qquad (2.27)$$

Where D is the diffusion coefficient, T is the temperature, k is the Boltzmann constant, and E_a is the activation energy of the diffusion process. Using this equation, along with experimentally determined values for the activation barrier (E_a) to H atom diffusion, the diffusion rate (in jumps per second) has been calculated as a function of temperature, arriving at a value of around 10^4 s^{-1} for H atoms at 70 K.[53] Although a number of studies have been conducted to study the mobility of H atoms and water molecules in ASW, as yet, there do not appear to be any measurements of OH or O atom hopping rates. [54,55] Previous work by Kimmel *et al* indicated that the onset of OH mobility occurs around 60-100 K, but similar studies are yet to be performed to investigate mobility of the O radical.

Ionic defects

Ionic point defects, for example H_3O^+or OH^-, are formed by the transfer of a proton between molecules in the lattice.[56] Diffusion of ionic defects then proceeds via a series of thermally-activated jumps, according to the same Arrhenius relationship shown in equation (2.27). In comparison with molecular defects, which are transferred by the movement of an atom or molecule from one vacancy to another, ionic defects are transferred by reorientation of bonds within a hydrogen-bonding chain.

2.4. Dissociative Electron Attachment (DEA)

At energies approaching the ionisation energy of a medium, low-energy electrons interact either by excitation of neutral molecules or attachment to the molecule, forming a TNI, described previously (2.1.1). Excitation may be accompanied by dissociation of the molecule into neutral ground state or excited fragments, or alternatively the excited molecule may decay by energy transfer. In approximately 85% of cases, decay of the TNI formed in electron attachment proceeds within a few femtoseconds, by re-emission of the incident electron ("auto-detachment"), leaving the molecule in a vibrationally and rotationally excited state.[57] However, the TNI may alternatively decay by dissociation, completing a mechanism known as dissociative electron attachment (DEA).

Despite its relatively small cross-section (~1.3×10^{-18} cm^2 in water vapour),[58] DEA is the dominant mechanism where the incident electron energy is less than the ionisation threshold of the medium.[59] Equation 2.44 shows the general equation for DEA. The energy state of the parent (AB), along with the energy of the incident electron, largely determines the lifetime and the fate of the TNI.

$$AB + e^- \rightarrow [AB]^{*-} \rightarrow A^- + B \qquad (2.28)$$

Although there is considerable information available concerning low energy electron impact excitation of water, dissociative electron attachment has proved more difficult to observe and measure. Observation of the low ion yields in DEA requires high resolution, high sensitivity techniques, some of which have only been developed in recent years.

Since the work of L. Sanche and others identifying the importance of this mechanism for biological processes, there has been a resurgence of interest in this field.1 Given

the biological relevance of H_2O, a number of studies have been conducted to study DEA in water, as well as a wide range of other molecules from simple organics such as methanol[60] and acetonitrile[61] to complex biological molecules such as DNA bases[62] and antipyretics.[63]

2.4.1. DEA in gas-phase H_2O

Dissociative electron attachment was first observed in gas-phase water by W. W. Lozier as early as 1930, clearly discernible in measurements of anion yields as a function of electron energy, due to the resonant nature of the process.[64] The planned studies of DEA in water will be conducted in the gas-phase, which is therefore the focus of this discussion.

Three resonances have been observed and assigned in DEA to water, each arising from a different electronic state of the TNI, H_2O^{*-}. The energies of these resonances have been estimated by measuring anion yields (see equations 2.45-2.49) as a function of incident electron energy. Table 2 summarises the results of a number of studies of DEA in gas-phase H_2O, showing the energies attributed to the three resonances of DEA. In the discussion which follows, the widely accepted values of 6.5 eV, 8.5 eV, and 11.8 eV will be used to refer to DEA resonances in water.[65]

Table 2 - Incident electron energy at which peak anion yield is observed/eV

	Electron energy at which peak anion yields were measured / eV			
Reference	*Compton & Christophorou (1967)*[66]	*C. E. Melton (1972)*[67]	*Jungen, Vogt &Staemmler (1978)*[68]	*Belic, Landau & Hall (1981)*[65]
1st resonance	6.5 ± 0.1	6.4 ± 0.2	7.0 ± 0.1	6.5 ± 0.1
2nd resonance	8.6 ± 0.2	8.4 ± 0.2	9.1 ± 0.1	8.5 ± 0.1
3rd resonance	11.4 ± 0.1	11.2 ± 0.2	11.8 ± 0.1	11.8 ± 0.1

Each of the three resonances in DEA to water is formed when a low-energy electron collides with a neutral H_2O molecule, promoting an electron from a core orbital of the neutral water molecule to a high-energy Rydberg orbital, the 3s orbital. In ground-state H_2O, the 3s orbital is strongly coupled to the $4a_1$ orbital, therefore this orbital is sometimes denoted $3s{:}4a_1$. The strongly anti-bonding character of the $4a_1$ orbital ultimately causes the water anion to dissociate. The exact orbital from which the core electron is excited depends upon the energy of the neutral water molecule and the degree of excitation caused by the incident electron.

The ground state electron configuration of water is $^1A_1\ (1a_1)^2(2a_1)^2(1b_2)^2(3a_1)^2(1b_2)^2$, shown in Figure 3. As described, electron attachment involves the promotion of an electron from a core-orbital to the $3s{:}4a_1$ anti-bonding orbital. The three resonance forms of H_2O^{*-} at 6.5, 8.5 and 11.8 eV are assigned to electron promotion from the $1b_1$, $3a_1$ and $1b_2$ orbital, respectively.

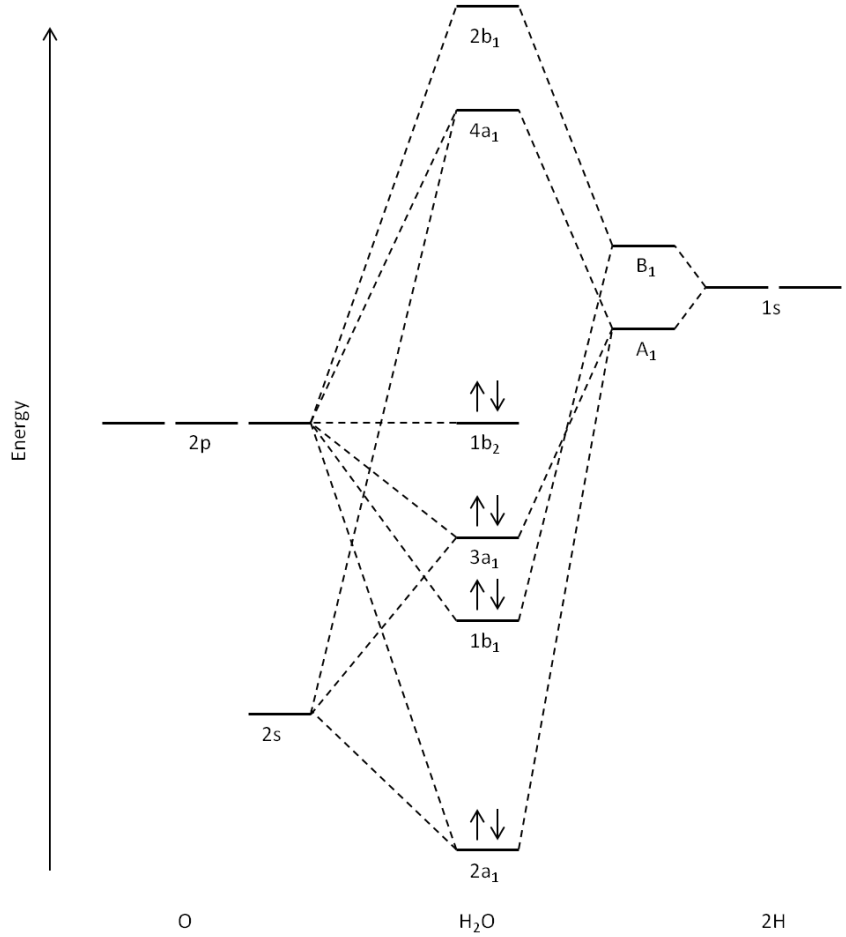

Figure 3 - Ground state electronic configuration of H_2O

Early studies proposed that in DEA the incident electron may occupy the vacancy left by the excited core-electron, forming a shape resonance, accompanied by ro-vibrational excitation of the molecule which however remains in its electronic ground state. However, the preferred explanation is that the incident electron attaches to the same Rydberg orbital as the core-excited electron, resulting in a core vacancy and an electronically excited state of the anion. If the energy of this state is lower than the energy of the ground state anion, then the anion may not simply decay by re-emission of an electron and the incident electron is therefore effectively trapped in a quasi-bound state known as a Feshbach resonance. Typically, for atoms and small molecules, the lifetime of the TNI is on the order of 10-100 fs, however the nature of

the Feshbach resonance results in a relatively long lifetime of the anion, which is more favourable for dissociation.[69]

Following electron attachment to H_2O, the excited state TNI dissociates into fragments. The following list shows the 3 main pathways (2.29-2.31), as well as a proposed 3-body route, reaction (2.32).

$$H_2O^{*-} \rightarrow OH + H^- \quad (2.29)$$

$$H_2O^{*-} \rightarrow O^- + H_2 \quad (2.30)$$

$$H_2O^{*-} \rightarrow OH^- + H \quad (2.31)$$

$$H_2O^{*-} \rightarrow O + H^- + H \quad (2.32)$$

A detailed discussion of the relative cross-sections, anion yields and energy partitioning in the fragments is reserved for chapter 2.4.3; the following is meant only to give an overview of what is generally accepted about reactions (2.29)-(2.32). Both in simulation studies and experiments measuring ion yields, pathways (2.29) and (2.30) have been found to be the most prolific in terms of ion production at all three resonances, with H^- production dominating except at the third resonance, when dissociation via reaction (2.30) has the higher cross-section.

Fragmentation via (2.31) has proved controversial, as production of OH^- by DEA is not predicted by theoretical studies and is observed only in very low concentrations. As such, many authors preferred to explain observation of OH^- as the result of further reactions of the ion fragments following dissociation (equation 2.33 and 2.34).[70]

$$H^- + H_2O \rightarrow OH^- + H_2 \quad (2.33)$$

$$O^- + H_2O \rightarrow OH^- + OH \quad (2.34)$$

Given the high electron affinity of OH (1.83 eV) compared to H and O (0.75 and 1.45, respectively),[71] as well as a relatively low ionisation threshold, it is at first surprising that production of the OH^- anion has the lowest cross-section, however explanation in terms of the geometry of the TNI state has been offered (chapter 2.5.2).

Equation (2.32) shows a 3-body dissociation of the water anion, which proceeds via an excited state of the OH^- ion, proposed by Ram *et al* to account for unexpectedly low kinetic energies observed in H^- anions.[72] Currently, no further studies have been conducted to support or refute the existence of this pathway.

2.4.2. DEA in the condensed phase of H_2O

In addition to gas-phase studies, DEA has also been reported for water in the condensed phase, by observation of H_2 and H^- yields, and by Monte Carlo simulations. Rowntree *et al* conducted the first study which identified DEA in amorphous water-ice by observing H^- anion yields from the surface of thin ASW films irradiated with low energy electrons (0-12 eV).[73] Their observations of the low kinetic energy (0-0.5 eV) of the desorbing fragments, for anions produced at an incident electron energy between 5.9-10.4 eV, suggest that H^- anions produced by DEA react further in the bulk before desorption.

The electronic structure of water ice has been studied both experimentally and theoretically. The lowest energy electronic excitation of H_2O ice has a threshold at 7.3 eV with a maximum at ~8.6 eV. This has been assigned to the $^{3,1}B_1$ ($1b_1 \rightarrow 3s{:}4a_1$) transition, which occurs in gas-phase H_2O at ~7.4 eV. In electron-irradiation of amorphous ice, however, the onset of H_2 yield was recorded at 6.3 ± 0.5 eV, and therefore cannot be produced by dissociation of electronically excited H_2O^*.[74] Instead, production of H_2 by a dissociative attachment mechanism was proposed at

energies below 8.6 eV. Specifically, it was suggested that H^- ions produced in DEA to water (with an onset around 6 eV and a maximum at 7.6 eV)[73] react with H_2O to produce H_2 and OH^-, as shown in equations (2.35) and (2.36). This indirect mechanism is consistent with the low anion kinetic energy results of Rowntree *et al*.

$$H_2O + e^- \rightarrow H_2O^- \rightarrow H^- + OH \qquad (2.35)$$

$$H^- + H_2O \rightarrow H_2 + OH^- \qquad (2.36)$$

The TNI state of H_2O^- at this energy is thought to be the $^2B_1$ state, formed by the promotion of an electron from the $1b_1$ to the anti-bonding $3s{:}4as_1$, which has been previously proposed in the condensed phase by Michaud and Sanche.[75] This state corresponds the 6.5 eV resonance in gas-phase DEA.

The experimental studies are supported by Monte Carlo simulations of low energy electrons in liquid water, which identified that the yield of H_2 could not be fully accounted for without DEA mechanisms at low energies.[76] The authors agree with Kimmel *et al* that DEA produces H^- anions, which react further within the ice to produce H_2. Their simulations appear to discount direct production of H_2 by dissociation of H_2O^- (equation 2.37) as this would necessarily be accompanied by production of O^-, which has not been observed in studies of condensed phase H_2O.

$$H_2O + e^- \rightarrow H_2O^- \rightarrow H_2 + OH^- \qquad (2.38)$$

A further investigation of condensed-phase DEA to water showed three peaks in the H^- anion yield from ASW films, corresponding to the $^2B_1$, $^2A_1$ and $^2B_2$ states observed in the gas-phase.[77] In accordance with earlier studies, the peak energies for these resonances were higher than their gas-phase equivalents, at ~7.0, ~9.0 and ~11 eV. An additional peak in the anion yield in the region 18-32 eV was tentatively

attributed either to the onset of ion pair formation (based on similar observations of the yield of O^- in water vapour by Melton and Neece)[78] or alternatively another previously unreported TNI state formed by promotion of a core electron from the $2a_1$ orbital, however this has yet to be reported elsewhere.

In summary, the DEA process proceeds in the condensed phase via the same dissociative states of H_2O: $^2B_1$, $^2A_1$ and $^2B_2$, which are formed at higher energies in ice, most likely as a result of increased hydrogen bond strengths in solid water, and changes in electron density.

2.4.3. Cross-sections for DEA in water

The relative contribution of a particular scattering process (*i*) to the overall interaction of electrons with water is defined by the electron scattering cross-section (σ_i). Cross-sections are calculated using Beer's law (2.39) for the change in intensity of an electron beam interacting with some density of molecules, *N* over a distance, *l*.

$$I = I_0 \exp(-N\sigma l) \qquad (2.39)$$

As demonstrated by equation (2.39), the change in intensity of the electron beam is proportional to the fraction of molecules which take part in the particular scattering reaction being measured, given by σ, in cm^2.

Cross-section data for electron interactions with water vapour has been recently reviewed by Itikawa and Mason; cross-section values recommended in their review for a number of electron scattering processes in water are shown in Figure 4.[14]

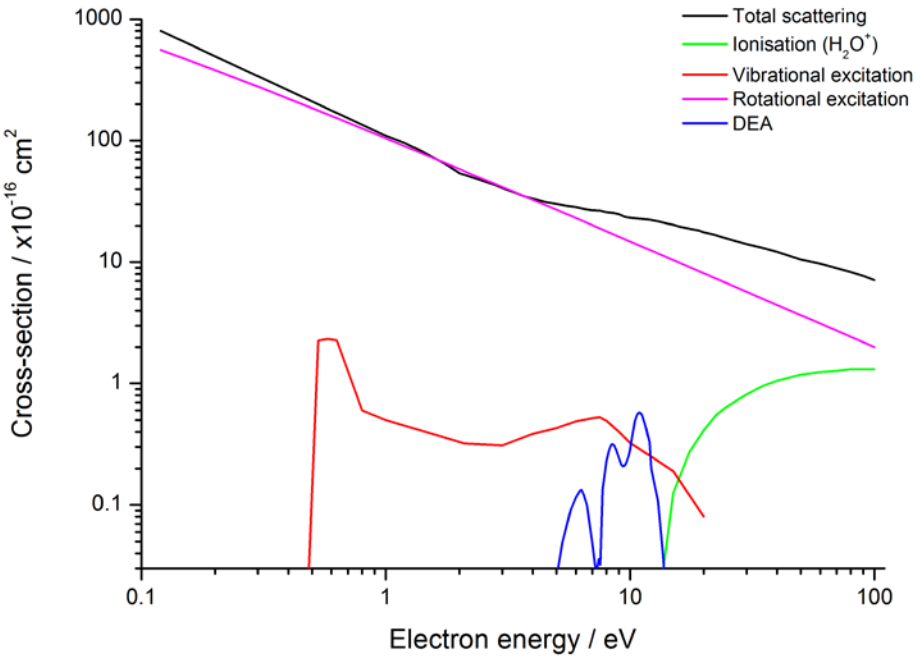

Figure 4 - Recommended cross-section data for electron interactions with water vapour as a function of incident electron energy

The ionisation cross-section falls to zero at ~12 eV, as expected, as this is approximately the ionisation threshold of water. At low electron energies, the highest cross-sections are for rotational excitation, which makes a smaller contribution as electron energy increases, where ionisation and inelastic scattering processes may be accessed. The dissociative electron attachment (DEA) cross-section shows the fine structure associated with the resonant nature of this process. The figure shows that for a narrow range of low energies, DEA contributes significantly to the total scattering cross-section.

In summary, in the region where DEA occurs (5.5-12 eV), the total scattering cross-section is on the order of 25×10^{-16} cm^2, while the total DEA cross-section is 5.76×10^{-17}cm^2, two orders of magnitude smaller. Values for the maximum cross-

sections measured by recording H- and O- ions from gas-phase DEA to water are summarised in Table 3, for reference.

Table 3 - Summary of cross-section measurements for H^- and O^- yields from DEA to water at each resonance

DEA Resonance	**σ_{max} for H^- anion production and (O^- anion production) from DEA in water / x10^{-18} cm^2**			
Reference	*Compton and Christophorou (1967)*[66]	*C. E. Melton (1972)*[67]	*Haxton et al (2007)*[79]	*Krishnakumar et al (2007)*[80]
6.5 eV	6.9 (−)	6.37 (0.13)	10.37 (0.012)	4.6 (0.039)
8.5 eV	1.3 (−)	1.17 (0.32)	4.14 (−)	1.3 (0.13)
11 eV	− (−)	− (0.57)	0.521 (0.187)	0.12 (0.27)

In the condensed phase, cross-sections for low energy electron scattering processes differ quite considerably from the gas-phase measurements.[69] Cross-sections for DEA in the condensed phase are generally lower than the corresponding gas-phase measurements.[81] This is due to a combination of effects of the condensed medium, including polarization response, intermolecular interactions and the availability of additional decay channels. Cross-sections for DEA to water-ice have not been made absolute, as they are highly dependent on the ice morphology, thickness and influence of surface reactions.

2.5. Previous studies of DEA to water

As discussed, each resonance in the cross-section for DEA in water arises due to the dissociation of a different excited state of H_2O. Initial assignments of the dissociative states of the H_2O^{*-} molecule in DEA by experiment were made by comparison of observed anion yields with theoretical calculations of vertical excitation energies of H_2O. More recently, using ion momentum imaging, angular distributions of the products were recorded. These measurements give a clearer picture of the resonance state as each state has a symmetry determined by its electronic configuration, and it is this which dictates the angular behaviour of the dissociated fragments. In the following discussion, only gas-phase DEA is considered, as this will be the focus of experiments using the LIF apparatus.

2.5.1. Assignment of resonance forms

Following on from early observations of H^- ions from electron impact on water by Buchelnikova,[82] and Dorman,[83] the first complete description of DEA in water as a resonant process peaking at 6.9, 8.9 and 11.4 eV was reported by Compton and Christophorou in 1967.[84] Assignment of the resonance forms of H_2O^{*-} at each energy has since been carried out in a number of papers, which are now addressed.

First resonance

Weiss and Krauss were the first to propose an assignment for the dissociative state of H_2O^{*-} formed at ~6.5 eV, arguing for dissociation via the $^1B_1$ state of H_2O^{*-} based on observed H^- anion yields.[85] The $^1B_1$ state is formed when the core-excited electron is promoted from the $1b_1$ orbital to the $3s{:}4a_1$ orbital. Angular distribution measurements by Hall *et al* in 1974 recorded H^- distributions peaking at 100°, which is consistent with dissociation via the $^1B_1$ state.[86] Further angular distribution

measurements as well as energy distribution of the H^- fragment by Hall *et al* supported this conclusion.[65] Calculations of the vertical excitation energy of various states of the H_2O anion, parent and grandparent states by Staemmler *et al* showed that dissociation of water via the $^1B_1$ state at ~7 eV is exothermic by ~3.5 eV, which would contribute to high vibrational, rotational and translational energies of the fragments. This is consistent with the experimental observations of Hall *et al*, which showed high kinetic energies for H^- fragments, with high vibrational excitation of OH produced at this resonance.

Second Resonance (8.5 eV)

Initially, the second DEA peak was assigned to the $^2B_1$ resonance,[67] however, studies which followed preferred dissociation via the $^2A_1$ state, which is formed by electron attachment to the first excited state of the water cation (H_2O^+), $^3A_1$ $(3a_1)^{-1}(3sa_1)$. Two papers by Hall *et al*[87] showing measurements of the angular distribution of H^- ions identified the $^2A_1$ state and this was backed up by *ab initio* calculations performed study by Staemmler *et al*.[68] Weiss and Krauss also proposed dissociation via the $^2A_1$ state.[85] Theoretical studies by Haxton and co-workers appear to corroborate dissociation via the $^2A_1$ state.[88]

In their early experiments on DEA, Curtis and Walker expressed doubts at the existence of a purely $^2A_1$ channel, instead proposing pre-dissociation via the $^2B_1$ state.[60] More recently, Ram *et al* also proposed dissociation via the $^2B_1$ state following observations of H^- anions which deviated considerably from the axial recoil approximation, which implies that no rotational or structural change in the bond orientation occurs before dissociation. Instead, they presented a model combining both the $^2A_1$ and $^2B_1$ pathways.[72] Although this model could convincingly

explain the O^- anion yields at this energy, the $OH + H^-$ pathway would not be observed at all. Their assignment of a mixed state or even pure $^2B_1$ state was withdrawn in 2012, in favour of agreement with other momentum imaging studies, which support dissociation via $^2A_1$.[89, 90]

Third Resonance (11.8 eV)

The dissociative state of H_2O^{*-} at the third resonance, which peaks at around 11.8 eV, is thought to be a $^2B_2$ state formed by promotion of an electron from the $1b_2$ orbital of the water anion.[65] There is much less data available concerning the third resonance, partly due to the considerably lower cross-section for this pathway compared with DEA at the first two resonances, however, anion yields typically show a broad peak at ~11.8, which approximately corresponds to the vertical excitation energy of 12.75 eV calculated for $^2B_2$ state.[68] This state is also consistent with assignment of resonance forms in electron attachment to H_2S which has a similar electronic configuration to H_2O.[91]

Summary

Currently, the strongest evidence currently points to three resonances in the dissociative attachment to water: via the $^2B_1$ state at ~6.5 eV, via $^2A_1$ at ~8.5 eV, and via $^2B_2$ at ~11.8 eV. The maximum energy of each resonance is in good agreement with calculations of the vertical excitation energies of each of these states relative to the ground state: 6.65 eV, 9.26 eV and 12.75 eV for the $^2B_1$, $^2A_1$ and $^2B_2$ states, respectively.[92] The three states are formed by promotion of an electron to the $3s{:}4a_1$ orbital from the $1b_1$, $3a_1$ and $1b_2$ core orbitals, accompanied by attachment of an incident electron also to the $3s{:}4a_1$ orbital.

2.5.2. Dominant dissociation pathway at each resonance

Dissociation of the TNI in DEA to water may proceed by three main routes, described in chapter 2.4.1 (equations 2.29-2.31). At each resonance, all three routes may be observed; the following is a discussion of the relative yields of anions at each resonance, arriving at an assignment of the dominant dissociation pathway for each.

According to measurements by Schulz, the total anion yield at each resonance appears in the ratio 8:2:1 for the first, second and third resonances respectively, indicating that in general, the cross-section for anion production at the first resonance is highest.[93] This agrees in principle with earlier cross-section calculations for anion yields at each resonance, which assigned values of 6.7×10^{-18}, 1.4×10^{-18}, and 0.6×10^{-18} to the first, second and third resonances, respectively. In their 2001 paper, Harb *et al* showed that processes (2.29) and (2.30) dominate for DEA in H_2O.[94] This is supported by measurements of the relative anion yields: typically, H^- has the highest cross-section, with peak yields up to 2.5 times the yield of O^- anions, while reported OH^- yields are around 5% the magnitude of O^- yields at the same resonance.[67]

The yield of H^- anions is highest in the first resonance, suggesting that reaction (2.29) may dominate at this resonance. The dissociation partner of H^-, OH has also been recorded at this resonance, in the electronic ground state, but in a state of ro-vibrational excitation. Reaction (2.30) also occurs at this resonance, as observed in measurements of O^- yields. The branching ratio of these two reactions seems counter-intuitive, as O has a higher electron affinity than H. However, investigations by Haxton *et al* suggested that dissociation to O^- and H_2 requires changes to the geometry of the transition state, which makes it a less favourable route compared

with H^- + OH, which is accessible without altering from the C_{2V} equilibrium geometry of H_2O.[88, 92]

The second resonance is more equally divided between dissociation by reactions (2.29) and (2.30), though production of H^- still remains dominant. A small contribution from reaction (2.31) is also recorded at this resonance, but overall this resonance has the lowest cross-section for production of OH^- and is therefore not the major channel.

Until measurements by Belic *et al* in 1981, it was thought that no H^- was produced at the third resonance, due to the lack of observation of H^- at this energy. Belic *et al* reported H^-yields around 600 times lower at 11.8 eV than at 6.5 eV, which explains why less sensitive earlier experiments had not observed this channel. The yield of O^- peaks at the third resonance, suggesting that reaction (2.30) dominates dissociation at this energy. The total cross-section for anion production at this resonance is considerably lower than at the first two; Schulz reported the overall cross section for the third resonance to be in 1:8 ratio with the cross-section of the first resonance, even including the contribution of the primary channel at this resonance: $O^- + H_2$.[93]

OH^- is observed in very small quantities at all three resonances, meaning that the dissociation into H and OH^- fragments is unlikely to be a dominant pathway for any of the three resonances.[95] In fact, a number of early studies questioned whether OH^- is formed directly through DEA or whether it is in fact produced by further reactions of H^- or O^- ions, referring to the steep increase in the levels of OH^- after O^- and H^- have peaked, as well as the apparent dependency of the OH^- yield on pressure.[96] Formation of OH^- by DEA is not predicted in theoretical models.[92,97] Based on the findings of Melton,[67] Fedor *et al* carried out further experiments to prove that OH^-

could indeed by formed by DEA in water, however the debate persists due to the continued absence of OH^- in theoretical studies.

2.5.3. Energy partitioning in the parent and product ions

In studies of DEA, the vibrational and rotational energies of the parent anion are particularly important. In their 1989 paper, Chen and Chantry reported that the so-called vibrational temperature has a dramatic effect on the cross-section of DEA in C_3F_8.[98] In similar experiments on HCl and DCl, Allan and Wong also showed that an increase in the gas temperature from 300 to 1200 K caused an enhancement of several orders of magnitude in the cross section for DEA of these molecules.[99] These and other comparable findings are supported by the theoretical studies of Bardsley and Wadehra, who conducted a semi-empirical analysis of DEA in H_2 and D_2, concluding that the DEA cross-section near threshold is enhanced significantly by vibrational or rotational excitation of the initial molecule.[100] As such, knowledge of the excited states and potential energy curves for the molecules concerned forms an essential part of the understanding of DEA.

DEA in water is an exothermic process, which has the result that the H_2 molecule and OH radicals produced are often in a highly excited state and with high kinetic energies.[68] Fedor *et al* state that typically 30-50% of the energy in DEA is portioned to kinetic energy of the fragments.

The energy portioned to the fragments is not evenly distributed between the two dissociation partners. By measuring the kinetic energy of one of the dissociated fragments, it is possible to deduce the internal energy of the partner. Equation (2.40) shows the relationship between the internal energy of OH (E_{OH}), the incident electron energy (E_i) and the kinetic energy of the H^- anion (E_H).

$$E_{\mathrm{OH}} = \left(1 - \frac{m}{M}\right)(E_{\mathrm{i}} - D - E_{\mathrm{H}}) \qquad (2.40)$$

Here, *m* and *M* are the masses of H and H_2O, respectively, while *D* is the dissociation energy of H_2O^- to H^- and OH.

A study by Kawazumi and Ogawa found that as little as one seventeenth of the energy released in the dissociation is portioned to OH. Nonetheless, OH from DEA to water has been observed in both the ground and first electronic excited state, and is always recorded in a high state of vibrational and rotational excitation.

2.5.4. OH Production Channels in DEA to H_2O

At each resonance described, the excited anion may dissociate in any of the three ways described by (2.29-2.31) above. The intention of this work is to examine OH production in gas-phase DEA of water using laser-induced fluorescence (LIF) spectroscopy. Since OH is the dissociation partner for H^- anions, it is reasonable to assume that OH is produced at all three pathways where H^- is observed.

First Resonance

The main dissociation channel at this resonance produces H^- (1S) and OH ($X^2\Pi$). According to experiments by Ram *et al*, the threshold for production of OH occurs at 4.35 eV, with peak OH production observed at 6.5 eV.[72]

The OH produced via this channel is in a high vibrationally excited state. Although the H^- generated at this energy has very high kinetic energy, suggesting only very little ro-vibrational excitation of OH, the broad range in energy observed points to at least some excitation of the OH molecule.[92] Hall and co-workers reported observations of broadening of vibrational lines in the optical spectrum of ground state OH, suggesting rotational excitation.[65] This is consistent with observations of

vibrational lines in the spectra of H^- recorded by Belic *et al* and with reported relative intensities of vibrationally excited levels of OH up to $\nu = 4$ (Table 4).[65]

Table 4 - Relative intensities of vibrational levels of OH fragment at 6.5 eV

V	**Relative intensity**
0	1.00
1	0.82
2	0.57
3	0.32
4	0.25

Second Resonance

At the second resonance, H_2O^- again dissociates into H^- and $OH(X^2\Pi)$. The OH molecule is both vibrationally and rotationally excited. By fitting simulated vibrational state data to the observed H^- energy distribution, Ram *et al* reported OH molecules in vibrational states from $\nu = 0$ to $\nu = 9$, with the relative intensities shown in Table 5. These values show the most probable vibrational state of OH at 8.5 eV to be $\nu = 2$, which is consistent with observations by Belic *et al*, however, calculations by Haxton *et al* predict the peak probability to be $\nu = 1$.[101]

OH shows high rotational excitation at this resonance compared with the first resonance, which makes it difficult to observe vibrational fine structure. The excess of rotational energy may result from the rapid changes in orientation required to dissociate the $^2A_1$ state. Currently, no studies have been conducted to directly record rotationally-resolved internal energy distributions of OH spectra from the dissociative electron attachment process in H_2O.

Table 5 - Rotational energy distribution of OH at 8.5 eV

V	**Relative intensity**
0	0.26
1	0.42
2	1.00
3	0.96
4	0.88
5	0.74
6	0.46
7	0.39
8	0.20
9	0.11

Computing the accurate rotational energy of the OH ($X^2\Pi$) fragment produced here has important implications for the debate over whether it is the $^2A_1$ state or $^2B_1$ state which dissociates here. In addition, discrepancy in rotational energies may account for much of the uncertainty on this subject, so clearly it would be of use to obtain high-resolution rotational spectra for the OH produced here. Despite the volume of high resolution studies of OH produced from electron impact on H_2O, none directly address the internal energies of OH produced in DEA (rather than inferring them from H^- measurements).

Third Resonance (11.8 eV)

The third resonance is by far the weakest channel for production of OH and is somewhat different in that OH is produced both in the ground state and in its first electronically excited state: $OH(A^2\Sigma)$, which may return to the ground state by fluorescence. The $OH(A^2\Sigma)$ produced also shows vibrational and rotational excitation.

There is some evidence for the total dissociation of OH ($A^2\Sigma$) to produce H and O radicals, which gives further credence to the arguments alluded to previously for 3-body fragmentation at the third resonance.[58]

In summary, in DEA to water, OH is recorded in both the electronic ground and first excited states, with carrying degrees of ro-vibrational excitation, as shown in equations (2.41)-(2.43), depending on the energy of the incident electron, and the amount of dissociation energy apportioned to H^-.

$$H_2O^{*-} \rightarrow H^- + OH(X^2\Pi)(v) \qquad (2.41)$$

$$H_2O^{*-} \rightarrow H^- + OH(X^2\Pi)(v,r) \qquad (2.42)$$

$$H_2O^{*-} \rightarrow H^- + OH(A^2\Sigma)(v,r) \qquad (2.43)$$

2.5.5. Previous Studies of OH ($X^2\Pi$) formed by electron impact on H_2O

As discussed, OH is produced in two forms by DEA in water: ground state OH ($X^2\Pi$) and the first electronically excited state OH ($A^2\Sigma$). Some studies of the internal energy distribution of OH produced in electron impact on water have been conducted, by observation of direct fluorescence from OH ($A^2\Sigma$) produced at the second and third resonances, [102] and by laser-induced fluorescence (LIF) of ground state OH ($X^2\Pi$).[103] Currently, only one study has attempted investigate OH produced specifically by DEA to water, although OH LIF spectra were not successfully recorded.[94]

Kawazumi and Ogawa reported the first measurements of the internal and translational energies of the OH ($X^2\Pi$) fragment produced by controlled electron impact on water for incident electron energies of 100 and 150 eV. [104] At these incident electron energies, high rotational excitation of the ground state was

observed, with rotational states up to 25 populated. The rotational "temperatures" of the OH R_1 and P_1 branches were measured to be 560 ± 50 K and 470 ± 50 K, respectively. In addition, Doppler profiling of individual rotational lines was used to calculate the translational energy of OH fragments produced, which demonstrated a dependence on electron impact energy.

Another LIF study of OH by electron impact in the electron energy range 30-300 eV calculated rotational energies of the R_1 and P_1 branches of 200±20 and 217±10 K. The authors suggested that the difference between their rotational temperatures and those of Kawazumi and Ogawa was due to a greater effect of H_2O cooling provided by their molecular beam source compared with the room temperature sample introduction used in the latter experiments. Both studies show that for the higher electron energies observed, OH is preferentially found in the first excited state, ($A^2\Sigma$).

The first study OH LIF of electron impact to take into account the OH produced by DEA was reported by McConkey and co-workers.[94] They report an onset for OH ($A^2\Sigma$) production at ~8.9 eV, which is consistent with previous anion observations by Hall *et al.*[105] Below this energy, OH is produced in the ground state ($X^2\Pi$), with the cross-section for this process peaking at ~7 eV. However, the authors conclude that in their experiments it is "not feasible to obtain a full LIF spectrum at the low energy where the attachment process dominates", due to the low cross-section for OH production in this energy range.

3. Laser-Induced Fluorescence (LIF) Spectroscopy of OH

3.1. Principles of Fluorescence

Fluorescence is one process by which a molecule may relax following electronic excitation. When an excited electron returns to the ground state, energy is released in the form of a photon whose wavelength, λ, is related to the energy difference, ΔE, according to equation (3.1), where h is Planck's constant and c is the speed of light.

$$\Delta E = \frac{hc}{\lambda} \qquad (3.1)$$

Different wavelengths of fluorescence photons result from decay to different ro-vibrational levels of the ground state. The schematic in Figure 5 shows excitation of a system and decay to a number of different vibrational levels, each of which is split further in to rotational levels

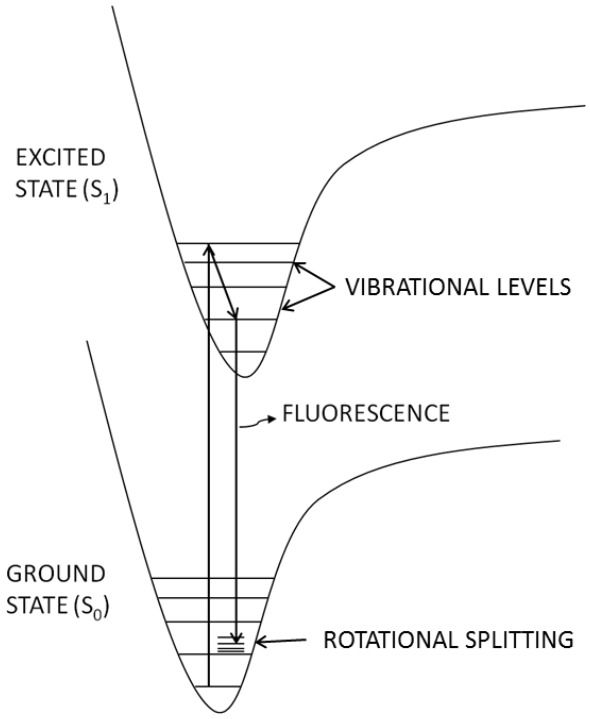

Figure 5 - Schematic showing initial excitation and subsequent emission to a ro-vibrational level of the ground state.

The fluorescent transitions in an excited molecule are determined according to a number of selection rules. The selection rules for fluorescence from the first electronically excited ($A^2\Sigma^+$) state of OH are addressed in chapter 3.3.

Lifetimes for fluorescence (typically ~200 ns - 2μs) are considerably shorter than for other processes, such as phosphorescence. This has important implications for measurements using fluorescence, as the window for signal detection is small. In addition, relaxation processes with similar timescales to fluorescence cause "quenching" of the fluorescence signal, decreasing the proportion of molecules which relax by fluorescence.

Fluorescence decay is a typical first-order process with a single rate constant, k_f. The lifetime of fluorescence, τ, is simply the inverse of the rate constant for fluorescence, as shown in equation (3.2).

$$\tau = \frac{1}{k_f} \qquad (3.2)$$

3.2. Laser-Induced Fluorescence (LIF)

Laser-induced fluorescence spectroscopy (LIF) is a powerful tool for studying chemical dynamics, particularly for investigating short-lived or nascent species.[106] By employing a pulsed laser source to excite specific electronic and vibrational transitions in molecules, LIF can be used to probe the internal energy state distributions of short-lived species such as radicals in chemical reactions. In addition, decay of the LIF signal can be used to determine fluorescence lifetimes.[107]

LIF uses the principle that fluorescence intensity (I_N) for a particular transition is proportional to the population (n_N) of the rotational level (N) of the ground state, according to equation (3.3)

$$n_{\mathrm{N}} \propto \frac{I_{\mathrm{N}}}{BP} \qquad (3.3)$$

Where B is the Einstein absorption coefficient (a combination of the Franck-Condon and Hönl-London factors) and P is the laser power.[108]

The method for recording a LIF spectrum begins with electronic excitation of a specific ro-vibrational transition using the monochromatic output of a laser. By using a dye laser, the excitation wavelength may be scanned across a narrow range, in order to excite all of the available rotational transitions associated with the selected electronic-vibrational transition. Decay to a range of rotational states in the lower electronic-vibrational state results in emission of fluorescence, which is detected and plotted as a function of excitation wavelength. In this way, the relative intensities of lines in a LIF spectrum give information about the rotational state distribution (and other fine structure) of the ground state.

In this work, the $A^2\Sigma(v=1)\leftarrow X^2\Pi(v=0)$ transition of the OH molecule is excited by scanning across the wavelength range 281.2-283.2 nm. To record a LIF spectrum, fluorescence from the $X^2\Pi(v=1)\leftarrow A^2\Sigma(v=1)$ transition is detected using a PMT, and plotted as a function of excitation wavelength. Figure 6 is an example of LIF spectrum of the $A^2\Sigma(v=1)\leftarrow X^2\Pi(v=0)$ of OH showing the intensities of the fluorescent transitions as a function of excitation wavelength.

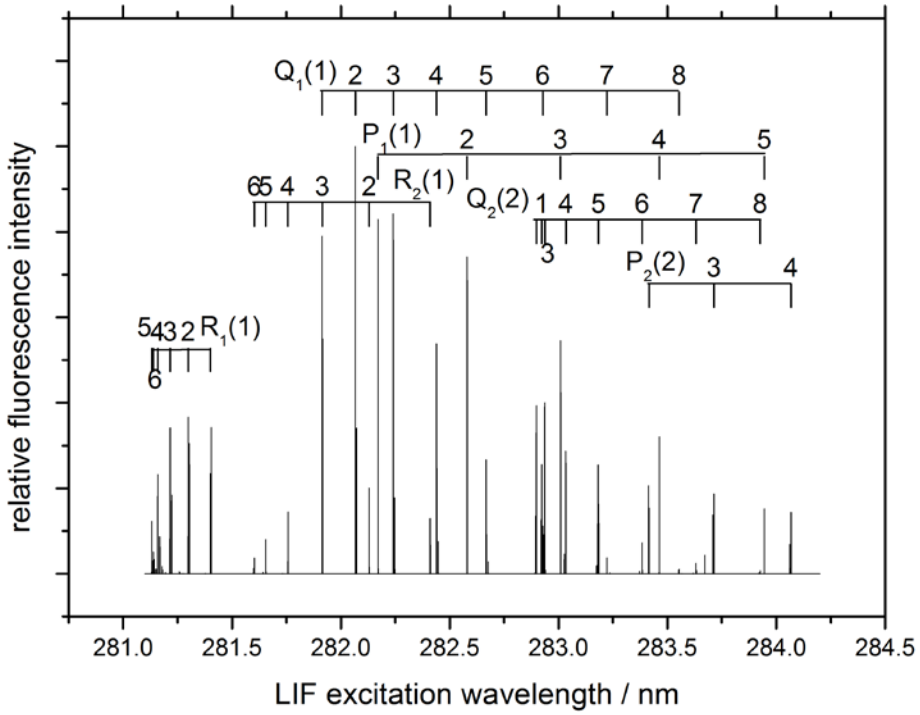

Figure 6 - Assigned simulated LIF spectrum for the$A^2\Sigma(v=1)\leftarrow X^2\Pi(v=0)$ transition in OH, simulated using LIFbase

In LIF spectra, the intensity of the signal at each wavelength depends on the population of the specific state, however, the overall signal response depends a property of the fluorescence itself, the fluorescence quantum yield, φ, which quantifies the amount of photons emitted compared with the number absorbed by the sample (equation 3.4).

$$\phi = \frac{\text{number of photons emitted}}{\text{number of photons absorbed}} \qquad (3.4)$$

The maximum fluorescence yield will be observed if every molecule in a sample which absorbs a photon decays by fluorescence, that is, a quantum yield of 1. However, in general, some portion of the molecules will relax by other processes, such as phosphorescence or non-radiative decay, with the result that only a fraction of the absorbed photons are detected in LIF spectra.

The advantage of LIF as a technique is not purely in the magnitude of the signal, but of the signal to noise ratio (S/N). By exciting the transitions with light of a particular wavelength and detecting fluorescence at a different wavelength, LIF is, in principle, background-free.

A second advantage of LIF is the timescales on which species can be detected. In combination with high and ultra high-vacuum conditions, and a molecular beam source (chapter 4.3) LIF can be used to observe OH radicals produced by DEA to water before undergoing collisions which will alter their internal energy. The fluorescence lifetime of OH is around 0.6 μs.[109] By using a pulsed dye laser and pulsed molecular beam source, it is possible to record LIF spectra before the fluorescence signal decays.

3.3. Molecular Energy Levels of OH

There are a number of electronic, vibrational and rotational states associated with any given molecule determined by the molecule's electron configuration. Transitions between these states (excitation or relaxation) are governed by a number of selection rules.

The molecular orbitals of OH are shown in Figure 7. There is good orbital overlap between the 1s (H) orbital and the $2p_z$ (O) orbital, forming a pσ-orbital. The ground state configuration of OH is therefore $(1s\sigma)^2(2s\sigma)^2(2p_z\sigma)^2(2p_x\pi)^2(2p_y\pi)^1$.

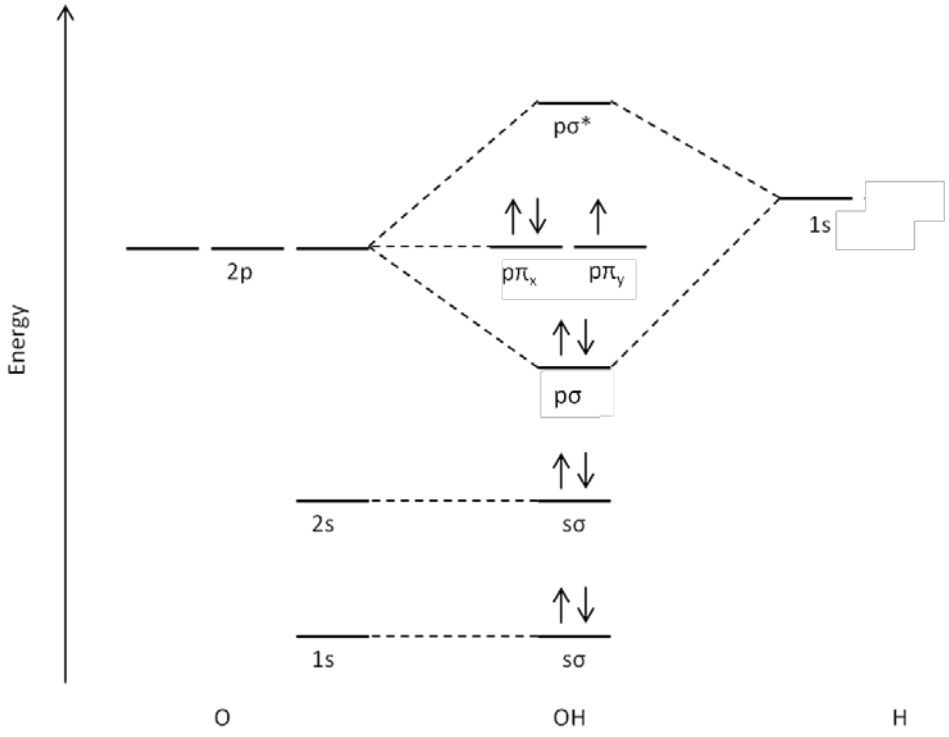

Figure 7 - Molecular orbital diagram for ground state OH

The term symbol for the ground state of OH is $X^2\Pi$. In the ground state, OH has one unpaired electron, which results in a spin (S) of ½ and a multiplicity (M) of 2S+1 = 2. In OH, where the unpaired electron occupies a π-orbital, the component of angular momentum about the internuclear axis, Λ, is equal to 1, denoted by the Π

state. Since $\Lambda \neq 0$, Λ-type doubling also occurs, causing a splitting of each vibrational level, indicated by ± labels (Figure 8). In addition, spin-orbit coupling causes a further splitting of the ground state into $^2\Pi_{3/2}$ and $^2\Pi_{1/2}$. The highest occupied molecular orbital (HOMO) of OH ($X^2\Pi$) is the $2p_{xy}\pi_{3/2}$, which is split into Π^+ and Π^-; a Λ-doublet.

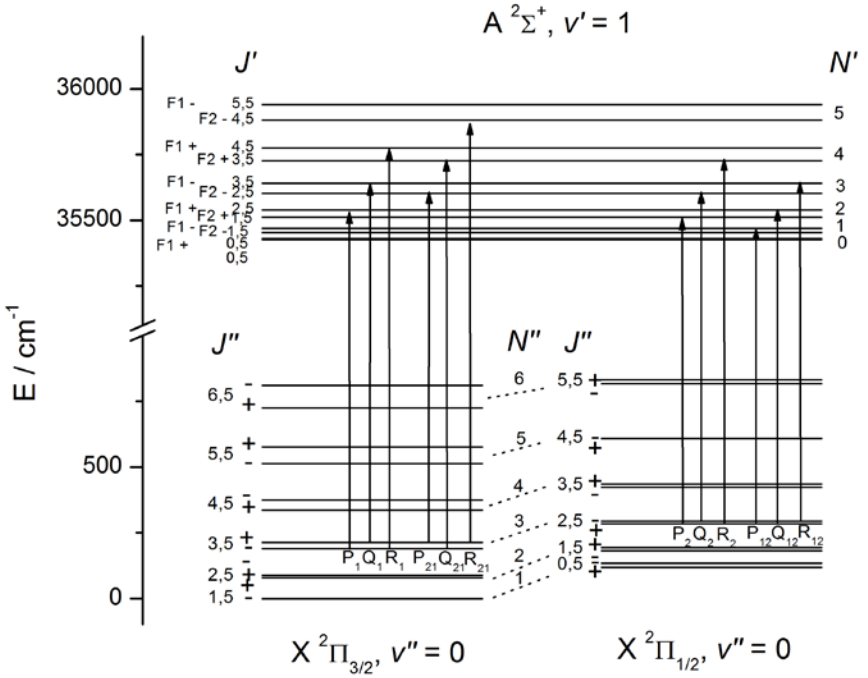

Figure 8 - Partial energy level diagram of OH $X^2\Pi$ and OH $A^2\Sigma^+$

In the first electronic excited state, an electron is promoted from the $2p_z\sigma$ orbital to the $2p_y\pi$, so that the new configuration is $(1s\sigma)^2(2s\sigma)^2(2p_z\sigma)^1(2p_x\pi)^2(2p_y\pi)^2$. Since there is still an unpaired electron, both the spin and multiplicity of the excited state stay the same, however, there is a change in the value of Λ as the unpaired electron is now in a σ-orbital, therefore $\Lambda = 0$. The term symbol for the first excited state of OH is $A^2\Sigma^+$. The $^+$ refers to the symmetry of the orbitals relative to a plane of reflection through both nuclei in the molecule.

Selection Rules

Selection rules govern which transitions between energy levels are allowed. The following selection rules are applicable to our system, and will assist in assigning the peaks of LIF spectra to the appropriate transitions in OH.

The first selection rule is for the change in total angular momentum quantum number:

$$\Delta \mathrm{J} = 0, \pm 1$$

In addition, there may be no transition from $\mathrm{J} = 0$ to $\mathrm{J} = 0$. This rule results in three types of transition, which are manifest as three sets of peaks or "branches" in a typical fluorescence spectrum: The Q-branch ($\Delta \mathrm{J} = 0$); the P-branch ($\Delta \mathrm{J} = -1$); and the R-branch ($\Delta \mathrm{J} = +1$).

There must be no change in spin multiplicity during a transition:

$$\Delta S = 0$$

4. Experimental Apparatus (Gas-phase studies)

4.1. Overview of the gas-phase experiment

This chapter describes in detail the experimental design used to investigate the gas-phase dissociative electron attachment to water by detecting the laser-induced fluorescence of OH radicals. In brief, for the gas-phase experiments, a low energy electron gun provides a beam of electrons (energies 0-100 eV), which interacts with a molecular beam of H_2O seeded in He provided by a nozzle and a skimmer, causing dissociation of the H_2O molecules. Nascent OH fragments are excited by scanning across the 281-285 nm output of a tuneable dye laser and the fluorescence decay at ~ 312 nm is recorded by a photomultiplier tube. Data collection and control of the wavelength scanning was carried out using the LabView programme in conjunction with an oscilloscope. All of the gas-phase experiments were carried out within the high-vacuum apparatus (typical base pressure ~1×10^{-7}) shown in Figure 9.

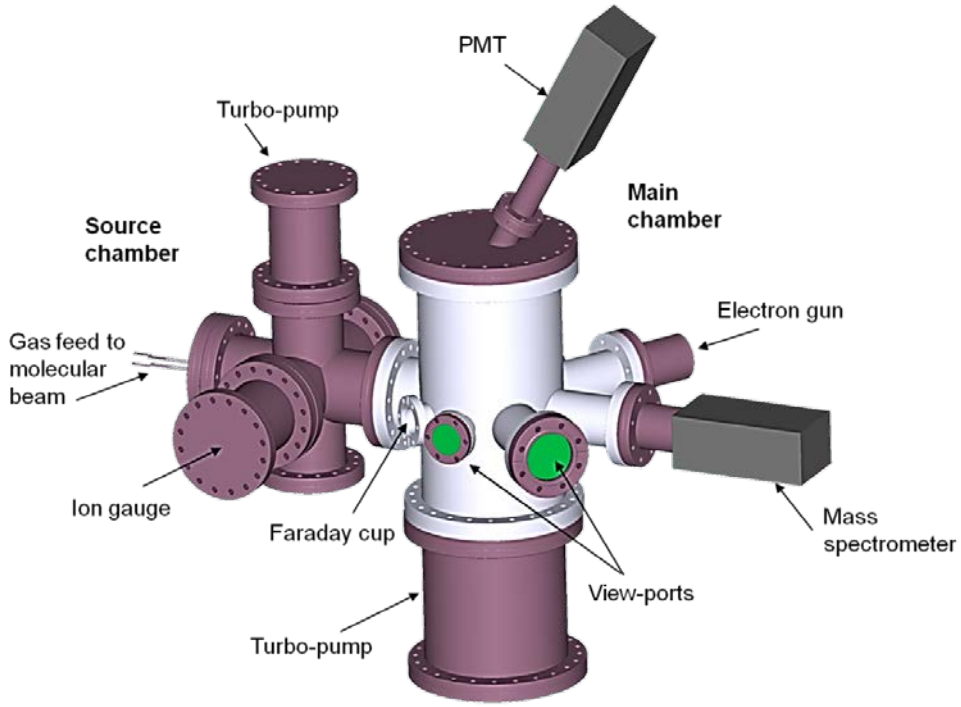

Figure 9 - CAD drawing of high vacuum apparatus for gas-phase experiments

4.2. High Vacuum (HV) System

4.2.1. Vacuum chambers

The vacuum system in these experiments (Figure 10) consists of two connected stainless steel (316N) chambers. The source chamber houses a molecular beam valve and skimmer. It consists of a simple crossed arrangement of six DN100 CF-flanged ports (LewVac, 6-way cross), each of length 75 mm, totalling an approximate volume of ~9.3 L. The main chamber, in which the reactions will take place, consists of a large cylindrical chamber of diameter 230 mm with an approximate volume of 12 L (Vacom, custom piece). The chamber incorporates 12 CF-flanged ports of varying sizes in order to accommodate an electron gun, Faraday cup, two view-ports for the LIF laser, vacuum pumps, pressure gauges, mass spectrometer, viewing windows and the optical detection system for LIF.

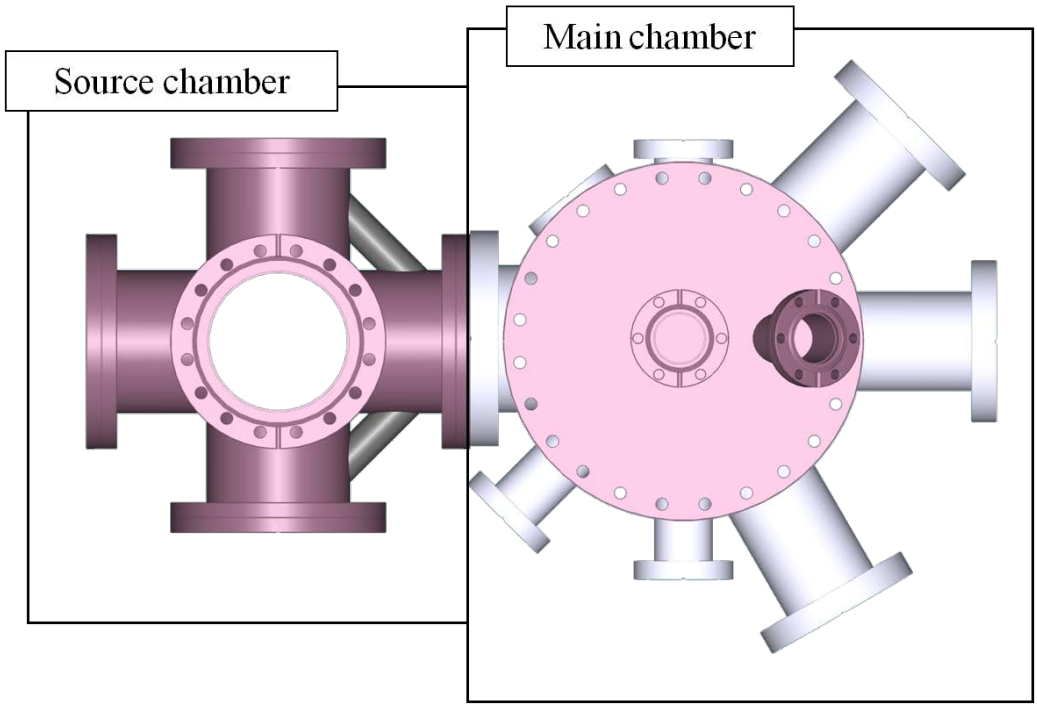

Figure 10 - CAD drawing of high vacuum chamber, showing main chamber and source chamber from above

4.2.2. Vacuum principles

In the gas-phase studies, high vacuum (HV) conditions are necessary to limit the number of inter-molecular collisions. In gas kinetic theory, the mean free path, λ_{MFP}, is the distance travelled by a single particle between two collisions. An increase the mean free path corresponds to an increase in the time between collisions. In gas-phase dynamics, where nascent species are to be studied, it is vital that the time between collisions is greater than the time between the birth of the species and the arrival of the probe laser. Maintaining HV conditions in the gas-phase experiments (or UHV conditions for surface studies, see later) enables the study of nascent OH radials.

Given the wide usage of vacuum conditions in scientific study, naming conventions have arisen to identify the quality of vacuum required (Table 5).[110] In the gas phase experiments detailed in this thesis, high vacuum conditions are used, where λ_{MFP} is usually in the range 50 cm – 1 km.

Table 6 - Naming conventions for vacuum regimen

	Pressure /Torr	**Mean free path /cm**
Atmospheric conditions	760	7×10^{-6}
Rough vacuum	10^{-4}	50
High vacuum (HV)	10^{-6}	5×10^{3}
Ultra-high vacuum (UHV)	10^{-9}	5×10^{6}

Equation (4.1) relates the mean free path, λ_{MFP}, of a molecule in the gas-phase to the pressure in the container.

$$\lambda_{\mathrm{MFP}} = \frac{kT}{\sqrt{2}\sigma p} \qquad (4.1)$$

In this equation, k is the Boltzmann constant (1.380×10^{-23} m^2 kg s^{-2} K^{-1}), T is the temperature of the gas in K, and p is gas pressure in Pa. The quantity σ is the collision cross-section of the molecules in m^2, which defines the area in which a second molecule must approach the first in order for a collision to take place.[50] The collision cross section is related to the diameter, of the molecules in question, according to equation (4.2)

$$\sigma = \pi d^2 \qquad (4.2)$$

4.2.3. Vacuum pumps

In order to evacuate large volumes a high throughput vacuum pump is required. In these experiments, turbo-molecular pumps are used in conjunction with oil-sealed rotary backing pumps. An Edwards STP-1000C turbo-molecular pump is used to evacuate the main chamber and a refurbished Edwards STP-1003 for the molecular beam chamber. Each turbo-pump is backed up by a separate rotary vane pump (Edwards E2M28).

Turbo-molecular pumps

A turbo-molecular pump (turbo-pump) is a type of mechanical pump, which forces gas through an exhaust using compression. Turbo-pumps of the type used here can achieve a compression ratio of up to 10^6:1 provided with sufficient backing, and are capable of pumping a capacity of 10,000 L s^{-1}. Each pump consists of eight sets of rotating blades spinning at high speeds, which force any molecule that comes into contact with the blades to be accelerated towards the outlet by transfer of momentum. In the two Edwards pumps used here, which operate at speeds of 35,000 rpm, the rotors are magnetically levitated to reduce friction and avoid the use of lubricants.

Rotary Pumps

For operation of the turbo-pumps, the volume to be pumped must be kept below 0.1 Torr, which requires the use of a secondary pump or "backing pump". In this case, the backing pumps are oil-sealed rotary vane pumps (Edwards E2M28). Rotary vane pumps are a type of gas-replacement pump, which typically operate in the pressure range 10^{2}- 10^{-4} Torr, in the laminar flow regime.[111] Figure 11 shows an example of a rotary vane pumps in which a single rotor is used to drag gas from the volume to be evacuated towards the exhaust outlet of the pump. The evacuated gas is expelled through an oil-sealed one-way valve outlet.

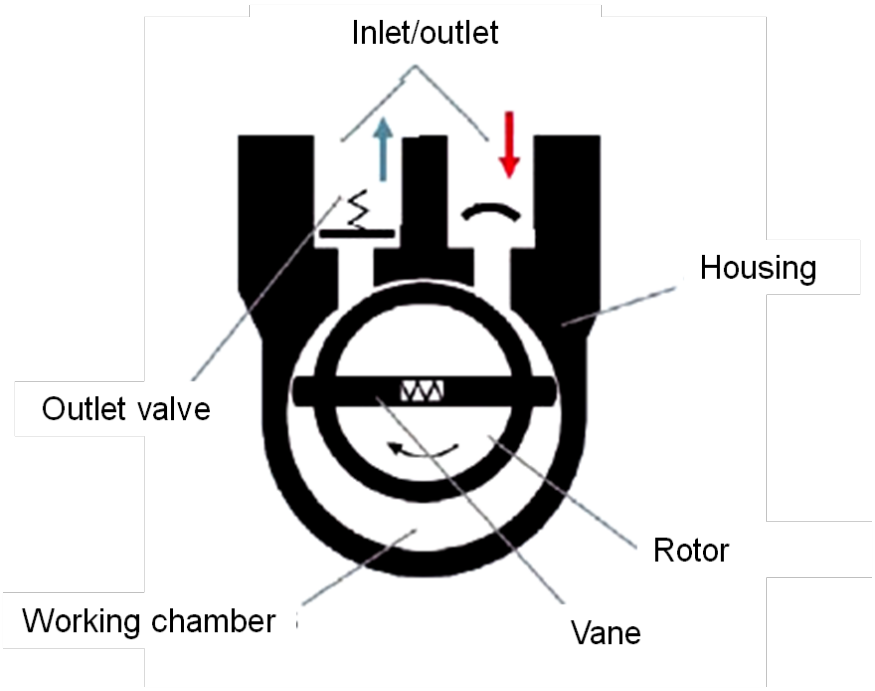

Figure 11 - Cut-through of a rotary vane pump[112]

In order to prevent oil vapours from escaping through the pump inlet and condensing in the turbo-pumps or in the chamber, oil mist filters are installed on the pump inlet. In optimum conditions, the rotary pumps used here are capable of maintaining a base pressure of 10^{-3}- 10^{-4} Torr.

4.2.4. Monitoring Pressure

In order to monitor the pressures at various points in the vacuum system, two different types of pressure gauge are used. Two Pirani gauges (SRS PG105-UHV) are used to monitor the low-vacuum rotary pumps; the pressures in both the source chamber and main chamber are monitored using ion gauges (Edwards AIG-8). The Pirani gauges are controlled using an SRS IGC 100 ion gauge controller, while the Edwards ion gauges are controlled by an Edwards TIC instrument controller.

Pirani gauges, used to monitor the pressure across each of the rotary pumps, are a type of thermal conductivity gauge. As the pressure of a gas decreases, so too does its thermal conductivity; using a filament kept at constant temperature, a Pirani gauge is able to compute the gas pressure by sensing changes in the resistivity of the filament.

For lower pressures, and applications requiring a greater degree of accuracy, Pirani gauges are not sufficient. To monitor the HV conditions within the chamber itself, ionisation gauges are used. Ionisation gauges also use a filament, but in this case the filament is used to generate electrons to ionise surrounding gas molecules; the ions are attracted to a negatively charged collector wire which detects the resulting current, which is proportional to the pressure of the gas, assuming equal ionisation efficiencies for the various gases present.

4.2.5. Preparing the UHV chamber for surface studies

It is intended that surface experiments will follow successful gas-phase studies using this apparatus with some adaptations. While a HV environment is adequate for gas-phase studies, surface studies typically require ultra-high vacuum (UHV) conditions ($\leq 10^{-9}$ Torr) in order to guarantee a clean surface.

At the low pressures associated with UHV conditions, the problem of out-gassing must be taken into account. Out-gassing is a property of materials which refers to the rate of evolution of gas molecules from pores in the material. In stainless steel, out-gassing is approximately 10^{-7} Torr l cm^{-2} s^{-1}, although this may be reduced to around 10^{-8} after a day or so of continuous pumping. In order to achieve UHV conditions, the steel of the chamber is baked at around 230 °C for a few hours to drive out CO and H_2.[113]

4.3. Molecular Beam

4.3.1. Molecular Beam Hardware

A molecular beam is a form of sample introduction that allows gases to be studied under high-vacuum conditions. A pulsed molecular beam provides a collimated, narrow beam of molecules, formed by the supersonic expansion of a gas through a nozzle into a region of lower pressure. A molecular beam is particularly suitable to probe internal energy states of H_2O in the DEA process as the internal energy of the H_2O molecules is well-defined with only the lowest vibrational energy states populated and a narrow range of translational energies. The other main advantage of using a molecular beam is that HV conditions can be maintained in the chamber, ensuring that OH molecules may be detected in their nascent state, whilst maintaining a high density of H_2O molecules in the beam to maximise the number of OH molecules created.

The molecular beam apparatus consists of a valve (General Valve Series 9, 500 μm aperture) fed by a custom gas manifold (assembled using Swagelok parts) and mounted in a brass "cage" within the source chamber, as shown in Figure 12.

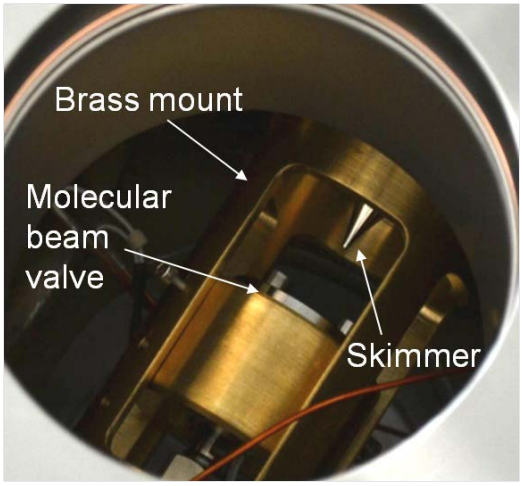

Figure 12 - Molecular beam valve and skimmer in a brass mount within the source chamber

The beam is pulsed using an externally triggered pulse driver (Iota One – Parker Automation) set to a repetition rate of 10 Hz, providing pulses 400 μs in duration. A skimmer (Beam Dynamics, Model 2, 1.2mm aperture), mounted with its base flush with the entrance to the reaction chamber, separates the source chamber and reaction chamber. The distance between the nozzle and the skimmer is 15 mm.

Gas Manifold

The gas manifold (Figure 13) supplies a mixture of the target gas seeded in helium to the nozzle at a relative pressure of ~2 bar (200 kPa, 1500 Torr). For the purpose of method development, the gas manifold incorporates two alternative methods for supplying gas to the nozzle: via a bubbler or using a gas mixing cylinder.

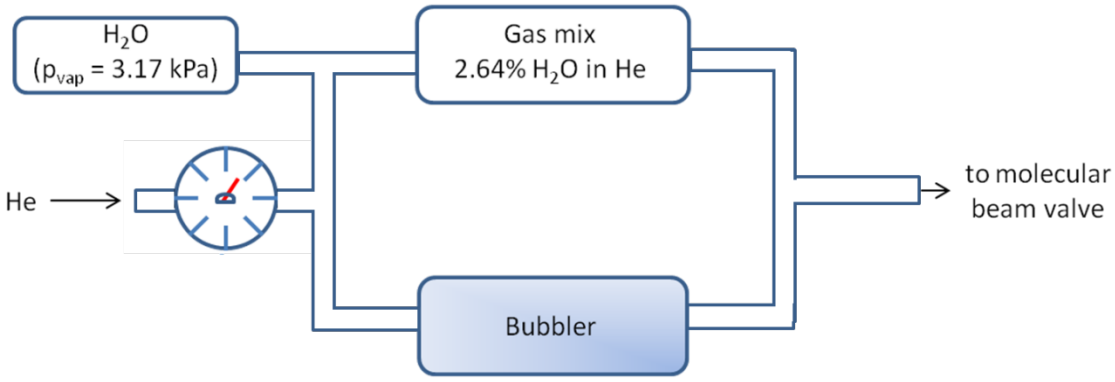

Figure 13 - Schematic of gas manifold showing two alternative routes for sample introduction to molecular beam

In the first method the bubbler is filled with the target chemical, for example water or allyl alcohol, and helium is bubbled through the liquid and into the nozzle. In this method the helium “picks up” molecules of the target species and carries them to the molecular beam, however the use of a bubbler limits the pressure behind the beam to ~1.2 bar. In the second method, a mixture of helium and the target compound is prepared in advance of the experiment by mixing them in a small gas cylinder (2.13 L) to be released through the manifold into the nozzle. The advantage of this

method is that higher pressures may be achieved, however the volume of the gas cylinder limits the amount of experiments which may conducted using a single mixture.

Heating

The introduction of the target gas into the chamber relies upon the vapour pressure of the species in question. As shown in Figure 14, the vapour pressure of a substance varies with temperature; as such, by heating the substance and the lines of the manifold, it is possible to increase the vapour pressure, and by extension increase the proportion of target gas in the molecular beam.

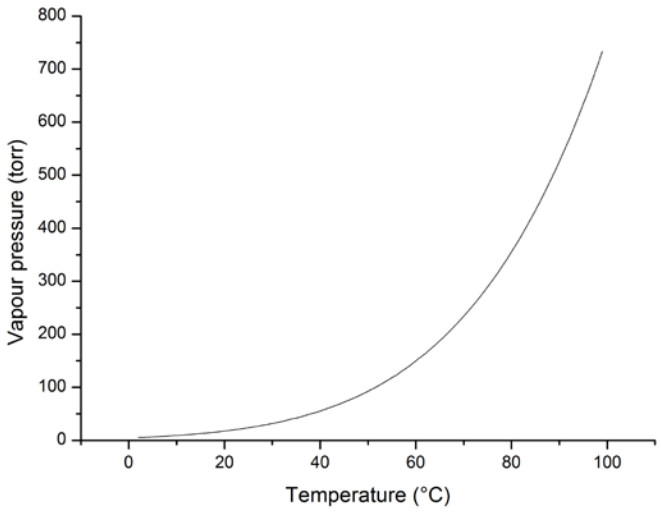

Figure 14 - H_2O vapour pressure (Torr) vs. temperature (°C)

Two types of heating tapes are used to heat the exterior and HV lines to the molecular beam valve: Omegalux SRT-102-020L for the external lines and Omegalux KHL-0504/10 for inside the source chamber. K-type thermocouples (Omega 5SRTC-TT-KL-24-2M) are used to monitor the temperature of the lines in

several places, both to ensure uniform heating and to guard against over-heating of components in the nozzle.

4.3.2. Principle of Molecular Beams

A molecular beam is produced from a supersonic expansion, which is generated simply by forcing molecules through an aperture separating an area of high pressure from an area of low pressure. In the experiments described, the high pressure zone is provided by a small chamber of gas in the molecular beam valve, which is then released through an aperture into the high vacuum conditions of the source chamber.

If the diameter, *d*, of the aperture is greater than the mean free path, λ, of the molecules in the high pressure ("stagnation") region, then a hydrodynamic flow is created through the aperture. Under these conditions, the momentum of the collisions is transferred to coherent motion through the aperture, resulting in a supersonic jet (Figure 15).

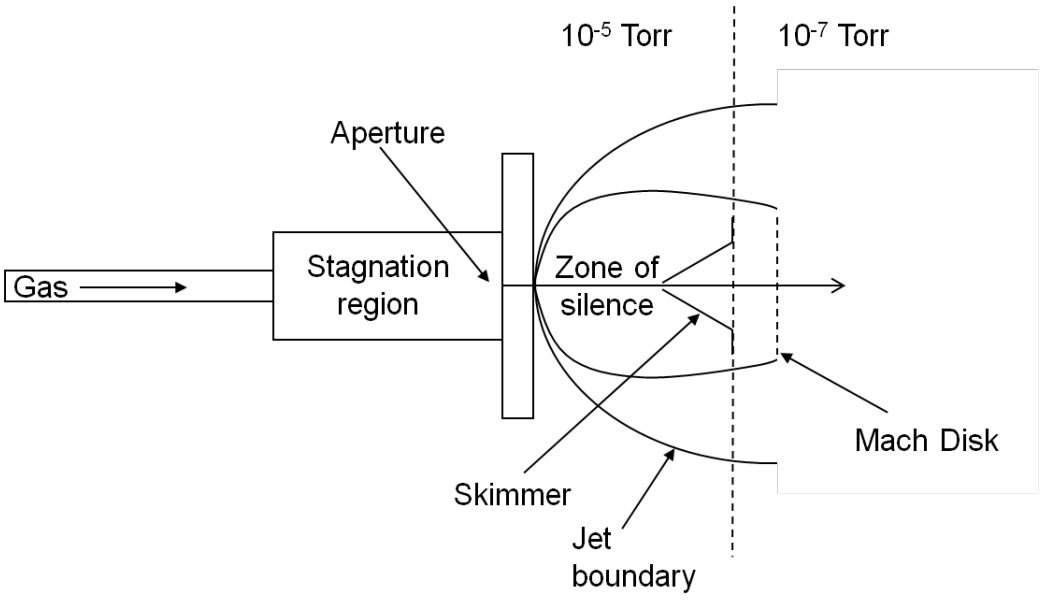

Figure 15 - Schematic showing generation of a molecular beam using a valve and skimmer

As the molecules in the jet expand into the vacuum, differences in pressure between the high-density beam and the high vacuum chamber create shock waves in the beam. As the molecules push outwards form the beam the pressure around the beam increases, forcing subsequent molecules to turn back inwards towards the beam. As the molecules turn inwards however, the pressure rises at the centre of the beam, forcing the molecules back towards the edges. In this way, the pressure is equalised in certain regions, forming edges to the beam known as the jet boundary (Figure 15). A similar effect creates a shock wave in the path of the beam, known as the Mach disk. The Mach disk marks the end of the "zone of silence", in which all of the molecules travel in parallel, collision-free paths.

A molecular beam is created from a supersonic jet by siphoning off cold molecules from within the zone of silence. A small hollow cone called a skimmer is placed between the nozzle and the zone of silence, skimming off the edges of the jet and isolating a molecular beam.

In order to place the skimmer at the correct distance from the nozzle, the position of the first Mach disc in the beam may be calculated using Equation (4.3)

$$x = 0.67d\sqrt{\frac{P_v}{P_s}} \qquad (4.3)$$

Here x is the distance of the Mach disc from the aperture, d is the diameter of the aperture, and P_v and P_s are the pressures in the valve and source chambers, respectively. Under our conditions, this equates to a distance of ~240 cm to the first Mach disk (assuming 1.2 mm aperture, P_v = 900 Torr, P_s = 10^{-5} Torr)

4.3.3. Alternative forms of sample introduction

In preliminary experiments using the molecular beam, OH LIF detection was not found to be possible. In order to address the possibility that the number density of molecules in the molecular beam were below the limits of detection, alternative methods of sample introduction were investigated.

For experiments where gas pressures of $\geq 1x10^{-2}$ Torr were used, allyl alcohol vapour was introduced directly into the chamber from a glass vial via a gas manifold, described in 4.3.1. Gas pressures of allyl alcohol of around 5 Torr were obtained by heating the vial.

For later experiments, in which lower gas pressures were required, a needle valve was favoured as the best way to attain pressures $< 1x10^{-2}$ Torr. Using the needle valve, it was possible to record gas pressures in the chamber of around $1x10^{-4}$ Torr. This pressure is sufficiently low to run the turbo-molecular pumps, thereby allowing us to use the electron gun.

4.4. Electron Gun

4.4.1. Electron Gun Design

An electron gun is used to provide a collimated beam of electrons with energies up to 100 eV. Though electron guns are commonly found in cathode ray tubes, more specialised versions can be constructed in order to give high energy definition for research applications. The electron gun in the following experiments (Figure 16) is based upon a design by Murray and co-workers.[114]

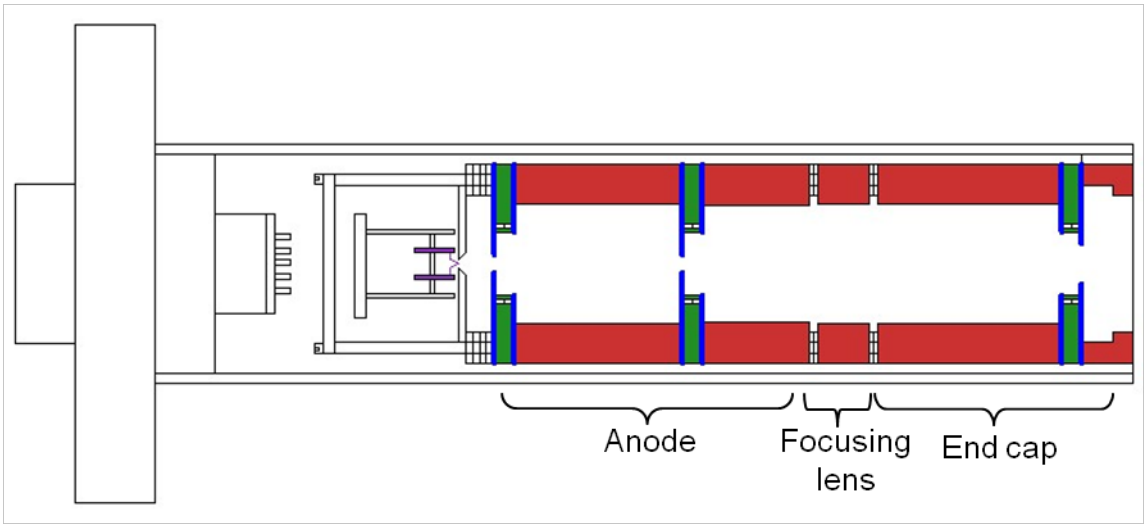

Figure 16 - Schematic of electron gun showing filament (purple), lens elements (red), apertures (blue) and deflectors (green)

The gun consists of a titanium tube containing a series of cylindrical molybdenum lenses (red), apertures (blue) and deflectors (green) mounted on four ceramic rods arranged as corners of a square. Ceramic spaces separate components with different applied voltages. Electrons are produced by thermionic emission from the filament (purple), which receives a current of around 2 A.

Lens system

The electron gun used in these experiments is based on a typical 3-element lens design (Figure 17), where the first element (“anode”) is set relative to the filament to

give the gun energy, the third element (“end cap”) is at ground potential, and the middle element (“focusing lens”) is varied to focus the beam. The length of the middle element is approximately equal to the diameter, *D*, of the lens system, in addition, the separation between each of the lens elements is equal to 0.1*D*.[115]

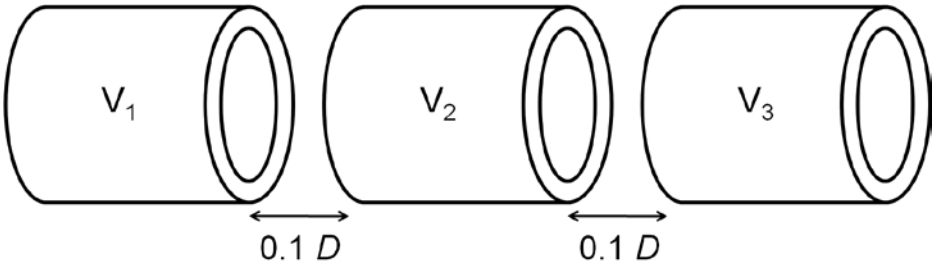

Figure 17 - 3-cylinder lens system showing 0.1*D* separation of lens elements

The focal length of the gun is varied by changing the ratios between the three potentials, V_1, V_2 and V_3. Changing the ratio of V_3/V_1 will accelerate or decelerate the electrons; if $V_1 = V_3$, the speed (and energy) remains constant, but V_2 may still be altered to achieve a focussing effect. Simulations were conducted (Figure 18) to demonstrate how varying only the voltage applied to the central lens element affects the focal length of the electron gun. These conditions produce an electron beam in which electrons with a wide range of energies emitted from a filament exit the gun with a uniform, defined energy and a known focal length.

In these simulations, the gun energy is set at 10 eV (i.e. −10 V relative to ground potential), the grid is held at −6 V relative to the gun energy (i.e. −16 V) and the end cap is set at ground potential. The focusing lens is held at 200 V relative to ground in order to accelerate the electrons away from the filament.

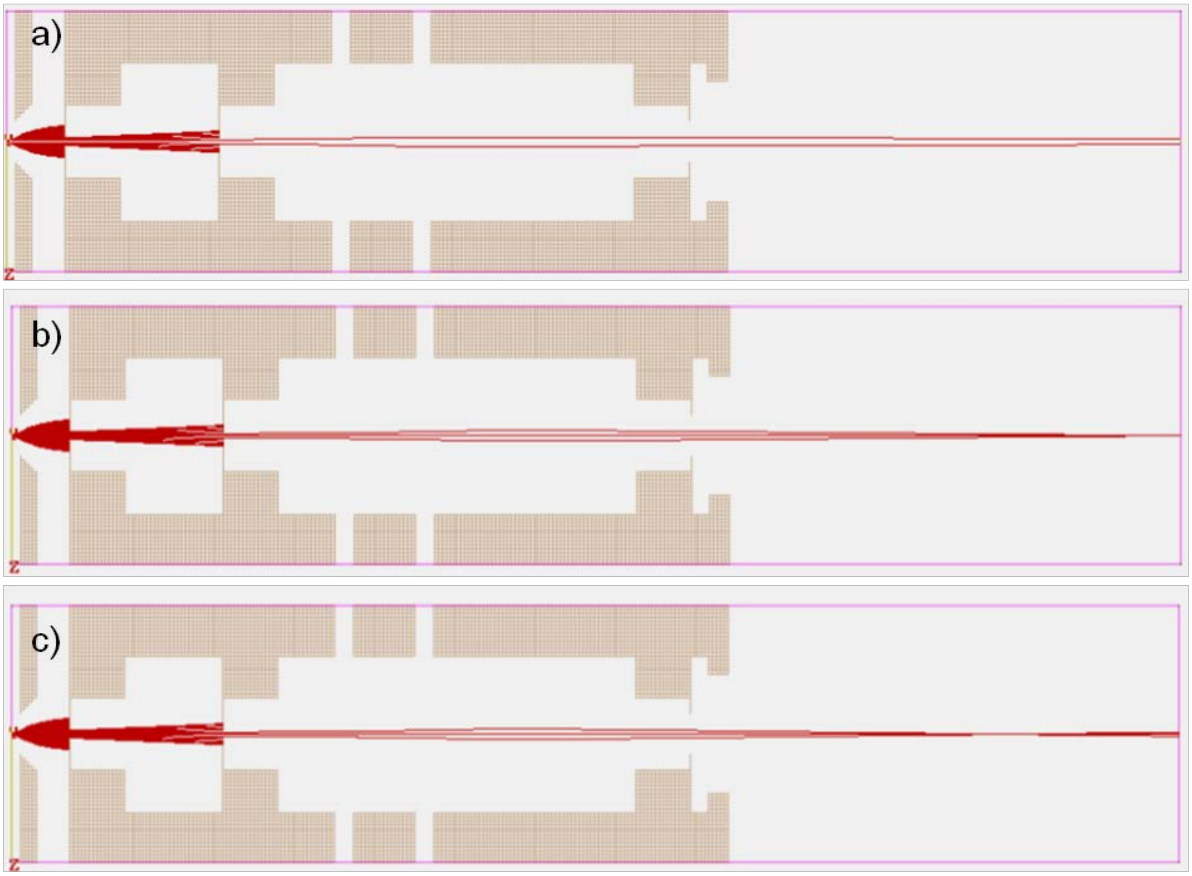

Figure 18 - a) Lens element held at 0 V b) Lens element held at 250 V c) Lens element held at 300 V

Pierce grid

In addition to the 3 lenses, the electron gun uses a Pierce diode or “grid” to initially focus the filament emission into a beam (Figure 19). The Pierce system is essentially an optimised form of the conventional diode, in which the electrons are accelerated towards an anode, whilst being shielded from the filament by a cathode. In the Pierce system, the cathode (“grid”) is shaped so as to reduce scatter and more effectively direct electrons through the anode opening. The Pierce system effectively reduces the effects of space charge, which is a form of divergence caused by mutual repulsion of the like electron charges.

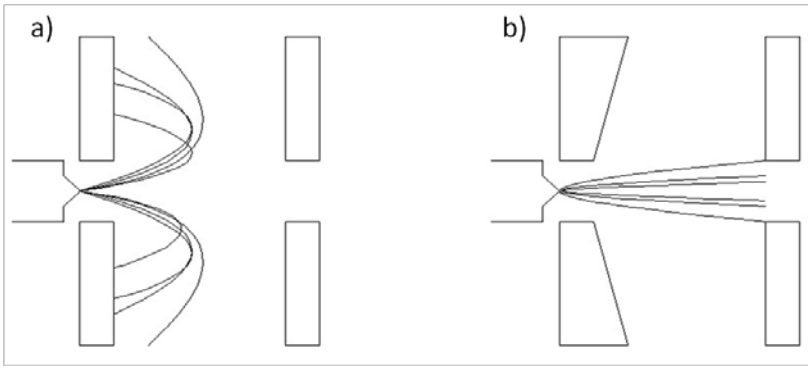

Figure 19 - Emission from a filament accelerated by a) a simple straight-sided diode system b) a Pierce grid system

Apertures and deflectors

In addition to the lens elements, the electron gun also comprises a number of apertures (shown in blue, Figure 16). The purpose of the apertures is to skim the edges of the beam where the electrons are lower in energy and more disperse, creating a narrow, uniform beam profile. The apertures are each machined from 0.5 mm thick molybdenum, and their voltages are set according to the adjacent lens.

Finally, three deflectors are used to make small corrections to the path of the beam to account for the effect of stray fields within the gun. Each deflector consists of 4 perpendicular molybdenum plates whose potential can be varied between ±10 V relative to the adjacent electrode (Figure 20).

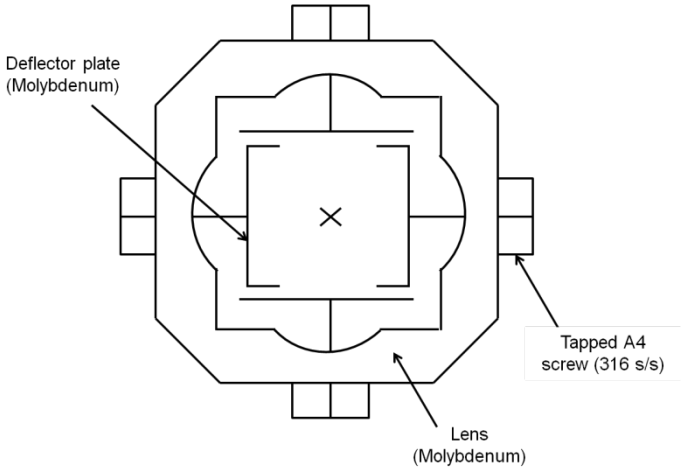

Figure 20 - Schematic of deflector

Using the deflectors, the focal point can be carefully adjusted relative to the gun so as to maximise the current density at the centre of the reaction region.

4.4.2. Electron Gun Hardware

The lens elements, apertures, shielding tube and end cap are all machined from molybdenum. The deflectors are also machined from molybdenum; each deflector plate is held in place by an A4 M3 screw, which is non-magnetic and UHV compatible. Each piece is mounted on four ceramic rods and, where necessary, shielded from its neighbours by cylindrical ceramic spacers (Figure 21). An AO54 Agar hairpin tungsten filament is mounted in a 316 stainless steel holder, which is also mounted on the ceramic rods.

There are 18 electrical connections within the electron gun which connect each component (including each individual deflector plate) with a custom-built 19-pin electrical feed-through. Figure 21 shows the electron gun with 3 connections wired using insulated wires to the three lens elements. Connections to the deflectors, grid and filament were made using thinner Advance wire, which is spot-welded to the components, due to space constrictions.

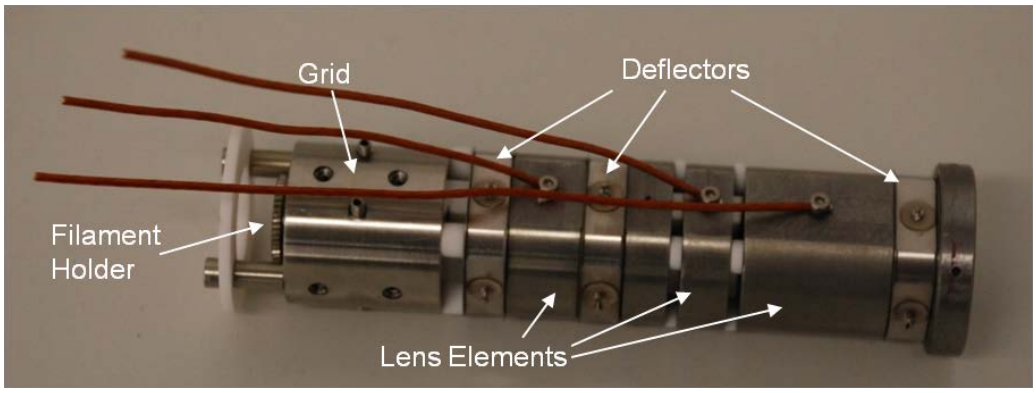

Figure 21 - Photograph of electron gun

4.4.3. Helmholtz coils

Stray magnetic fields can significantly alter the trajectories of low-energy electrons once they leave the gun. Helmholtz coils are used to counteract the effect of magnetic fields in the reaction region, including the earth's magnetic field.

Helmholtz coils consist of a pair of coaxial wire coils with a radius, *R* equal to the distance between the two coils. For a set number of turns or coils in the wire (*N*), the current (*I*) may be adjusted to bring the field at the centre of the coils to zero (Figure 22).

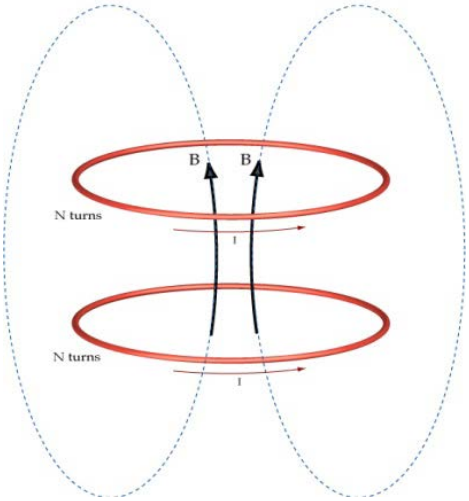

Figure 22 - Diagram showing arrangement of Helmholtz coils

The magnetic field, B at any point along the shared axis of the coils (z) may be determined as follows (4.6a):

$$B=0.32\frac{NI}{R}\left\{\left[1+\left(\frac{z}{R}\right)^2\right]^{-3/2}+\left[1+\left(1-\frac{z}{R}\right)^2\right]^{-3/2}\right\}\ \text{gauss} \qquad (4.6a)$$

At the central point along the shared axis between a pair of Helmholtz coils, $\frac{z}{R}$ is equal to 0.5, in which case the equation becomes (4.6b)

$$B=0.32\frac{NI}{R}\left\{[1.25]^{-\frac{3}{2}}+[1.25]^{-\frac{3}{2}}\right\}\text{ gauss} \qquad (4.6b)$$

In order to counteract the fields in all directions around the experiment, three pairs of Helmholtz coils were placed along the x, y and z axes, defined in Figure 23. The field produced by this arrangement of Helmholtz coils produces a highly uniform field within a small volume. Outside of this volume, the field uniformity quickly diminishes, making it extremely important that the coils are carefully centred about the reaction region.

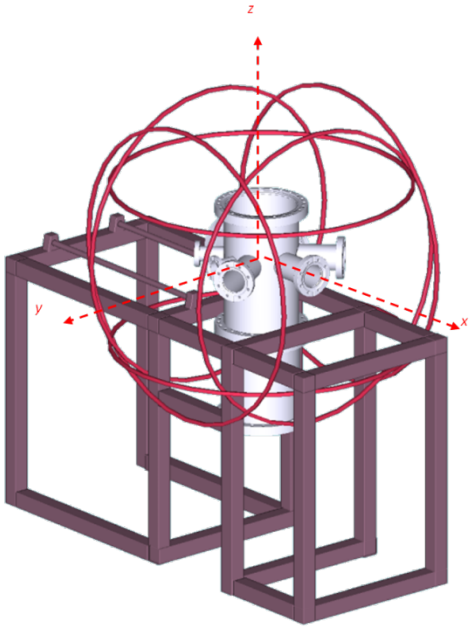

Figure 23 - Positioning of Helmholtz coils around the UHV chamber

The required specifications of the Helmholtz coils were determined using equation (4.4b). The radius of each pair of Helmholtz coils was limited by the dimensions of the chamber and table, resulting in two pairs of coils with r = 60 cm (x and y) and one pair with r = 50 (z). Before choosing the number of coils in each Helmholtz pair, measurements of the magnetic field along the x, y and z axes in each direction at around 10-15 cm from the centre of the reaction chamber were recorded using a

gauss-meter (Hirst Magnetic Instruments GM07). It was found that the magnetic fields around the centre of the chamber varied between 0.48-0.6 G in x and y, and between 0.13-0.86 G in z. Approximately 30 coils of wire were used in each pair of Helmholtz coils, allowing operating currents to remain below 2 A, in order not to overheat the coils.

Optimisation of Helmholtz coil current configurations

Optimisation of the Helmholtz coil currents was carried out over the full range of electron energies (5-100 eV). As shown in Figure 24, much higher currents are required in z, most likely due to the presence of a magnetically levitated turbo-pump mounted below the chamber on this axis. Conversely, the Helmholtz coils on the x-axis have much less impact, while the y-axis coils have some considerable effect. The current in the y and z axis coils varies according to a similar pattern, initially falling as the electron energy is increased and then rising slowly.

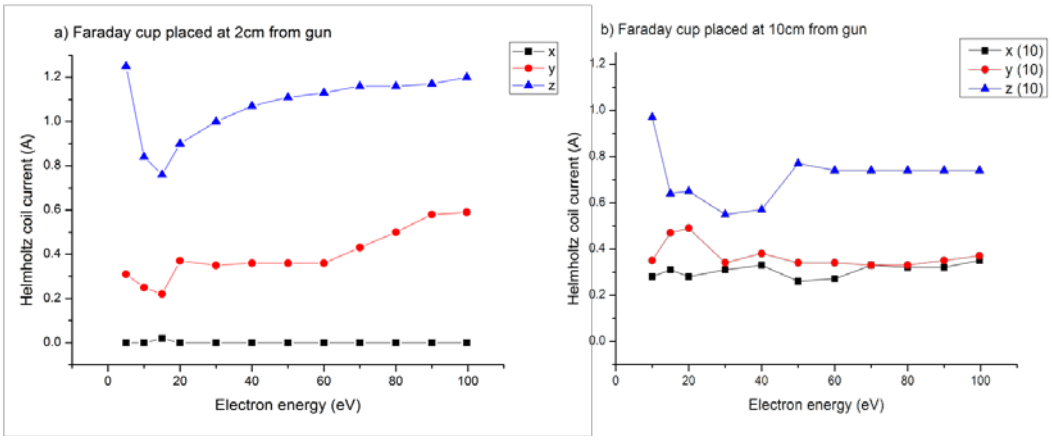

Figure 24 - Optimal Helmholtz coil current settings vs. electron gun energy for a) Faraday cup at 2 cm from gun and b) 10 cm from gun

4.4.4. Electron Beam Characterisation

The electron gun current was measured for the full range of electron energies (5-100 eV) using a Faraday cup mounted on a 2¾″ port directly opposite the electron gun, at a distance of approximately 20 cm. A Faraday cup (Figure 25) consists simply of a metal "cup" biased to some positive potential, which collects electrons from the beam as they arrive. The cup is connected to an external BNC connection via a copper wire, from where the current is read out using an ammeter (Keithley 6485 Picoammeter). To minimise the effect on the current reading of secondary electrons, which may be released from the metal of the cup upon impact of an arriving electron, the cup is shielded by a larger metal cylinder held at ground potential

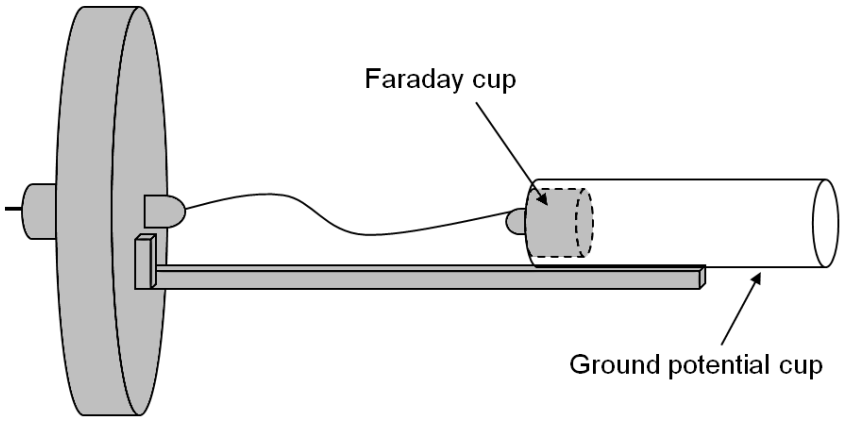

Figure 25 - Schematic of Faraday cup

Table 6 lists the voltage potentials across each of the electron gun components in the following measurements. For all measurements, a current of 2.45 A was supplied to the filament, and the Faraday cup was held at a voltage of +20 V. The current settings for each set of Helmholtz coils were optimised before each measurement according to Figure 24.

Table 7 - Voltage potentials applied across electron gun components during Helmholtz coil optimisation

Component	**Voltage applied (V)**
Grid	-30.85
Anode	255
Lens	0.02

Figure 26 shows the current detected by the Faraday cup, mounted at approximately 2 cm and 10 cm from the end cap of the electron gun; at the centre of the chamber and at the opposite port across the chamber, respectively.

For the trace in which the Faraday cup is mounted 10 cm from the gun, the current plateaus at around 2.7 μA for energies > 50 eV. A similar trend is observed in the measurements at 2 cm, except that the variation in the current above 50 eV is greater. The appearance of a continued increase in current above 50 eV for measurements made at 2 cm is most likely due to systematic error on the ammeter at higher currents.

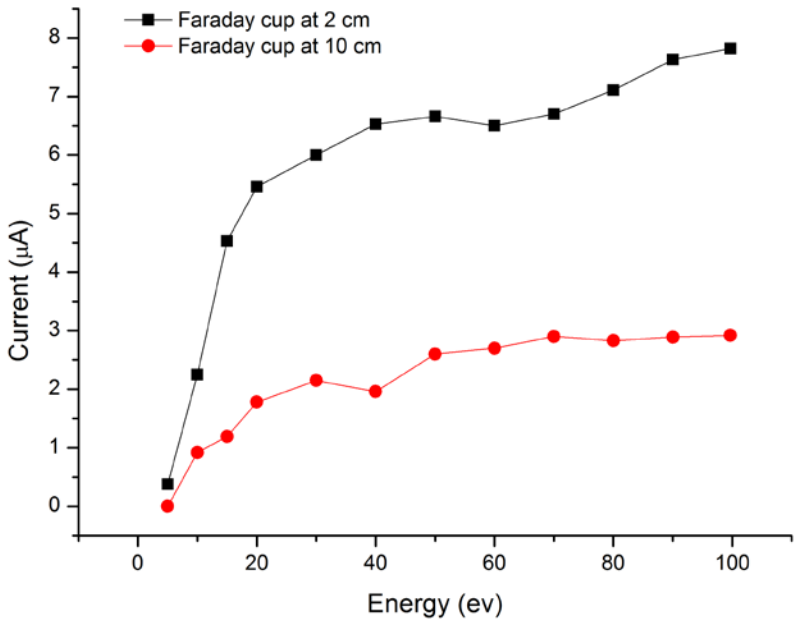

Figure 26 - Electron gun current as a function of electron energy for a filament current 2.45 A, measured at 2 cm and 10 cm from the electron gun end cap

The reduction in electron current for the measurements at a greater distance from the gun is likely to be due to beam widening as the focusing effect of the Helmholtz coils is greater at the centre of the chamber. Previous beam characterisation of another electron gun made to the same design showed an increase in space charge effects at higher filament currents, causing a broadening of the beam profile and a resultant loss of electron current density at the centre of the beam.[116] In these experiments, the filament energy was varied between 2.1-2.25 A, whereas in the experiments outlined in this thesis, typical filament currents of 2.45 A were used in order to maximise the number of electrons in the chamber.

4.5. Optical System

In the LIF experiments, a Nd:YAG pumped dye laser is used to excite OH radicals from the dissociation of H_2O into their first electronically excited state. In addition, preliminary experiments to test the molecular beam delivery and detection systems use an ArF excimer laser to produce OH radicals by photo-dissociation of allyl alcohol.

4.5.1. Nd:YAG Laser

An Nd:YAG laser (Continuum Surelite II-10) is based on an yttrium aluminium garnet ($Y_3Al_5O_{12}$) crystal, doped with around 1% Nd^{3+} contained within 2 mirrors, which form an intrinsic laser cavity. It is optically pumped using two flash-lamps with a repetition rate of 10 Hz.

The laser employs active Q-switching, by combining a polarizer, Pockels cell and λ/4 plate. The polarizer rejects laser light with a vertical polarisation while transmitting horizontally-polarised light. The quarter wave plate introduces a λ/4 rotation in the 1064 nm lasing, so that it has the opposite polarization, meaning that the lasing cannot escape through the polariser and the laser pulse is “off”. The Pockels cell is composed of two crystals in opposite orientation, which rotate the lasing by a further λ/4 when a voltage of ~3600 V is applied, so that the light is once again horizontally polarized and may exit the cavity. This method of Q-switching allows the Nd:YAG laser to provide high energy pulses at well-defined times.

The 1064 nm output of the Nd:YAG is doubled to produce light of wavelength 532 nm using a KDP crystal. The Nd:YAG energy is optimised by tuning the harmonic crystals. Typical pulse energies for the 532 nm output of this laser at a repetition rate of 10 Hz are around 170 mJ per pulse.

4.5.2. Dye Laser

The 532 nm light from the Nd:YAG is used to pump a dye laser (Radiant Dyes Narrowscan). For these experiments, a solution of Rhodamine 6G dye is used, made up to 120 mg/mL concentration in ethanol. The dye laser may be scanned over a wavelength range of 100s nm, with a maximum at around 564 nm for Rhodamine 6G.

The dye laser consists of two dye cells: an oscillator and pre-amplifier, and an amplifier cell. Light from the Nd:YAG laser is split into three beams: the first excites the dye in the oscillator cell causing stimulated emission from the excited dye molecules. Stimulated emission from the dye resonates within a cavity formed by a semi-reflective (around 80%) mirror known as the output coupler and a diffraction grating (shown in Figure 27). It then escapes from the cavity through the output coupler. The pre-amplifier stage is pumped by the second beam of the original Nd:YAG beam as well as stimulated emission induced by the output from the oscillator. The pre-amplified laser beam, as well as the Nd:YAG beam pumps the dye in the amplifier dye cell before escaping.

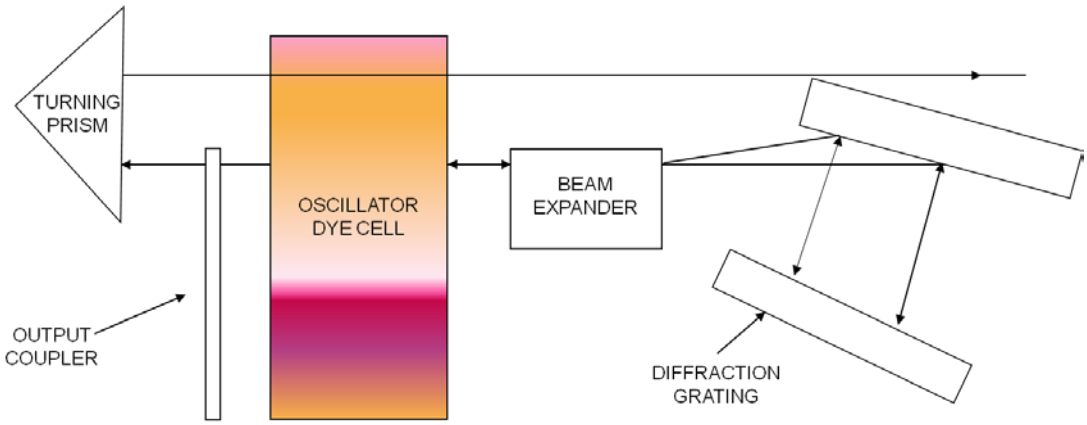

Figure 27 - Schematic of dye laser cavity

The amplified laser light is passed through a frequency conversion unit (FCU) consisting of a BBO doubling crystal (shown in blue, Figure 28) in combination with a compensator (shown in green, Figure 28). Finally, the doubled light is separated from the fundamental wavelength by a set of 4 Pellin-Broka prisms (shown in purple, Figure 28).

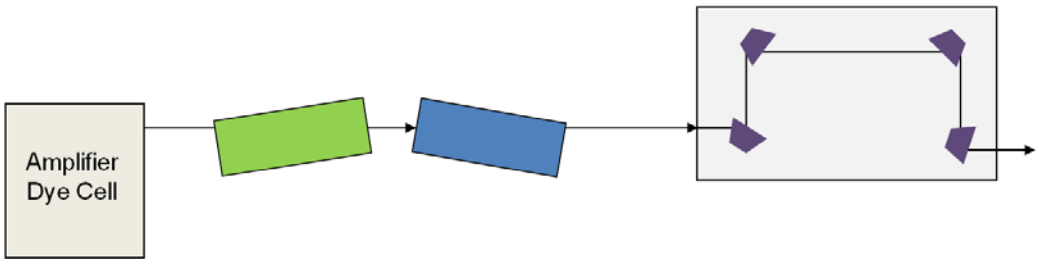

Figure 28 - Frequency conversion unit (FCU) and Pellin-Broka prisms in dye laser

The diffraction grating which forms part of the cavity may be rotated using a stepper motor to allow tuning of the laser to different wavelengths. The dye used in these experiments is Rhodamine 6G, which gives a tuneable laser output in the range 558-570 nm, with a maximum at around 565 nm. The laser light is doubled in order to excite the fluorescent transition in OH. Figure 29 shows typical pulse energies of the doubled light at 282 nm as a function of doubled wavelength.

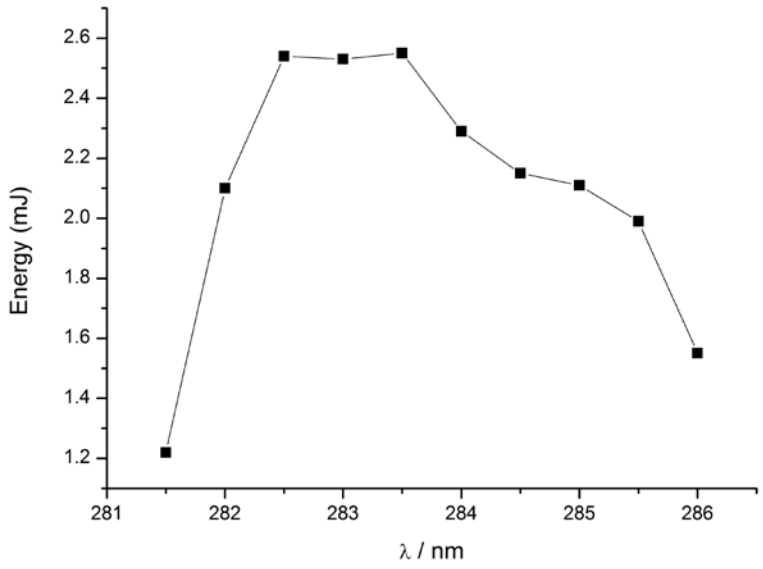

Figure 29 - Typical energy output of Rhodamine 6G dye laser as a function of wavelength[117]

The energy output of the dye laser is optimised by careful alignment of the pump beam and resonator. For normal operation, it is not necessary to adjust these after the full initial alignment has been completed, however, the position of the FCU is specific to each particular wavelength, and must therefore be adjusted accordingly. In the collection of LIF spectra, the laser is scanned over a narrow wavelength range, and the FCU must adapt to the correct position for each one. This is carried out by recording an initial calibration curve by optimising the position of the FCU at each wavelength over the desired wavelength range.

4.5.3. Excimer Laser

In addition to the dye laser, an excimer laser (Questek Series 2000 Excimer) is used to generate OH radicals from allyl alcohol, $CH_2CH(OH)$, for initial instrument calibration.

An excimer is an excited dimer which is dissociative in its ground state, and has a very short lifetime, usually on the order of nanoseconds. In an Excimer laser, a

combination of a halogen (e.g. F, Cl) and a rare gas (e.g. Ar, Kr, Xe), seeded in a carrier gas such as He is excited by a high voltage electrical pulse, forming the excimer species. The excimers decay by fluorescence to their ground state, before dissociating. The fluorescence resonates within the cavity formed by mirrors on either end of the chamber, resulting in the production of laser light. The laser beam exits the chamber through the semi-reflective output coupler at one end of the cavity. Repeated electrical pulses generate a pulsed output (10 Hz) from the excimer laser.

For the purposes of these experiments, a mixture of approximately 10% Ar and 0.35% F_2 in He is used, producing 193 nm laser light. Using a repetition rate of 10 Hz, typical pulse energies are 2 mJ per pulse (around 12 ns).

4.6. Detection Systems

4.6.1. Photomultiplier Tube (PMT)

LIF detection is carried out using a photomultiplier tube (PMT), which collects fluorescence via a liquid light guide (LLG). The PMT used in this work is an ET Enterprises 9235QB with a quartz window and a spectral response in the range 160 – 630 nm, peaking at around 150 and 350 nm (trace 'Q', Figure 31).

A PMT detects photons using the photoelectric effect. Photons arriving at the surface of the detector with a minimum energy (the work function of the detector material) cause electrons to be produced in the medium which are then accelerated towards an anode mesh via a series of dynodes arranged in order of increasing potential difference (Figure 30). In this way, the electrons are both accelerated and multiplied towards the final detector, making a PMT very sensitive to small signals.

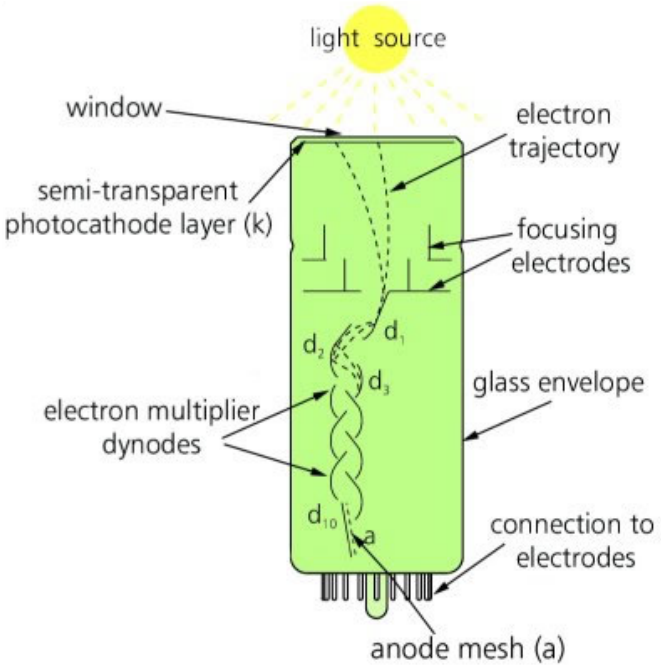

Figure 30 - Cross section of PMT, showing photocathode, dynodes and anode detector[118]

The two main criteria for characterising a PMT are spectral sensitivity and gain, though time response of a PMT may also be taken into account, particularly in pulse applications.[119]

Spectral sensitivity describes how the sensitivity of the PMT varies with wavelength. Usually expressed in units of quantum efficiency per incident photon, it is a measure of the percentage of photons of a specific wavelength which will produce electrons from the photo-cathode. Figure 31 shows the spectral response curve for the PMT used in this work.[120]

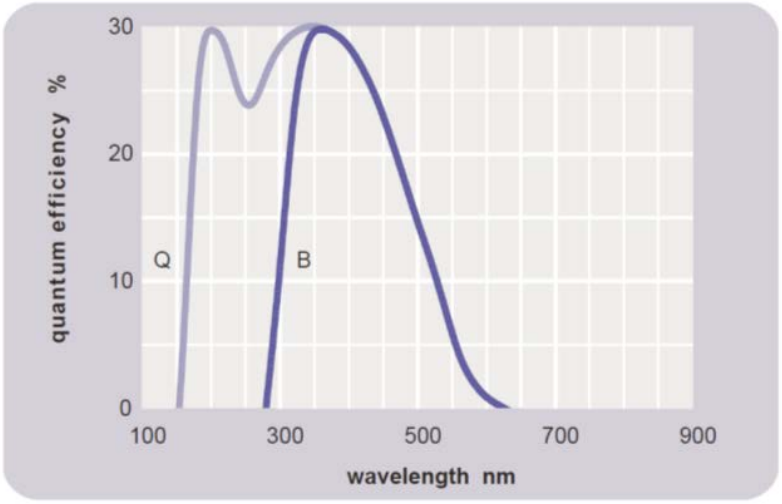

Figure 31 - Spectral response for the ET Enterprises 9235QB PMT (trace Q) [120]

Gain, or voltage gain, is a measure of the sensitivity of the anode detector, given in Amperes per lumen (A/lm) at a specified voltage. For a required sensitivity, the gain can be used to determine what voltage should be applied across the PMT (anode and dynodes). The typical voltage gain characteristics of the PMT used in these experiments is shown (Figure 32).

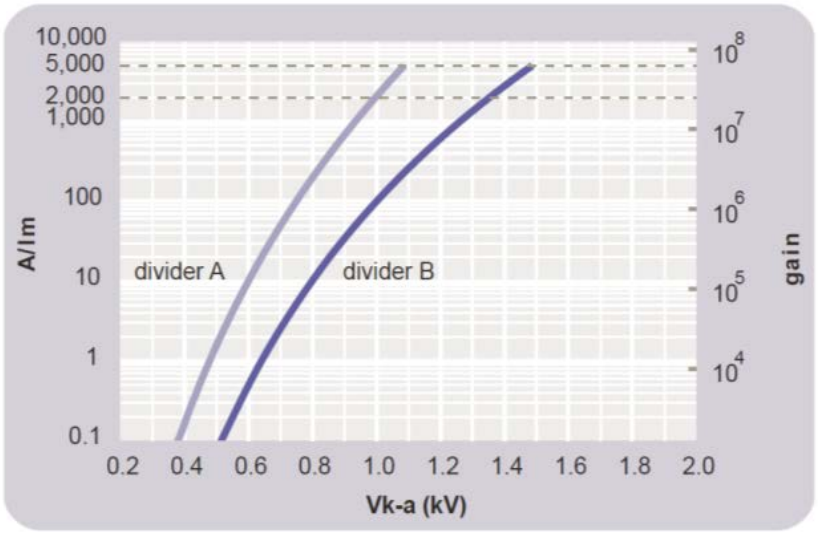

Figure 32 - Typical voltage gain characteristics for the ET Enterprises 9235QB PMT [120]

The time response of a PMT is the delay between the incidence of light upon the photocathode and detection of the signal by the anode. Time response takes into account the length of time taken for electrons incident upon the window to arrive at the detector, the variation in this value from pulse to pulse, and time taken for the signal to rise to its maximum value (rise time) and to "recover" to baseline levels.

4.6.2. Reduction of scattered light

The LLG and PMT are mounted perpendicular to the reaction region as shown in Figure 33. In order to suppress the background signal from scattered laser light detected by the PMT whilst still recording laser-induced fluorescence, three filters have been installed; two long-pass filters (Schott FWG-29525 and Schott FWG-30525), which attenuate wavelengths below 295 nm and 305 nm, respectively; and one band-pass filter (CVI Melles Griot F10-313.0-4-25.0M) with a bandwidth of 10.0 nm centred on 313.0 nm which excludes light outside of this wavelength band.

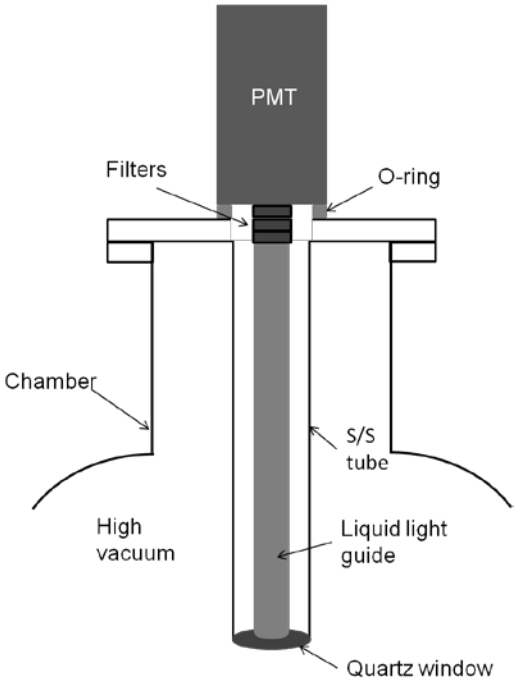

Figure 33 - Schematic of LIF detection system showing UHV mount for LLG, filters and PMT

Additional measures to minimise the amount of backscattered laser light in the chamber include an exit window tilted at the Brewster angle, which decreases internal reflection from the laser exit viewport. The Brewster angle, θ_b is determined according to (4.7), where n_1 and n_2 are the refractive indices of 282 nm light in vacuum and in fused silica (which the window is made from), respectively.

$$\tan\theta_b = \frac{n_2}{n_1} \qquad (4.7)$$

Equation (4.7) is applicable for p-polarised light hitting a surface at the Brewster angle. Under such conditions, the light is not reflected, but instead goes straight through the window, thus limiting the amount of laser light which is reflected back into the chamber.

4.7. Experimental Control and Signal Processing

4.7.1. Delay generator

The timing of the molecular beam valve, excimer laser (if used), and probe laser (Nd:YAG-pumped dye laser) in the gas-phase experiments was controlled using a delay generator (Stanford Research Systems DG-645). The delay generator has four channels, each of which outputs a TTL (transistor transistor logic) pulse at 2.5 V to trigger the relevant experimental module. Figure 34 shows the pulse sequence and typical timings for firing of the molecular beam, excimer and probe lasers.

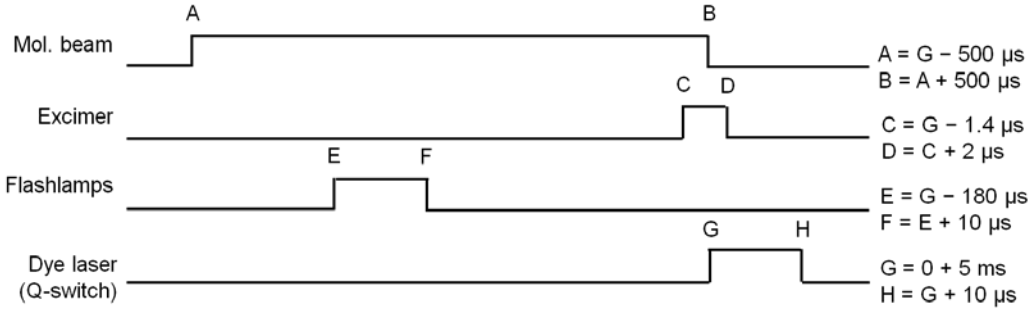

Figure 34 - Delay generator pulse sequence for triggering of the molecular beam, excimer and probe lasers

4.7.2. Data acquisition

The OH LIF signal detected by the PMT is output to an oscilloscope (LeCroy Wavesurfer 454). The oscilloscope trace is output to a PC by means of a standard Ethernet cable. The PC is also connected to the probe laser by an RS232 serial connection in order to adjust the wavelength range over which the laser is scanned during LIF experiments. A custom-written LabView program was used to set the wavelength range and step size of a LIF experiment. The program was also used to set the window (with respect to time) over which the LIF signal is integrated. For each point on the LIF spectrum, the integral of a number of traces was calculated and then plotted as a function of excitation wavelength.

5. Experimental Methods (Condensed phase)

5.1. Overview of condensed phase experiments

Studies of low energy electron interactions in layered ASW/CO/ASW ices were carried out using the EMSL facilities at Pacific North-west National Laboratory (PNNL) in Richland, WA. The ices were deposited on Pt (111) and TiO_2 (110) surfaces under ultra-high vacuum (UHV) conditions with a typical base pressure of $1x10^{-10}$ Torr. Each surface was mounted on a manipulator, cooled using a helium cryostat inside an ultra-high vacuum chamber. Deposition of water and CO onto the surface was performed using a calibrated nozzle. The ices were irradiated with electrons of a pre-selected energy (87 eV) using an electron gun (Kimball Physics ELG-2) by repeatedly scanning the electron beam over a 0.662 cm^2 area, with a single scan typically lasting 0.48 seconds. Products of the electron-stimulated reactions were analysed using temperature-programmed desorption (TPD), electron stimulated desorption (ESD) and reflection-absorption infra-red spectroscopy (RAIRS).

5.2. Sample preparation

5.2.1. Surface preparation

Initial TPD and ESD experiments were performed making use of a rutile TiO_2 (110) crystal (10 x 10 x 1 mm^3, Princeton Scientific) mounted on a resistively heated tantalum base plate. The crystal was maintained at a base temperature of approximately 25 K using a closed-cycle helium cryostat (Advanced Research Systems CSW 204B). RAIRS experiments were carried out using a Pt (111) crystal for increased reflectance. Both crystals were mounted on a rotation stage to give precise tuneability of the crystal position. All sample temperatures were monitored using a *K*-type thermocouple spot-welded to the rear side of the sample.

The TiO_2 (110) crystal surface was prepared by sputtering with 2 keV Ne^+ ions and then annealing for up to 10 minutes under vacuum at 950 K. The Pt (111) surface was prepared using 1.5 keV Ne^+ ion sputtering and annealing at 950 K. The surface cleanliness and crystalline order of the sample were verified using Auger electron spectroscopy and low energy electron diffraction. Before each experiment, the surface was heated rapidly to 950 K and annealed for 2 minutes to ensure that no adsorbates remain on the surface.

5.2.2. ASW/CO ice deposition

Thin films of ASW were deposited on the TiO_2 (110) or Pt (111) surface at 120 K using a H_2O molecular beam at normal incidence to the surface. The molecular beam was turned on and off as required using which was turned on and off using micro-dispensing solenoid valves (TheLeeCo) with ~1 ms time resolution. The typical water flux used for growing the thin films was 1×10^{14} molecules cm^{-2} s. The coverage of the water films is determined by the dosing time and checked by measuring the temperature programmed desorption (TPD) spectrum of water.

Water adsorbs molecularly to the clean surface of Pt (111).[121] On the defect-free TiO_2 (110) surface, H_2O adsorbs molecularly, attaching to 5-coordinate Ti^{4+} atoms, however, preparation of the TiO_2 results in a partially reduced (110) surface with about 7-8% oxygen vacancies where H_2O adsorbs dissociatively forming bridging hydroxyls between the oxygen vacancies.[122] By convention, a single water monolayer (ML) on TiO_2 (110) is defined as a coverage of 5.2×10^{14} molecules cm^{-2}, which in fact corresponds to occupation of only around half of the available adsorption sites. Water coverages here, both on TiO_2 and Pt, are reported such that 1 ML = 1.2×10^{15} molecules cm^{-2}.

CO was dosed on the ASW "spacer" layer at base temperature, which was 28 ±3 K. Since the sticking coefficient for CO on ASW is ~1 at T < 30 K, coverage of CO may be determined from the dosing time using the known flux of the molecular beam line. A typical CO layer in these experiments is approximately 3 ML thick, with a density of ~4×10^{14} molecules cm^{-2}.

Trapping of CO by ASW is discussed in later chapters, but in brief, experiments confirm that CO is effectively trapped by 10 ML ASW, and investigations by Kay and co-workers have demonstrated that diffusion of atoms and small molecules in ASW is negligible below ~120 K.[123]

5.3. Electron-stimulated desorption (ESD)

The interaction of electrons with solid surfaces can cause the removal of atomic, molecular, or ionic species from the surface, via a number of possible mechanisms, known collectively as electron-stimulated desorption (ESD). As an experimental technique, ESD is used in two main ways to study a substrate/adsorbate system: either by direct detection of desorbed species, or by monitoring changes in the characteristics of the surface.[124] In this way, ESD is used to investigate characteristics including total desorption yields, energy and angular distributions of desorbed species, and changes to properties of the surface following electron bombardment. In the work presented here, ESD is combined with particle detection (by quadrupole mass spectrometry, QMS) to monitor total desorption yields during electron bombardment of ices.

5.3.1. Principles of ESD

In a review paper by Ramsier and Yates Jr., the authors state that a typical ESD experiment may be described in terms of isolated electron-adsorbate interactions where electronic energy transfer plays the predominant role, particularly in systems with strong chemisorption bond energies (1-8 eV).[125] The main exception to this picture of ESD is the case of physisorbed species, which are usually more weakly bound, and direct momentum transfer may be responsible for desorption.

Historically, energy analysers have most commonly been used in ESD studies, for the detection of positive ions desorbed from the surface.[126] This technique is relatively simple to set up and can be used to determine cross-sections by measuring ion yields per electron, however it has the clear disadvantage that it cannot distinguish between different ions. In the work presented in this thesis,

desorbed species were monitored by means of a quadrupole mass spectrometer (QMS), so that the yield of a specific ion or mass fragment may be monitored.

5.3.2. ESD Experimental Conditions

To record an ESD trace in these experiments, the sample was irradiated with 87 eV electrons from an electron gun positioned at 35° to the sample normal. Desorbed species are collected in the QMS entry channel positioned at normal incidence to the sample. During irradiation a single mass channel is monitored using a quadrupole mass spectrometer (Extrel, EXM720). As the sample is irradiated, the mean intensity of the mass channel under investigation is plotted as a function of time. This produces a trace of product yield vs. time, which may be integrated to give the total yield over the course of the irradiation. Figure 35 is a typical ESD trace for the irradiation of a 60 ML thick pure ASW film, showing the important features, including a delay in onset of desorption, corresponding to a delay beginning irradiation; a rapid increase in the yield of H_2O as irradiation starts; and a rapid decline in the yield of H_2O as the irradiation is stopped.

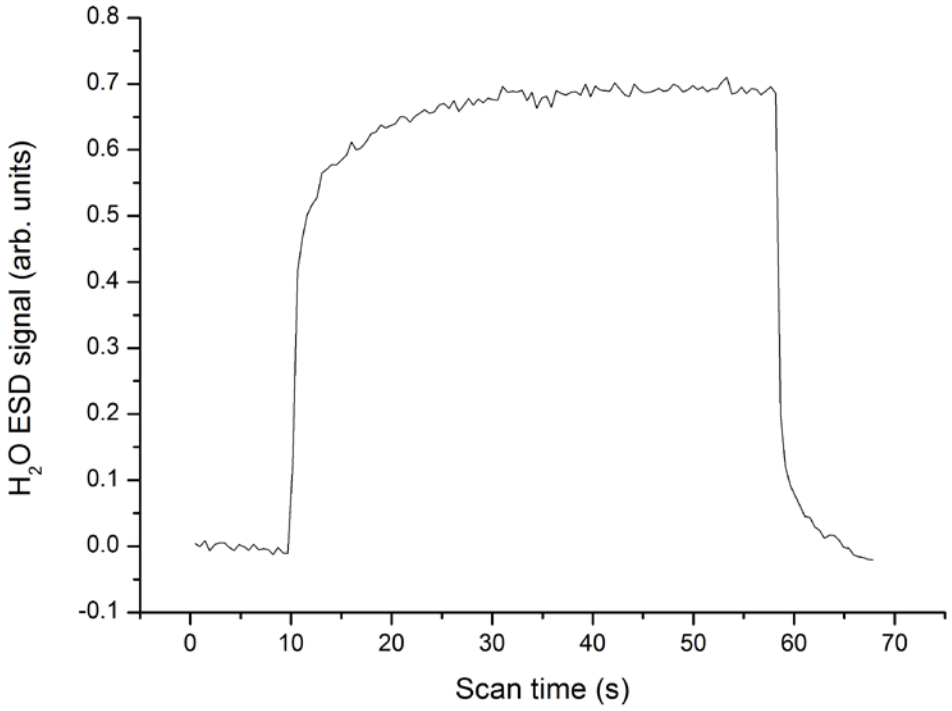

Figure 35 - H_2O ESD from 60 ML pure ASW film adsorbed on TiO (110) , irradiated for 200 cycles at 25K

In addition to these points, which confirm that a successful ESD has been recorded, characteristics specific to the desorption of ASW from TiO_2 (110) may also be observed, for example a gradual build up of H_2O yield following the initial rapid increase, finally reaching a plateau for H_2O desorption.

In the experiments which follow, electron irradiation is described in terms of number of scans, *N*. A single scan refers to rastering of the electron beam over a sample area of 0.662 cm^2, with a single scan lasting ~0.48 seconds. The typical electron current density in these experiments is 1.5×10^{15} electrons cm^{-2} s^{-1}. In these conditions, it is estimated that a single scan corresponds to an electron fluence of ~1×10^{15} electrons cm^{-2}.

5.4. Temperature-programmed desorption (TPD)

Temperature-programmed desorption (TPD), alternatively called thermal desorption spectroscopy (TDS), is a technique for studying desorption of atoms and molecules from a surface by heating. A TPD trace gives information about which species desorb from a surface, as well as the rate of desorption of each.

5.4.1. Principles of TPD

A species adsorbed to a surface at low temperature can remain in that state almost indefinitely, however if the temperature of the substrate is increased, the species may desorb from the surface and return into the gas phase. In the absence of thermal reactions, the desorbing species will generally be the same as that originally adsorbed, which means that TPD is a useful technique for investigating the species adsorbed on a surface.

In TPD, the sample is heated linearly according to a heating programme, and the yield of desorbed species is monitored as a function of temperature. The technique relies on the principle that the intensity of the desorption signal, *I*, at temperature *T*, is proportional to the rate at which the surface concentration of adsorbed species, *N*, is decreasing, according to Equation (5.1).[127,128]

$$I(T) \propto -\frac{dN}{dT} = \frac{\upsilon N^{x}}{\beta} exp\left(\frac{-E_a^{des}}{RT}\right) \qquad (5.1)$$

In this equation, x represents the order of the rate constant for the desorption process. Typically, an atomic or simple molecular desorption is first order, while a recombinative desorption (e.g. desorption of O atoms from Pt as O_2) is second order. E_a^{des} is the activation energy for the desorption process, which may also be estimated

from a TPD trace. β is the heating rate in K s^{-1}, assumed to be linear, such that $T(t)=T_0+\beta t$. This equation is derived from the Arrhenius equation for desorption, using the pre-exponential factor ν, which is effectively the "frequency of desorption attempts", in Hz.

5.4.2. TPD Experimental Conditions

In a TPD experiment, following deposition, the crystal is heated to 350 K at a rate of 2 K s^{-1} and then allowed to return to base temperature. A QMS (Extrel, EXM720) is used to monitor the evolution of up to 3 mass channels during heating; the intensity of each mass peak is plotted as a function of temperature.

TPD measurements were conducted for various compositions of mixed CO/ASW films deposited on TiO_2 (110). In each experiment performed, TPD traces were recorded both with and without irradiation of the sample, as shown in Figure 36.

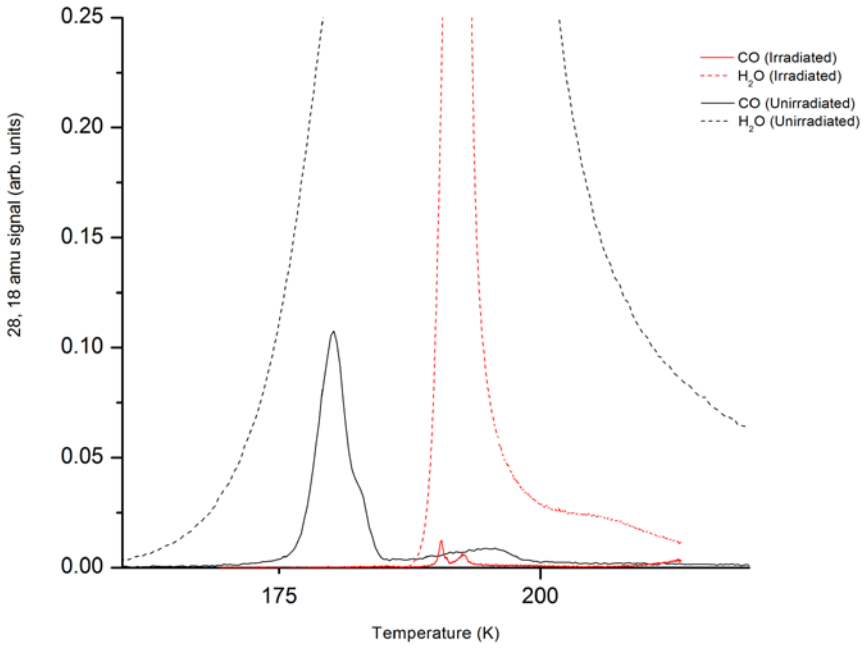

Figure 36 - TPD traces showing yield of CO from both irradiated (red) and unirradiated (black) layered ASW/CO/ASW ices (traces for H_2O also shown - dashed lines)

The peak integrals for the non-irradiated TPD trace are subtracted from the peak integrals in the TPD of the irradiated sample to give a “corrected” value for each. This calculation gives the total yield of reaction products, CO and ASW remaining in the film following irradiation.

5.5. Reflection-absorption infra-red spectroscopy (RAIRS)

RAIRS spectroscopy is used in the following work to observe changes in the species present in the ice films *in situ*. This technique uses IR radiation to probe the chemical species in the ice without the need for desorption.

5.5.1. Principles of RAIRS

Fourier transform infra-red spectroscopy (FTIR) is an analysis technique based on irradiation of a sample with infra-red light, causing vibrational excitation of chemical bonds within the sample. In an IR spectrum, the absorbance, A, of the sample is plotted as a function of the wavenumber in cm^{-1}. The absorbance of the sample is related to the intensity of the intensity, I, of the IR beam according to the Beer-Lambert Law (equation 5.2)

$$A = -\ln\left(\frac{I}{I_0}\right) \qquad (5.2)$$

The intensity of the transmitted light is in turn related to the concentration, c, of a particular species according to equation (5.3).

$$\frac{I}{I_0} = \exp(-\sigma l N) \qquad (5.3)$$

In equation (5.3), σ is the total (absorption and scattering) cross-section for IR light interacting with the sample, l is the path length of light through the sample, and N is the number density of molecules in the sample.

As a result of this relationship, the absorbance in an IR spectrum not only shows what bonds are present in a sample, but may also be used as a quantitative technique.

RAIRS is a form of FTIR used for solid samples, particularly metal single crystals, in which the IR beam is incident on the front face of the sample at a shallow angle (a

"grazing" angle); this allows substrate/adsorbate systems to be investigated by IR. The main drawback of the RAIRS technique is that sensitivity is rather low (compared with liquid IR techniques) due to the small number of adsorbing molecules. The other notable disadvantage is that often low frequency modes cannot be detected, so surface-molecule bonds are not usually observed, only bonds within the molecules themselves. Finally, it should be noted that only those vibrational modes which give rise to an oscillating dipole perpendicular to the surface are IR active and give rise to an observable absorption band.[127]

5.5.2. RAIRS Experimental Conditions

In the experiments which follow, a Fourier-transform infrared spectrometer (Bruker, Vertex 70) was used for RAIRS studies of layered ASW/CO/ASW films. Since, the amount of CO is small compared to the amount of ASW, new species created by the electron-stimulated reactions are typically difficult to discern in the raw spectra. In order to observe these new species, spectra are recorded from the samples both before and after irradiation, and the difference between these spectra is calculated. Examples of RAIRS spectra for irradiated and non-irradiated samples are shown in Figure 37.

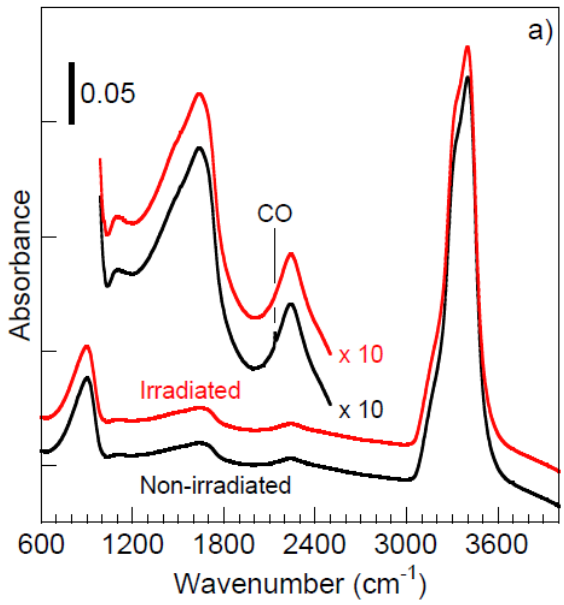

Figure 37 - RAIRS spectra of layered ASW/CO/ASW ices both irradiated and non-irradiated at 25 K

An alternative to this is to repeat irradiation experiments with and without CO and calculate the difference here. This procedure is useful since electron irradiation leads to changes in the IRAS spectra of the ASW films that can make it difficult to observe the small signals associated with the CO-H_2O reaction products.

6. Laser-induced fluorescence studies of DEA in water

6.1. Preliminary Experiments

The aim of the gas phase studies was to record and analyse LIF spectra for nascent OH radicals formed by dissociative electron attachment to water. Details of the high vacuum chamber, electron gun and laser system for these experiments have been outlined (Chapter 4). Instead of beginning with DEA to water, initial OH LIF spectra were recorded using two alternative sources: photo-dissociation of tertiary butyl hydroperoxide at ~280 nm; and photo-dissociation of allyl alcohol at 193 nm in order to confirm detection of OH radicals and to optimise the experimental conditions. The following is a discussion of the results of these preliminary experiments and how they have influenced changes to the apparatus.

In the first experiments, photo-dissociation of t-butyl hydroperoxide was performed using the same dye laser wavelength which was used to excite the $A^2\Sigma^+(v=1) \leftarrow X^2\Pi_i(v=0)$ transition in OH. This has the practical advantage over two-colour experiments that only one laser is required and one set of steering optics, which avoids complications arising from temporal and spatial overlap of the dissociation and LIF lasers. The dye laser was focused using a 23 cm focal length lens. Figure 38 shows the arrangement of the laser optics for the one-colour experiments.

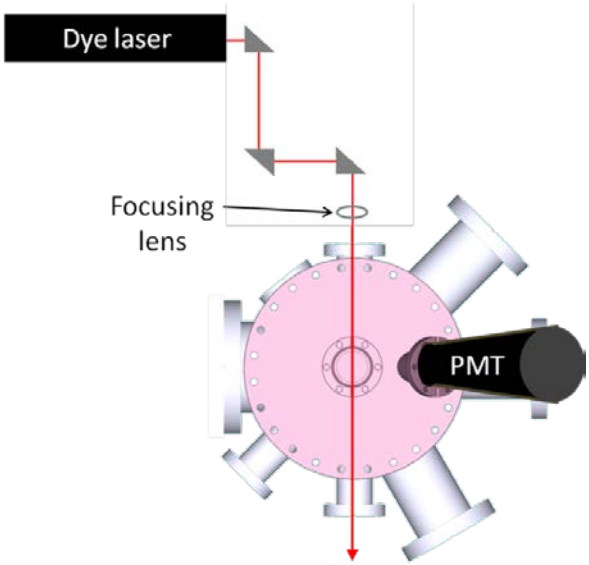

Figure 38 - Laser alignment for one-colour experiments, showing steering optics and focusing lens

The spectrum in Figure 39 is an example of a typical OH LIF spectrum recorded using t-butyl hydroperoxide. This spectrum was recorded at a precursor gas pressure of around 5 Torr in the chamber. The reason for using such high pressures is that early experiments were conducted without optimisation of any of the experimental or detector conditions, S/N etc, so high pressures were needed initially in order to observe OH LIF.

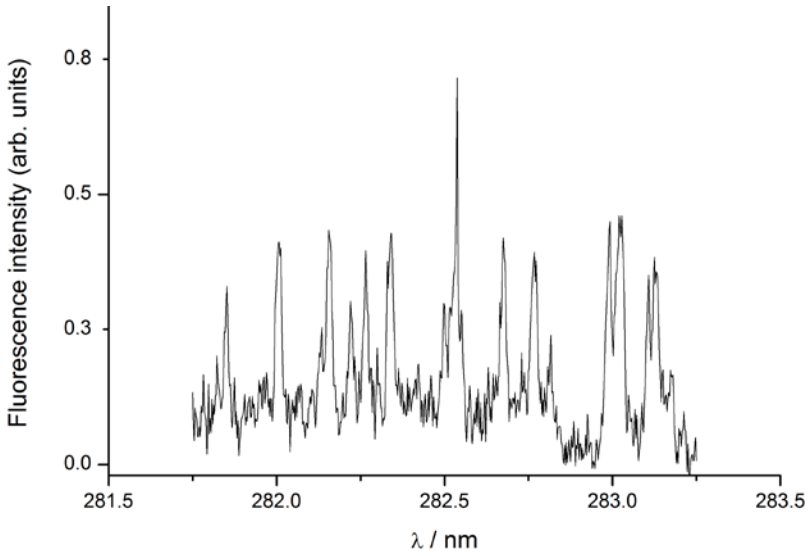

Figure 39 - OH LIF spectrum recorded by photo-dissociation of 5 Torr t-butyl hydroperoxide at ~280 nm

By comparison with peaks in the LIFbase spectrum of OH (Figure 8), it is clear that the spectrum shown in Figure 35 shows peaks identifiable as OH $A^2\Sigma^+(v=1) \leftarrow X^2\Pi_i(v=0)$ fluorescence. Later experiments in Section 5.2 detail efforts made to reduce noise in this experimental set-up, however, an increase in signal strength could also improve the S/N shown here. Immediate gains in signal strength may be made by using a precursor gas which has a higher dissociation cross-section, which will produce more OH. Table 7 lists the dissociation cross-section for t-butyl hydroperoxide, compared with other molecules which may be photo-dissociated to give OH molecules.

Table 8 - Dissociation cross-sections and vapour pressures for OH precursors

Precursor	**σ/cm^2 (wavelength/nm)**	**P_v/kPa (T/°C)**
t-butyl hydroperoxide	2×10^{-21} (280)	3.07 (20)
allyl alcohol	3.35×10^{-19} (200)	2.4 (20), 4.3 (30), 7.4 (40)
water	2.05×10^{-16} (50 eV electrons)[129]	3.17 (25)[130]

In order to record OH LIF spectra by photo-dissociation of allyl alcohol, an excimer laser was introduced in addition to the dye laser, as described in Chapter 4.5.3. Figure 40 shows a typical OH LIF spectrum recorded by photo-dissociation of allyl alcohol at 193 nm where the pressure of the allyl alcohol in the chamber was approximately 5 Torr, as before.

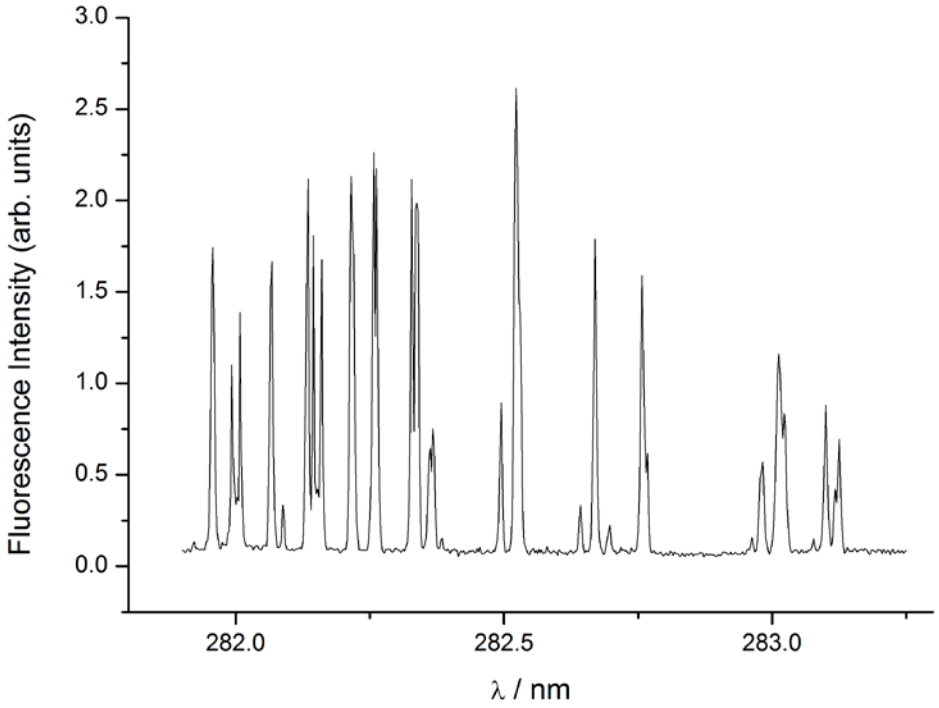

Figure 40 - OH LIF recorded by photo-dissociation of 5 Torr allyl alcohol at 193 nm

It is clear from this spectrum that the increase in dissociation cross-section by using allyl alcohol has dramatically increased the signal and improved the overall S/N in the OH LIF spectrum. Given the gain in signal for the same initial pressure of precursor gas, allyl alcohol was selected for use in all further optimisation experiments.

6.2. OH LIF spectra for low pressure of precursor gas

The OH LIF spectra shown in the previous discussion were recorded at near-atmospheric pressures of precursor gas in order to give the largest possible signal for optimisation experiments. To fulfil the stated aim of these experiments and record LIF spectra for nascent OH radicals formed by DEA to water in a molecular beam, further optimisation is required.

Lower pressures are eventually required to produce a molecular beam, which will generate cold H_2O molecules with a well-defined energy distribution, and minimal ro-vibrational excitation. In order to operate the electron gun within the recommended conditions for the filament, the pressure must be no more than 10^{-4} Torr.

The conditions for recording nascent OH LIF spectra are discussed in greater detail in Section 5.4, but in brief, for OH to be nascent within the confines of our experiment, the time between OH collisions (Δt) must be greater than the time between dissociation of allyl alcohol by the excimer laser and excitation of OH by the LIF laser. The delay between the lasers is set to 1.4 μs by the delay generator (Figure 34); however according to the signal recorded by the oscilloscope, the delay is shorter, ~0.5 μs (Figure 44). In order to record nascent OH, a pressure on the order of ~100 mTorr or less is required (unless a molecular beam is used).

A number of experiments have been conducted to determine how precursor gas pressure affects the OH LIF spectra recorded by our kit. For these experiments, instead of a full spectrum of the $A^2\Sigma^+(v=1) \leftarrow X^2\Pi_i(v=0)$ transition in OH, only the $Q_1(1)$ line was recorded, between 281.9 nm - 282.1 nm.

The first experiments to reduce the pressure of the precursor gas involved filling the chamber via the gas manifold to a pressure of 6.7 x 10^{-1} Torr of allyl alcohol. Under these conditions, both the turbo-molecular pumps and the rotary vane pumps are switched off. To reduce the pressure, the rotary pumps were briefly turned on and then off again, and the pressure remaining in the chamber was recorded. Figure 41 shows a number of OH LIF spectra *vs.* increasing pressure of allyl alcohol recorded in this experiment.

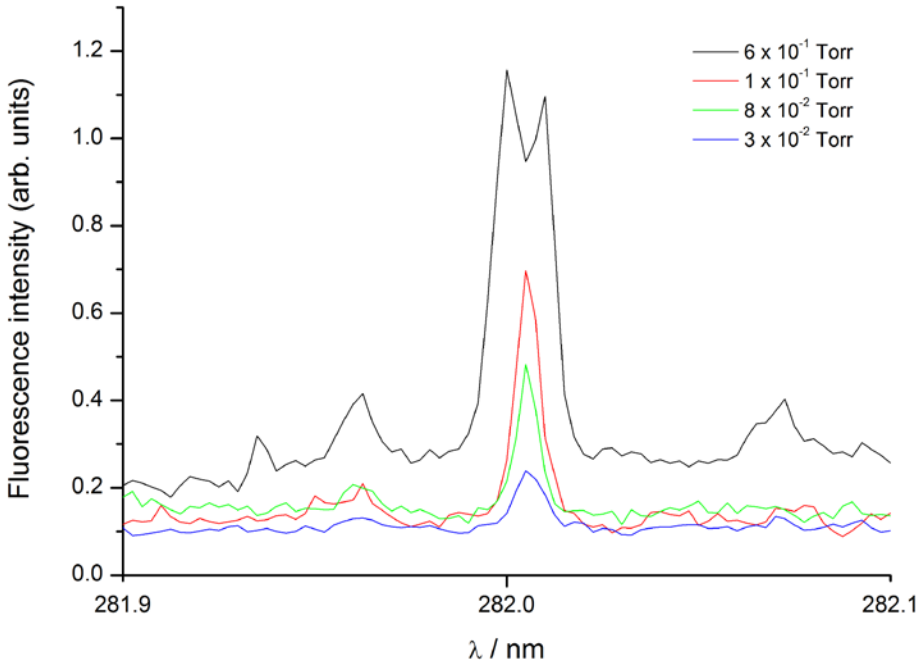

Figure 41 - Effect of gas pressure on LIF intensity from 193 nm photo-dissociation of allyl alcohol

This set of spectra shows that our apparatus is able to record OH LIF after 193 nm photo-dissociation of allyl alcohol at pressures down to 3×10^{-2} Torr. As a test of the detection system and proof of concept for recording OH LIF in the photo-dissociation experiments, this can be considered a success. Using this method of

reducing the pressure of allyl alcohol, the minimum pressure which may be reached is around 5×10^{-3} Torr. In order to record further experiments at lower pressures, a needle valve was used as an alternative method of sample introduction.

A needle valve may be used to introduce a small, well-controlled pressure of gas in to the chamber, whilst both the rotary vane pumps and turbo-molecular pumps are running. In order to observe OH LIF for lower pressures of precursor gas, improvements were made to S/N to give the greatest chance of resolving the small amounts of signal from the noise. Efforts to reduce noise and improve S/N are detailed in 6.3. Briefly, optimisation of laser energies, temporal and spatial overlap of beams, integration parameters and PMT operating parameters was carried out. Results of the low pressure experiments are shown in Figure 42.

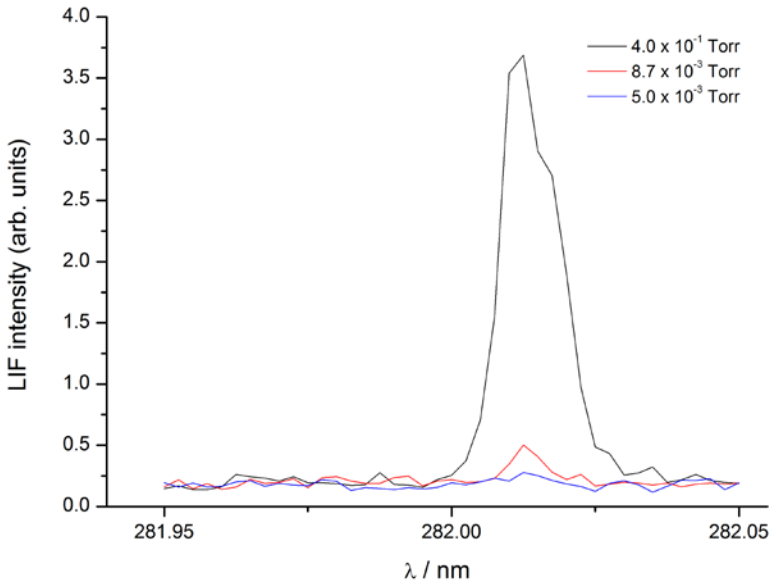

Figure 42 - Effect of gas pressure on OH LIF intensity from 193 nm photo-dissociation of allyl alcohol using needle valve for sample introduction

The results in Figure 42 show that with optimised S/N conditions it is possible to record OH LIF spectra for starting conditions of 8.7 x 10^{-3} Torr. This is a gain of an

order of magnitude compared with the lowest recorded pressures in previous experiments. It is clear from these spectra that there is considerable signal loss in decreasing the precursor gas pressure from 10^{-1}Torr to 10^{-3} Torr.

The HV chamber in these experiments is equipped with a molecular beam nozzle, which produces pulses of cold H_2O seeded in helium. Use of this beam would allow studies of the ro-vibrational state distribution of OH radicals to be conducted where the energy of the parent H_2O is well-defined. In theory, the high number density of molecules in a molecular beam should be sufficient to record OH LIF spectra, however, in practice it has not been possible using this method.

Number density of molecules in a molecular beam

The number density of molecules in the molecular beam formed in this experiment should be in the region of 10^{15}-10^{20} molecules cm^{-3}. The number density of molecules in an ideal gas, such as the gas mixture in the molecular beam source chamber (the "stagnation region"), is given by equation (4.4)

$$p = nk_BT \qquad (4.4)$$

In the experiments described, the pressure, p, of the gas is ~1 bar (1 x10^5 Pa); k_B is the Boltzmann constant; and T is the temperature, 300 K. This gives a number density of 2.4×10^{19} molecules cm^{-3}.

Equation (4.5) is used to determine the number of molecules of H_2O which cross the electron beam within the detection region (see section 6.4) per second, or the intensity, I. [131]

$$I = \frac{1}{4\pi}\frac{A_d}{l_0^2}n\bar{v}A_s \qquad (4.5)$$

Here, A_d and A_s are the areas of the detection region (4.44×10^{-4} m^2) and slit (in the beam nozzle, 1.96×10^{-7} m^2), respectively; *n* is the number density of H_2O molecules, as determined above; and $\bar{v}$ is the average velocity of the H_2O molecules, estimated to be ~300 ms^{-1}.

Using this equation yields a value of $\sim 3 \times 10^{18}$ molecules s^{-1} m^{-2} intersecting the electron beam within the detection region of the PMT. However, since water makes up only a small fraction (~2.6%) of the molecules in the beam, giving a total intensity of $\sim 8 \times 10^{16}$ molecules s^{-1} m^{-2}, it is possible that the number density of H_2O is too low despite the overall density of the beam.

6.3. Improvements in signal to noise ratio

In order to maximise the chances of recording OH LIF spectra for low number densities of precursor gas, it is useful to first optimise the signal to noise ratio. The following account details steps which were made in order to learn the effect of different experimental variables on the S/N in our experiments.

As described in Chapter 4.6.1, the voltage applied across the PMT dynodes is related to the sensitivity of the device. By increasing the PMT voltage, the sensitivity may be increased. The advantage of increasing the PMT voltage is of course a gain in signal intensity, but this is accompanied by a corresponding increase in noise detection. Figure 43 shows OH LIF spectra recorded at four different PMT voltages.

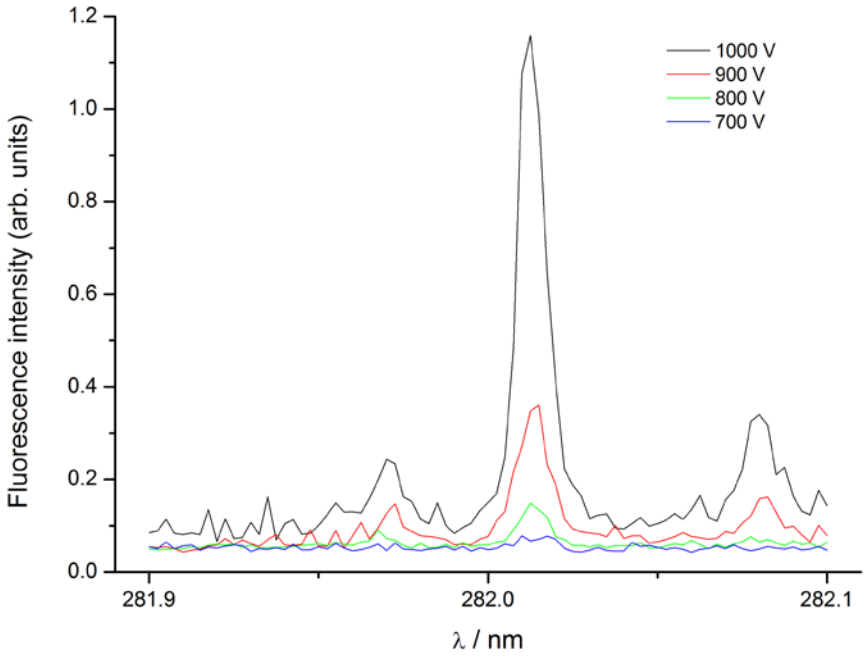

Figure 43 - Change in LIF intensity and S/N ratio as a function of PMT voltage for OH produced by 193 nm photo-dissociation of 10^{-2} Torr allyl alcohol

By comparing the traces in Figure 43, it appears that although the main peak intensity at 1000 V is large compared with the signal for lower voltages, there is a considerable increase in noise in the baseline of this particular LIF spectrum.

Table 9 lists the S/N values determined by analysis of the signal intensity of the $Q_1(1)$ line versus the baseline noise. These values confirm that the gain in signal at 1000 V does not sufficiently compensate for the increase in noise in the baseline. Instead, the optimum PMT voltage in terms of S/N is at 900 V, as the S/N peaks at this voltage, falling at lower voltages due to losses in signal strength.

Table 9 - S/N ratio for OH LIF spectra as a function of PMT voltage

PMT Voltage / V	**S/N Ratio**
1000	16.8
900	23.6
800	21.3
700	6.61

In order to extract a LIF spectrum from the fluorescence signal, the signal is integrated over a certain range (time, s) and then plotted against excitation wavelength. Figure 44 shows the oscilloscope trace recorded with both the excimer and dye lasers running, but no fluorescence. The signal at -1×10^{-7} s corresponds to the firing of the excimer laser and is due to scattered photons from this laser. The larger signal at 4×10^{-7}s is also due to scattered photons, in this case from the dye laser.

Since it has been impossible to completely eliminate a small amount of noise due to scattered light in the vacuum chamber, some of the fluorescence signal which is integrated will be due to noise. The size of the integration range affects the amount

of signal which is integrated and how much noise contributes to that signal. By optimising the integration window, it may be possible to improve the S/N ratio.

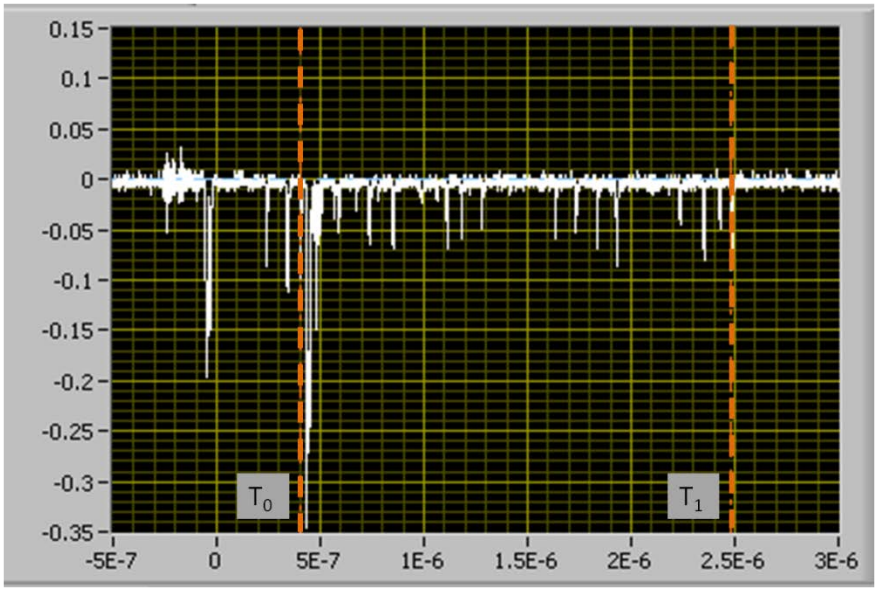

Figure 44 - Oscilloscope trace, showing the relative timings of the excimer and dye lasers, and the settings T_0 and T_1

In a typical experiment, the onset of OH fluorescence is observed $\sim 4\times10^{-7}$ s, which overlaps the signal due to scattered photons from the dye laser. The lower and upper limits of the integration window, T_0 and T_1 respectively, are highlighted in Figure 44. In order to reduce the effect of noise resulting from this overlap, the lower limit of the integration window for the fluorescence signal, T_0, can be varied. In addition, the upper limit, T_1, defines how much of the signal is integrated.

Figure 45 shows the effect of varying T_0, whilst maintaining a fixed value of $T_1 = 3.0\times10^{-7}$ seconds. Based on the results shown here, it appears that the optimum value for T_0 is $\sim 4.5\times10^{-7}$ s.

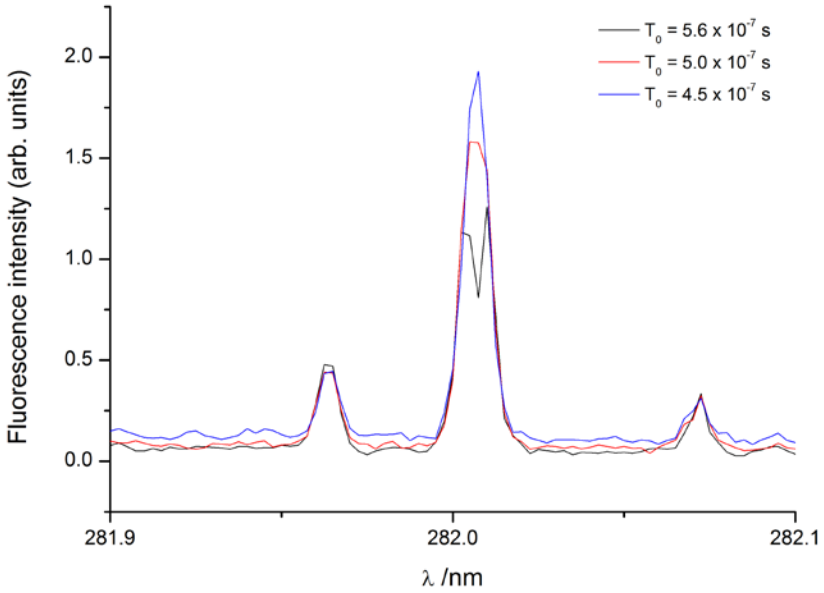

Figure 45 - Effect of T_0 on S/N for LIF spectra of OH from 193 nm photo-dissociation of allyl alcohol at 1×10^{-2} Torr

A similar experiment was carried out in which T_0 was set to 5.0 x 10^{-7} s, while T_1, the upper limit of the integration window, was varied; the results are shown in Figure 46.

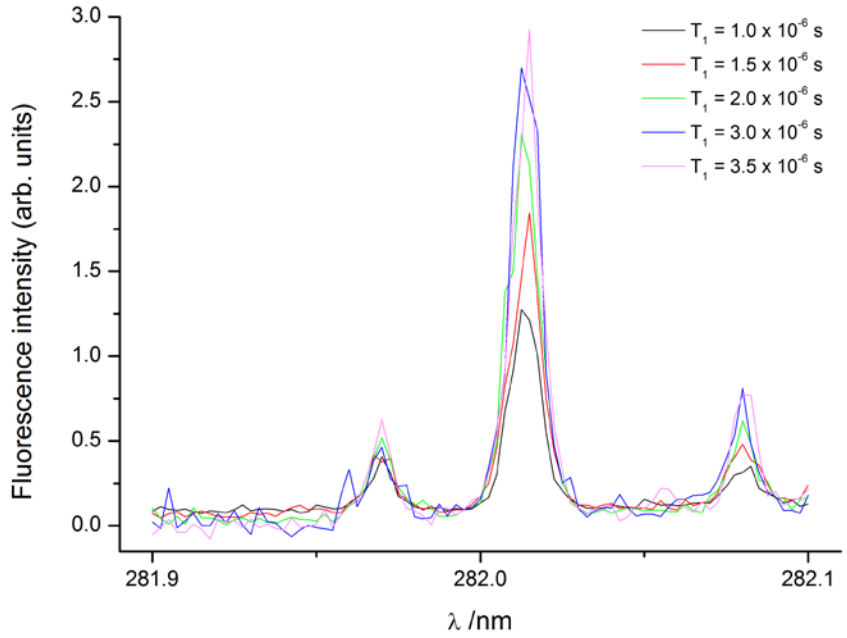

Figure 46 - Effect of T_1 on S/N of LIF spectra of OH from 193 nm photo-dissociation of allyl alcohol at 1×10^{-2} Torr

Figure 46 shows an increase in signal as T_1 is increased, due simply to integrating a greater amount of fluorescence. However, there is a significant increase in the noise for T_1 = 3.0 μs and above. This is most likely due to the fact that the fluorescence lifetime of OH (~0.6 μs)[109] is much shorter than this time period and therefore everything that is integrated after this time is purely additional noise.[132] Any appearance of a gain in signal here is most likely due to a greater contribution of noise to the signal.

Table 9 shows the S/N analysis for each LIF spectrum *vs.* T_1; the results indicate that $T_1 = 2.0\times10^{-6}$s gives the best S/N. Based on these results, the recommended integration window for optimum S/N conditions is T_0 = 0.45 μs to T_1 = 2.0 μs.

Table 10 - S/N ratio for OH LIF spectra as a function of T_1 ($T_0 = 5.0 \times 10^{-7}$ s)

T_1 / seconds	**S/N Ratio**
1.0×10^{-6}	35.7
1.5×10^{-6}	53.5
2.0×10^{-6}	54.2
3.0×10^{-6}	38.4
3.5×10^{-6}	34.3

A dye laser is used to excite the fluorescent transitions in OH by scanning over the wavelength range 281.9 - 283.25 nm. A minimum energy per laser pulse is required in order to excite enough OH molecules that a sufficient fluorescence signal may be detected by the PMT. A higher laser energy per pulse should result in greater OH fluorescence signal. Conversely, a laser energy which is too high may cause saturation of the transition, as well as increasing the signal from scattered light in the chamber. The energy of the laser may be varied by adjusting the Q-switch delay in the pump laser (a Nd:YAG laser; see Chapter 4.5.1 for more details). Figure 47

shows a comparison of LIF spectra recorded at two different LIF laser energies under otherwise identical conditions.

The figure clearly demonstrates the importance of maintaining a high dye laser energy to observe the maximum OH fluorescence possible. One hurdle to this is that the energy of the laser gradually reduces over time as the number of the shots fired by the flash-lamps in the Nd:YAG laser increases and the energy of this laser consequently decreases. In order to maintain the best signal possible, the dye laser energy should be monitored and, where possible, improvements and maintenance made to the laser hardware in order to prevent the energy falling significantly.

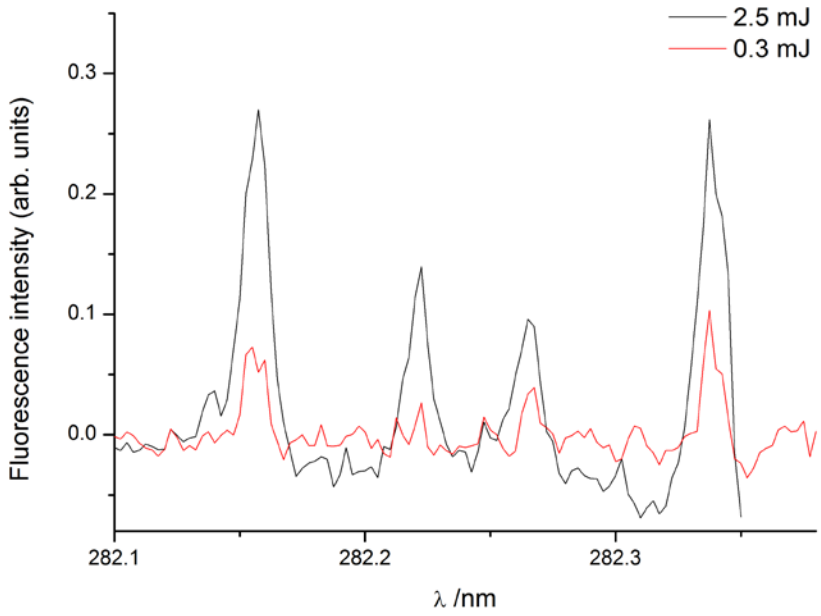

Figure 47 - Effect of dye laser energy on OH LIF intensity and S/N

In addition to the changes detailed, further improvements to S/N were made by adjusting the time delays in the experiment. The relative time delays between excimer laser, dye laser and PMT gate are set by the delay generator (chapter 4.7.1); by varying these time delays, it is possible to increase the S/N.

The excimer laser is fired before the dye laser to dissociate allyl alcohol and produce OH for excitation. However, since the OH is created with a certain kinetic energy, the dye laser pulse must arrive soon after the dissociation event in order to capture the maximum population of OH within the diameter of the dye beam. It is helpful to have a delay between firing of the two lasers, partly to ensure that excitation only occurs after dissociation, but also to reduce noise caused by scattered excimer laser photons within the integration window. Excimer laser photons do not contribute as much to the noise on the signal as dye laser photons, due to the wavelength of the excimer, which is filtered.

Spatial overlap between the two laser beams was also optimised to increase the S/N ratio. This was achieved by setting the LIF laser wavelength to an intense line in the LIF spectrum and small adjustments to the alignment of the lasers with respect to one another while monitoring the response on the oscilloscope.

6.4. Calculations of number density of OH molecules

Despite losses in signal at lower pressures, the preliminary experiments demonstrated that the apparatus is capable of recording LIF spectra for OH molecules produced by dissociation of allyl alcohol at pressures of $\sim 9\times10^{-3}$ Torr and established conditions for LIF detection. The aim of the LIF experiments was to record OH LIF by 8.5 eV electron attachment to water in a molecular beam; this section details calculations to determine the feasibility of recording this experiment successfully using the system described. Three variations of the experiment are addressed: OH LIF detection by 193 nm photo-dissociation of allyl alcohol (as described in the previous section); OH LIF detection by 100 eV electron collisions with H_2O; and OH LIF detection by 8.5 eV electron dissociation of H_2O in a molecular beam. Starting with the conditions in which a LIF spectrum has been successfully recorded allows for the OH LIF sensitivity of the current system to be determined. The second set of conditions tests the possibility of recording OH LIF by electron collision at higher electron energies, where the cross-section for dissociation is higher; while the third set of conditions represents the OH LIF by dissociative electron attachment experiment which was the aim of this work.

Detection region

In the experiments described, the LLG detects fluorescence over a cone angle of 70°, as shown in Figure 48. This results in a detection region (shaded) in which OH fluorescence must fall in order to be detected. Depending upon the other experimental conditions, such as the relative diameters of the photolysis and LIF lasers, and the diameter of the electron beam, the volume of this detection region may vary. For each set of conditions, the volume of this region is stated.

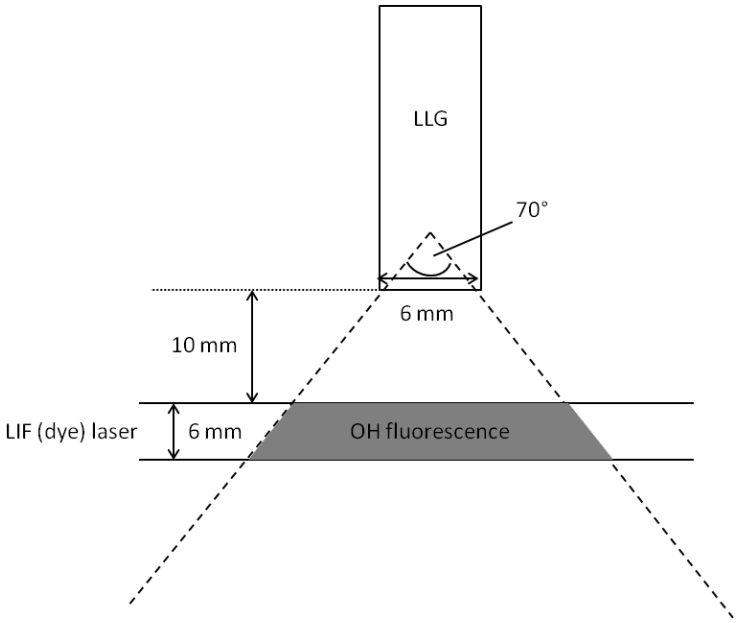

Figure 48 - Schematic showing the detection region of the LLG relative to the LIF laser

6.4.1. Photo-dissociation of allyl alcohol at ~9×10^{-3} Torr

To determine the LIF sensitivity of the current system, the following calculations assume these conditions (shown in Figure 49):

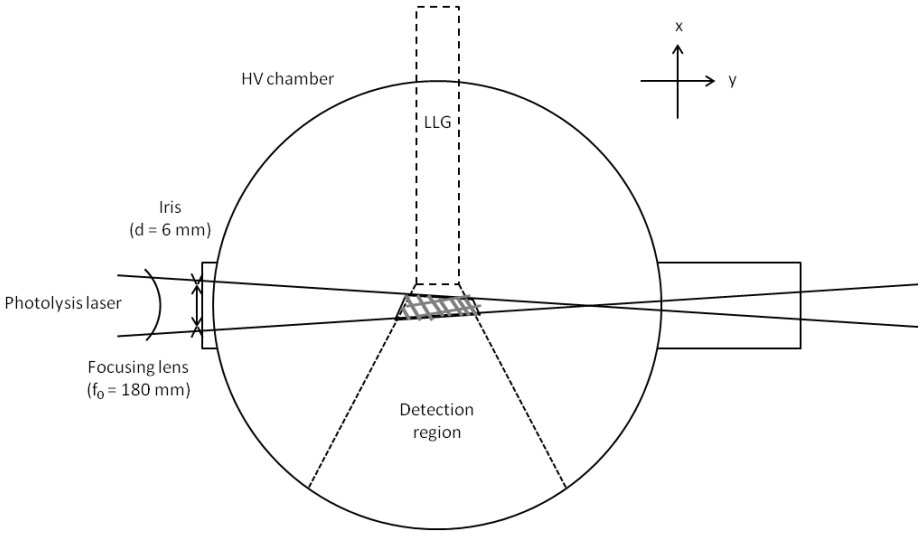

Figure 49 - Schematic showing the conditions for photo-dissociation by excimer laser of allyl alcohol at a pressure of 9×10^{-3} Torr

- Gas pressure = 9×10^{-3} Torr allyl alcohol
- Photolysis laser average beam diameter within detection region, d = 0.5 mm
- Path length of excimer laser through detection region, l = 10 mm
- Typical energy per pulse, E = 2.0 mJ
- Dissociation cross-section of allyl alcohol, $\sigma = 3.35\times10^{-19}$ cm^2
- Volume of LIF detection region (hashed area, Figure 1) = 163 mm^3

Number density of allyl alcohol at 9×10^{-3} Torr

The number density, N_{alc}, of allyl alcohol molecules is calculated using the ideal gas law (equation 6.1) where P is the gas pressure, in Pa; N_i = number density of the

molecule of interest, in m^{-3}; k is the Boltzmann constant, in m^2 kg s^{-2} K^{-1}; and *T* is the temperature, in K.

$$P = N_i kT \qquad (6.1)$$

This gives a value of 2.80×10^{20} m^{-3} for the number density of allyl alcohol molecules. This equates to approximately 3.64×10^{13} allyl alcohol molecules within the detection region.

Number density of excimer laser photons per pulse

The excimer laser beam within the detection region is assumed to have an average diameter, d = 0.5 mm. Equation (6.2) is used to calculate the energy of a single excimer photon, of wavelength, λ = 193 nm.

$$E = \frac{hc}{\lambda} \qquad (6.2)$$

In this equation, *E* is equal to the energy in J; h is Planck's constant ($6.626\text{x}10^{-34}$ J s); c is the speed of light (2.99×10^8 m s^{-1}); and λ is the wavelength of the incident photons, in m. A single 193 nm photon has an energy, $E = 1.03\times10^{-18}$ J. Assuming a laser energy of 2 mJ $pulse^{-1}$, this gives the number of photons per pulse = 1.9×10^{15}.

Number density of OH radicals produced by photolysis of allyl alcohol

Production of OH from allyl alcohol by laser dissociation at 193 nm is a single-photon process with a dissociation cross-section, $\sigma = 3.35\times10^{-19}$ cm^2. Using the Beer law (equation 6.3) it is possible to estimate the fraction of excimer photons which will dissociate allyl alcohol and consequently the number density of OH molecules.

$$\frac{I}{I_0} = \exp(-N\sigma l) \qquad (6.3)$$

Here, I_0 and I are the initial and final intensities of the excimer laser beam; $\frac{I}{I_0}$ represents the fraction of the photons which have been not been absorbed in dissociation of allyl alcohol. N is the number density of allyl alcohol, in m^{-3}; and l is the path length of the laser through the detection region, assumed to be 10 mm. The result of this calculation is ~0.99, implying that a small fraction ($\sim 9.38\times10^{-5}$) of the photons in the beam are absorbed by allyl alcohol, leading to a dissociation event. This leads to an estimate of 1.78×10^{11} OH molecules cm^{-3} $pulse^{-1}$ for the number density of OH molecules created within the detection region during each laser pulse under these pressure conditions.

Number of OH molecules which fluoresce following laser-excitation at ~283.5 nm

The LIF laser enters the chamber through the same iris as the photolysis laser, but is unfocused; this gives an average beam diameter for the LIF laser of 6 mm. It is therefore reasonable to assume that the LIF laser fully overlaps the excimer beam along the whole length of the detection region and that all OH radicals formed by photolysis may interact with the LIF laser.

Equation (6.2) is used to calculate the energy of a single dye laser photon. The dye laser scans over a range of wavelengths, with an average value of λ = 283.5 nm, giving a photon energy of $\sim 7\times10^{-15}$J. Assuming a typical pulse energy of 1 mJ per pulse, the number of dye laser photons per pulse is equal to 1.4×10^{13} photons per pulse. Since this value is greater than the number density of allyl alcohol molecules, it is assumed that every OH radical created by photolysis may also be excited by the dye laser and subsequently produce fluorescence. Therefore under the conditions stated for pressure of allyl alcohol, laser energy per pulse, and using a LIF laser with a typical pulse energy of ~1 mJ per pulse for detection, an estimate for the OH LIF

sensitivity of this experiment of at least 1.78×10^{11} OH molecules cm^{-3} $pulse^{-1}$ has been calculated.

In addition to those listed at the start, the calculations in this section assume that the OH radicals do not fly out from the location in which they are created on the timescale of the experiment, and also that every collision between a LIF laser photon and an OH radical results in fluorescence. The more realistic case for each of these assumptions would, however, give a better LIF sensitivity than has currently been determined.

6.4.2. 100 eV electron dissociation of water at 1×10^{-4} Torr

Since OH LIF detection by photo-dissociation of allyl alcohol has proved possible, the next steps towards detection of OH LIF by electron attachment to water are to use an electron gun rather than photolysis laser to dissociate the precursor molecule, and to use water, rather than allyl alcohol. In these preliminary experiments, dissociation of water by 100 eV electrons will be studied, as the cross-section for this process is much higher than dissociation via DEA and is therefore more likely to produce a measurable LIF signal. The electron gun current at higher energies is also likely to be higher, further increasing the likelihood of recording a signal.

The following calculation is intended to indicate whether OH LIF detection by electron collision with H_2O at 10^{-4} Torr is possible. This pressure of H_2O is chosen to be as high as possible to maximise H_2O number density, but below the recommended operating pressure of the filament in the electron gun. In the current set-up, the electron gun produces a continuous beam of electrons, rather than a pulsed beam. However, it is intended that a pulsed electron beam will be employed for these

experiments therefore a typical pulse length of ~1 ms is used in the calculations. In addition to these points, the following assumptions are made here:

- Gas pressure = 10^{-4} Torr H_2O
- Diameter of electron beam, d = 0.5 mm
- Typical current at 100 eV is 2.0 mJ
- Dissociation cross-section for 100 eV electron collisions with H_2O, $\sigma = 2.05\times10^{-16}\text{cm}^2$
- Volume of detection region = ~282.7 mm^3

Figure 50 shows a schematic of the sample volume of OH LIF in this section. The diameter of the electron beam is assumed to be approximately 10 mm. In the absence of a molecular beam, the electron beam may be assumed to dissociate allyl alcohol molecules in a region which describes a cylinder of diameter 10 mm, across the diameter of the chamber (~180 mm). The LIF laser crosses this cylinder of OH radicals at an angle of 45°, creating an oblique cylinder of fluorescent OH radicals within the detection region. This volume has radius 10 mm and height 10, corresponding to a total volume of approximately 282.7 mm^3.

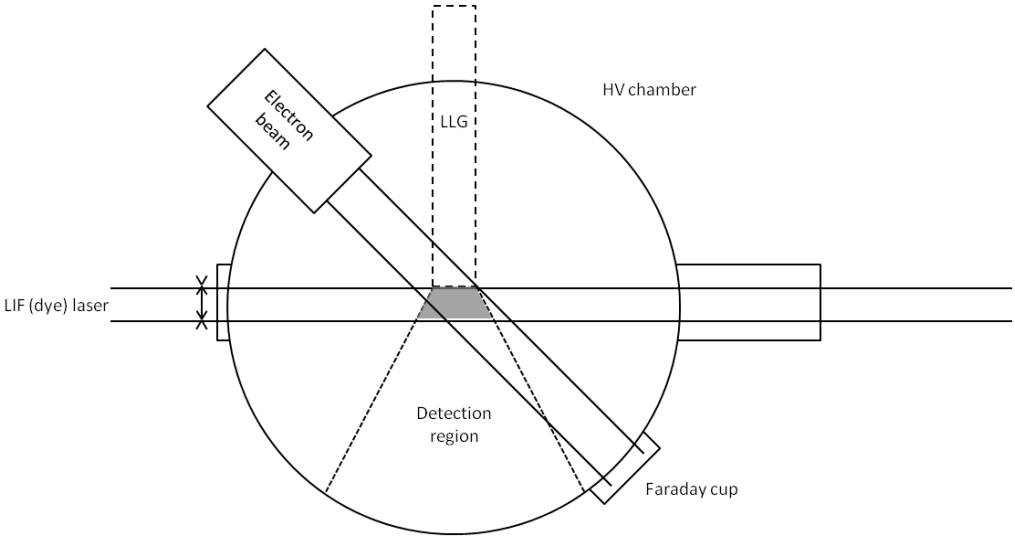

Figure 50 - Schematic showing the path of electron and LIF laser beams through the detection region in the second set of experimental conditions

Number density of OH radicals produced following electron collision dissociation

At 100 eV, the electron current is ~3 μA (section 4.4.4), which equates to an electron fluence of 1.25×10^{10} electrons pulse^{-1}. Equation (6.1) is used to calculate the number density of H_2O molecules at a pressure of 1×10^{-4} Torr; giving a value of $N_{H2O} = 3.1 \times 10^{18}$ molecules m^{-3}. The dissociation cross-section for 100 eV electron collisions with H_2O, $\sigma = 2.05 \times 10^{-16}$cm^2.[129]

As before, Equation 6.3 is used to determine that the fraction of electrons which will cause dissociation of H_2O and produce OH radicals; this gives a value of ~ 6.4×10^{-4}. In the pressure conditions described, this equates to approximately 2.35×10^7 OH molecules pulse^{-1} cm^{-3}. This number density is ~4 orders of magnitude lower than the calculated LIF sensitivity of the experimental set-up.

The detection region under these conditions is nearly twice the volume of the detection region in the first set of calculations, which will increase the signal

detected by the PMT and could therefore improve OH LIF sensitivity by as much as a factor of 2.

Apart from a maximum pressure of H_2O of 10^{-4} Torr, one other limitation in the electron irradiation experiments is the current density of the electron beam, at 1.25×10^{10} electrons per pulse, is lower than the number density of photons in the photolysis laser beam, equal to 1.9×10^{15} photons per pulse. Given the gains in signal due to increased detection volume and dissociation cross-section in the second experiment, optimising the number density of electrons may provide a route to successful OH LIF detection under these conditions. It may be possible to adjust the focal point of the electron beam to give a higher current density in the detection region, resulting in a greater number density of OH radicals.

6.4.3. 8.5 eV electron dissociation of water in a molecular beam

The stated aim of this work is to probe the internal energies of OH molecules produced by DEA to H_2O. In the previous sections, the OH LIF sensitivity and potential for recording electron dissociation of water have been estimated. In this final section are modelled the conditions for recording OH LIF spectra following dissociative electron attachment to water at 8.5 eV using a molecular beam of water seeded in helium.

The purpose of a molecular beam is to give a narrow distribution of energies in H_2O. In section 6.2, the intensity of water in the molecular beam was estimated to be $\sim 8 \times 10^{16}$ molecules s^{-1} m^{-2} in the detection region, a decrease of around 2 orders of magnitude compared with H_2O at 10^{-4} Torr.

Figure 51 shows the experimental conditions for this experiment, demonstrating that the width of the molecular beam in the chamber completely overlaps the detection region, meaning that this volume is not reduced as a result of the molecular beam.

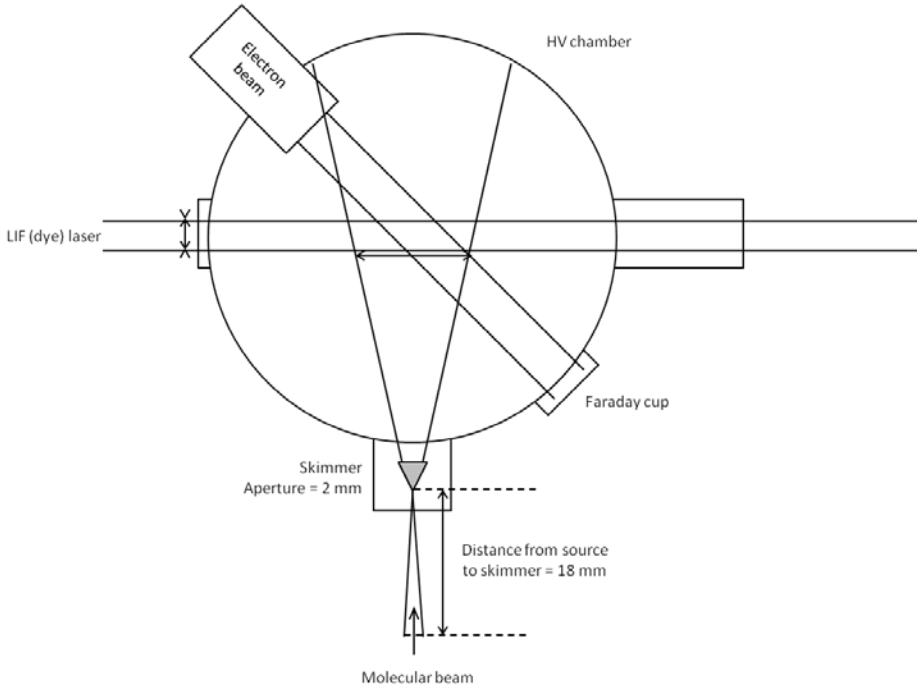

Figure 51 - Schematic showing the intersection of the electron, LIF and H_2O molecular beams relative to the LLG detection region

Another point to consider under these conditions is that at 8.5 eV the electron current is considerably lower, around 1 μA, meaning that the current density in DEA experiments is another order of magnitude lower than at 100 eV, meaning that fewer OH radicals will be created. As before, it may be possible to make some gains in OH number density by adjusting the focus of the electron beam so as to increase the current density where the beam crosses the molecular beam. It may also be possible to increase the proportion of H_2O in the molecular beam, which would significantly increase the amount of OH which is produced. Changes to the LIF detection system,

as well as other possible avenues for increasing OH LIF signal in these experiments are discussed in the following section.

In assessment of the potential to record OH LIF spectra from DEA to water, one other factor to take into account is the translational energy of the OH molecules. OH molecules produced by dissociation do not remain in their original location for the duration of the experiment, but are created with a range of translational energies, and travel away from their point of origin before the LIF laser fires. Following excitation, they may still travel further before decaying by fluorescence. As a result of this, the PMT records fluorescence from only a fraction of the OH molecules which were originally formed in the detection. In electron impact on H_2O, the OH radicals are created with high translational energies, whereas in DEA not only is the energy of the dissociation lower, due to accessing low energy resonance forms, studies show that a smaller amount of energy is proportioned to the OH radicals, compared with the H^- dissociation partner.[104] A possible result of this is that although the cross-section for the low-energy process is considerably lower, a greater fraction of the OH molecules produced may be excited. It may happen that the loss in number density of OH in the low-energy dissociation of H_2O does not have the expected magnitude effect on fluorescence signal recorded by the PMT.

Similarly, OH molecules produced by dissociation of cold H_2O in a molecular beam may have lower translational energy than OH produced from room temperature H_2O at a certain pressure in the HV chamber, which may result in an increase in signal.

6.5. Discussion

6.5.1. Verification that OH radicals are nascent

Calculations have been performed to estimate the current OH LIF sensitivity of the experiment and to determine the feasibility of furthering the experiment. In principle, the OH LIF profiles recorded in these experiments should be for nascent OH radicals, requiring that the OH molecules do not undergo any collisions before detection by the LIF laser.

In OH LIF detection by photolysis of allyl alcohol, an OH molecule is nascent if the time between OH collisions, Δt, is greater than or equal to the time between the photolysis and LIF lasers, that is $\Delta t \geq 0.5$ μs.

Assuming an average speed of 500 ms^{-1}, the mean free path, λ_{MFP} of allyl alcohol can be calculated to be 2.5×10^{-5} m. Equation (6.4) is used to determine the number density of allyl alcohol molecules corresponding to this mean free path length.

$$\lambda_{MFP} = \frac{1}{\sigma_{al} \times N} \qquad (6.4)$$

Here, the number density of allyl alcohol is given by N, in m^{-2}, and σ_{al} is the collision cross-section of allyl alcohol (3.87×10^{-20} m^2). This yields 1×10^{20} molecules cm^{-2} for the maximum number density of OH molecules, corresponding to a pressure ~0.5 Torr. By comparing this value with the typical number densities of OH produced in the experiments detailed, it is clear that the OH LIF spectra recorded at 10^{-2} Torr allyl alcohol are for nascent OH radicals, as the number densities are considerably below the calculated limit. It is therefore possible to record LIF spectra of nascent OH radicals using the experimental apparatus detailed.

6.5.2. Potential to record LIF of OH produced by DEA to H_2O

The results of the calculations in section 6.4 show that the OH number densities in the 100 eV electron experiments are about 4 orders of magnitude lower than the calculated detection limit for OH LIF (1.78×10^{11} molecules pulse^{-1} cm^{-2}), offering some justification for why OH LIF spectra have not yet been recorded by electron impact on H_2O. As discussed, it may still be possible under the current conditions to record OH LIF, as the detection region is larger in these experiments, but other enhancements are likely to be needed to give a greater signal. The following is a more detailed discussion of other experimental variables which could be adjusted in order to potentially increase the yield of OH radicals or improve the LIF detection sensitivity.

Increasing the current density in the electron beam

The current density of the electron gun has been referred to in previous discussion. In order to increase the current density per pulse, the simplest approach would be to increase the pulse length of the electron gun. Although this would increase the minimum time between collisions, Δt, required to study nascent OH, this is well within the reach of the current HV chamber, which can maintain pressures as low as 10^{-7} Torr, corresponding to $\Delta t = 1.46$ s. Of course, if the nascent OH molecules were to fly for this length of time, they would no longer be observable in the region of the PMT. However, even assuming a maximum path length, λ = 1cm, it would be possible to use a pulse length of 200 ms and record nascent OH radicals. Another possibility for increasing the electron current density is to change the focal point of the electron gun, so that it is closer to the path of the molecular beam. Using

SIMION simulations (see section 4.4.1), it may be possible to choose electron gun settings which shift the focal point of the beam.

Electron filament

An alternative possibility for increasing the likelihood of recording LIF spectra of OH radicals formed by electron dissociation is to use a more basic method for introducing electrons, rather than the electron gun. The electron gun produces a beam of electrons which overlaps the region in which OH is generated, however it may be possible to have a higher current over a wider area by simply mounting a filament in the chamber and applying a voltage across it. Without the use of a lens system, it will not be possible to form a directed beam nor focus the electrons on a particular point, however a simple filament may provide a sufficiently high current of electrons to dissociate water molecules over a large volume and attempt LIF detection by this method. This is one method which may be useful to test whether LIF spectroscopy of OH radicals produced in electron dissociation of water is possible, and provide a stepping stone to recording OH LIF spectra by DEA to water.

Increasing the number density of H_2O

Another variable to address is the density of H_2O in the molecular beam. Currently the pressure of H_2O in the beam is based on the vapour pressure of H_2O at 20 °C, which is a constant and cannot be altered. Attempts to increase the amount of H_2O in the molecular beam have been detailed in previous sections, and include heating of the water and gas manifold, and use of a bubbler. However, these attempts were hindered to some extent by certain inherent limitations of the equipment, for example the nature of the glass bubbler limits the stagnation pressure in the molecular beam nozzle to 1.2 bar, while the lines were heated to a maximum of around 40°C to avoid

degrading rubber components in the molecular beam nozzle. Calculations in section 6.4 showed that H_2O does not undergo collisions on the timescales of the current experiment even at a pressure regime of ~10^{-4} Torr H_2O, which means that it is possible to record useful OH LIF spectra of H_2O without using the molecular beam arrangement, although of course the H_2O will not have the low rotational temperature or well-defined energy that occurs in a molecular beam.

Arrangement of PMT/LLG detection system

Another factor which may affect the sensitivity for LIF detection is the arrangement of the PMT and LLG. As shown in section 4.6.1 (Figure 33), the LLG is suspended within a stainless steel (s/s) tube capped with a quartz window. It is possible that the reflective surface of the window reduces the signal to the LLG. Alternatively, it may be that fluorescence of the window caused by absorption of scattered dye laser photons in fact increases the noise on the signal. This system for mounting the LLG within the chamber was designed with the intention of maintaining UHV conditions, which are, however, unnecessary for gas-phase experiments, in which HV conditions are sufficient. It may therefore be an advantage to redesign the mount so that the LLG is quite simply suspended in the chamber without the surrounding steel and quartz casing. In this way, the signal picked up by the LLG may be increased and any noise due to the quartz window may be reduced. Figure 52 shows a simple alternative mount, which would allow this (the current system is also included for comparison).

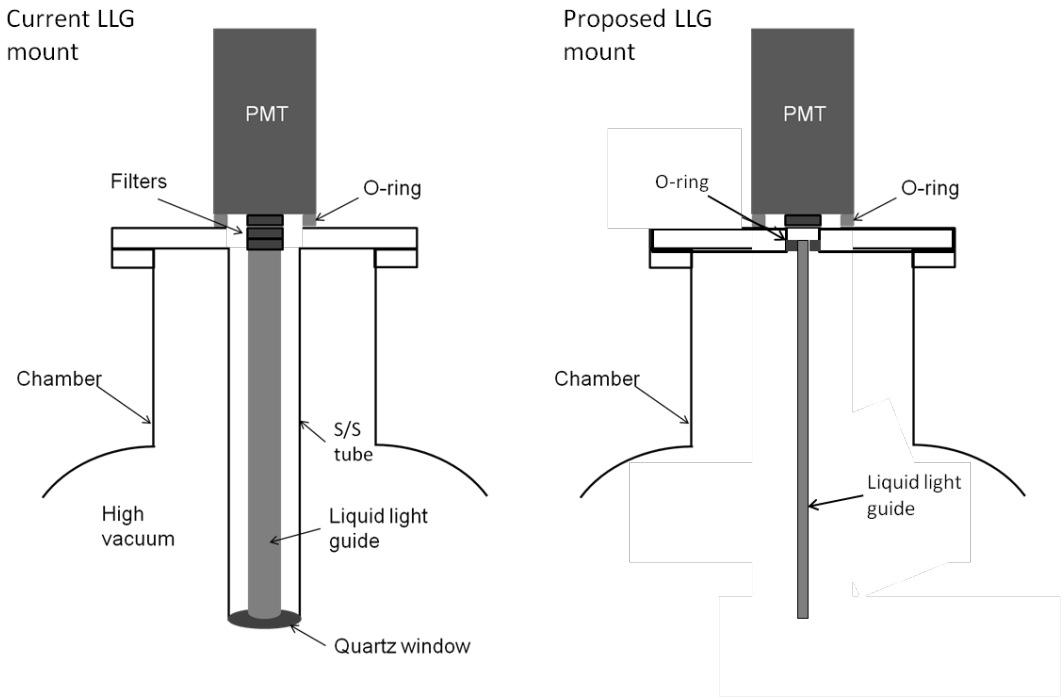

Figure 52 - Schematic showing the current and proposed mounts for the LLG/PMT detection system

Ellipsoidal mirror system

The positioning of the s/s tube relative to the reaction region is also important; if the overlap between the OH fluorescence and the viewing range of the LLG is not optimised, it is possible that the PMT receives only a fraction of the fluorescence signal produced by LIF of OH. As shown in Figures 48-51 in section 6.4, the detection region of the LLG/PMT is a small cone extending into the chamber, which means that the actual signal we wish to detect forms a much smaller fraction of the detection region than the rest of the chamber. Another point is that the LLG is positioned at a 45° angle above the region where LIF is formed, meaning that much of the LIF signal, which is emitted in all directions, will be emitted away from the LLG, and will therefore not be detected.

In Section 6.4, the number density of fluorescent OH radicals within the detection region was calculated per pulse of the laser. This is the limit of fluorescent OH radicals which are available in this region however it may be possible to increase the amount of fluorescence photons which are detected by the PMT by using an arrangement of ellipsoidal mirrors, such as those shown in Figure 53.

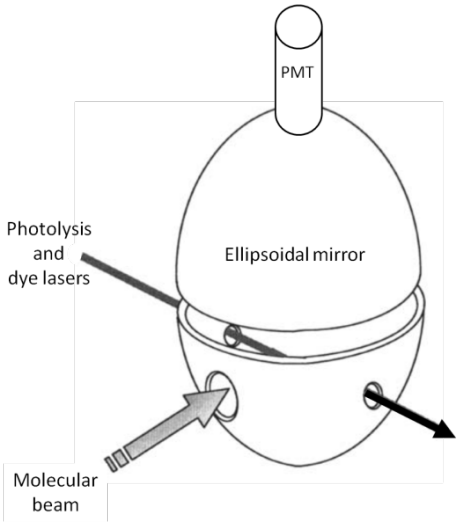

Figure 53 - Schematic showing proposed ellipsoidal mirror system

The photons emitted by excited OH radicals are emitted in all directions, rather than specifically in the direction of the LLG; by using an arrangement of mirrors shown in Figure 53, it should be possible to redirect much of the fluorescence signal towards the detector, thereby increasing the intensity of the LIF signal.

7. Electron-stimulated reactions of ASW/CO films

7.1. Experimental Results

7.1.1. Effect of CO on radiolysis of ASW

As described in chapter 5.2, a typical film consists of a layer of CO (~3 ML) trapped between two thick layers of ASW (~60 ML). In order to confirm that the CO is effectively trapped in the film both pre- and post-irradiation, ESD experiments were recorded for three types of film: a pure ASW film, an uncapped film of 3 ML CO on a 60 ML ASW spacer layer; and a capped film comprising a 60 ML ASW spacer, 3 ML CO and a 5 ML ASW capping layer.

All of these films were irradiated under the same conditions. Figure 48 shows the results of the ESD for each film sample, providing evidence that CO may be trapped in the film by as few as 5 ML of ASW.

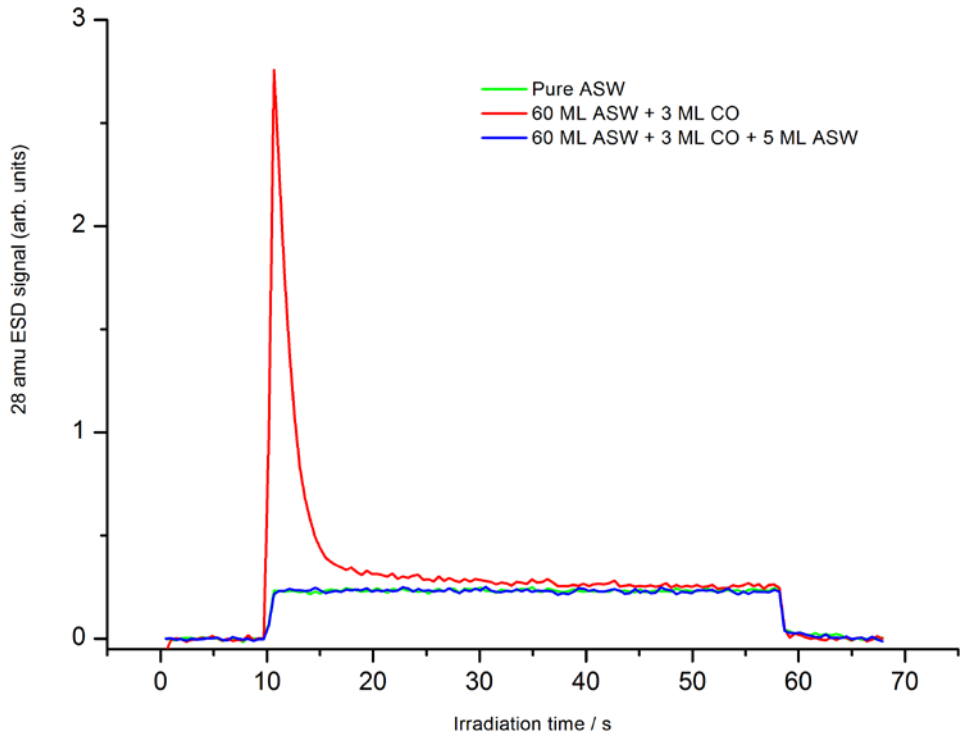

Figure 54 - ESD traces for different film compositions showing effective trapping of CO with a 5 ML ASW capping layer. Films were irradiated at 25 K for N = 100 scans

For the sample in which the CO sits on the top of the film, the ESD rises quickly, as the CO is sputtered away. In contrast, when the CO is capped with ASW, the ESD trace matches the pure water ESD, confirming that no CO desorbs from the buried layer.

In TPD experiments, one factor which affects CO desorption is the crystallisation temperature of the capping ASW layer. Typically, at around 170 K, ASW becomes crystalline, creating pores through which gaseous CO may escape. This phenomenon shows up as a peak of CO detection known as the “volcano” (Figure 49).

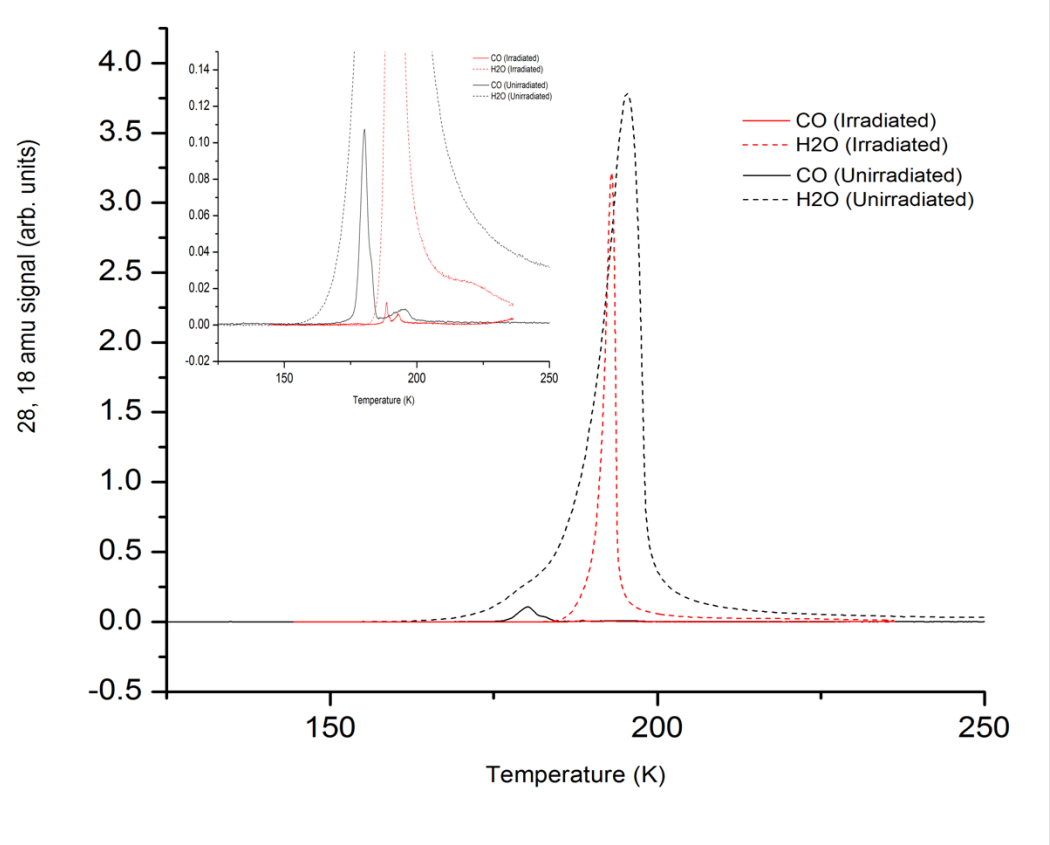

Figure 55 - Unirradiated and post-irradiation TPD traces for desorption of H_2O and CO from layered ASW/CO/ASW. Inset: desorption of CO in the "volcano"

In post-irradiation TPD, this volcano occurs at a lower temperature, suggesting that electron irradiation affects the structure of the ASW layers, reducing the

crystallisation temperature. This is most likely the result of energy deposition in the film by the incident electrons, which facilitates reorientation of water molecules in the ice structure, leading to a higher level of order, more closely approaching crystallinity, than in unirradiated films. The presence of the CO peak in post-irradiation TPD, however, attests to the fact that CO remains trapped in the film until it thermally desorbs, despite changes to the film structure during irradiation. The temperature shift of the CO peak is taken into account when identifying the amount of CO desorbed from irradiated and non-irradiated samples.

Experiments were conducted to monitor the effect of CO in the film on the electron-stimulated desorption of H_2, O_2 and H_2O from the film. In Figure 50, ESD traces with and without a buried layer of CO for each of the desorbing species are compared.

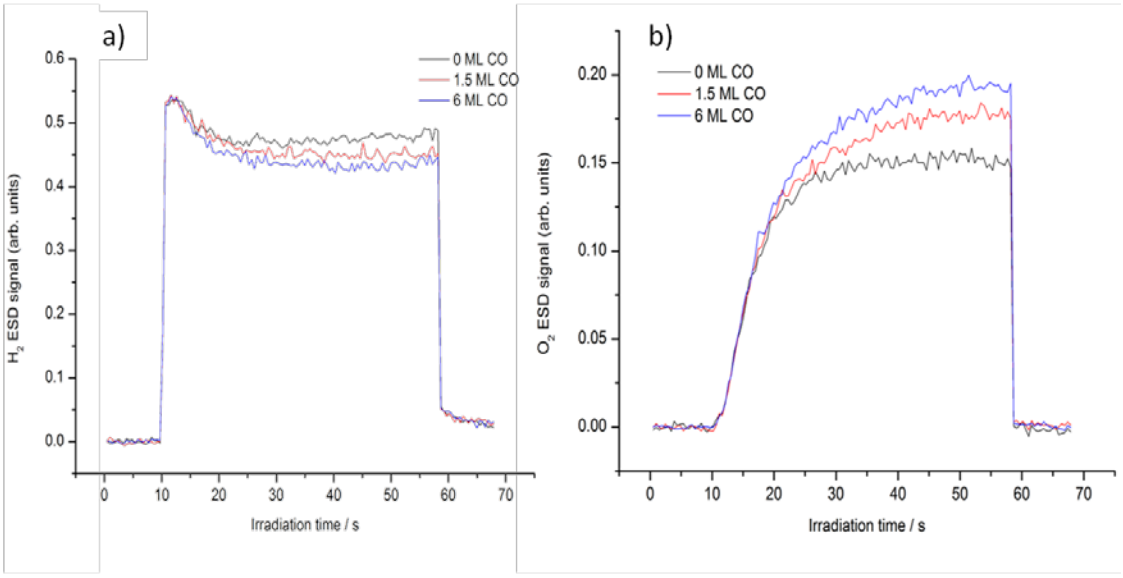

Figure 56 - ESD traces for desorption of a) H_2 and b) O_2 from layered ASW/CO/ASW films with varying CO thicknesses. Films irradiated at 25 K for N = 100

Firstly, the difference between the shapes of the two ESD traces is immediately evident. Whereas the O_2 yield builds up gradually to a maximum, the H_2 ESD rapidly

reaches a peak yield, before decreasing slightly to the steady-state concentration of desorbed molecules. This is a symptom of the reaction mechanisms which produce O_2 and H_2 respectively. Production of H_2 occurs by two channels: either by combination of H atoms produced in dissociation of H_2O, or by direct dissociation of H_2O into H_2 and O (minor channel). In comparison, the production of O_2 relies on the reaction of OH or HO_2 molecules, which are secondary radiolysis products and have lower mobility in the ice than H atoms.

In ESD of H_2, although the rapid component of the ESD is unaffected, it appears that the overall yield of H_2 is decreased when CO is present; this suggests that the presence of CO affects the reactions of H atoms deeper in the film. The presence of CO offers an alternative route for the consumption of H atoms, producing HCO rather than H_2. This in itself will reduce the yield of H_2 in comparison with the yield from pure ASW, as some fraction of the H atoms will react instead with CO.

In Figure 50 b), the O_2 ESD appears significantly enhanced by the presence of CO. In pure ASW films, the main limitation to production of O_2 is the consumption of OH radicals by recombination with H atoms to produce H_2O. If the presence of CO in the film promotes consumption of H atoms, or offers a preferential reaction (i.e. H+CO rather than H+OH), this may contribute to the increase in O_2 yield, as a greater proportion of OH and HO_2 radicals may react to produce O_2.

7.1.2. Decomposition of CO

Following irradiation, the amount of CO observed in TPD is decreased. For higher radiation doses, there is a greater decrease in the post-irradiation CO signal. Based on previous studies, it is likely that CO is consumed by electron-stimulated reactions with water, producing both reduction and oxidation products.

Figure 51 shows the amount of CO remaining in a layered ASW/CO/ASW film post-irradiation, as a function of electron fluence, measured by TPD. There is a clear negative trend, with post-irradiation CO falling rapidly at first, before consumption slows at higher doses.

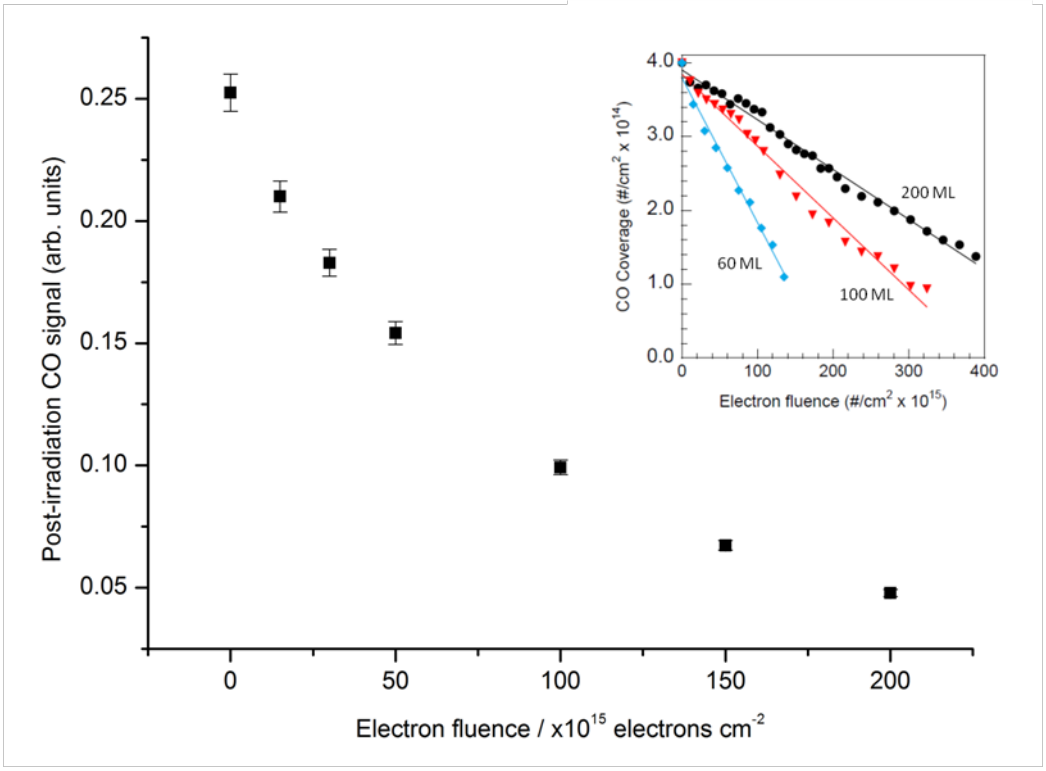

Figure 57 - Decomposition of CO as a function of electron fluence in layered ASW/CO/ASW films capped with 40 ML ASW, irradiated at 25 K. Inset: Linear dependence of CO decomposition on electron fluence for films capped with 60, 100 and 200 ML, irradiated at 100 K (RAIRS results).

The second graph (inset) shows a similar set of experiments, in which RAIRS was used to investigate CO consumption as a function of electron fluence, but for thicker films irradiated at higher temperature (T = 120 K). Contrasting the two graphs, it appears that in changing to thicker films and higher temperatures, the kinetics of CO consumption also change.

In order to study the effect of film thickness on the consumption of CO, TPD experiments were performed in which the thickness of the capping ASW layer was

varied between 5-120 ML on top of a 60 ML ASW spacer and a 3 ML CO layer. As shown in Figure 52, the amount of CO decomposition initially increases with thicker capping layers, before starting to decrease, however CO decomposition does not fall to zero, implying that reactions may still be occurring with CO as deep as 120 ML into the film. The initial increase in CO consumption suggests that CO is not primarily decomposed by direct interaction with incident electrons, as increasing film thickness limits the number and energy of electrons which can reach the CO layer, which would correspond to a fall in the amount of CO consumed. Instead, it appears that CO is decomposed by reactions with the products of low-energy water radiolysis, principally, H and OH.

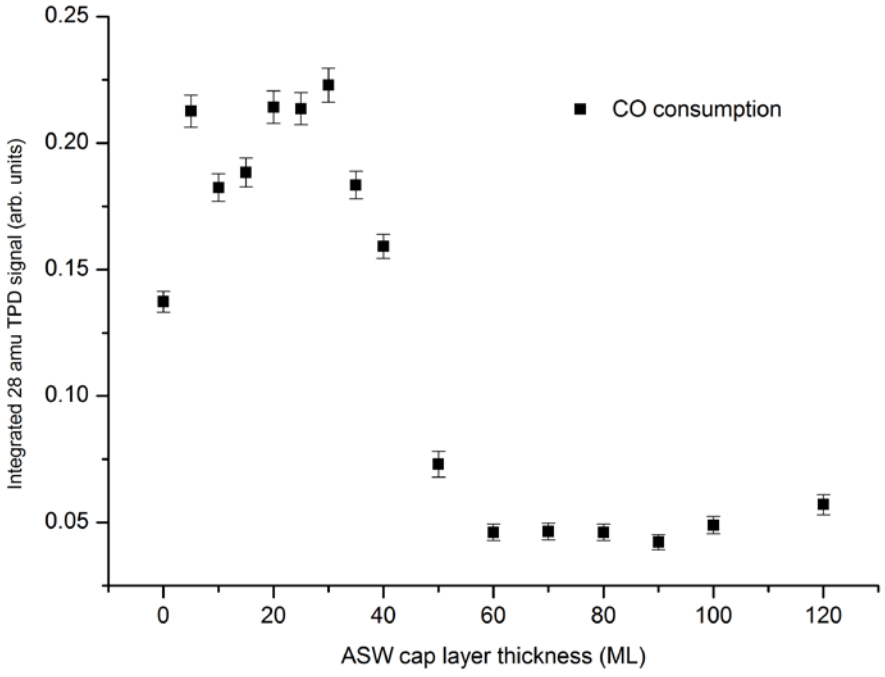

Figure 58 - Decomposition of CO as a function of H_2O capping layer thickness. Films were irradiated for N = 100 at 25 K.

Even assuming that CO reacts with products of water radiolysis rather than by direct interaction with electrons, the initial distribution of these products in the film will be

similar to the penetration depth curve for electrons.[133] This implies transport of energy to the CO layer after the initial irradiation.

To determine the products of CO consumption in these experiments, TPD and RAIRS spectra were compared with previous observations of electron-stimulated reactions between CO and H_2O, listed in Table 11.

In the past, studies have recorded carbon dioxide (CO_2), formic acid (HCOOH), formaldehyde (H_2CO) and methanol (CH_3OH).[47] Other studies tentatively report carbonic acid (H_2CO_3).[134] Although the identity of the major products of electron-stimulated reactions of ASW/CO is quite well-established, questions remain about the efficiency of conversion of formaldehyde to methanol, formation of methane, the identity of the CH_3O intermediate, and the mechanism of H atom diffusion through CO and H_2O ices.

Table 11 - IR band and m/z peak assignment for products of ASW/CO radiolysis

Species	**IR band assignment/cm^{-1}**					**m/z (Temp/ K)**
Reference	*Hudson and Moore, 1999*[47]	*Oba et al, Astrophys J, 2010*[134]	*Yoshinobu et al, Chem Phys Lett, 2004*[48]	*Watanabe and Kouchi, Astrophys J, 2002*[156]	*Fuchs, Cuppen et al, A&A, 2009*[46]	*Hiraoka, Kihara et al, Astrophys J, 1998*[135]
CO	2137 (C=O stretch)			2142	2143	
HCO	1853 (C=O stretch)					
H_2CO (Formaldehyde)	1496 (H_2 scissor)			1722 (m), 1499, 1249, 1178, 2991, 2887, 2832	1732 (m), 1479, 2812, 1246, 1175, 2991, 2880, 2812	29 (110), 30 (145)
CH_3O	1017 (C-O stretch)					
H_2COH	1456 and 1050					
CH_3OH (Methanol)	1033			1032 (m), 1118, 2958	1035 (m), 1125	31 (160)
HCOOH (Formic acid)	1219 (C-O stretch)					
CH_4 (Methane)	1302 (C-H bend)					15 (48, 145, 156)
H_2CO_3 (Carbonic acid)		1745 (may be HCOOH or H_2CO)				
CO_2		2344 (C=O stretch)	2345, 2279, 2328, 2308			
HOCO		1848 (trans-), 1797 (cis-)				

Initial TPD experiments were conducted for the 44 amu and 29 amu mass channels, corresponding to CO_2 and HCO, respectively. As shown in Figure 53 a), both of these species were observed in post-irradiation TPD, providing evidence that both oxidation and reduction of CO takes place in the film.

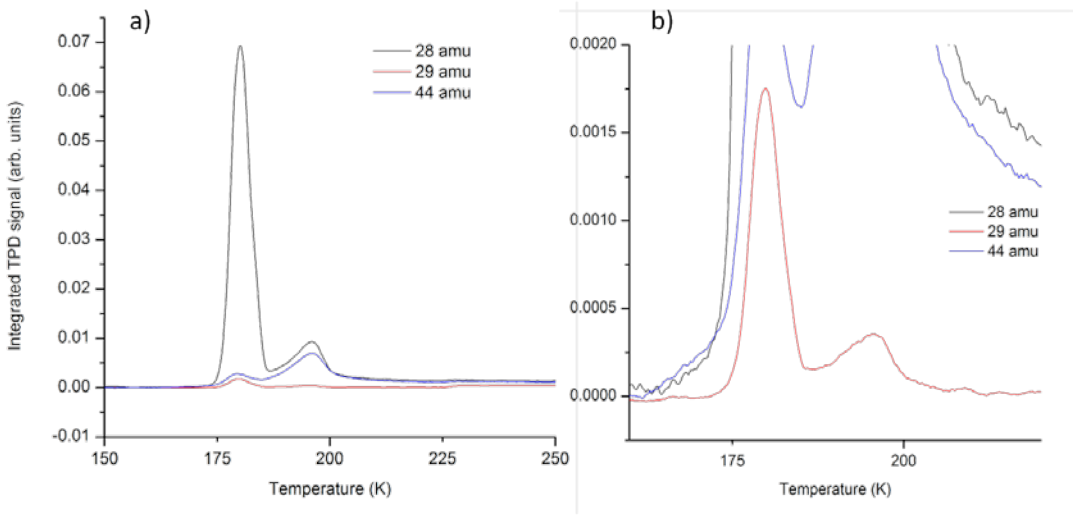

Figure 59 - Evidence for reduction and oxidation pathways in TPD for a) the temperature range 150-250 K and b) splitting in the peak desorption of mass channel 29 amu in the range 175-200 K

Figure 53 b) shows splitting in the TPD peak of mass channel 29 amu. This corresponds to slight differences in the desorption temperatures of formaldehyde (lower temperature) and methanol (higher temperature). The behaviour of the TPD peaks in their unique mass channels, 30 (formaldehyde) and 31 (methanol) demonstrated the same desorption characteristics, giving further evidence that the splitting of the peak at 29 amu is a result of recording both formaldehyde and methanol. The difference in desorption temperature is also in agreement with the assignments given in Table 11.

The bands in the RAIRS experimental data were also assigned using the IR data in Table 11. Assigned RAIRS spectra for films capped with a 30 ML water layer are shown in Figure 54, showing evidence for sequential reductions through to methanol as the radiation dose to the film increases.

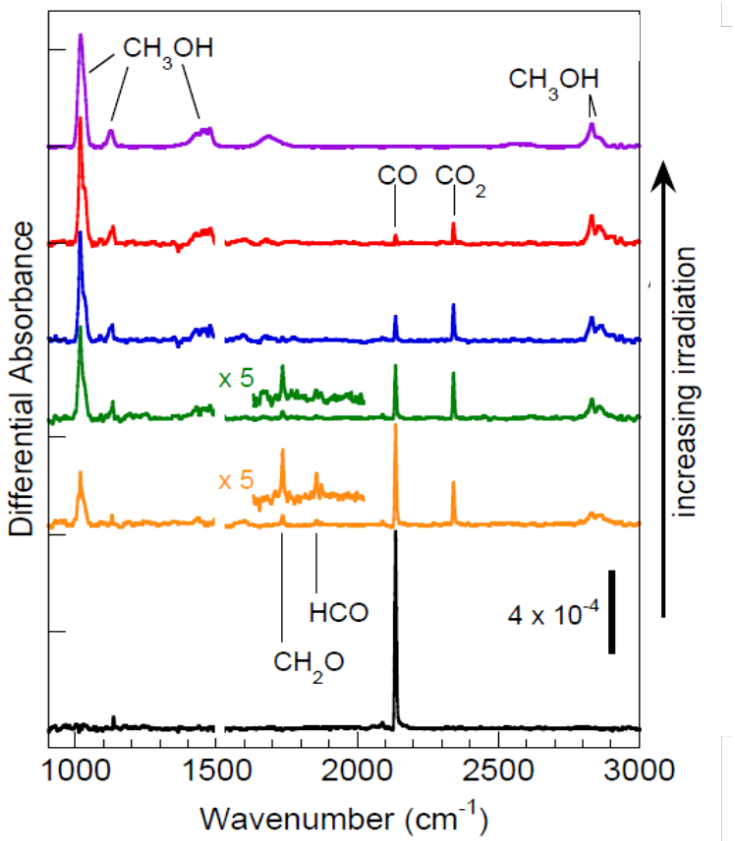

Figure 60 – Assigned RAIRS spectra for films capped with a 30 ML water layer, irradiated with 100 eV electrons at 90 K, shown as a function of increasing radiation dose.

The peak in IR at ~1850 cm^{-1} is tentatively assigned to the C=O stretch of the formyl radical, HCO. This band was originally assigned to HCO in 1964, in matrix isolation experiments by Milligan and Jacox.[136] In more recent experiments to study irradiation of mixed CO-H_2O ices, Hudson and Moore observed a broad peak in the IR spectrum of electron-irradiated CO-H_2O ice with a maximum in the region 1850-1853 cm^{-1}, which they assigned to the formyl radical (HCO) on the basis of Milligan and Jacox' work.[47] Yoshinobu *et al* also referenced this assignment in their study of electron irradiation of low temperature mixed CO-H_2O ices, where a peak at 1856 cm^{-1} is labelled as HCO.[48] Hudson and Moore also reference work by Allamandola *et al* on photolysis of H_2O-CO and H_2O-H_2CO ices, in which the peak at 1853 cm^{-1} is assigned to the formyl radical.[137]

Certain other studies of CO hydrogenation report no band in the region around 1850 cm^{-1}. Neither Watanabe *et al* nor H. Linnartz *et al* appear to observe this band in the IR spectra of CO ices which are bombarded with H atoms at low temperature;[138, 46] however a study by Ellinger *et al*, offers an explanation for this difference.[139] Ellinger *et al* conducted two sets of experiments to observe the hydrogenation of CO ice. In the first, CO and H atoms were co-deposited at low temperature and then annealed up to 50 K, while in the second set of experiments pure CO ice was deposited first and then bombarded with H atoms before annealing. The IR spectra of the co-deposited ices showed a peak at 1856 cm^{-1}, while the H-atom bombarded ices did not. Elligner *et al* assigned this peak to the HCO radical, and concluded that this species is observed only where CO and H are co-deposited, but not in H atom bombardment of pure CO. This is consistent with the observation of a peak at 1850 cm^{-1} in the work presented here, and in work by Hudson and Moore, Yoshinobu and Allamandola, and explains the non-appearance of the peak in Watanabe and Linnartz' work.

Another minor peak, observed at ~1700 cm^{-1} in the most highly irradiated sample (purple trace) cannot be satisfactorily identified. In a summary report on the IR spectra of simple organic molecules, Kaiser suggests two possible identities for a peak at this wavenumber: HCOOH or CH_4.[140] However, while either of these molecules are possibilities within the conditions of these experiments, the IR spectra of both would be expected to show additional peaks which are not observed here. HCOOH would show a second, rather broad peak at ~1200 cm^{-1}, while in the spectrum of CH_4 there is a large, fine peak at ~1300 cm^{-1}. An alternative assignment for this peak is an altered form of formaldehyde, CH_2O, in which the bond angle is altered due to interaction with water molecules in the ice.[141] Further investigation is

needed to assign this peak, and to investigate why it is observed only for very high radiation doses.

The peak at 1735 cm^{-1} is assigned to H_2CO; finally, peaks at 1018, 1126, 1430, 1450, 1462, 1478, and 2831 cm^{-1} are assigned to methanol. The assignments for methanol are supported by studies of non-irradiated methanol/ASW ice, which show the same peaks.[41]

7.1.3. Oxidation Channels

The oxidation of CO by reaction with radiolysis products of H_2O produces CO_2, which is fully oxidised. Experiments were conducted to study the effect of radiation dose and film composition on the yield of CO_2 following electron radiolysis of ASW/COASW ices with 100 eV electrons.

Figure 55 shows the variation in CO consumed and CO_2 produced as a function of the radiation dose (in terms of electron fluence) which the ice receives. As the dose of radiation increases, so does the yield of CO_2, increasing steeply at first before showing an approximately linear increase with increasing fluence. The amount of CO remaining in the film post-irradiation decreases in a steeper curve, as observed in previous experiments (Figure 51).

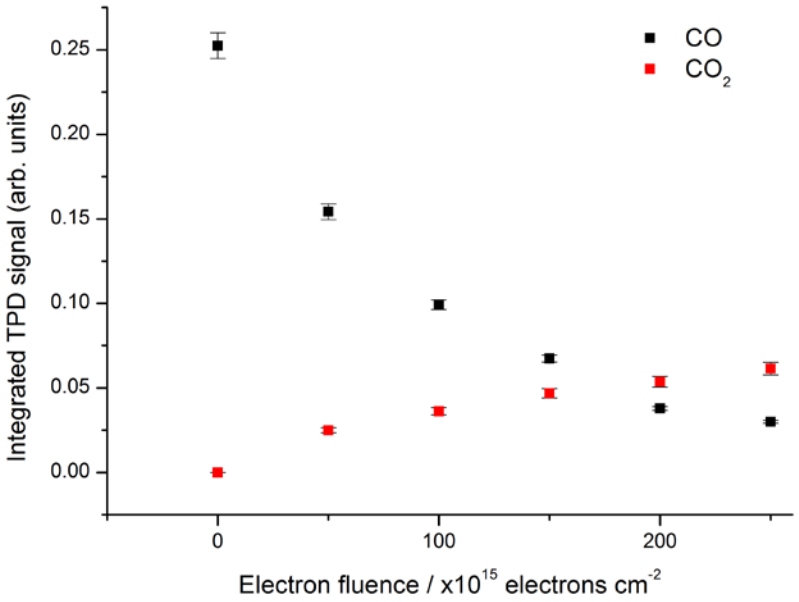

Figure 61 - Effect of radiation dose on CO_2 production from films capped with a 60ML capping layer, irradiated at low temperature (T = 25 K)

The effect of capping layer thickness on the oxidation pathway is shown in Figure 56, as well as CO decomposition and production of formaldehyde and methanol. For low cap layer thicknesses <25 ML, it appears that CO_2 production is the dominant pathway in consumption of CO, accounting for almost all CO consumed post-irradiation. For thicker films, however, the production of CO_2 falls off quickly. As the thickness of the cap layer increases, the CO layer is more distant from the source of radiolysis products in the film.

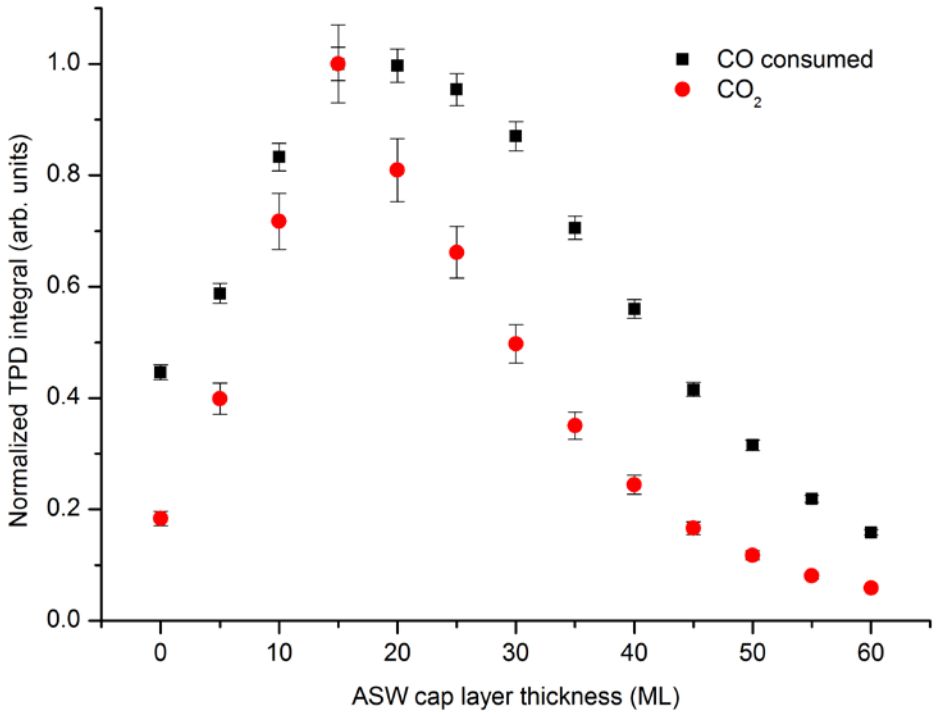

Figure 62 - Effect of H_2O cap layer thickness on production of CO_2 for irradiation dose N=50 cycles, irradiated at 25 K

Although CO_2 production decreases for thicker cap layers, there is still significant consumption of CO for films capped with 60 ML ASW.

To further investigate the effect of film composition, Figure 57 shows the results of experiments in which the film thickness was kept constant at 100 ML, but the spacer layer below the CO was increased by 10 ML and the capping layer decreased by 10 ML for each repeat, in order to give the effect of moving the CO layer closer to the vacuum interface.

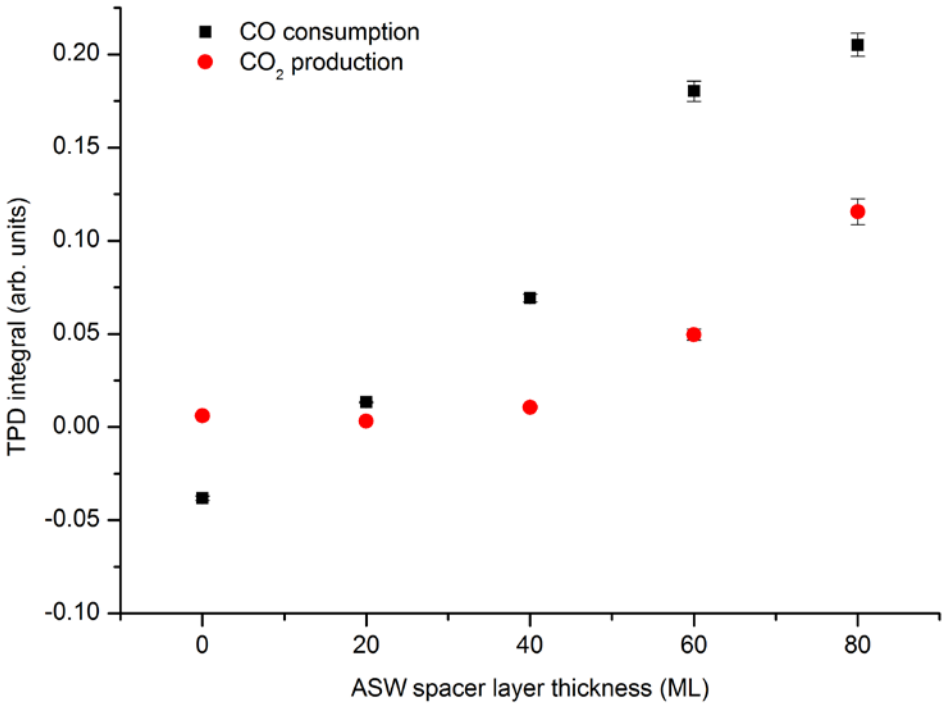

Figure 63 - Variation in CO_2 production with increasing vicinity to film surface for irradiation dose N=50 cycles, irradiated at 25 K)

The graph clearly shows an increase in CO_2 production as the CO approaches the surface maximising when the CO is placed within 20 ML of the vacuum interface. This is consistent with earlier results for films with a constant thickness of spacer layer, but with increasing capping layer thickness; the greatest CO_2 production is observed for the thinnest capping layers.

7.1.4. Reduction Channels

Reduction of CO culminates in the production of methanol, which is fully reduced. In order to monitor the reduction channel in these experiments, the yield of methanol has been monitored. The kinetics of formation of methanol and other reduction products including formaldehyde and the HCO radical are also discussed.

Figure 58 shows the variation in methanol production as a function of cap layer thickness. The first point to note is that, in a similar way to CO_2 production, the yield of methanol initially increases with increasing cap layer thickness, implicating radiolysis products in the reduction, rather than direct excitation of CO by electrons. Unlike CO_2 production, however, the peak yield of methanol occurs at 30 ML, twice as deep as the maximum CO_2 production, which suggests long-range energy transfer through the film.

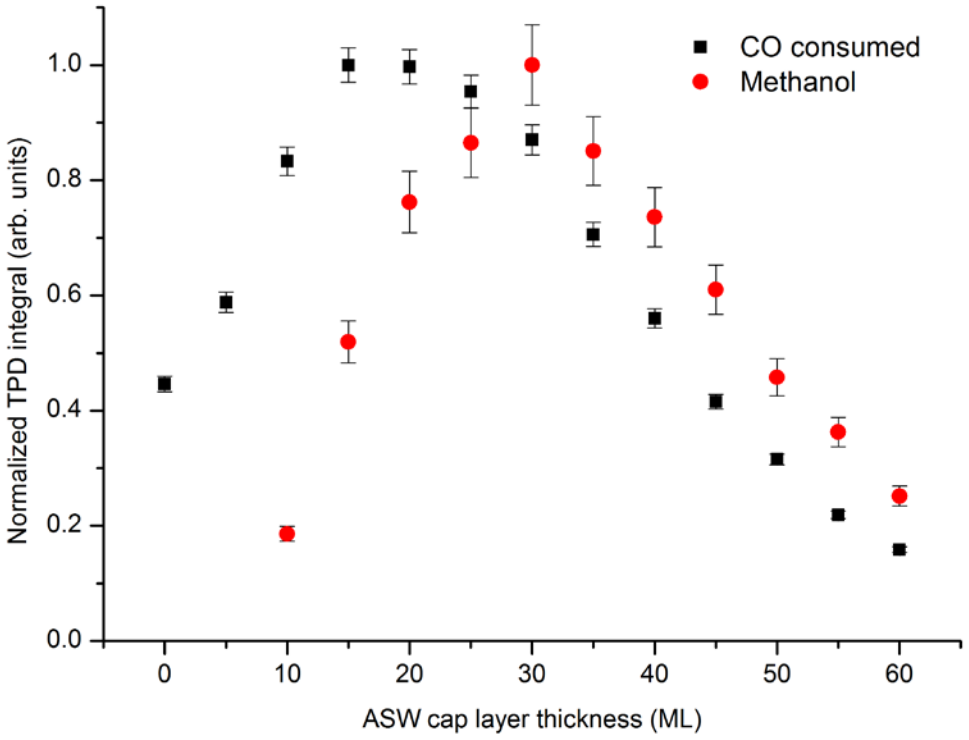

Figure 64 - Production of methanol by reduction of CO as a function of cap layer thickness. CO decomposition is also included, for comparison. Films irradiated at 25 K for N = 100 scans

The electron-stimulated reduction of CO is thought to occur in a series of sequential reactions (7.1)-(7.4). Radical species shown in red are alternative forms of a transition state generally modelled as the linking step between formaldehyde and

methanol, they are argued to have an important role, possibly even as part of the rate-limiting step in the formation of methane in the ISM.[142,143,144]

$$CO + H \rightarrow HCO \quad (7.1)$$

$$HCO + H \rightarrow H_2CO \text{ (formaldehyde)} \quad (7.2)$$

$$H_2CO + H \rightarrow H_3CO \text{ or } H_2COH \quad (7.3)$$

$$H_3CO \text{ or } H_2COH + H \rightarrow CH_3OH \text{ (methanol)} \quad (7.4)$$

Evidence for formation of HCO, formaldehyde and methanol was recorded by monitoring 29, 30 and 31 amu mass channels, respectively. By monitoring the behaviour of each of these channels separately, it has been possible to show evidence for sequential hydrogenation of CO in these experiments.

Figure 59 shows variation in the yields of formaldehyde and methanol as a function of radiation dose. After a rapid initial increase in the yield of formaldehyde, the rate of production slows. Conversely, production of methanol increase steadily after a slightly delayed onset. At higher electron fluences, the yield of methanol slows, corresponding to an accompanying decrease in the yield of formaldehyde. This provides strong support for mechanism involving conversion of formaldehyde into methanol in the final step, although the intermediate in this reaction has not been definitively identified.

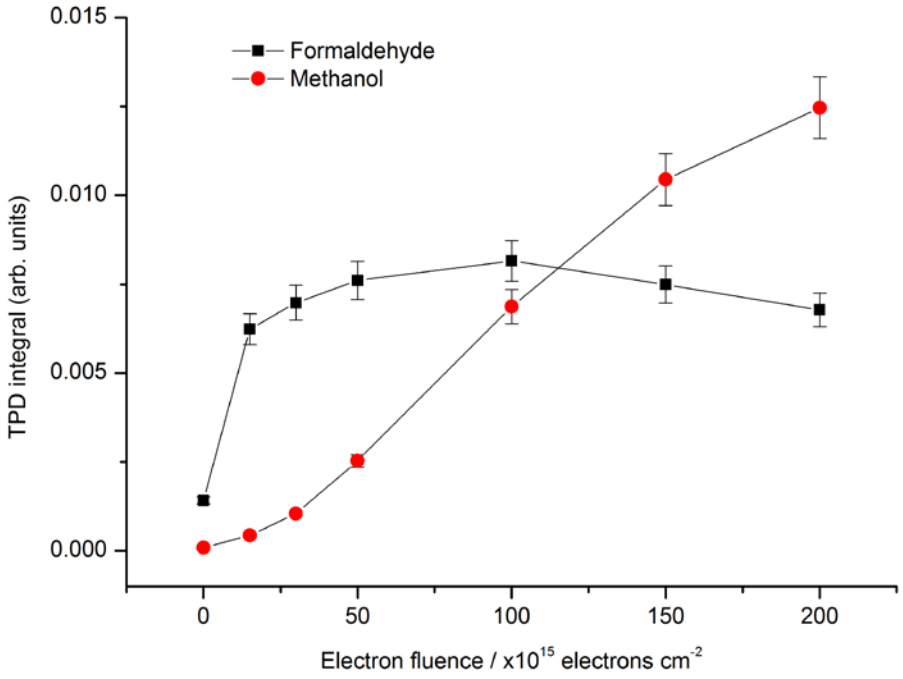

Figure 65 - Yields of formaldehyde and methanol as a function of radiation dose. Films capped with 60 ML ASW and irradiated at 25 K. Lines intended only to guide the eye.

Similar behaviour for the two reduction products is observed in Figure 60, which shows the yield of reduction products of CO varies with increasing capping layer thickness. Firstly, should be noted that for these conditions in TPD (25 K, N = 100) a much smaller fraction of CO consumed is converted via the reduction pathway, compared with the amount that is oxidised. Subsequent RAIRS experiments have been performed in which the conditions for reduction of CO were identified and optimised. These are discussed in greater detail in chapter 7.2.2.

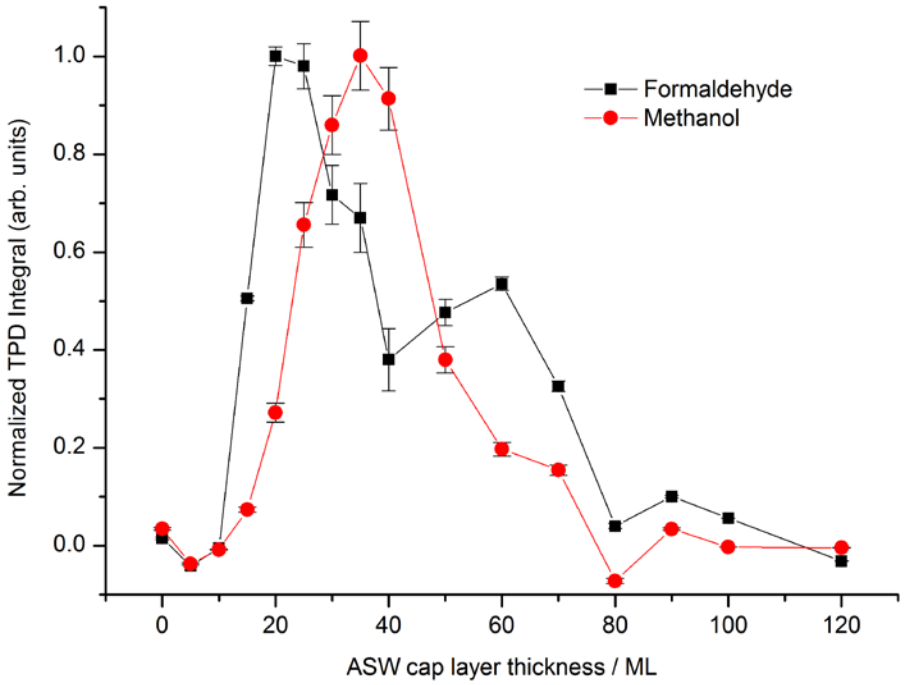

Figure 66 - Effect of H_2O cap layer on production of formaldehyde and methanol from films irradiated at 25 K for N = 100. Lines are intended only to guide the eye.

The behaviour of each trace in Figure 60 appears to support the sequential hydrogenation scheme, as it is consistent with conversion of formaldehyde into methanol. Initially, the yield of methanol is low, while the amount of formaldehyde in the film increases rapidly. The initial increase in cap layer thickness increases the amount of H atoms which can participate in hydrogenation reactions. As the cap layer thickness increases further, the amount of formaldehyde appears to decrease, but this may be explained by a corresponding increase in the amount of methanol. After reaching a maximum, the yield of both products decreases as a function of capping layer thickness, with the exception of a feature at around 50 ML, at which point the yield of formaldehyde once again increases, followed by a corresponding small increase in the yield of methanol.

As further evidence of a sequential hydrogenation pathway, Figure 62 shows a series of spectra for increasing dose of irradiation to films capped with 30 ML ASW, irradiated at 100 K. The kinetics for variation in product yields appears to support the conversion of HCO to formaldehyde in the second step of CO reduction to methanol.

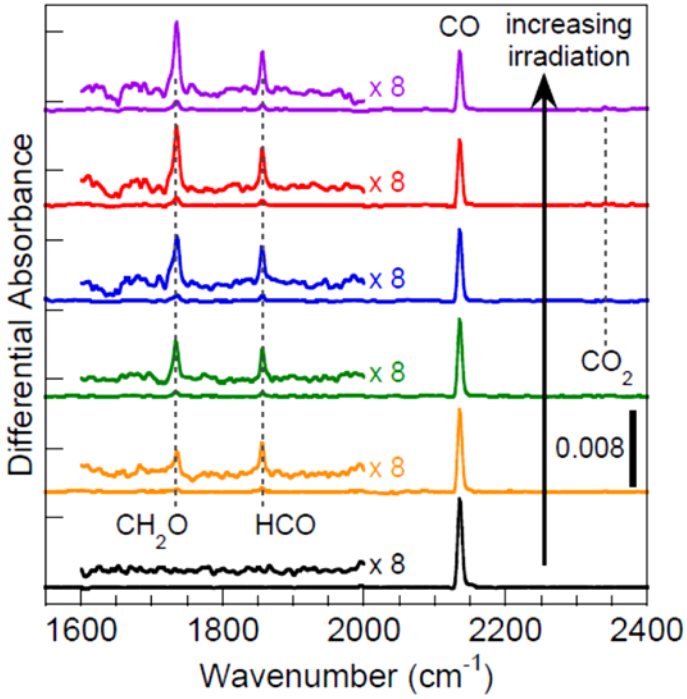

Figure 67 - RAIRS spectra showing the variation in HCO and H_2CO signal vs. increasing radiation dose

7.2. Sources of Error

In the experiments described, efforts have been made to minimise the error on any results, for example, by using automation of many aspects of the sample deposition, heating and data collection, however, some error remains. The following is a discussion of sources of error in this work, and how it has been calculated. The sources of error are categorised into sample preparation, irradiation and ESD, and data collection (specifically by TPD and RAIRS).

7.2.1. Sample preparation

Preparation of the surface

As described in the experimental section, both Pt (111) and rutile TiO_2 (110) surfaces were cleaned before deposition of the water/CO films. The TiO_2 sample was prepared by sputtering with 2 keV Ne^+ ions and then annealing for a minimum of two minutes up to a maximum of ten minutes in vacuum at 950 K. The 1 cm^2 Pt(111) sample was cleaned by neon ion sputtering and annealing at 1050 K in vacuum. Previous experiments to investigate surface preparation in this experimental system using an auger electron spectrometer indicate that surface cleanliness does not depend on the duration of the annealing cycle over 2 minutes, therefore the surface preparation in this work can be assumed to give a clean surface. During TPD experiments, the sample is heated to 350 K, which desorbs all of the deposited material from the surface. After each set of similar TPD experiments, the surface is annealed to 950 K under UHV conditions in order to maintain the cleanliness of the surface. This method of surface preparation gives a high repeatability in terms of sample preparation, and contributes to the low % error between TPD experiments.

Measurement of film thickness

The thickness of the water films is not measured directly, but it is assumed to be proportional to the water coverage, which is calibrated in terms of mono-layers. The area of the first monolayer peak in the TPD spectrum of H_2O was used to calibrate the water coverage dosed by a molecular beam. The molecular beam is turned on and off using mini solenoid valves with ~1 ms time resolution. A standard method template, written in BASIC, is used to determine the dosing times for a given mono-layer coverage of H_2O, CO or other compound (for example H_2O^{18} or D_2O), thus ensuring the repeatability of the coverages. The coverage of H_2O in any experiment has been examined for systematic error by comparing data-sets for similar experiments and looking at the standard deviation across all of the data. It was found that there was less than a 1% variation in the dosing time for a given coverage of H_2O. Repeatability of the film thickness was also examined by comparing TPD integrals for experiments with the same H_2O coverage and this was found to produce an error of ~1%.

The initial coverage of CO was determined by using the known sticking coefficient of CO (~1 at T < 30 K), measured flux of the molecular beam and the measured dosing time. In order to adsorb the capping layer of ASW, the film is heated to 100 K, causing approximately 1/3 of the CO to desorb, however the remaining CO is trapped within the film and, in the absence of electron irradiation, does not otherwise desorb on the timescale of these experiments. By comparing sets of both TPD integrals and recorded dosing times for deposition of CO, the repeatability of the CO thickness has been estimated at ±1%. In the graphs shown in the prior results section (7.1), the minimum area shown on any measurement is given as ±3%, to take into account the total possible variation in film thickness resulting

from deposition of a spacer layer and capping layer of ASW, as well as a layer of CO.

7.2.2. Irradiation and ESD

The irradiation of samples, described in section 5.1, is a fully automated process, controlled by the same BASIC script which automates the deposition of the layered films. This automation makes the radiation dose to each sample highly repeatable, with a very low % error.

The electron beam itself has an energy spread of ~0.3 eV and a beam spot-size of ~1.5 mm. To account for any variation in the size of the beam, the films were irradiated by repeatedly scanning the electron beam over an area slightly larger than the film. Each individual scan of the sample was typically 1 s in duration and comparison of scan times for five sets of films receiving the same dose showed an error of < 0.02%. Experiments have been conducted previously which demonstrate that TPD and RAIRS results of the nature presented in this thesis are not reliant on the electron flux within the error on the electron beam, but are more dependent on the fluence. In addition, the low incident electron flux has been found to cause negligible heating of the ice film. Any effect of charging during irradiation is also essentially eliminated by the method used for preparation of the surface; multiple ion sputtering and annealing produces a reduced TiO_2 surface, which increases the sample conductivity. No effects attributable to charging have been observed in this or in previous experiments using this method.

In order to generate a single ESD trace, an average of several hundred reading of the QMS is calculated for each pixel in the scan, all of which are then averaged over a number of complete scans to give the final ESD trace. This gives a high signal to noise ratio in addition to the < 0.02% error on the irradiation itself.

7.2.3. Data collection

TPD measurements

TPD traces were produced as described in section 5.4, and constitute the main part of the data analysed in this report. Aside from those issues associated with preparation and irradiation of the sample, which have been discussed previously, possible sources of error in TPD measurements include the accuracy of the temperature measurement and heating rate, and the sampling of the QMS. However, due to automation of the dosing, irradiation, temperature control and QMS sampling, any error here is inherent in the entire data-set. As such, the main source of error in the TPD measurements is in calculation of the integrals for each mass fragment.

By comparing the standard deviation across sets of values and across the average of multiple data-sets, I have estimated the percentage error on TPD integrals for CO (28 amu), formaldehyde (29 amu), methanol (31 amu) and CO2 (44 amu). These values, in combination with error on film thickness (calculated in section 7.2.1.), have been used to produce error bars shown on the graphs in the results and discussion sections of this report, and are listed in Table 12.

Table 12 - Estimated % error on TPD integrals for mass fragments studied in the present work

Molecule (mass fragment/amu)	Estimated % error
CO (28)	±2%
H_2CO (29)	±2%
CH_3OH (31)	±7%
CO_2 (44)	±5%

RAIRS measurements

In recording RAIRS spectra of the film samples, the main sources of error are in the effect of the IR radiation on the sample (in terms of heating) and in any measurements made from IR data using the difference or integral of the signal. Yields of reaction products pre- and post-irradiation were measured by subtracting the corrected unirradiated spectrum from the corrected post-irradiation spectrum. The absence of any calibration as yet in this experiment makes these values purely qualitative , and varies considerably from one species to another, depending on the specific sensitivity of the IR spectrometer to each species. An alternative method for studying the relative yield of reaction products was to repeat the same experiment both with and without CO and calculate the difference between the spectra for the same electron fluence. This procedure is useful as electron irradiation leads to changes in the RAIR spectra of the ASW films that can make it difficult to observe the small signals associated with the CO-H_2O reaction products. However, qualitatively similar results were obtained using both methods. Since no qualitative data has been extracted from RAIRS for comparison in this thesis, a full estimation of the errors has not been performed; however, the repeatability of RAIRS data is expected to be good. No effect attributable to heating has been observed in any of the RAIRS studies conducted for this thesis.

7.3. Discussion

As described in the previous chapters, the electron-stimulated reactions of mixed ASW/CO films have been studied as a function of film thickness, electron fluence and temperature. In the experiments performed, the complete decomposition of CO by a combination oxidation and reduction was observed in films which are thick compared with the typical penetration depth of 100 eV electrons in ASW. Products of the reactions were monitored using mass spectrometry, and RAIRS. The major products were identified as HCO, CO_2, H_2CO and CH_3OH, as discussed in the previous section. RAIRS spectra also showed peaks assigned to the formate ion, (HCO_2^-), and formic acid (HCOOH). ESD spectra for non-carbon products O_2 and H_2 were also recorded.

Depending on the film structure and irradiation temperature, CO may be converted almost entirely into methanol or into CO_2. The results appear to show a dependence on CO location within the film for oxidation and reduction pathways. Near to the ASW/vacuum surface, for cap layers around 20 ML or less, oxidation reactions dominate, while for thicker cap layers, reduction takes over completely.

The following deals with the oxidation and reduction pathways in turn, in order to discuss the different mechanisms which may be occurring within the films.

7.3.1. Electron-stimulated oxidation of CO

Both TPD and RAIRS results indicate that oxidation of CO to CO_2 occurs primarily in the near-surface region, specifically < 20 ML from the ASW/vacuum interface. In this region of the film, oxidation is prolific, accounting for up to 90% of CO consumed, depending on the experimental conditions. In order to discover what it is which causes this preferential near-surface oxidation, possible mechanisms involved in electron-stimulated oxidation of CO are discussed.

Primary radiolysis reactions of water generate a balance of oxidising (OH, O, H_2O^+, H_3O^+) and reducing (H, H_2, e^-) products near the vacuum interface of the film. Reactions of these products may also produce a number of other species including H_2O_2, HO_2, H_2O, O_2 and H_2. The probability of reaction between CO and any of these species depends upon a number of properties, including the mobility of these species in the ASW, the relative concentration of a particular product in the film, and the rate constant for the reaction at the temperature of the ice.

Oxidation of CO to CO_2 may occur by any of the following reactions:

$$CO + O \rightarrow CO_2 \qquad (7.5)$$

$$CO^* + CO \rightarrow CO_2 + C \qquad (7.6)$$

$$CO + OH \rightarrow CO_2 + H \qquad (7.7)$$

$$CO + O_2 \rightarrow CO_2 + O \qquad (7.8)$$

$$CO + H_2O_2 \rightarrow CO_2 + H_2O \qquad (7.9)$$

$$CO + HO_2 \rightarrow CO_2 + OH \qquad (7.10)$$

In (7.5), CO reacts directly with ground-state atomic oxygen in a reaction which has been shown to have a high activation barrier.[145] Bombardment of CO-ice with cold O atoms did not produce any measurable yield of CO_2, although O atoms formed through the photo-dissociation of N_2O, which yields O in the excited ^1D state, were found to react with CO in an argon matrix.[146,147] CO_2 was also observed where CO films were capped with water and heated, or where energetic O atoms are used. Estimates of the temperature corresponding to the onset of this reaction vary between 290 K - 1000 K, making it highly unlikely that this reaction is the source of CO_2 in

these experiments. Goumans and Adersson proposed an alternative route involving tunneling, which would considerably lower the activation barrier for this reaction, however this is a weak effect in oxygen atoms and although the study found that tunneling would be possible on surfaces where the CO and O molecules were tightly bound to the surface in a transition state, they concluded that reaction with OH would be more likely even under these conditions.[148] Given that the reactions studied in this work are expected to take place mostly in the bulk, and at low temperatures, it is unlikely that this mechanism for reaction of CO and O atoms is a major pathway.

The recombination of excited CO molecules (7.6) has been experimentally demonstrated, but is energetically unfavorable and unlikely to occur in the low temperature, low energy irradiation conditions of our experiments.[149,150] Results of experiments to study CO decomposition as a function of cap layer (Figure 52) also indicated that dissociation of CO via direct excitation or ionization is unlikely, as CO decomposition increases for a greater thickness of cap layer.

Reaction (7.7) is one of the most commonly proposed reaction routes for the production of CO_2 in CO/H_2O reactions. The onset of this reaction usually occurs around 80 K, although values of up to 500 K have been reported.[151] Recent experiments to study the reaction of CO with the products of H_2O photolysis on surfaces found the reaction produced observable yields of CO_2 even at 10 K.[152] Hydroxyl radicals produced by the dissociation of water in radiolysis are often highly excited, therefore easily able to overcome the activation barrier.

The reaction most likely proceeds via an energetic HOCO intermediate, which absorbs in IR at around 1848 cm^{-1}.[134] Unfortunately, this band has not been observed

in these experiments, although this may be due to the highly reactive nature of the HOCO species; HOCO may quickly dissociate via a number of pathways, producing CO_2, H, OH, and CO. Previous studies of CO_2 formation in water ices irradiated with 8 MeV protons[24] reported IR bands attributed to HOCO, while other authors noted the absence of any peak for HOCO.[48,47]

An alternative explanation for the absence of any HOCO peaks in IR is isomerisation of trans-HOCO to form HCO_2. Unfortunately, studies of the IR signature of HCOO are limited, and it has not been possible to qualify whether HCOO was observed in this work. Subsequent RAIRS experiments on this question have yielded observation of the formate ion, HCO_2^-, which could be formed by electron attachment to HCOO. However, studies have not yet ruled out production of HCO_2^- by dissociation of HCOOH. Further experiments are required in order to confirm the intermediates in this route to oxidation of CO.

Equations (7.8-7.10) show reactions of CO with secondary radiolysis products. Reaction (7.8) is the least likely, as O_2 has been shown to efficiently desorb from the surface of the film (Figure 50), leading to a higher proportion of HO_2 and H_2O_2 in the near-surface region.[23]

To test whether reaction with OH radicals or secondary species such as HO_2 or H_2O_2 are responsible for CO oxidation, experiments were conducted in which the ASW spacer layer is irradiated prior to deposition of CO and the capping ASW layer. In this way, radiolysis products form in the spacer layer and subsequently react with CO. In order to distinguish between reactions of OH and reactions of secondary products, the irradiated spacer layer is annealed at temperatures in the range 25 -

140 K. At higher temperatures, thermal reactions of OH will result in a higher concentration of secondary products in the spacer layer. Results of these "pre-irradiation" experiments are shown in Figure 62.

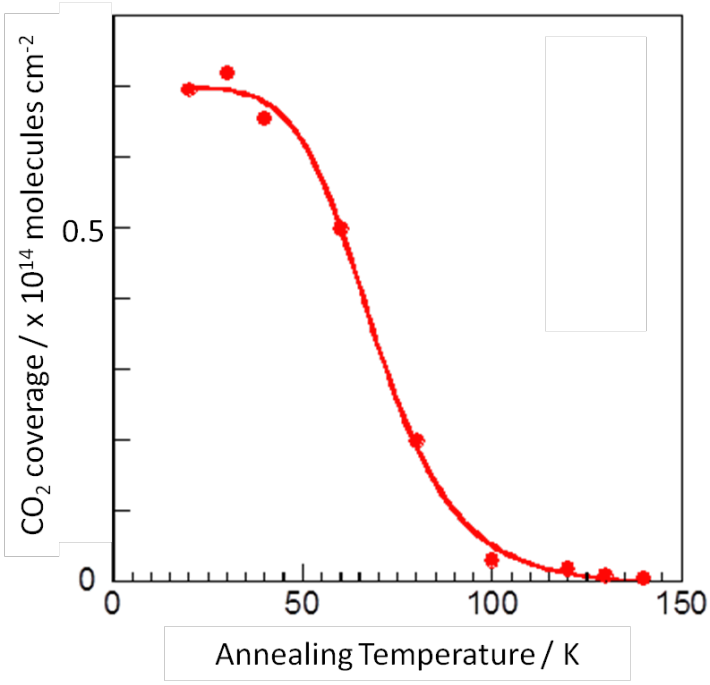

Figure 68 - CO_2 coverage as a function of annealing temperature of the pre-irradiated spacer layer.

The formation of CO_2 in these experiments confirms that CO reacts with products of water radiolysis concentrated near the ASW surface, which remain trapped in the film during irradiation at 20 K. Given the high yield of CO_2 for low temperature annealing, it appears that the reaction of CO $\rightarrow$ CO_2 conversion is very efficient and practically barrier-less. This is consistent with a mechanism for CO radiation oxidation in low-temperature ices proposed by Garrod and Pauly.[153]

The decrease in CO_2 production for higher temperature annealing of the pre-irradiated layer indicates that thermal reactions of radiolysis products reduce the availability of CO_2 precursors. This effect lends weight to reaction (7.7) as the primary oxidation pathway, as OH could be consumed during high-temperature annealing, leading to a higher concentration of H_2O_2 and HO_2 in the pre-irradiated

layer. These results are also in agreement with reported thermal activation of mobility and reactions of OH radicals trapped in an ASW matrix in the temperature range 60 - 100 K.[23]

One other reaction which may be a source of CO_2 is the oxidation of HCO, rather than CO (7.11).

$$HCO + O \rightarrow CO_2 + H \qquad (7.11)$$

In their 2011 paper, Garrod and Pauly cite reaction (7.11) as one of the three most likely processes for CO_2 formation alongside (7.5) and (7.6).153 The reaction itself is barrier-less, although it requires the production of both HCO and O. Although HCO has a reported temperature barrier of around 500 K, yet experimental results clearly show efficient production of hydrogenated CO products, which could provide a rich source of HCO for oxidation by O atoms.[154]

In their 2003 paper, Watanabe et al state that "the presence of CO_2 does not affect production of formaldehyde or methanol", which would appear to reject the role of this reaction in oxidation of CO. Furthermore, if CO_2 and HCO are produced in different regions of the film, as the data appears to show, it is likely that this reaction would be minor or even non-existent

Taking the current experimental results into account, as well as previous studies, it appears that the most likely source of CO_2 following low-energy electron irradiation of layered ASW/CO/ASW ices is via barrier-less reaction of CO with the short-lived OH radical, as shown in equation (7.7). Further work is required to confirm the intermediates in this reaction. Contributions of HCO oxidation to the formation of CO_2 have been considered, but require further investigation in order to quantify the role of this reaction under various conditions in amorphous ice.

7.3.2. Kinetics of sequential hydrogenation of CO

Both TPD and RAIRS data for the decomposition of CO show evidence of the reduction pathway. Formaldehyde and methanol have been identified, as well as the HCO radical. In both sets of experiments, reduction products of CO were observed for CO buried under cap layers which are thick compared to the electron penetration depth, but the amount of reduction products increases with increasing cap layer. For films capped with > 20 ML ASW, the reduction pathway completely dominates CO decomposition, with combined production of methanol and formaldehyde accounting for up to 70% of CO consumed.

The reduction of CO to methanol is thought to proceed via the sequential hydrogenation of CO, HCO and H_2CO, described in chapter 7.1.4, equations (7.1) - (7.4). The trends in product yield versus electron fluence observed in TPD and RAIRS experiments support a mechanism in which HCO is converted to formaldehyde, which is subsequently converted into methanol. There are still questions about the intermediate in the reaction which converts formaldehyde to methanol, specifically, whether it exists as CH_3O or CH_2OH. Unfortunately neither of these forms has been observed in TPD or RAIRS experiments, which is most likely a result of the lifetime of this species, which is thought to be very short.

Calculations for the energy barrier in the first step have been carried out in the gas phase, giving an approximate energy barrier of 17 kJ mol^{-1} for the reduction of CO to HCO.[155] Due to the presence of the HCO fragment in TPD and H-CO stretch in RAIRS, it has not been possible to track the conversion of CO to HCO in the current experiments.

Figure 63 shows the results of RAIRS experiments to monitor the yield of formaldehyde from the second step as a function of radiation dose, along with the post-irradiation yield of CO. The rapid and prompt decrease in yield of formaldehyde suggests that $HCO + H \rightarrow H_2CO$ is an efficient reaction, unlikely to be the rate-determining step in the reduction mechanism.

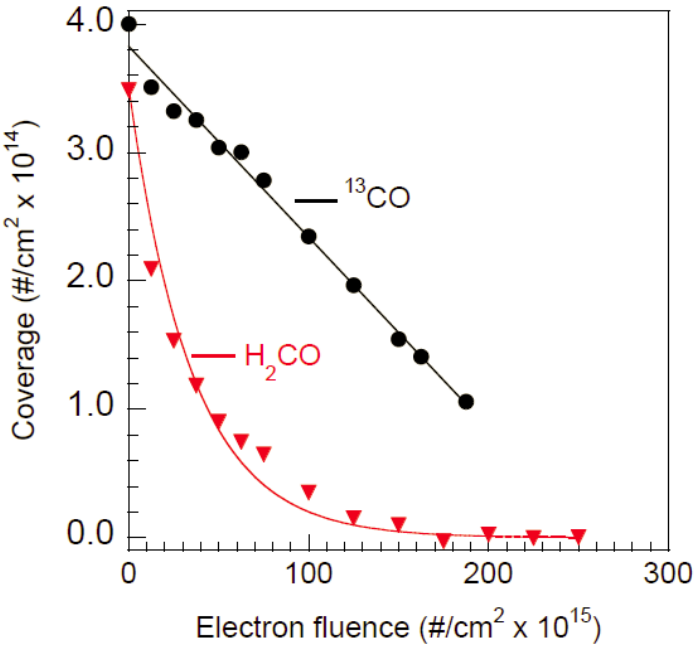

Figure 69 - Production of formaldehyde vs. electron fluence (70 ML cap, T = 100 K) Lines through show exponential and linear fits to the data for H_2CO and ^{13}CO, respectively.

Previous papers have discussed the efficiency with which CO is converted into methanol in a range of film thicknesses, irradiated temperatures and H atom fluxes. In these experiments, the electron fluence is on the order of 10^{15} electrons cm^{-2}, which is comparable with the H atom flux measured in Watanabe *et al*, 2002/3. In attempting to reproduce these results computationally, Yamamoto *et al* produced a MC model of CO reduction in thin ASW/CO films vs. H atom flux over times up to 80 minutes (equating to a total H atom fluence of 9.6×10^{18} electrons cm^{-2}).

The results of these simulations compare very favorably with the data we have measured on the evolution of methanol with increasing electron fluence (Figure 64). Both the current data and Watanabe and Yamamoto's data all show a rapid increase in methanol production with increasing fluence. In Watanabe's 2002 paper, the authors report no observation of intermediates, indicating that the conversion of these intermediates to formaldehyde and methanol are the fastest reactions

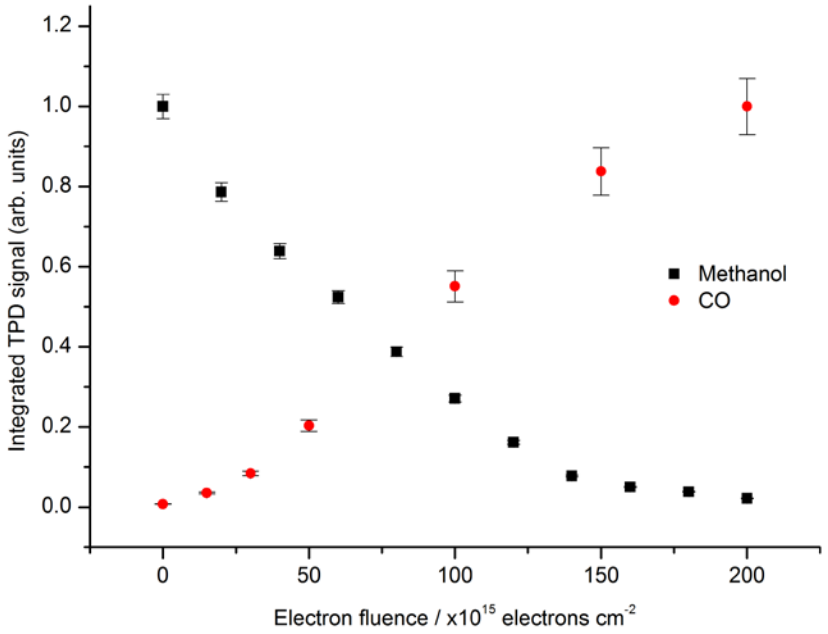

Figure 70 - Yield of methanol as a function of electron fluence; post-irradiation CO yield also shown for comparison. Films were capped with a 40 ML capping layer, irradiated at 25 K.

The absence of any delay between the decomposition of CO and the onset of methanol production suggests that conversion to methanol is efficient and that the final step, $CH_3O + HCO \rightarrow CH_3OH$ is not the limiting step in the reduction of CO to methanol.

For comparison, the change in yields of CO and formaldehyde versus electron fluence are shown in Figure 63. The yield of formaldehyde decreases promptly as the

radiation dose increases; the initial rate of decrease is ~7 times larger for H_2CO compared to CO.

RAIRS data supporting the TPD data for methanol was also recorded, shown in Figure 65 a) and b).

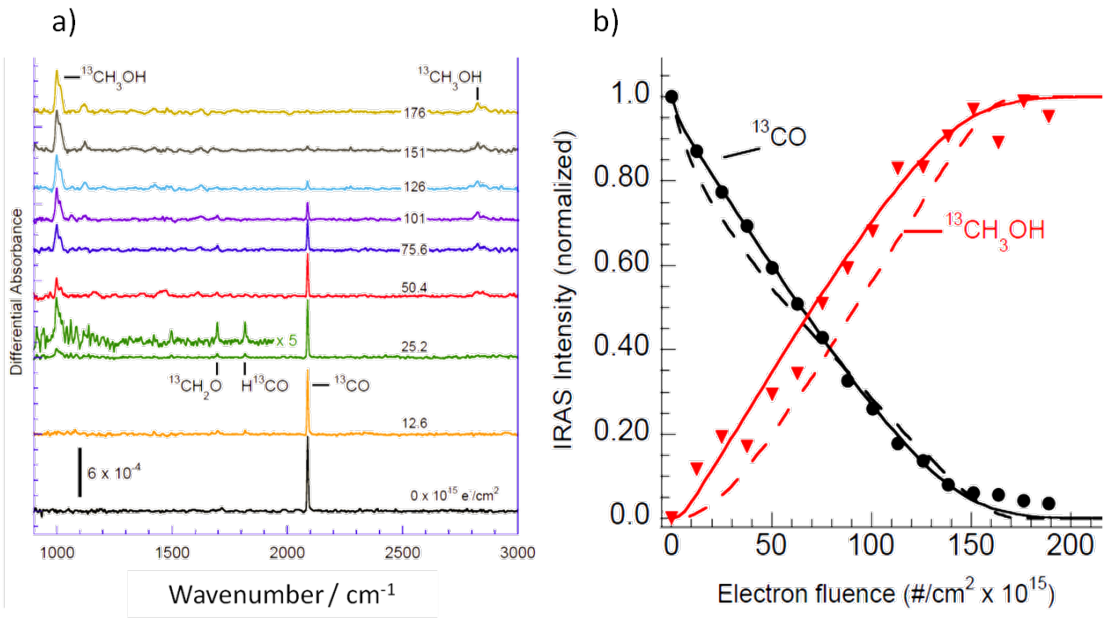

Figure 71 - Integrated CO (●) and CH3OH (red triangles) signal vs. electron fluence in ASW/CO films with cap = 60 ML and Tirr = 100 K. The solid and dashed lines are simulated CO and CH_3OH concentrations for two different reaction probabilities

Taking all of this data into account, it would appear that the rate-limiting step in reduction of CO is the first step, in which CO is converted to HCO. Further discussion of this, including simulations, follow in chapter 7.3.2.

7.3.3. Mechanism of electron energy transfer in reduction of CO

Due to the depth at which the reduction reactions occur within the films, it is not immediately apparent what the mechanism is for these processes. Hydrogenation products have been observed in previous experiments with mixed CO/ASW films, initiated by H atoms striking an ice surface, however these experiments are for thin films and focus on the surface reactions.[156,157,158,] Bergeld and Chakarov[159] studied photo-ejection of water molecules from thick water films, observing reaction at a

depth of 50 ML, which is greater than the penetration depth of electrons in water.[133] While the energy for water decomposition reactions is absorbed in the bulk of the water film, it was concluded that hydrogen is not produced primarily by direct reaction of H atoms diffusing to the surface, as diffusion of such species is very slow in ASW at low temperature160. Instead, the authors proposed a mechanism involving electronic excitations (H^2O^*) or defects (H^3O^+ or OH^-), which diffuse to the interfaces to initiate reactions which then lead to the formation of H^2. This hypothesis is consistent with ideas put forward by Petrik and Kimmel stating that "most reactions do not proceed via diffusion controlled encounters of reactive partners, however electronically excited species...can still move due to electronic coupling of the excitations between neighbouring sites".[31] An alternative explanation is a mechanism involving the creation of H radicals by water radiolysis, which may then diffuse to the CO before reacting.

In order to test whether proton hopping or H atom diffusion is responsible for long-range energy transfer to the CO layer, experiments were performed using isotopically labelled layers of D_2O and H_2O as shown in Figure 66.

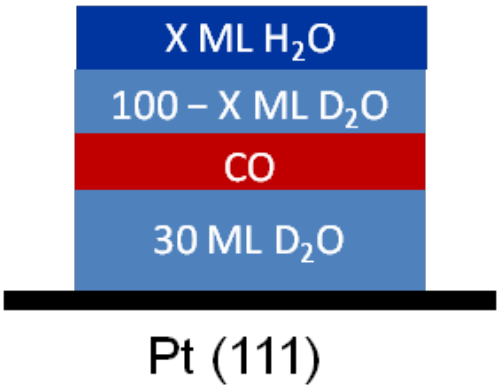

Figure 72 - Schematic of film composition showing a constant film thickness with varying ratio of H_2O:D_2O in the cap layer.

A 30 ML spacer layer of D_2O was deposited on a Pt (111) substrate, on top of which was deposited a layer of CO. The thickness of the capping layer was kept constant (100 ML), while the ratio of H_2O:D_2O was varied. As shown in Figure 68, X ML of H_2O was laid on top of 100-X ML of D_2O. As the thickness of H_2O at the vacuum interface increases, the amount of D_2O in the film decreases.

Figure 67 shows the yield of HCO from these isotopically labeled films, following irradiation with 100 eV electrons at 110 K. The observation of HCO produced from these films indicates a diffusion, rather than proton-hopping mechanism. The nature of the proton-hopping mechanism would result primarily in DCO, rather than HCO, as D_2O is always the layer closest to the CO in these experiments. Since relatively higher yields of HCO than DCO are recorded (not shown), this points to a mechanism involved H atom diffusion.

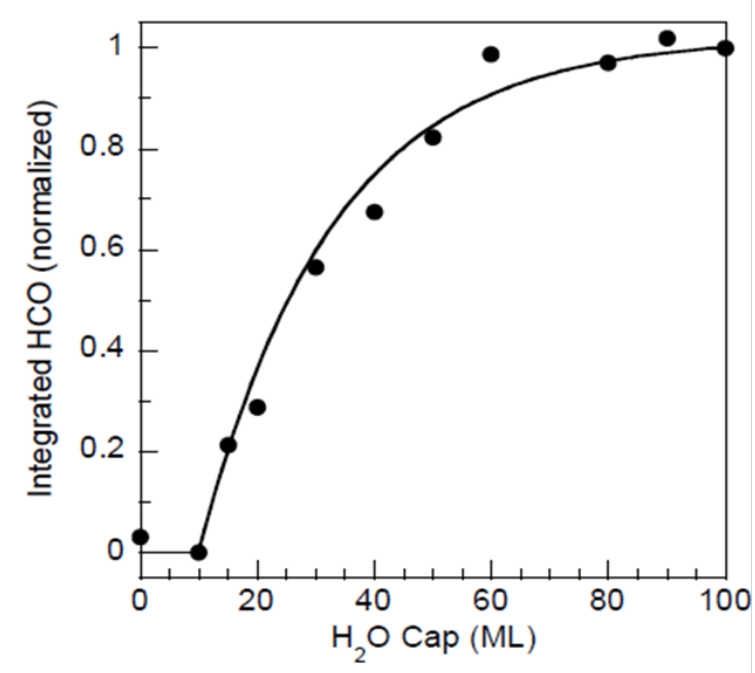

Figure 73 - Integrated HCO signal vs. amount of H_2O in capping layer (line is to guide the eye only)

Other key points of this graph are the delay in onset of HCO production, which begins at a H_2O thickness of around 15 ML, and the early point at which the maximum HCO yield is reached, at around 60 ML H_2O. Assuming a H-diffusion mechanism, this data suggests that the H atoms are produced in the region 15-60 ML below the vacuum interface of the film.

As a further test for diffusion of H atoms, a second set of experiments using isotopic labelling was conducted. Figure 68 shows the composition of the film used in these experiments.

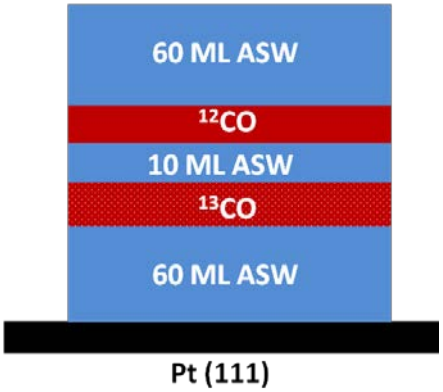

Figure 74 - Schematic showing film composition for experiments to test for diffusion of H atoms

Two layers of CO, one ^{13}CO and one ^{12}CO, separated by 10 ML of ASW were deposited on a 60 ML spacer layer of ASW. The film was capped with a 60 ML capping layer and irradiated with 100 eV electrons at 110 K. In theory, if H atoms are produced near the surface of the film and then diffuse, then the upper ^{12}CO layer will be depleted more quickly, while the deeper ^{13}CO layer will show a delay in consumption of CO. Conversely, if energy transfer through the film produces H atoms preferentially at or near to the CO layer as a result of some interface effect of the CO, then the two CO layers should be approximately equally depleted.

The results of these experiments, for increasing coverage of ^{12}CO in the upper layer, are shown in Figure 69. As predicted, there appears to be a trend towards increased delay in the onset of ^{13}CO consumption in the deeper layer as the fractional coverage of the ^{12}CO layer is increased. After the onset of CO consumption, however, the rate of consumption appears to be independent of the coverage in the upper layer.

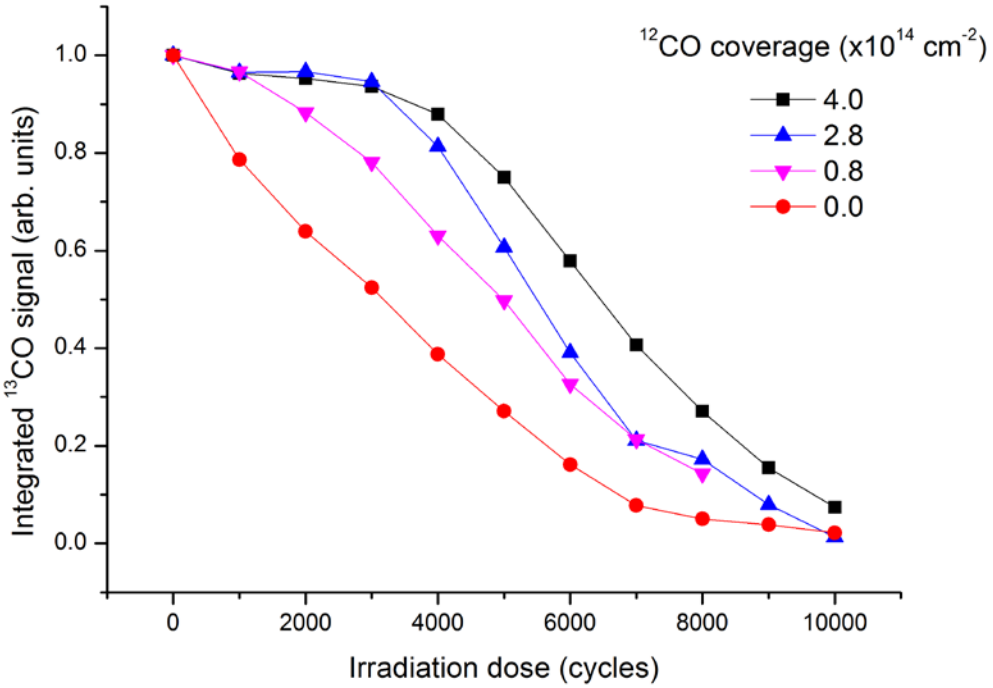

Figure 75 - Consumption of ^{13}CO vs. electron fluence in experiments with two isotopically labelled layers of CO

These observations are consistent with a mechanism for reduction which is based on diffusion of a reactive species to the CO layer. In particular, the delay in reaction of CO in the more deeply buried layer lends support to the idea that H atoms originate in the near-surface region, preferentially reacting with the ^{12}CO layer before diffusing to greater depths in the film.

The decomposition of CO as a function of electron fluence has been recorded for a number of different cap layer thicknesses. Figure 70 shows the linear decrease in CO consumption as a function of radiation dose for films with thick cap layers.

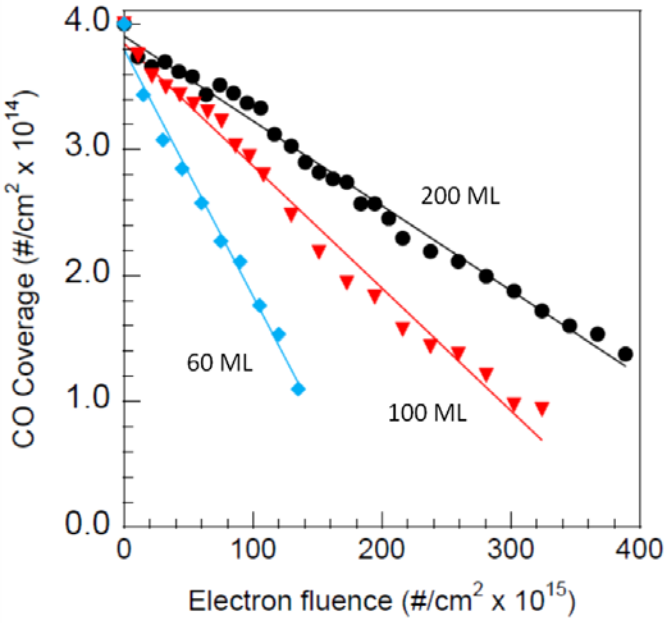

Figure 76 - CO signal vs. electron fluence for irradiated ASW/CO/ASW films for θ_{cap} = 60, 100, or 200 ML (labelled), irradiated at 100 K. Lines show best fit to experimental data.

The number of reactions per electron may be calculated from the best fit in Figure 70, which is essentially a reaction probability for each CO molecule. Figure 71 shows the reaction probability of an electron with CO vs. cap layer coverage for a number of films.

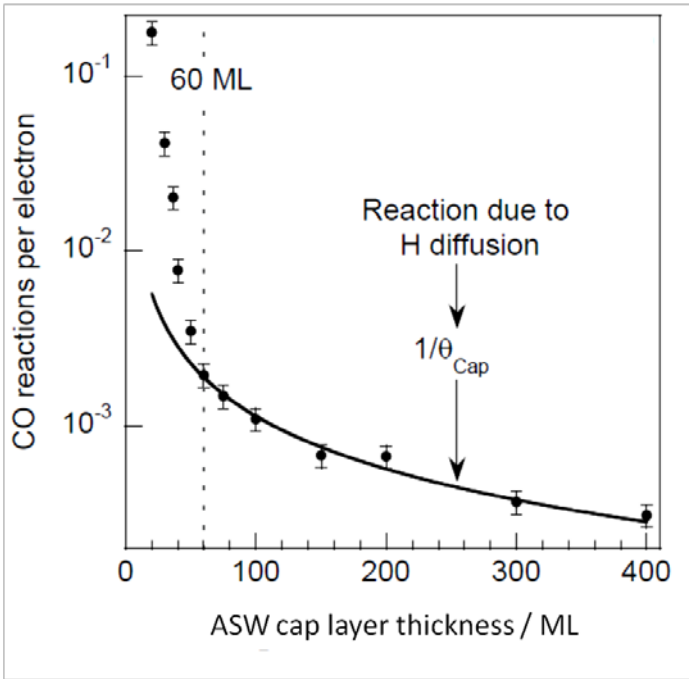

Figure 77 - CO reactions per incident electron (reaction probability) as a function of cap layer thickness. For θ_{cap} > 60 ML, the reaction probability is proportional to $1/\theta_{cap}$.

Initially, the CO signal decreases linearly, but for thicker films, in which reduction pathways dominate, the reaction probability decreases as a function of $1/\theta_{cap}$. According to Fick's first law of diffusion, the flux (*J)* in mol s^{-1} m^{-2} of a species, (*A*) at a depth *l*, in m, in a medium is proportional to 1/*l*, according to equation (7.12)

$$J = D\frac{[A]_0}{l} \qquad (7.12)$$

Here $[A]_o$ is the initial concentration, in mol m^{-3}, of species A. Assuming that the reaction probability for CO is directly related to the concentration of H atoms at the CO layer, then a $1/\theta_{cap}$ dependence as shown in Figure 71 provides further strong evidence for a hydrogenation mechanism involving diffusion of H atoms.

7.4. Monte Carlo simulations of H atom diffusion

A Monte Carlo model for the diffusion of H atoms within a layered ASW/CO/ASW ice was developed using the random walk model of diffusion. The model is based on the premise that the electrons incident on the ices in the experiments react rapidly with the water molecules to produce H and OH. The H atoms may then diffuse through the film to react with CO and products of CO reduction.

7.4.1. Monte Carlo Model

The model ice is a 3-dimensional array with equal x and y, and the ice thickness, Z_{ASW} measured along the z direction (Figure 72). The thickness of the film is a user input parameter.

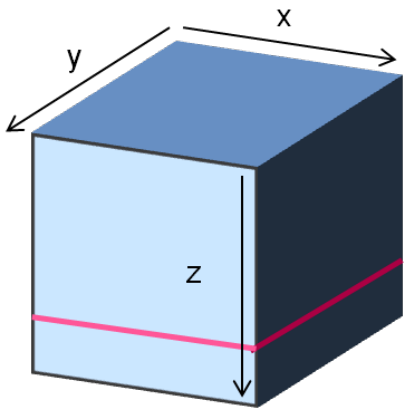

Figure 78 - Model of ice film including CO layer (indicated in red) with dimensions x, y and z

Each unit of the array is populated with a single water molecule, resulting in a simple cubic arrangement in which each water molecule may interact with six others. A layer of CO molecules is also inserted into the array, at a depth Z_{CO}, which is an input parameter. Available sites in x and y at this depth are randomly populated with CO until the fractional coverage of CO input by the user is reached.

H atoms are deposited into the array one atom at a time, originating at a position θ_i which is modelled on the typical penetration distribution of low energy electrons in water ice (Figure 73).[133] The x and y coordinates of the starting position are chosen at random.

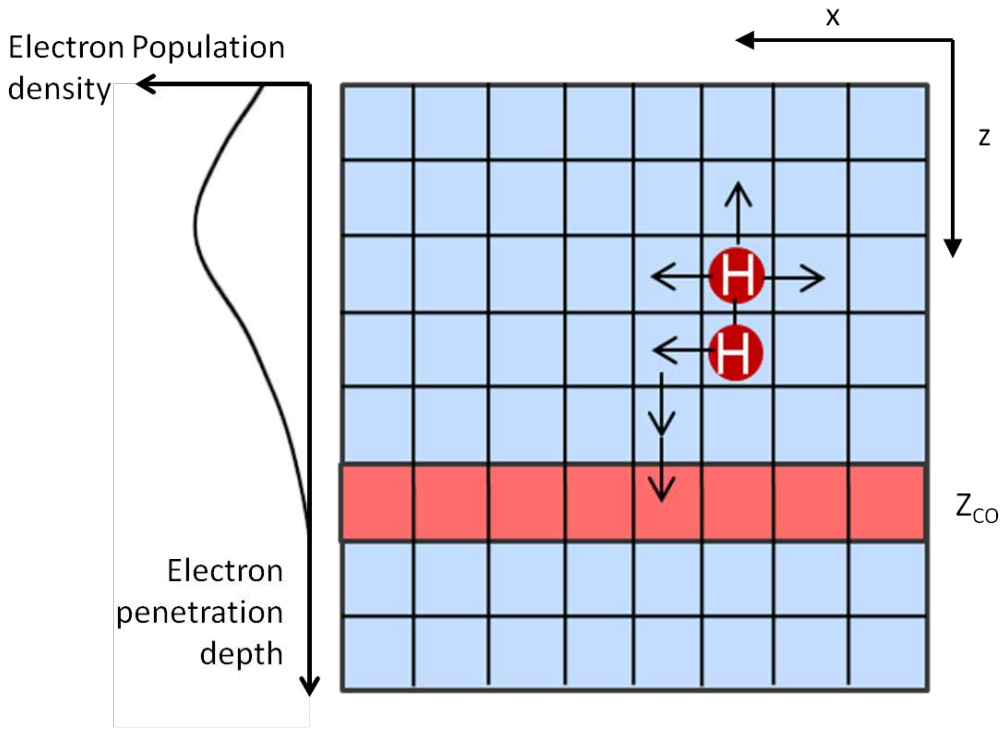

Figure 79 - Random walk model of H atom diffusion showing distribution of H atom starting positions and steps indicative of random walk. Curve is for descriptive purpose only; not shown to scale.

An H atom may take a single random step in ±x, ±y, or ±z, chosen by a random number generator. The model operates periodic boundary conditions in x and y. In the event that a random step would put the H atom at $z < 0$ or $z > Z_{ASW}$, that particular iteration is completed, and the H atom is considered "lost", either to vacuum or by adsorption to the substrate. If the random step causes the H atom to encounter anything other than a water molecule or methanol (i.e. CO, HCO, H_2CO, or H_3CO), then a "reaction" occurs with a specified probability input by the user, for each of the following reactions:

(1) $CO + H \rightarrow HCO$

(2) $HCO + H \rightarrow H_2CO$

(3) $H_2CO+H \rightarrow H_3CO$ or H_2COH

(4) $H_3CO + H \rightarrow H_3COH$

In the following discussions, the notation (x_1, x_2, x_3, x_4) will be used to define the reaction probabilities (x_i) allocated to the reactions (1-4).

If a reaction occurs, then that H atom has been consumed and that particular iteration of the simulation is concluded. If, however, there is no reaction, the H atom continues its random diffusion until it is either lost or consumed by reaction. Similarly, if an H atom encounters either an H_2O or CH_3OH molecule, no reaction occurs and the H atom's random path simply continues.

After a single iteration of the simulation, the next begins automatically, placing an H atom randomly in x and y and according to the probability distribution in z, as before. The simulation may repeat as many times as required by the user, either by defining a maximum number of H atoms, or by recording the yields of products output and halting the simulation at a particular value. For example, the simulation may run until all CO has been consumed or until all products have been completely converted to methanol.

The simulations are programmed to output information about the amount of CO remaining in the film and the amount of methanol which has been produced as a function of the number of H atoms.

7.4.2. Monte Carlo Simulation Results

The aim of the MC simulations is to investigate whether a mechanism based on diffusion of H atoms formed by low-electron radiolysis of water supports the following experimental observations:

- A linear decrease in CO vs. electron fluence
- $1/\theta_{cap}$ dependence of CO reaction probability
- The delay in the loss of the deeper CO layer in 2-layer experiments

In attempting to reproduce these experimental data, the simulations can be used to show whether sequential hydrogenation of CO is a reasonable model for CO reduction, and whether the first step is the rate-limiting step, as well as whether diffusion of H atoms is a likely mode of energy transfer.

In order to reproduce the linear dependence of CO consumption on radiation dose, four simulations were performed; in each simulation, one of the reaction probabilities was set to 0.1, while all the others remained at 1. In this way, the rate-limiting step can be identified. The results of these simulations are shown in Figure 74.

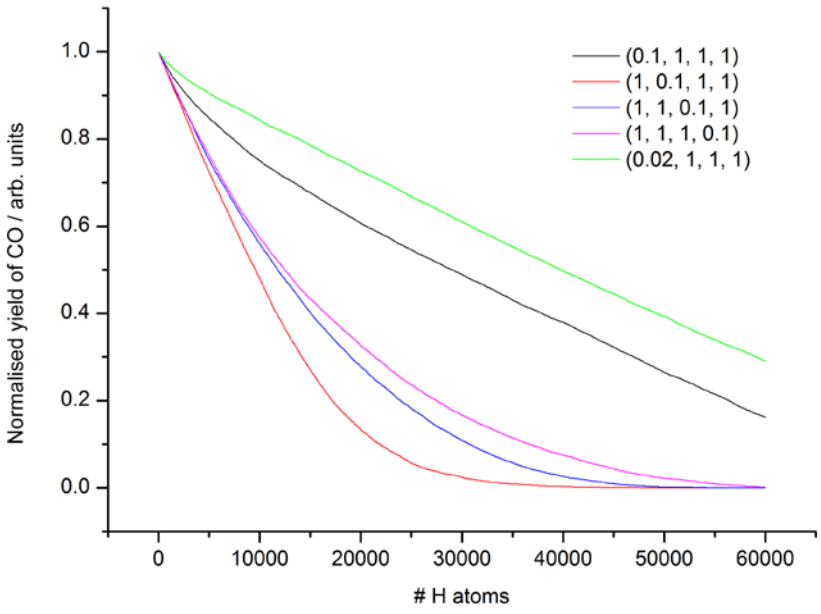

Figure 80 - CO yield as a function of irradiation time for simulations in which the reaction probabilities x_i were varied according to (x_1, x_2, x_3, x_4)

In all of the simulations with $x_1 = 1$, the initial increase in CO yield is linear as a function of irradiation time, however, deviation from linear behaviour begins before the yield of CO has fallen to ¼ its original value. The experimental findings show linear dependence continuing until at least ¼ the original value, suggesting that these conditions differ from the simulation. The result of setting $x_1 = 0.1$ gives the closest approximation to a linear dependence on irradiation dose, though with a slight curve at high yields. In order to test the effect of limiting this step even further, an additional simulation was performed in which the reaction probabilities were set to (0.02, 1, 1, 1). The result of this experiment is a further increase in the linearity, suggesting that the first step has been correctly identified as the rate-limiting step. The slight curve at high yields is still observed, however, a closer look at the experimental data appears to show a similar trend. This subtle change in the gradient of CO consumption at high yields is most likely due to a slight delay in the onset of

reactions 2, 3 and 4. Although the reactions have the same probabilities, there is initially only CO for H to react with, resulting in a steep gradient in CO consumption before HCO and further hydrogenated products are formed.

In order to calculate the reaction probability per CO as a function of cap layer and examine whether the $1/\theta_{cap}$ dependence can be reproduced by the model, a second set of simulations were performed. In these simulations, the reaction probabilities were set to (0.02, 1, 1, 1); the results are shown in Figure 75.

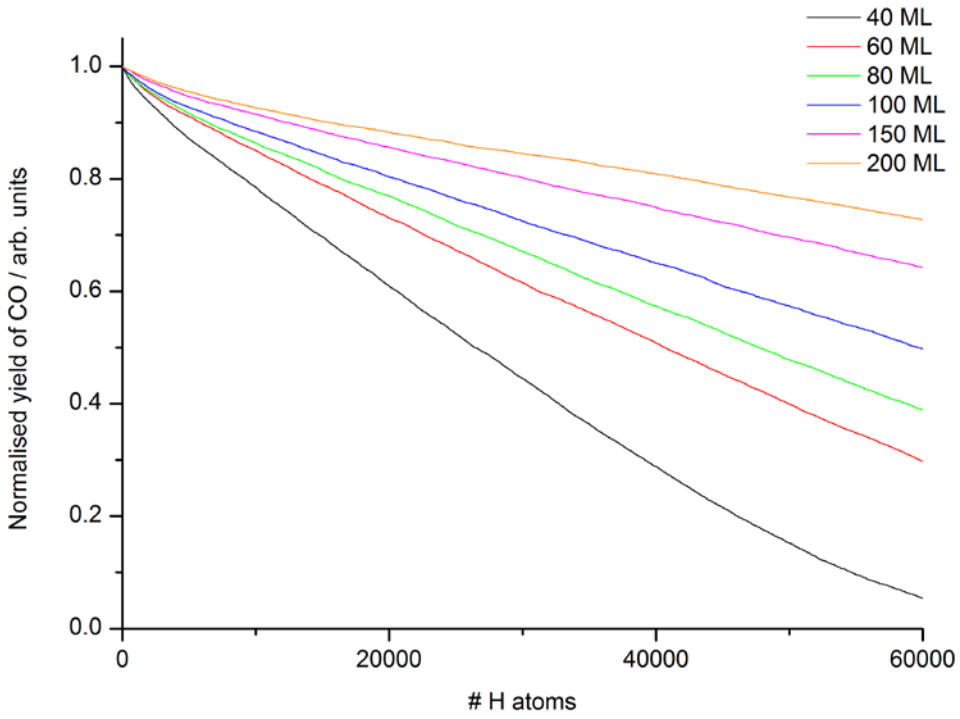

Figure 81 - Monte Carlo simulation data showing linear decrease in CO signal for films capped with 40, 50, 60, and 70 ML ASW, as a function of the number of H atoms.

The figure shows a clear change in gradient with increasing cap layer thickness. The linear dependence on radiation dose is also reproduced by the model for the full range of film thicknesses shown.

The probability for CO reaction with H atoms following irradiation with 60,000 H atoms has been calculated as a function of cap layer by taking the gradient of each of

the lines in Figure 75. A second line, corresponding to a constant divided by θ_{cap}, is shown for comparison.

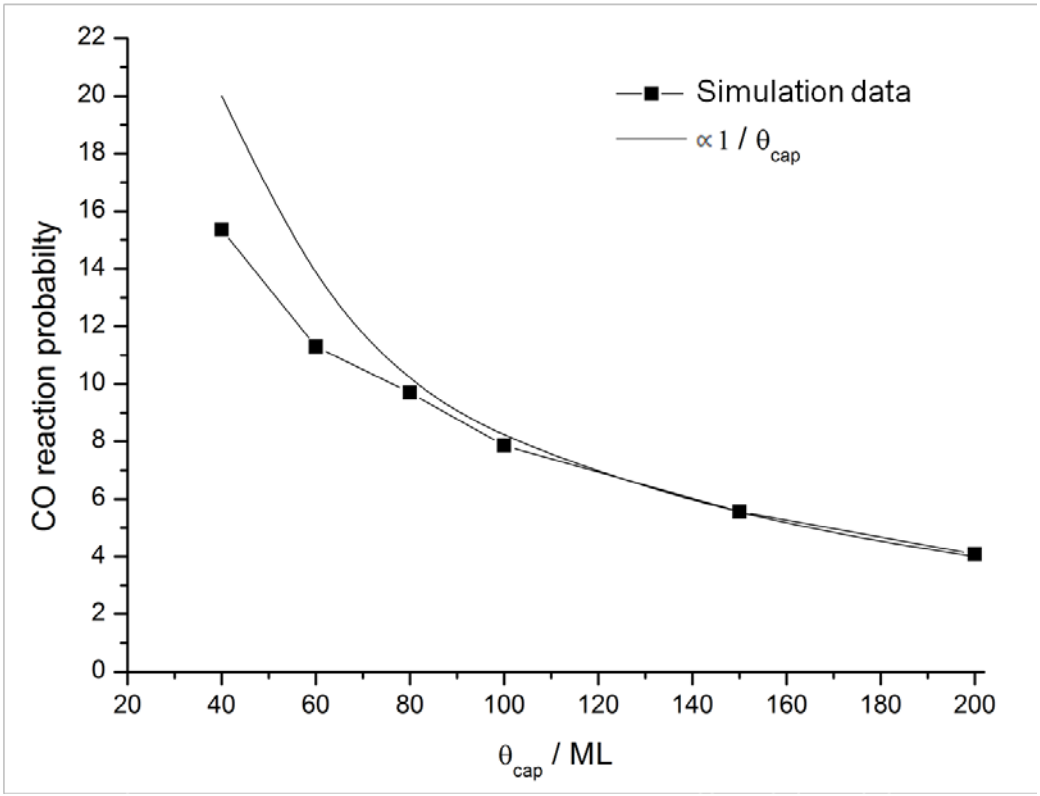

Figure 82 - CO reaction probability as a function of cap layer, showing the simulated data and a curve proportional to $1/\theta_{cap}$, for comparison

As Figure 76 clearly shows, a diffusion-based model appears to be a good representation of the mechanism CO decomposition in thick ice films. The trend in reaction probability as a function of cap layer is a very close approximation to a true dependence on $1/\theta_{cap}$, as shown by the solid line. Since the model is based on the random walk model of diffusion, in which the diffusion depth of an H atom is proportional to $1/l$, this dependence is naturally reproduced.

As a further test of the diffusion model as a mode of energy transfer in layered ices, simulations were performed in which a ^{12}CO and a ^{13}CO layer were buried in the film, at a depth of 60 and 70 ML, respectively, in analogy to similar experiments

performed in the laboratory. The ^{12}CO consumption as a function of irradiation dose for both the simulation and experimental data is shown in Figure 77. In these experiments, the reaction probabilities are set to (0.02, 1, 1, 1).

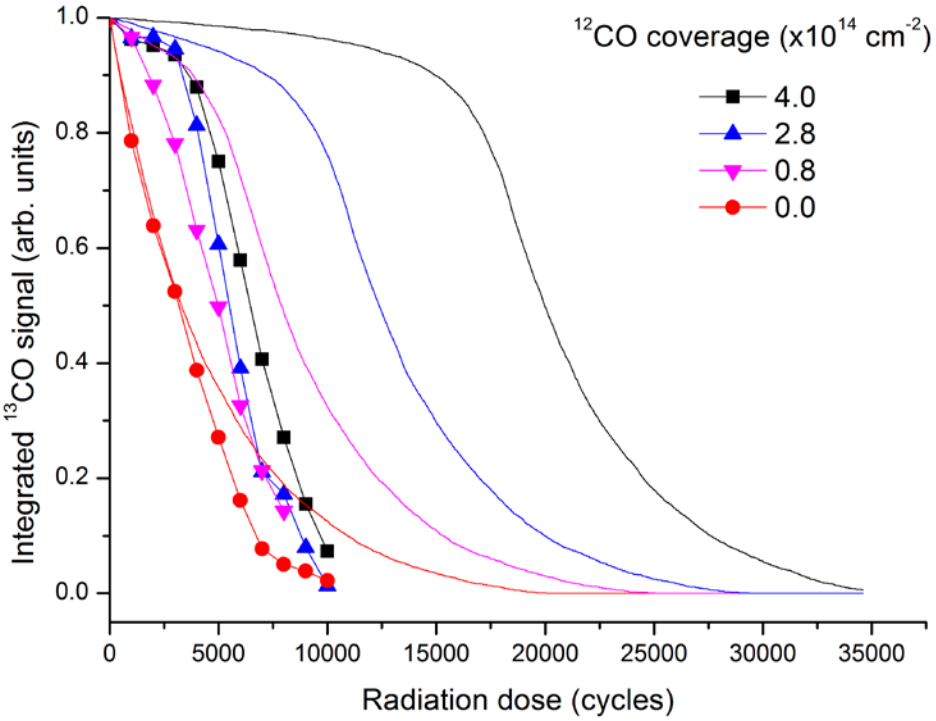

Figure 83 - Comparison of experimental vs. MC simulation data for ^{13}CO consumption in experiments with 2 layers of CO: a near-surface ^{12}CO layer, and a deeper ^{13}CO layer

Figure 77 demonstrates that a Monte Carlo model based on H atom diffusion can successfully reproduce the general shape of the 2-layer experiments. The simulations also accurately reproduce the linear decomposition of CO. The delay in the onset of CO consumption, however, is greatly over estimated by the model. The model differs from the experimental situation in a number of ways, which may contribute to observed deviation from the experimental results. One key difference between the model and laboratory conditions is that in the model only one H atom diffuses through the ice at a time, whereas in ice, all of the H atoms are created at

approximately the same time and diffuse through all at once. This alone may be sufficient to explain the initially slow rate of CO consumption by the model.

The model is based on the assumption that H atoms involved in reduction of CO are formed by dissociation of water by low-energy electron impact. However, the model neglects to take into account the H atoms produced in other reactions, such as dissociative electron attachment (nearer the end of the electron path) or dissociation of intermediates in the hydrogenation reactions.

The other main point on which the model and the experiments differ is the reactions which may take place. In order to put together a simple model for diffusion of H atoms, a number of reaction pathways were excluded. Reaction between H atoms to form H_2 was not included, however this is unlikely to be the cause of the difference in initial CO consumption rate, as H_2 is likely to be formed quickly near the vacuum interface of the film when the density of H atoms is highest, meaning that H atoms which react by this pathways are essentially invisible to the CO layer. Alternative reaction routes between H atoms and reduction products, for example $H + HCO \rightarrow H_2 + CO$ and production of formic acid, were also excluded. Earlier discussion (chapter 7.1.3) covered previous work on the importance of these reactions, although it has not been possible to determine the extent to which they contribute in the experimental conditions. The absence of oxidation reactions in this model is unlikely to have an effect, as the experiments have determined that oxidation and reduction take place in different places in the film, and it is therefore fair to leave them out of any model of reduction of CO buried under thick capping layers.

8. Conclusions

8.1. LIF studies of low-energy electron interactions with H_2O

A high-vacuum apparatus for LIF studies of low-energy electron interactions with water vapour has been built, incorporating a molecular beam, electron gun, laser system and PMT detector.

A number of studies have been carried out to optimise PMT voltage, integration window, and dye laser energy in order to attain a good S/N ratio. Efforts to discriminate against the scattered light signal in LIF detection have also been detailed. A pulsed molecular beam of 2.4% H_2O in He has been commissioned for sample introduction, as well as a needle valve used in preliminary experiments. Electron currents up to ~7.5 μA have been recorded by choosing the electron gun grid, anode and lens voltages according to SIMION simulations, and by using the Helmholtz coils to focus and steer the electron beam.

LIF spectra of the $A^2\Sigma(v=1)\leftarrow X^2\Pi(v=1)$ transition in nascent OH radicals were successfully recorded by 193 nm photo-dissociation of allyl alcohol at 3×10^{-2} Torr. By analysis of these experiments, the LIF sensitivity of the apparatus in optimised S/N conditions was estimated at 1.78×10^{11} molecules $pulse^{-1}$ cm^{-3}.

LIF of OH produced by electron interactions with water has proved more difficult to record due to the low cross-sections, relatively low electron current density and low precursor gas pressures required for operation of the electron gun. Alterations to the experimental apparatus which may help to advance the recording of OH LIF spectra from DEA to water have been discussed, and possible routes forward have been identified.

8.2. Low-energy electron interactions in ASW/CO/ASW ices

The aim of the condensed-phase work was to study the electron-stimulated reactions of layered ASW/CO/ASW ices, in particular to investigate mechanisms of energy transfer in thick ice films and to monitor the kinetics of low-energy electron stimulated reactions.

Using a combination of RAIRS and MS, decomposition of CO has been observed in ices which are thick compared with the penetration depth of 100 eV electrons. The results show both efficient oxidation and reduction of CO by reaction with the products of ice radiolysis, specifically H and OH. The major reaction products have been identified as carbon dioxide and methanol; formaldehyde, formic acid and the formyl radical (HCO) have also been observed. Experiments in which the film thickness was varied showed distinctly different kinetics for the consumption of CO. These differences are manifest as different zones in the film; oxidation of CO preferentially occurs in the region < 20 ML from the vacuum interface of the film, while reduction dominates CO decomposition in thicker ice films.

Experimental data points to oxidation of CO by reaction with OH, which is formed by low-energy electron radiolysis of the water-ice at or near the vacuum interface. The relatively low mobility of OH radicals in ice leads to a preferential zone of oxidation in the near-surface region. The reaction itself seems approximately barrier-less, and a high rate of conversion of CO to CO_2 (~70%) is observed for films capped with up to 20 ML ASW.

The reduction of CO by sequential reactions with H atoms has been investigated. Observation of the yield of methanol as a function of capping layer thickness indicated reduction of CO buried under capping layers as thick as 120 ML. At this

depth, the combined yield of formaldehyde and methanol accounts for up to 50% of the CO consumed. The reaction pathway for reduction of CO has been discussed in detail; experimental evidence supports efficient, even barrier-less conversion of formaldehyde to methanol in the final step, as well as a relatively rapid rate of conversion of HCO into formaldehyde. These observations, in combination with apparent temperature dependence for the onset of the reduction pathway, lead to the suggestion that the first step, in which CO is converted to HCO, is the rate-determining step.

A Monte Carlo model was developed to test the possibility that for high cap layer coverage energy transfer to the CO layer proceeds via diffusion of H atoms. The simulations, based on the random walk model of diffusion, were able to reproduce the dependence on cap layer thickness observed in the experimental work, providing evidence for a diffusion-controlled reaction mechanism.

In the simulations, the CO consumption showed the same linear dependence on electron fluence as observed experimentally, for simulations where the probability of the first step was reduced. This supports the suggestion that $H + CO \rightarrow HCO$ is the rate-limiting step.

9. Further Work

9.1. LIF spectra of OH by DEA to water

LIF spectra for nascent OH from photo-dissociation of allyl alcohol have been successfully recorded using the experimental apparatus described. In order to record OH LIF spectra from DEA to water at 8.5 eV, adjustments to the LIF sensitivity of the experiment, detailed in section 6.5, must be implemented.

The first step towards recording electron impact OH LIF spectra is simplify the experiment somewhat, to use a simple filament instead of an electron gun, and to use low pressures of H_2O in the chamber, rather than a molecular beam. The LLG should be mounted much more simply, in the HV system proposed in section 6.5 (Figure 52) in order to improve the S/N ratio. Painting the chamber black may also help to reduce noise; however this would make the lining of the chamber permanently incompatible with UHV. In this system, which should give the highest possible yield of OH fluorescence, it will be possible to test whether OH LIF from electron collisions with H_2O can be recorded.

Assuming that these preliminary experiments are successful, work may begin on installation of an electron gun pulser, so that well-defined pulses of electrons may be fired, optimisation of the molecular beam, so as to have the highest possible number density of H_2O in the beam, and potentially installing an ellipsoidal mirror system to maximise the amount of LIF signal detected by the PMT.

If implementation of the suggested changes does indeed provide the increase in S/N and LIF sensitivity required to record OH LIF spectra, then it should be possible to study the internal energy of OH formed in DEA to H_2O. Directly recording the

energy state distributions of OH formed at the 8.5 eV resonance in cold H_2O should provide evidence to support or contradict dissociation by the $^2A_1$ state.

9.2. Further studies of layered ASW/CO/ASW ices

The results of studies of the low-energy electrons interactions with condensed phase water appear to show a diffusion-controlled mechanism of energy transfer, contradicting previous studies. Diffusion of H atoms in amorphous ice proceeds by hopping between vacancies in the H-bonding network. As such, this work could be extended to investigate the effect of ASW porosity on the reduction and oxidation pathways in layered ASW/CO/ASW films. A number of studies have been conducted to study the effect of varying ice porosity on anion desorption following electron irradiation of thin ice films, but so far these studies have not addressed the influence of morphology on energy transfer in thick films.[161,162]

In order to extend the Monte Carlo simulations to further investigate energy transfer within thick, layered ices, it may be useful to run the simulation such that multiple H atoms run simultaneously, rather than one at a time. This should give a better representation of the mechanism as it occurs in experimental ice irradiation. Additional reaction pathways could also be included in future versions of the model, for example back reactions in the reduction pathway, combination of H atoms to produce hydrogen, and oxidation pathways.

9.3. Condensed phase studies of DEA in water

Once the gas-phase experiments have been concluded, the apparatus can undergo the changes needed to convert it for use in surface studies.

Some studies of DEA to water ice have been reported, but have been limited to measurements of anion yields from thin films.[73] Given the importance of low-energy electron interactions in the gas and liquid phases, it is vital to gain an understanding of the role of DEA in solids. In studies of icy dust grains in the ISM, or long-term disposal of radioactive waste, where the timescales are on the order of thousands of years, low-energy electron processes may contribute significantly to the production of reactive radical species leading to the formation of more complex molecules.

The apparatus designed for the gas-phase studies is equipped with two turbo-molecular pumps, sufficient to pump out both the source and main chambers and maintain a base pressure of at least 10^{-9} Torr. In order to achieve such low pressures, it will be necessary to bake out the chamber, removing CO and H_2 trapped in pores in the chamber walls. This may be performed using the same heating tapes which were used to raise the temperature of the gas lines to the molecular beam.

The chamber will also be fitted with a cryogenically-cooled manipulator on which to mount the crystal so that fine adjustments may be made to its position with respect to the laser, the electron gun, and the molecular beam, which may be used for sample deposition. A mass spectrometer will also be installed on the chamber for use in sample analysis and calibration of the sample deposition.

In order to build on the condensed phase studies detailed in this thesis, the redesigned experimental chamber can be used to study the interaction of low-energy electrons with layered or mixed ASW/hydrocarbon ices.

The UHV LIF apparatus can be used to study the DEA process in mixed ices. In the experiments which I have conducted on layered ASW/CO/ASW ices, the contribution of DEA to the product yields has not been estimated, but may be significant, given the low initial energy of the electrons, and the likelihood of thermalization within the dense ice film. DEA to CO has been documented in the condensed phase, and may also play a role, for example in the enhanced yield of O_2 from the layered films. Observation of direct fluorescence and LIF of OH, as well as mass spectrometry of desorbing fragments should provide a large amount of information on the processes underway in electron-irradiated ice films.

Appendix

THE JOURNAL OF CHEMICAL PHYSICS **140**, 204710 (2014)

Electron-stimulated reactions in layered CO/H_2O films: Hydrogen atom diffusion and the sequential hydrogenation of CO to methanol

Nikolay G. Petrik,[1] Rhiannon J. Monckton,[2] Sven P. K. Koehler,[2] and Greg A. Kimmel[1,a)]
[1]*Physical Sciences Division, Pacific Northwest National Laboratory, MSIN K8-88, P.O. Box 999, Richland, Washington 99352, USA*
[2]*School of Chemistry, The University of Manchester, Manchester M13 9PL, United Kingdom; Photon Science Institute, The University of Manchester, Manchester M13 9PL, United Kingdom; and UK Dalton Cumbrian Facility, The University of Manchester, Moor Row, Whitehaven CA24 3HA, United Kingdom*

(Received 11 February 2014; accepted 6 May 2014; published online 28 May 2014)

Low-energy (100 eV) electron-stimulated reactions in layered $H_2O/CO/H_2O$ ices are investigated. For CO layers buried in amorphous solid water (ASW) films at depths of 50 monolayers (ML) or less from the vacuum interface, both oxidation and reduction reactions are observed. However, for CO buried more deeply in ASW films, only the reduction of CO to methanol is observed. Experiments with layered films of H_2O and D_2O show that the hydrogen atoms participating in the reduction of the buried CO originate in the region that is 10–50 ML below the surface of the ASW films and subsequently diffuse through the film. For deeply buried CO layers, the CO reduction reactions quickly increase with temperature above ~60 K. We present a simple chemical kinetic model that treats the diffusion of hydrogen atoms in the ASW and sequential hydrogenation of the CO to methanol to account for the observations. © *2014 AIP Publishing LLC*. [http://dx.doi.org/10.1063/1.4878658]

I. INTRODUCTION

Non-thermal reactions in aqueous systems are important for a number of areas including radiation chemistry and nuclear technology,[1] radiation biology,[2] and photocatalysis.[3,4] When interacting with condensed matter, most forms of high-energy radiation (γ-rays, α, β, etc.) generate large numbers of low-energy secondary electrons, and these secondary electrons, which are chemically active, are responsible for many of the radiation-induced chemical reactions.[3] Due to the high-scattering cross sections that lead to very short mean-free path lengths, the interactions of low-energy electrons with liquid water are difficult to study directly. To surmount this difficulty, many experiments have been performed with low-energy sources (electrons, ions, and photons) on amorphous solid water (ASW) and crystalline ice films adsorbed on cold substrates in ultrahigh vacuum.[5–30]

Non-thermal reactions in water ices, with or without other co-adsorbed molecules, are also of interest in astrochemistry and planetary sciences.[31–34] For example, dust grains in cold molecular clouds are coated with molecular ices for which water is typically the main component. Thermal and non-thermal processing of these icy dust grains produces some of the complex molecules that have been observed in interstellar space.[35,36] Reactions in water ices are also important in comets and some of the moons of the gas-giant planets.[31,32,34] In cold, dense molecular clouds, CO is an abundant component in icy grain mantles,[37–39] and reactions in CO/H_2O ices contribute to the wide variety of organic molecules that have been observed in these environments. As a possible route to the production organic molecules, the non-thermal reactions in CO/H_2O ices have been investigated for photon, electron, and ion irradiation.[17,27,37,39–41]

Both reduction and oxidation reactions are observed in irradiated CO/H_2O ices.[17,27,37,40,41] These reactions occur because the interaction of ionizing radiation with condensed water leads to water dissociation through a variety of channels producing both oxidizing and reducing species:[1,3]

$$H_2O + (\gamma, e^-, A^+) \rightarrow H_2O^* \rightarrow H + OH, \quad (1a)$$

$$H_2O + (\gamma, e^-, A^+) \rightarrow H_2O^* \rightarrow 2H + O, \quad (1b)$$

$$H_2O + (\gamma, e^-, A^+) \rightarrow H_2O^* \rightarrow H_2 + O, \quad (1c)$$

$$H_2O + (\gamma, e^-, A^+) \rightarrow H_2O^+ + e^- \rightarrow H_2O^* \rightarrow H + OH, \quad (1d)$$

$$2H_2O + (\gamma, e^-, A^+) \rightarrow H_3O^+ + e^- + OH \rightarrow H_3O^* + OH \rightarrow H + OH + H_2O. \quad (1e)$$

The oxidation products of CO are typically the most abundant products observed.[17,37,39,40] For example, Hudson and Moore used 800 keV protons to irradiate mixed CO/H_2O ices, and found that the predominant reaction was the conversion of CO to CO_2.[37] However, small amounts of the formyl radical (HCO),[27,37,40] formaldehyde (CH_2O),[27,37,40,41] methanol (CH_3OH),[27,37,41] formic acid (HCOOH),[27,37,41] and methane (CH_4)[37] are also observed.[37] Sequential reactions with hydrogen atoms are believed to convert CO to methanol (CH_3OH):[37,41–43]

$$CO + H \rightarrow HCO, \quad (2)$$

$$HCO + H \rightarrow CH_2O, \quad (3)$$

a)Author to whom correspondence should be addressed. Electronic mail: gregory.kimmel@pnnl.gov

$$CH_2O + H \rightarrow CH_3O, \quad (4a)$$

$$CH_2O + H \rightarrow CH_2OH, \quad (4b)$$

$$CH_3O + H \rightarrow CH_3OH, \quad (5a)$$

$$CH_2OH + H \rightarrow CH_3OH. \quad (5b)$$

The hydrogenation reactions can be initiated by gas-phase hydrogen atoms that strike the surface[41,42,44–47] or from H atoms produced by non-thermal dissociation of water in the ice mantles.[17,37,41,42]

Yoshinobu and co-workers investigated the electron-stimulated reactions in CO/H_2O ice.[17] In their experiments, CO was dosed on 5 nm thick water films, then capped with 30 nm thick water layers, and irradiated with 200 eV electrons. Similar to other experiments, they observed both oxidation products (e.g., CO_2) and reduction products (HCO, CH_2O, and CH_3OH). However, since the penetration depth of 200 eV electrons in condensed water is considerably less than 30 nm,[48] the mechanism by which these reactions occurred is not immediately clear. One possibility is that the CO diffused through the ASW cap layer to the region near the surface where it reacted with species produced by the energetic electrons.[49,50] Another possibility is that mobile species produced in the ASW (e.g., H, H_2O^*, or H_3O^+) diffused to the buried CO layer and subsequently produce the observed reactions.

We have previously studied electron-stimulated reactions in ASW films.[6,9–11,16,19,51–53] Some of those experiments demonstrated that the non-thermal reactions and the electronic excitations that initiate those reactions do not necessarily occur at the same location in the ASW. For example, H_2 is preferentially produced at the ASW/substrate and ASW/vacuum interfaces.[16,19,52] However, the energy that drives the reactions at the ASW/substrate interface is absorbed in the "bulk" of the ASW film.[16,19,52] Molecular oxygen is also produced in electron-irradiated ices,[12,20] but the reactions that produce O_2 occur primarily at or near the ASW/vacuum interface.[54,55] Our previous research on the spatial distribution of electron-stimulated reactions in neat ASW films and the results of Yoshinobu and co-workers motivated us to investigate the spatial distribution of the electron-stimulated reactions in CO/ASW films.

Here, we investigate the electron-stimulated reactions in layered H_2O/CO/H_2O ices as a function of the position of the CO layer within the water films. For CO layers buried within the first 50 ML of the vacuum/water interface, we find that both oxidation and reduction reactions occur as observed in earlier experiments.[17,27,37,40,41] However when the CO layer is buried deeper within the water film, only reduction products (HCO, CH_2O, and CH_3OH) are observed. For water cap layer coverages, θ_{Cap}, greater than 50 ML, the number of CO reactions per incident electron decreases as $1/\theta_{Cap}$. The hydrogen atoms, which are responsible for the CO reduction reactions, originate in the region between 10 ML and 50 ML below the vacuum interface and subsequently diffuse to the buried CO layer. For $\theta_{Cap} > 50$ ML, the number of CO reactions per electron decreases rapidly as the irradiation temperature decreases and is negligible for temperatures below 70 K. We present a simple kinetic model based on the diffusion of hydrogen atoms within the ASW film and the sequential hydrogenation of CO to methanol that qualitatively accounts for the observations.

II. EXPERIMENTAL PROCEDURE

The experiments were carried out in an ultrahigh vacuum (UHV) system that has been described previously.[56] The system is equipped with a molecular beam line for dosing water, CO, and other adsorbates on the sample, a closed-cycle helium cryostat for sample cooling, a low-energy electron gun (Kimball Physics, model ELG-2), a quadrupole mass spectrometer (Extrel, model EXM720), and a Fourier-transform infrared spectrometer (Bruker, Vertex 70). Infrared spectroscopy of the CO/water films was performed in reflection mode at a grazing angle of incidence (~84° with respect to the surface normal).

Water films were deposited on the Pt(111) using a calibrated molecular beam at normal incidence. Previous research has shown that this produces dense, smooth ASW films.[57–59] The coverage of the water films is determined by the dosing time and checked by measuring the water temperature programmed desorption spectra. Here, the water coverage is reported in monolayers (ML), where 1 ML = 1.14×10^{15} #/cm^{-2}, which is the areal density of a bilayer of crystalline ice at 100 K. The thickness of the water films is not measured directly, but it is proportional to the water coverage.[59] Since the sticking coefficient for CO on ASW is ~1 at T < 30 K,[60] the initial coverages of CO were determined from the dosing time using the known flux of the molecular beam line. [The CO flux was determined from our previous investigation of the adsorption of CO on TiO_2(110).[61]] Decreases in the CO coverages due to electron-stimulated reactions were then calculated from decreases in the integrated CO signals measured by infrared reflection absorption spectroscopy (IRAS).

An important aspect of the current work is to explore the electron-stimulated reactions between water and CO as a function of the depth of the CO within the water films. Therefore, it is important to control and characterize the position of the CO within the water films.[49,50] The typical procedure used to produce a CO layer trapped at a known location within a water film involved several steps. First, a non-porous water film was deposited on the Pt(111) using a molecular beam at normal incidence at 100 K.[57–59] The coverage of this "spacer" layer was usually 30 ML, which is sufficiently thick that the Pt(111) substrate was unlikely to influence the reactions. Several control experiments with thicker ASW layers confirmed this assumption (data not shown). Next, a layer of CO, typically with $\theta_{CO} \sim 4 \times 10^{14}$ molecules/cm^2, was adsorbed at T < 30 K. Finally, to bury the CO within the water film, ASW "cap" layers of varying coverages, θ_{Cap}, were adsorbed as follows: 10 ML of water was adsorbed at T < 30 K, then the temperature was set to 100 K and additional water was adsorbed to reach the desired θ_{Cap}. During the annealing of the initial 10 ML water cap to 100 K, unstable structures within the water relax effectively locking the CO in place.

The procedure described above for depositing the layered ASW/CO/ASW films was developed based on several control experiments that were conducted to determine the initial distribution of CO within the ASW films. For example, by measuring the amount of CO that desorbed upon subsequent heating as a function of the coverage of the water dosed at T < 30 K it was determined that a 3 ML H_2O film traps ∼50% of the CO, while a 10 ML H_2O film traps essentially all the adsorbed CO (see Fig. S1, supplementary material). Since investigations by Kay and co-workers have demonstrated that diffusion of atoms and small molecules in ASW is negligible below ∼120 K,[53] the results in Fig. S1 effectively give the width of the CO layer within the ASW/CO/ASW films (see inset, Fig. S1 in the supplementary material[84]). As described below, most of the results presented here will focus on experiments where $\theta_{Cap} > 50$ ML. As a result, the width of the CO layer (full width at half maximum ∼ 3 ML) is small compared to the width of the ASW cap layer. Experiments described below showing sequential reactions in two CO distinct layers of ^{13}CO and ^{12}CO separated by 10 ML of water also support the results shown in Fig. S1 of the supplementary material.[84]

For all the experiments reported here, the incident electron energy was 100 eV. As described previously, the electron beam was rastered over the surface to provide a uniform fluence of electrons.[19] Typical instantaneous current densities were ∼1.5 × 10^{15} #/cm^2/s with a beam diameter of ∼1.5 mm. Because electron-stimulated sputtering of the water films can be significant in the course of experiments involving large electron fluences,[62] additional water was dosed during the experiments to maintain the thickness of the ASW cap layer. Therefore, the typical experimental procedure included preparing the layered ASW film with the trapped CO (as described above) and obtaining an IRAS spectrum prior to irradiating the film. Next, the films were irradiated with energetic electrons. After the irradiation, additional water was dosed to account for the amount sputtered during the irradiation, and an infrared spectrum for the irradiated film was obtained. The sequence of electron irradiation, water dosing, and IRAS was then repeated the desired number of times to obtain a series of IRAS spectra for increasing electron fluences while maintaining an approximately constant water coverage. For example, for the results shown in Fig. 4(a), the amount of water sputtered during each irradiation cycle was ∼8 ML. Thus, for the experiment with a 60 ML cap, the coverage varied between 60 ML at the beginning of each irradiation cycle to ∼52 ML at the end, while the 200 ML cap varied between 200 ML and 192 ML. For several cases, we also repeated the experiments with smaller electron fluences (and thus less sputtering and redosing) per cycle and found similar results to those shown. Typically, the experiments depend on the electron fluence (i.e., #/cm^2), but not the electron flux (#/cm^2s). Also for the timescales of interest here, the reactions only occur when the electron beam is on. As a result, it is feasible to follow the progress of the electron-stimulated reactions using this repeated cycle of electron irradiations followed by water redosing and IRAS.

Because the amount of CO is a small compared to the water for most of the experiments, the new species created by the electron-stimulated reactions are typically difficult to discern in the raw spectra. However, the reaction products can be seen by taking the difference between the irradiated spectra and the spectra obtained prior to irradiation. Alternatively, experiments were repeated *without* CO and differential absorbance spectra were obtained from the irradiated ASW films with and without CO for the same electron fluence. This latter procedure is useful since electron irradiation leads to changes in the IRAS spectra of the ASW films that can make it difficult to observe the small signals associated with the CO-H_2O reaction products. However, qualitatively similar results were obtained using both methods.

For the results discussed below, the reaction probability refers to the number of reactions occurring per incident electron. The experiments do not measure the time-dependence of any of the electron-stimulated reactions, i.e., they do not measure the reaction rates. In addition, we will focus on experiments where the buried CO layer is spatially separated from the region near the ASW/vacuum interface where the energetic incident electrons create reactive species in the films. As a result of the spatial separation, simple kinetic models that assume the reactants are well-mixed are difficult to apply. Instead, the transport of reactants (H atoms in this case) needs to be addressed explicitly in any modelling.

III. RESULTS

Figure 1(a) shows the IRAS spectra for a CO/ASW film prior to electron irradiation (black lines) and after irradiation at 90 K (red lines) with 100 eV electrons. The CO was deposited on a 100 ML ASW layer and was capped with a 30 ML ASW layer as described in Sec. II. For this electron fluence and H_2O cap layer thickness, the loss of the CO peak due to electron irradiation is readily apparent in the IRAS spectra, while other changes are more difficult to detect. Figure 1(b) shows a series of differential absorption spectra from irradiated ASW films with and without trapped CO. As seen in the figure, the electron-stimulated reactions produce CO_2 (2343 cm^{-1})[37] and methanol (CH_3OH). The top curve in Fig. 1(b) (purple line) shows the differential absorbance spectra for a 75 ML ASW film with a buried layer of methanol for comparison with the irradiated spectra. All the main peaks observed in the methanol/ASW film (at 1018, 1126, 1430, 1450, 1462, 1478, and 2831 cm^{-1})[37,41,63] are also observed in the irradiated CO/ASW film. In the irradiated CO/ASW film, two small peaks at 1856 cm^{-1} due to HCO[37,41,64] and 1735 cm^{-1} corresponding to CH_2O[27,41,65] are also observed. For the largest electron fluence shown in Fig. 1(b), ∼95% of the CO has been converted to other species (primarily CH_3OH) by the electron-stimulated reactions.

The results in Fig. 1 show that for CO that is capped with a 30 ML ASW film, both reduction reactions leading to methanol and oxidation reactions producing CO_2 are observed, consistent with earlier experiments.[17,27,37,40,41] The reduction of CO due to reactions with hydrogen is also observed for CO trapped much deeper in the ASW films. For example, Fig. 2 shows several differential absorbance spectra for a CO layer that was capped with a 100 ML ASW film and irradiated with 100 eV electrons at 110 K. For this experiment, HCO, CH_2O, and methanol (not shown) are observed.

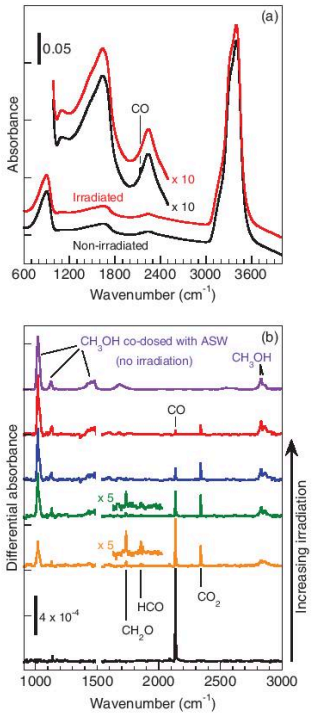

FIG. 1. IRAS spectra for electron-irradiated CO/ASW films with θ_{cap} = 30 ML and T_{irr} = 90 K. (a) Absorbance spectra before and after electron irradiation (fluence = 2.6 × 10^{16} #/cm^2). (b) Differential absorbance spectra for ASW films with and without CO for electron fluences of 0, 0.65, 1.3, 1.95, and 2.6 × 10^{16} #/cm^2 for the black, orange, green, blue, and red curves, respectively. The top curve (purple) shows the spectrum for a non-irradiated methanol/ASW film for comparison.

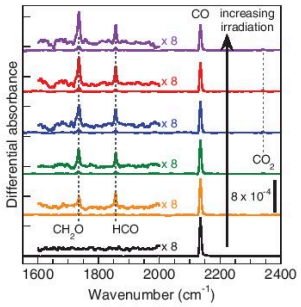

FIG. 2. Differential absorbance spectra for a CO/ASW with θ_{cap} = 100 ML irradiated at 110 K for electron fluences of 0, 1.3, 2.6, 3.9, 5.2, and 6.5 × 10^{16} #/cm^2 for the black, orange, green, blue, red, and purple curves, respectively. For this cap layer coverage, reduction products (HCO and CH_2O) are observed but very little oxidation products (CO_2). To obtain reasonable signal to noise for the small HCO and H_2CO peaks, the results shown are the average of 6 individual experiments.

However, essentially no CO_2 is produced. The HCO peak increases quickly and is then approximately independent of electron fluence, while the CH_2O peak increases in intensity for the range of fluences shown.

As the electron fluence increases, CO is converted to methanol. Figure 3 shows the integrated IRAS signals for CO and methanol versus electron fluence for a film where a ^{13}CO layer was capped with a 60 ML ASW film and irradiated at 100 K. (Figure S2 in the supplementary material shows a subset of the IRAS spectra for this experiment.[84]) The amount of CO decreases approximately linearly (Fig. 3, black circles), while the amount of methanol increases linearly (Fig. 3, red triangles). The magnitude of the CO and methanol IRAS signals indicates that most, or all, of the CO is converted to methanol in this experiment. This result is in contrast to previous experiments where CO_2 production is an important pathway in the irradiation of mixed CO/water films.[17,27,37,39–41]

As discussed below, the linear increase in the methanol signal without any appreciable induction suggests that the reaction of CO with hydrogen atoms has the lowest probability of the hydrogenation reactions (reactions 2–5).

The number of reactions per electron for the CO depends on the thickness of the ASW film that is covering the adsorbed CO layer. Figure 4(a) shows the amount of CO remaining in the irradiated films versus electron fluence for θ_{Cap} = 60, 100, and 200 ML. For these experiments, the films were irradiated at 100 K. The loss of CO, measured by the decrease in its integrated IRAS signal, reflects the contributions from all the non-thermal reaction channels. As θ_{Cap} increases, the reaction probability quickly decreases. For $\theta_{Cap} \geq$ 60 ML, the IRAS signal for CO decreases approximately linearly as the electron fluence increases. The solid lines in Fig. 4(a) show the best-fit lines for each coverage. For θ_{Cap} < 50 ML, the CO signal decreases approximately exponentially versus electron

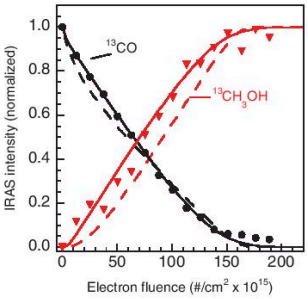

FIG. 3. Integrated CO (black circles) and CH_3OH (red triangles) IRAS signals versus electron fluence for θ_{cap} = 60 ML and T_{irr} = 100 K. The solid and dashed lines are simulated CO and CH_3OH concentrations for two different sets of reactions probabilities (see text).

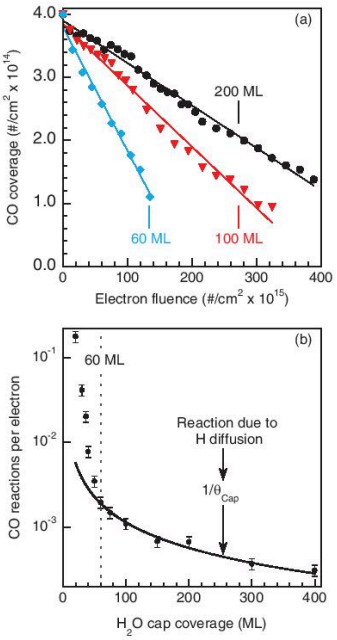

FIG. 4. (a) Remaining CO coverage versus electron fluence in irradiated CO/ASW films for $\theta_{Cap} = 60$, 100, and 200 ML and $T_{irr} = 100$ K. (b) CO reactions per incident electron (the reaction probability) versus θ_{Cap}. For $\theta_{Cap} \geq 60$, the reaction probability is inversely proportional to θ_{Cap}.

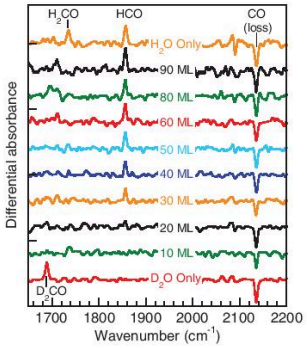

FIG. 5. Differential IRAS spectra for electron-irradiated CO/ASW films with various isotopic compositions for the water. For each spectrum, the thickness of the H_2O cap layer is listed with the spectra. The schematic in Fig. 6(a) illustrates the isotopic layering used for these experiments. Each film was irradiated at 90 K with an electron fluence of 6.5×10^{15} #/cm^2. For a CO/D_2O film (bottom curve), deuterated formaldehyde (D_2CO) is observed. For a CO/H_2O film (top curve), both HCO and formaldehyde (H_2CO) are observed. For films with increasing amounts of H_2O in the 100 ML cap layer, the amount of HCO gradually increases.

fluence, while for 50 ML $< \theta_{Cap} <$ 60 ML, the data can be fit with a combination of linear and exponential decays (data not shown). The number of CO reactions per incident electron can be obtained from the best fit (exponential or linear) for each coverage (Fig. 4(b), circles). For $\theta_{Cap} \geq 60$ ML, the reaction probability is inversely proportional to θ_{Cap} (Fig. 4(b), solid line). Because the probability for a particle to diffuse a distance L into a film falls as 1/L, the results in Fig. 4(b) suggest that, for $\theta_{Cap} \geq 60$ ML, reactants produced by the incident electrons near the ASW/vacuum interface diffuse into the ASW film and initiate the reactions with the buried CO layer.

For CO coadsorbed with water, previous research[37,41,42] and the results presented here suggest that sequential hydrogenation reactions lead to the formation of HCO, CH_2O, and CH_3OH. For the experiments where the CO is located below the typical penetration depth of the energetic electrons, the reaction mechanism is not immediately clear. One possibility is that hydrogen atoms produced by electronic excitations within the penetration depth of the energetic electrons subsequently diffuse through the ASW, producing the observed reactions. However, previous experiments investigating the electron-stimulated reactions that produce molecular hydrogen at buried ASW/Pt(111) interfaces have indicated that hydrogen atom diffusion is not the dominant mechanism in that case.[16,19] To test for hydrogen atom diffusion, we performed experiments where the isotopic composition of the ASW cap layer was varied. For the experiments shown in Fig. 5, a 30 ML D_2O film was deposited on Pt(111) at 100 K, and CO was dosed at T < 30 K. The CO was then covered with a layer of D_2O followed by a H_2O layer where the total cap layer coverage was fixed at 100 ML, but the amount of each isotope was varied (see schematic in Fig. 6(a)). Figure 5 shows the IRAS spectra for various amounts of H_2O in the 100 ML cap.[66] For a pure H_2O film, positive peaks at 1856 cm^{-1} and 1734 cm^{-1} are observed corresponding to HCO and CH_2O. For a pure D_2O film, there is a peak at 1688 cm^{-1} due to CD_2O, but no peak for DCO. (However, a previous matrix isolation experiment found that the C–O stretch in DCO was considerably weaker than in HCO.[64]) As the fraction of H_2O in the cap layer increases, the 1856 cm^{-1} peak for HCO quickly increases. Figure 6(a) shows the integrated intensity of the HCO peak normalized to the signal for a pure H_2O film versus the H_2O coverage in the cap layer. The HCO signal is approximately zero for $\theta(H_2O) \leq 10$ ML and then smoothly increases to its maximum value for 10 ML $< \theta(H_2O) <$ 60 ML. These results with layered H_2O/D_2O films indicate that hydrogenation of the buried CO is most likely associated with the H (or D) atoms primarily produced in the region from ~10 to 50 ML below the ASW/vacuum interface. Subsequent diffusion can transport the H atoms to the buried CO layer, leading to the observed hydrogenation reactions. The current results are distinct from earlier experiments investigating the electron-stimulated production of molecular hydrogen in layered H_2O/D_2O films.[16,19,52] In those experiments, molecular hydrogen produced at interface between the substrate and the

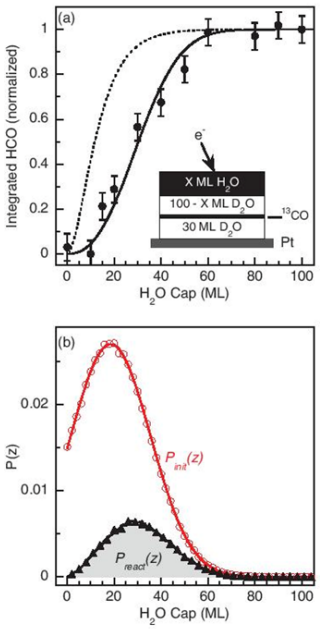

FIG. 6. (a) Integrated HCO IRAS signal (circles) versus the amount of H_2O in the 100 ML ASW cap. The films were irradiated at 100 K. The solid and dashed lines show integrated reaction probabilities for models with two different initial spatial distributions of hydrogen atoms (see text). The schematic illustrates the isotopic composition of the ASW films. (b) $P_{init}(z)$ (red circles) and $P_{react}(z)$ (black triangles) show the probability distributions of initial positions for all the hydrogen atoms and those that subsequently react with the buried CO layer, respectively. Because most of the H atoms diffuse to the ASW/vacuum interface and desorb, $P_{react}(z)$ is smaller than $P_{init}(z)$ and its maximum is shifted deeper into the ASW (see text for discussion).

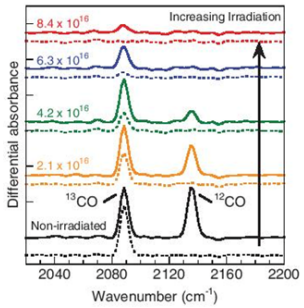

FIG. 7. Differential IRAS spectra for electron-irradiated ASW films with one (dashed lines) or two (solid lines) buried CO layers. For the experiments with two CO layers, the ^{12}CO and ^{13}CO layers were separated by 10 ML of ASW and capped with 60 ML of ASW (see inset of Fig. 8 for a schematic). The electron fluences (#/cm^2) for each experiment are shown in the figure. When two CO layers are present, the layer that is closer to the vacuum interface (i.e., ^{12}CO) reacts first, while the deeper (^{13}CO) layer is initially unchanged.

ASW films was not due to diffusion of H (or D) atoms through the ASW. Instead, a species that moved through the ASW without long range transport of the hydrogen atoms, such as hydronium ions or excitons, was implicated.[16,19,52]

As a further test for diffusion of H atoms within the ASW films, we performed experiments with two spatially separated and isotopically labeled layers of CO within the ASW films (Figs. 7 and 8). For these experiments a 60 ML ASW film was deposited on Pt(111) followed by a ^{13}CO layer, a 10 ML ASW layer, a ^{12}CO layer, and finally a 60 ML ASW layer (see schematic in Fig. 8). The films were then irradiated with 100 eV electrons at 110 K. The experiments were repeated with various coverages for the ^{12}CO and ^{13}CO layers. When no ^{12}CO is present, the ^{13}CO IRAS signal quickly decreases as the electron fluence increases (Fig. 7, dotted lines). With ^{12}CO present (Fig. 7, solid lines), the ^{13}CO signal initially decreases slowly while the ^{12}CO signal quickly decreases. Once a substantial fraction of the ^{12}CO has reacted, the ^{13}CO signal then decreases more quickly. Figure 8 (symbols) shows the integrated ^{13}CO and ^{12}CO IRAS signals versus electron fluence for several different coverages of the ^{12}CO and ^{13}CO layers. The number of reactions per electron for the ^{12}CO layer, which is closer to the vacuum, is independent of the coverage in the ^{13}CO layer. For example, the solid red and open red circles in Fig. 8 show the ^{12}CO coverage versus electron fluence for $\theta(^{13}CO) = 0$ and 4×10^{14} #/cm^2, respectively. In contrast, the reaction probability for the more deeply buried ^{13}CO layer is sensitive to $\theta(^{12}CO)$: As $\theta(^{12}CO)$ increases, the onset for appreciable reactions in the ^{13}CO layer increases (Fig. 8). These results also show that the H atoms come from the region near the vacuum interface and preferentially react with the first CO layer they encounter within the ASW film.

The experiments in Figs. 7 and 8 show that for $\theta(^{12}CO) > 1 \times 10^{14}$ #/cm^2, almost none of the hydrogen atoms can initially pass that layer to react with the deeper ^{13}CO layer. One possible explanation for these results is that the ^{12}CO layer physically blocks H atom diffusion to the deeper ^{13}CO layer. However, when the ^{12}CO layer is replaced with a Kr layer ($\theta(Kr) \sim 4 \times 10^{14}$ #/cm^2), the ^{13}CO decreases at the same rate as when no Kr or ^{12}CO is present (Fig. 8, black circles). Therefore, physical blocking does not appear to explain the results, and instead reactions with the first CO layer consume the hydrogen atoms.

The reaction probability for CO depends on the irradiation temperature. Figure 9 shows the CO reactions per electron for experiments at several temperatures with $\theta_{Cap} = 100$ ML. The CO reaction probability was determined from the decrease in the CO IRAS signal versus electron fluence at each temperature. For temperatures below ~70 K and $\theta_{Cap} = 100$ ML, the reaction probability is small and difficult to measure. For T > 70 K, the CO reaction probability increases approximately exponentially as the irradiation temperature increases with an apparent activation energy of ~5.4 kJ/mol. Experiments with H_2O and D_2O did not show an appreciable isotope effect, and the results shown in Fig. 9 include

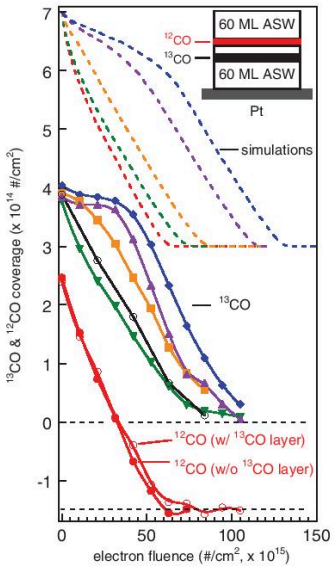

FIG. 8. ^{12}CO and ^{13}CO coverages versus electron fluence for experiments with two CO layers separated by 10 ML (see schematic). Bottom curves: Solid red and open red circles show the ^{12}CO signals for $\theta(^{13}\text{CO}) = 0$ and 4×10^{14} #/cm^2, respectively. Middle curves: ^{13}CO signals versus fluence for $\theta(^{12}\text{CO}) = 0$, 0.8, 2.8, and 4×10^{14} #/cm^2 (green, orange, purple, and blue symbols, respectively). When the ^{12}CO layer is replaced with a Kr layer (with $\theta(\text{Kr}) \sim 4 \times 10^{14}$ #/cm^2), the ^{13}CO signal promptly decreases when irradiated (black circles). The solid lines are added to guide the eye. Top curves: Simulated ^{12}CO (red) and ^{13}CO signals (green, orange, purple, and blue dashed lines) versus electron fluence for various initial ^{12}CO coverages. For ease of viewing, the bottom and top set of curves have been offset from 0 by -1.5×10^{14} #/cm^2 and 3.0×10^{14} #/cm^2, respectively.

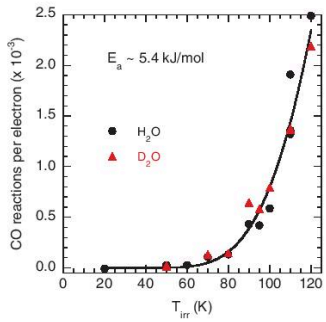

FIG. 9. CO reactions per electron versus irradiation temperature. CO layers capped with 100 ML H_2O (black circles) or D_2O (red triangles) films were irradiated at various temperatures and the depletion of the CO signal versus electron fluence was measured using IRAS. The initial CO coverages were 3.4×10^{14} #/cm^2. The results for H_2O and D_2O films are the same within the uncertainty.

both isotopes. Several processes could contribute to the temperature dependence of the reactions including the production of hydrogen atoms, their diffusion rate, and changes in the reaction probability (per encounter) with CO or its hydrogenation products. As a result, it is difficult to assign the measured activation energy to a single process. For example, previous research has found that non-thermal reactions in ASW, producing species such as H, H_2, and O_2, increase rapidly above 70 K.[8,54,62,67,68] However, the probability of overcoming the H + CO reaction barrier (~4.4 kJ/mol[46]) on any given encounter also increases as the temperature increases. This could also lead to increases in the overall reaction probability.[69] Thus, both increased production of H atoms and increases in the reaction probability per encounter are likely to contribute to the results shown in Fig. 9. Note that the results suggest that H/D isotope effects were not significant for the experiments with layered D_2O and H_2O films (Figs. 5 and 6).

One possible explanation for the reduced reaction probability at low temperatures shown in Fig. 9 is a decrease in H (or D) diffusion rate. In that scenario, the CO reaction probability would decrease at lower temperatures because the H atoms do not have sufficient time to reach the buried CO layer (i.e., the H atoms become "frozen" in the ASW). If that were the case, introducing a time delay between the electron irradiation and subsequent measurement of the IRAS signal should affect the results, particularly at temperatures where the reaction probability first becomes appreciable (~70–80 K in our experiments). However, experiments where such a delay time was introduced did not affect the results (data not shown), suggesting that a decrease in the H or D atom diffusion rate at lower temperatures was not primarily responsible for the decreasing CO reaction probability seen in Fig. 9.

Estimates of the time required for an atom to diffuse to the buried CO layer as a function of the temperature also indicate that changes in the H or D diffusion rate are not primarily responsible for the results in Fig. 9. The key point is that once the particles can diffuse far enough to reach the buried layer on the timescale of the experiments, further increases in the diffusion rate will not result in more reactions per incident electron. Using the diffusion rates measured by Bartels and co-workers,[70] we can estimate the time required for a H atom to diffuse from the region near the surface to the CO layer 100 ML below the surface: Since the hopping rate for both H and D in crystalline ice is ~10^4 jumps/s at 70 K,[71] the time to diffuse to the CO layer should only be ~1 s, which is already fast on the timescale of our experiments. Thus, at temperatures above ~70 K, the H and D atoms are already sufficiently mobile to reach the buried CO layer on the timescale of our experiments, and further increases in the diffusion rate will not lead to more reactions. This supports the observation that adding a waiting time after the irradiation did not change the results in Fig. 9. The activation energy for the results in Fig. 9 is approximately half the activation energy measured by Bartels *et al.*, for the diffusion of H or D atoms in crystalline ice.[70] If the activation energy for H diffusion in ASW is lower than

in crystalline ice, then the H and D atoms will become mobile at even lower temperatures, and thus will also not explain the observations.

Previous research has investigated the diffusion of H atoms on the surface of ASW at low temperatures (e.g., T $\leq$ 20 K).[42,44,46] Calculations suggest that H diffusion in ASW is slow enough that it does not play a role in the hydrogenation reactions for T $\leq$ 20 K. Instead it was suggested that surface diffusion, including the surfaces of cracks in the ASW, is important.[46] The H atom diffusion rate estimated above also suggests that any H atoms produced by the energetic electrons at temperatures below ~40–50 K will be frozen in the ASW in our experiments. However, since the reaction probability is small for T < 70 K, the results in Fig. 9 provide no further information on the mobility of the H atoms at these lower temperatures.

IV. DISCUSSION AND RANDOM WALK MODEL

Several species are detected in the irradiated films. For θ_{Cap} > 50 ML, HCO, CH_2O, and CH_3OH all are observed in the IRAS spectra while little or no CO_2 is observed. For θ_{Cap} < 50 ML, both reduced and oxidized reaction products are observed. The separation of the CO reactions into regions with both oxidation and reduction for θ_{Cap} < 50 ML and only reduction for θ_{Cap} > 50 ML probably results from different mobilities for the reducing species (primarily H atoms) versus the oxidizing species within the ASW films. As a result, the CO reactions provide a method for investigating the distribution of water dissociation events versus distance within the ASW films. The oxidation reactions occurring for CO trapped near the vacuum interface, and the distribution of water dissociation events will be the subject of a future publication. Here, we will concentrate on the CO reduction occurring in films with θ_{Cap} > 50 ML.

As discussed in the Introduction, previous research suggests that the production of methanol during the irradiation of mixed H_2O/CO ices proceeds by the sequential hydrogenation of CO (reactions 2–5),[37,41,42] and the experiments reported here are generally consistent with this hypothesis. In the gas phase, the calculated barrier for the reaction, CO + H → HCO, is ~17 kJ/mol.[72,73] Therefore, it has been assumed that the reaction occurs when energetic H atoms, produced from H_2O dissociation, collide with a CO. However, the current results show that thermalized H atoms diffusing through the ASW react efficiently with trapped CO. Recent experiments where H and CO were co-deposited in a neon matrix at T < 10 K have also demonstrated that thermalized H can react with CO.[43] Calculations suggest that tunneling can result in relatively efficient reactions even at temperatures where above-barrier reactions would be slow.[74] For CO trapped in ASW films, cage effects – which keep the H + CO next to each other for longer times – should promote the reaction by allowing sufficient time for tunneling to occur. Because we do not detect any appreciable difference in the reaction probability for CO trapped in H_2O or D_2O (Fig. 9), isotope effects do not appear to be important for these experiments.

A. Random Walk Model

To further explore the reaction of CO trapped in ASW with H atoms, we have developed a simple Monte Carlo diffusion model. The model is based upon the assumption that H atoms are produced by the interactions of the energetic electrons with water molecules in the ASW films (e.g., reaction 1), and once produced, these atoms can then diffuse through the film until they react. The possible reactions included in our model are (1) sequential hydrogenation of CO (i.e., reactions 2–5), (2) desorption from the film if the H atom reaches the ASW/vacuum interface, or (3) adsorption on the Pt(111) if it reaches the ASW/Pt interface. In the model, the diffusion of the H atoms takes place on a simple cubic lattice, where each layer of the ASW film, i, is represented by a plane ($z = i$) in the lattice, and the system has periodic boundary conditions in the x and y directions. The CO layers are assumed to occupy a plane that is parallel to the ASW/Pt interface at a position corresponding to θ_{Cap} for the experiment of interest (see Fig. S3 in the supplementary material[84]).

In the model, lateral coordinates (i.e., x and y) are randomly chosen for the CO adsorption sites until a desired CO coverage is obtained. The CO and its reaction products are assumed to be immobile. Initial lateral coordinates for the H atoms are also chosen at random, while the initial z, z_0, can be chosen from a specified distribution, $P_{init}(z_0)$. H atom trajectories are run sequentially and the atoms perform a random walk on the lattice until they react. If the atom encounters a site occupied with CO, HCO, CH_2O, or CH_3O, it reacts with a specified probability. If the atom does not react, it continues the random walk. The reaction sequence is assumed to stop at methanol. If an H atom reaches either interface of the film, it reacts (i.e., desorbs into vacuum or adsorbs on the Pt) with unit probability. H atom trajectories are run until all the CO is converted to CH_3OH. An advantage of this model over a mean-field chemical kinetics model is that it allows us to explicitly treat the position of the CO layer (or layers) relative to the source of the H atoms.

We have used this simple model to investigate several of the experimental observations: (i) the ~$1/\theta_{Cap}$ decrease in the CO reaction probability (Fig. 4(b)), (ii) the distribution of the initial positions for the H atoms that participate in the hydrogenation reactions (Fig. 6(a)), (iii) the nearly linear decrease in the CO signal versus electron fluence (Figs. 3 and 4(a)), and (iv) the delay in the loss of the more deeply buried CO layer in the two CO layer experiments (Figs. 7 and 8). Some of these observations depend sensitively upon the assumption of sequential hydrogenation reactions and their reaction probabilities, while others are largely independent of these details. For example, the model reproduces the $1/\theta_{Cap}$ dependence for the CO reaction probability seen in Fig. 4(b) because for any given $P_{init}(z_0)$ that is localized near the vacuum interface, the probability of the atoms randomly walking to a depth of z in the film is proportional to $1/z$ (results not shown).

B. Initial distribution of H atoms

The experiments shown in Figs. 5 and 6(a) provide information on the distribution of the initial positions of H

atoms within the ASW films that subsequently react with the CO layer, $P_{\mathrm{react}}(z_0)$. Specifically, the results in Fig. 6(a) correspond to the normalized integral of $P_{\mathrm{react}}(z_0)$ versus z_0: $I(z_0) = \int_0^{z_0} P_{react}(z')dz'$. Note, however, that $P_{\mathrm{react}}(z_0)$ is different than $P_{\mathrm{init}}(z_0)$ because atoms that are created closer to the vacuum interface are more likely to reach that interface and desorb from the film, while those that are created deeper in the film are more likely to reach the CO layer. The probability for an atom created at a depth, z_0, to diffuse to a CO layer buried at θ_{cap}, $P_{\mathrm{diff}}(z_0)$, is $P_{\mathrm{diff}}(z_0) = z_0/\theta_{\mathrm{Cap}}$. Therefore, $P_{\mathrm{react}}(z_0) = z_0 P_{\mathrm{init}}(z_0)/\theta_{\mathrm{cap}}$.[75] Previous simulations of the interaction of 100 eV electrons with water suggest that the initial excitations have an approximately exponential distribution, $P_{init}(z_0) = \alpha e^{-\alpha z_0}$, with $1/\alpha \sim 7$ ML (i.e., about 2.7 nm).[48] With this distribution of initial positions, the simulation does not reproduce the results (Fig. 6(a), dashed line). Specifically, in the experiments essentially none of the H atoms that react with the buried CO layer originate from the first 10 ML of the film, while almost half the H atoms come from that region in the simulation. Thus, the simulations suggest that the H atoms that react with the buried CO layer originate deeper within the film.

A distribution of initial positions, $P_{\mathrm{init}}(z_0)$, that peaks in the near surface region can better reproduce the experimental results in Fig. 6(a). For example, Fig. 6(b) shows $P_{\mathrm{react}}(z_0)$ (black triangles) for a simulation where $P_{\mathrm{init}}(z_0)$ is assumed to be a Gaussian distribution, $P_{init}(z_0) = \exp(-(z_0 - \mu)^2/2\sigma^2)/(\sigma\sqrt{2\pi})$, with $\mu = 18$ ML and $\sigma = 17$ ML (red circles). $P_{\mathrm{react}}(z_0)$ is also approximately Gaussian but the maximum is shifted deeper within the film ($\mu \sim 28$ ML). $I(z_0)$ obtained with this form of $P_{\mathrm{init}}(z_0)$ reproduces the experimental results reasonably well (Fig. 6(a), solid line).

The difference between the distribution of initial electronic excitations expected from theory and the $P_{\mathrm{react}}(z_0)$ that fits the data could have several causes. As illustrated in Fig. 6(b), part of the difference is likely due to the preferential desorption of H atoms created near the vacuum interface. However, this effect does not appear to be responsible for most of the difference. Another possibility is that H atoms can react with other species created in the ASW film by the energetic electrons. For example, H atoms can recombine with OHs created by the dissociation of H_2O. Since the concentration of OHs should be highest near the vacuum interface, the recombination probability should also be higher there, decreasing the chance that H atoms escape that region. A third possibility is that the initial excitation produces a mobile species that moves prior to creating a hydrogen atom. For example, H_2O^+ quickly reacts to form H_3O^+ which can move through the film via proton hopping.[3,76] Subsequent reactions with an electron can then produce a H atom in a different location from the initial excitation. Mobile excitons, H_2O^*,[77,78] produced by the energetic electron in the ASW can also dissociate to produce H and OH.[51,67,79,80] Interestingly, the form of $P_{\mathrm{react}}(z_0)$ that fits the experimental results presented here is qualitatively similar to previous experiments investigating the production of molecular hydrogen in electron-irradiated ASW films adsorbed on Pt(111) or TiO_2(110).[16,19,52] Those experiments also indicated that the location of the initial electronic excitations was different from the subsequent reactions that caused hydrogenation of the substrate. For both the current and the previous experiments, the length scales characterizing the processes are similar (i.e., ~10 nm), while the specific reactions are different.

C. Reaction probabilities

In the random walk model, the reaction kinetics (i.e., amounts of CO, HCO, etc. versus electron fluence) are largely determined by the reaction probabilities for the H atoms with each species, but are relatively insensitive to the assumed form for $P_{\mathrm{init}}(z_0)$. Experimentally, the amount of CO in a single layer decreases approximately linearly and the amount of methanol increases approximately linearly as the electron fluence increases (see Fig. 3), while the amount of the intermediate species is always small. Within the random walk model, this behavior can be reproduced if the reaction probability for H atoms with CO, P_{CO}, (Eq. (2)) is significantly smaller than the reaction probability for the other hydrogenation steps, P_{HnCO}, (Eqs. (3)–(5)). The solid lines in Fig. 3 show an example where $P_{\mathrm{CO}} = 0.02$, and $P_{\mathrm{HnCO}} = 1$ for $n = 1$, 2, and 3. However, a very low reaction probability for H with CO is problematic for two reasons. First, it is inconsistent with the experiments with two CO layers where the CO layer closest to the vacuum reacts preferentially with the H atoms (see Figs. 7 and 8). Specifically, if P_{CO} is too small, then the first CO layer becomes "transparent" to the H atoms and both CO layers decrease at nearly the same rate in the simulations. Second, the calculated gas-phase barriers for H + CO and H + CH_2O are comparable,[81] suggesting that their reaction probabilities should be similar.[82] In that case, we should expect that the amount of CH_2O will be comparable to the amount of CO in the irradiated films at intermediate electron fluences. This is not observed however: The amount of CH_2O in the irradiated films is always small during the experiments (see, e.g., Fig. 2), which suggests that $P_{\mathrm{CO}} < P_{\mathrm{H2CO}}$. To further investigate this issue, we performed experiments where we deposited a buried CH_2O layer in ASW and measured the loss of the CH_2O IRAS signal versus electron fluence (see Fig. S4 in the supplementary material[84]). Compared to a CO layer buried at the same depth, the CH_2O signal decreases with an initial rate that is ~7 times greater than the CO signal, indicating that the reaction probability for H + CH_2O is much larger than for H + CO.

The dashed lines in Figs. 3 and 8 show the simulations for the one and two layer experiments where $P_{\mathrm{CO}} = 0.1$, and $P_{\mathrm{HnCO}} = 1$ for $n = 1$, 2, and 3 (for both ^{12}CO and ^{13}CO). These probabilities represent a "best fit" for the experimental results in Figs. 3 and 8.[83] These best-fit probabilities are also consistent with results in Fig. S4 and the expectation that the radical reactions – H + HCO and H + CH_3O – are very efficient.[84] In Fig. 3, the simulation is similar to the experiments, but the methanol signal has a short induction period before it starts increasing that does not appear in the data, and the decrease in the simulated CO signal is not as linear as the experimental result. However, with these reaction probabilities and simulations with two CO layers, the initial rate of decrease for the deeper CO layer is larger than is observed in the experiments (Fig. 8, dashed lines). An even larger value

for P_{CO} results in a slower initial reaction rate for the second CO layer, but the larger induction period before methanol appears is inconsistent with the experiments (Fig. 3). Despite these short-comings, the model qualitatively reproduces the experimental results.

The random walk model presented here is too simple to capture all the processes that might be relevant for the experiments. For example, the energetic electrons produce a variety of reactive species within the ASW and any possible reactions between these species have not been included in the model. As mentioned above, such reactions could influence the form of $P_{init}(z)$ that fits the data in Fig. 6. Likewise, the model does not include several alternative reactions, such as $H + HCO \rightarrow H_2 + CO$ and $H + CH_2O \rightarrow H_2 + HCO$, that may also occur.[81] To get some idea of the sensitivity of the model results, we have tested several variations of the model including different reaction sequences, back reactions, possible blocking effects of the reactants on the H diffusion, the effect of broadening the CO layer(s) within the ASW, etc. Most of the model variants produce qualitatively similar results to the simplest model presented above. However, lacking specific data to motivate and constrain more complicated models, we feel that more detailed investigations of such models are not currently justified.

V. SUMMARY

We have investigated the electron-stimulated reactions of CO in amorphous solid water. For CO buried within 50 ML of the ASW/vacuum interface, both oxidation and reduction of the CO are observed. However, for CO buried more deeply in the film, only reduction reactions are observed. For films with CO buried under more than 50 ML of ASW, the observations are consistent with the sequential hydrogenation of CO to methanol due to hydrogen atoms. The H atoms are produced by electron-stimulated reactions in the ASW from ~10–50 ML and subsequently diffuse through the ASW where they can react with trapped CO (or one of its reaction products). A simple kinetic model which treats the diffusion of H atoms through the ASW film and the sequential hydrogenation of CO to methanol accounts for most of the observations.

ACKNOWLEDGMENTS

N.G.P. and G.A.K. were supported by the US Department of Energy (USDOE), Office of Basic Energy Sciences, Division of Chemical Sciences, Geosciences & Biosciences. R.J.M. and S.P.K.K. were supported by the Dalton Cumbrian Facility program in part funded by the Nuclear Decommissioning Authority. The work was performed using EMSL, a national scientific user facility sponsored by the Department of Energy's Office of Biological and Environmental Research and located at Pacific Northwest National Laboratory (PNNL). PNNL is a multiprogram national laboratory operated for DOE by Battelle under Contract No. DE-AC05-76RL01830.

[1]Farhataziz and M. A. J. Rodgers, *Radiation Chemistry: Principles and Applications* (VCH Publishers, New York, 1987), p. 641.
[2]B. Boudaïffa, P. Cloutier, D. Hunting, M. A. Huels, and L. Sanche, Science **287**, 1658 (2000).
[3]B. C. Garrett, D. A. Dixon, D. M. Camaioni, D. M. Chipman, M. A. Johnson, C. D. Jonah, G. A. Kimmel, J. H. Miller, T. N. Rescigno, P. J. Rossky, S. S. Xantheas, S. D. Colson, A. H. Laufer, D. Ray, P. F. Barbara, D. M. Bartels, K. H. Becker, H. Bowen, S. E. Bradforth, I. Carmichael, J. V. Coe, L. R. Corrales, J. P. Cowin, M. Dupuis, K. B. Eisenthal, J. A. Franz, M. S. Gutowski, K. D. Jordan, B. D. Kay, J. A. LaVerne, S. V. Lymar, T. E. Madey, C. W. McCurdy, D. Meisel, S. Mukamel, A. R. Nilsson, T. M. Orlando, N. G. Petrik, S. M. Pimblott, J. R. Rustad, G. K. Schenter, S. J. Singer, A. Tokmakoff, L. S. Wang, C. Wittig, and T. S. Zwier, Chem. Rev. **105**(1), 355–389 (2005).
[4]A. Fujishima, X. T. Zhang, and D. A. Tryk, Surf. Sci. Rep. **63**(12), 515–582 (2008).
[5]P. Rowntree, L. Parenteau, and L. Sanche, J. Chem. Phys. **94**(15), 8570 (1991).
[6]G. A. Kimmel, T. M. Orlando, C. Vezina, and L. Sanche, J. Chem. Phys. **101**(4), 3282 (1994).
[7]M. S. Westley, R. A. Baragiola, R. E. Johnson, and G. A. Baratta, Planet. Space Sci. **43**(10-11), 1311–1315 (1995).
[8]M. S. Westley, R. A. Baragiola, R. E. Johnson, and G. A. Baratta, Nature (London) **373**(6513), 405–407 (1995).
[9]G. A. Kimmel, R. G. Tonkyn, and T. M. Orlando, Nucl. Instrum. Methods, Phys. Res. B **101**, 179 (1995).
[10]G. A. Kimmel and T. M. Orlando, Phys. Rev. Lett. **77**, 3983 (1996).
[11]G. A. Kimmel, T. M. Orlando, P. Cloutier, and L. Sanche, J. Phys. Chem. B **101**(32), 6301–6303 (1997).
[12]M. T. Sieger, W. C. Simpson, and T. M. Orlando, Nature (London) **394**(6693), 554–556 (1998).
[13]W. C. Simpson, T. M. Orlando, L. Parenteau, K. Nagesha, and L. Sanche, J. Chem. Phys. **108**(12), 5027–5034 (1998).
[14]D. A. Bahr, M. Fama, R. A. Vidal, and R. A. Baragiola, J. Geophys. Res.-Planets **106**(E12), 33285 (2001).
[15]R. A. Baragiola, Planet. Space Sci. **51**(14-15), 953–961 (2003).
[16]N. G. Petrik and G. A. Kimmel, Phys. Rev. Lett. **90**(16), 166102 (2003).
[17]S. Yamamoto, A. Beniya, K. Mukai, Y. Yamashita, and J. Yoshinobu, Chem. Phys. Lett. **388**(4–6), 384–388 (2004).
[18]X. Pan, A. D. Bass, J. P. Jay-Gerin, and L. Sanche, Icarus **172**, 521 (2004).
[19]N. G. Petrik and G. A. Kimmel, J. Chem. Phys. **121**(8), 3736–3744 (2004).
[20]W. J. Zheng, D. Jewitt, and R. I. Kaiser, Astrophys. J. **639**(1), 534–548 (2006).
[21]T. Hama, A. Yabushita, M. Yokoyama, M. Kawasaki, and S. Andersson, J. Chem. Phys. **131**(5), 054508 (2009).
[22]T. Hama, A. Yabushita, M. Yokoyama, M. Kawasaki, and N. Watanabe, J. Chem. Phys. **131**(11), 114510 (2009).
[23]T. Hama, A. Yabushita, M. Yokoyama, M. Kawasaki, and N. Watanabe, J. Chem. Phys. **131**(11), 114511 (2009).
[24]J. D. Thrower, A. G. M. Abdulgalil, M. P. Collings, M. R. S. McCoustra, D. J. Burke, W. A. Brown, A. Dawes, P. J. Holtom, P. Kendall, N. J. Mason, F. Jamme, H. J. Fraser, and F. J. M. Rutten, J. Vacuum Sci. Technol. A **28**(4), 799–806 (2010).
[25]T. Hama, M. Yokoyama, A. Yabushita, M. Kawasaki, S. Andersson, C. M. Western, M. N. R. Ashfold, R. N. Dixon, and N. Watanabe, J. Chem. Phys. **132**(16), 164508 (2010).
[26]W. Zheng and R. I. Kaiser, J. Phys. Chem. A **114**(16), 5251–5255 (2010).
[27]C. J. Bennett, T. Hama, Y. S. Kim, M. Kawasaki, and R. I. Kaiser, Astrophys. J. **727**(1), 27 (2011).
[28]W. Zheng, Y. S. Kim, and R. I. Kaiser, Phys. Chem. Chem. Phys. **13**(35), 15749–15754 (2011).
[29]J. D. Thrower, M. P. Collings, F. J. M. Rutten, and M. R. S. McCoustra, Chem. Phys. Lett. **505**(4-6), 106–111 (2011).
[30]A. Yabushita, T. Hama, and M. Kawasaki, J. Photochem. Photobiol. C-Photochem. Rev. **16**, 46–61 (2013).
[31]R. E. Johnson and T. I. Quickenden, J. Geophys. Res., [Planets] **102**(E5), 10985–10996, doi:10.1029/97JE00068 (1997).
[32]T. E. Madey, R. E. Johnson, and T. M. Orlando, Surf. Sci. **500**, 838 (2002).
[33]N. Watanabe and A. Kouchi, Prog. Surf. Sci. **83**(10-12), 439–489 (2008).
[34]C. J. Bennett, C. Pirim, and T. M. Orlando, Chem. Rev. **113**(12), 9086 (2013).
[35]E. Herbst and E. F. van Dishoeck, Annu. Rev. Astron. Astrophys. **47**, 427–480 (2009).
[36]E. F. van Dishoeck, E. Herbst, and D. A. Neufeld, Chem. Rev. **113**, 9043 (2013).
[37]R. L. Hudson and M. H. Moore, Icarus **140**(2), 451–461 (1999).

[38]K. I. R. Oeberg, E. F. van Dishoeck, H. Linnartz, and S. Andersson, Astrophys. J. **718**(2), 832–840 (2010).
[39]N. Watanabe and A. Kouchi, Astrophys. J. **567**(1), 651–655 (2002).
[40]L. J. Allamandola, S. A. Sandford, and G. J. Valero, Icarus **76**(2), 225–252 (1988).
[41]N. Watanabe, O. Mouri, A. Nagaoka, T. Chigai, A. Kouchi, and V. Pirronello, Astrophys. J. **668**(2), 1001–1011 (2007).
[42]N. Watanabe, T. Shiraki, and A. Kouchi, Astrophys. J. **588**(2), L121–L124 (2003).
[43]C. Pirim and L. Krim, Chem. Phys. **380**(1-3), 67–76 (2011).
[44]N. Watanabe and A. Kouchi, Astrophys. J. **571**(2), L173–L176 (2002).
[45]T. Hama and N. Watanabe, Chem. Rev. **113**(12), 8783–8839 (2013).
[46]Z. Awad, T. Chigai, Y. Kimura, O. M. Shalabiea, and T. Yamamoto, Astrophys. J. **626**(1), 262–271 (2005).
[47]G. W. Fuchs, H. M. Cuppen, S. Ioppolo, C. Romanzin, S. E. Bisschop, S. Andersson, E. F. van Dishoeck, and H. Linnartz, Astron. Astrophys. **505**(2), 629–639 (2009).
[48]S. M. Pimblott, J. A. LaVerne, and A. Mozumder, J. Phys. Chem. **100**(20), 8595–8606 (1996).
[49]M. P. Collings, J. W. Dever, H. J. Fraser, and M. R. S. McCoustra, Astrophys. Space Sci. **285**(3-4), 633–659 (2003).
[50]M. P. Collings, J. W. Dever, H. J. Fraser, M. R. S. McCoustra, and D. A. Williams, Astrophys. J. **583**(2), 1058–1062 (2003).
[51]G. A. Kimmel and T. M. Orlando, Phys. Rev. Lett. **75**(13), 2606 (1995).
[52]N. G. Petrik and G. A. Kimmel, J. Phys. Chem. C **113**(11), 4451–4460 (2009).
[53]R. S. Smith, N. G. Petrik, G. A. Kimmel, and B. D. Kay, Acc. Chem. Res. **45**(1), 33–42 (2012).
[54]N. G. Petrik, A. G. Kavetsky, and G. A. Kimmel, J. Phys. Chem. B **110**(6), 2723 (2006).
[55]N. G. Petrik, A. G. Kavetsky, and G. A. Kimmel, J. Chem. Phys. **125**(12), 124702 (2006).
[56]C. D. Lane, N. G. Petrik, T. M. Orlando, and G. A. Kimmel, J. Phys. Chem. C **111**(44), 16319 (2007).
[57]G. A. Kimmel, K. P. Stevenson, Z. Dohnálek, R. S. Smith, and B. D. Kay, J. Chem. Phys. **114**, 5284 (2001).
[58]K. P. Stevenson, G. A. Kimmel, Z. Dohnálek, R. S. Smith, and B. D. Kay, Science **283**, 1505 (1999).
[59]Z. Dohnálek, G. A. Kimmel, P. Ayotte, R. S. Smith, and B. D. Kay, J. Chem. Phys. **118**(1), 364 (2003).
[60]A. Al-Halabi, H. J. Fraser, G. J. Kroes, and E. F. van Dishoeck, Astron. Astrophys. **422**(3), 777–791 (2004).
[61]N. G. Petrik and G. A. Kimmel, J. Phys. Chem. Lett. **3**(23), 3425–3430 (2012).
[62]N. G. Petrik and G. A. Kimmel, J. Chem. Phys. **123**(5), 054702 (2005).
[63]M. Falk and E. Whalley, J. Chem. Phys. **34**(5), 1554 (1961).
[64]D. E. Milligan and M. E. Jacox, J. Chem. Phys. **41**(10), 3032–3036 (1964).
[65]B. Nelander, J. Chem. Phys. **72**(1), 77–84 (1980).
[66]In this case, the spectra are the difference between the irradiated film and the same film prior to irradiation. Therefore, the loss of CO is seen as a negative peak in the spectra.
[67]T. M. Orlando and G. A. Kimmel, Surf. Sci. **390**, 79 (1997).
[68]R. A. Baragiola, R. A. Vidal, W. Svendsen, J. Schou, M. Shi, D. A. Bahr, and C. L. Atteberrry, Nucl. Instrum. Methods, Phys. Res. B **209**, 294–303 (2003).
[69]Because a diffusing H atom can potentially visit many CO sites before diffusing away from the buried CO layer, changes in the probability per encounter lead to smaller changes in the overall reaction probability.
[70]D. M. Bartels, P. Han, and P. W. Percival, Chem. Phys. **164**, 421 (1992).
[71]See Figure 12 in Reference 70.
[72]D. E. Woon, J. Chem. Phys. **105**(22), 9921–9926 (1996).
[73]C. J. Bennett, C. S. Jamieson, Y. Osamura, and R. I. Kaiser, Astrophys. J. **624**(2), 1097–1115 (2005).
[74]S. Andersson, T. P. M. Goumans, and A. Arnaldsson, Chem. Phys. Lett. **513**(1-3), 31–36 (2011).
[75]In the simulations, the initial positions of the H atoms are chosen using $P_{\mathrm{ini}}(z_0)$ and $P_{\mathrm{react}}(z_0)$ is then determined from the initial positions of those particles that subsequently react with the CO layer. The simulated results agree with the simple analysis given here.
[76]V. F. Petrenko and R. W. Whitworth, *Physics of Ice* (Oxford University Press, Oxford, 1999).
[77]K. Kobayashi, J. Phys. Chem. **87**(21), 4317–4321 (1983).
[78]P. H. Hahn, W. G. Schmidt, K. Seino, M. Preuss, F. Bechstedt, and J. Bernholc, Phys. Rev. Lett. **94**(3), 037404 (2005).
[79]D. M. Chipman, J. Chem. Phys. **122**(4), 044111 (2005).
[80]D. M. Chipman, J. Chem. Phys. **124**(4), 044305 (2006).
[81]D. E. Woon, Astrophys. J. **569**(1), 541–548 (2002).
[82]The hydrogenation of the radical species, HCO and CH_3O (or CH_2OH), are expected to be barrierless. This corresponds to large reaction probabilities in the model, consistent with the model results.
[83]We simulated the reactions with various combinations of reaction probabilities.
[84]See supplementary material at http://dx.doi.org/10.1063/1.4878658 for more information on (a) the trapped fraction of CO vs θ_{Cap}, (b) IRAS spectra for irradiated films with $\theta_{\mathrm{cap}} = 60$ ML and $T_{\mathrm{irr}} = 100$ K, (c) a schematic of the random walk model, and (d) CH_2O IRAS signal vs electron fluence for $\theta_{\mathrm{cap}} = 75$ ML and $T_{\mathrm{irr}} = 100$ K.

References

[1] B. Boudaïffa, P. Cloutier, D. Hunting, M. A. Huels, and L. Sanche, *Science* **287**, 1658 (2000)

[2] M. H. Parajon, P. Rajesh, T. Mua, S. M. Pimblott, and J. A. LaVerne, *Radiation Physics and Chemistry* **77** (2008) 1203– 1207

[3] C. D. Jonah, S. Kapoor, M. S. Matheson, W. A. Mulac, D. Meisel, *"Gas Generation from Hanford Grout Samples"*, 94-7, Argonne National Laboratory, Argonne, IL (1994)

[4] D. R. McCracken, K. T. Tsang, and P. J. Laughton, *"Aspects of the Physics and Chemistry of Water Radiolysis by Fast Neutrons and Fast Electrons in Nuclear Reactors"* AECL-11895; Atomic Energy of Canada Ltd.: Mississauga, ON, Canada (1998)

[5] W. Zheng and R. I. Kaiser, *J. Phys. Chem. A*, **114**, 5251–5255 (2010)

[6] A. G. M. Abdulgalil, D. Marchione, A. Rosu-Finsen, M. P. Collings, and M. R. S. McCoustra, *Journal of Vacuum Science & Technology A*, **30**, 041505 (2012)

[7] B. C. Garret *et al*, *Chem. Rev.*, **105**, 371 (2005)

[8] P. A. Riley, *International Journal of Radiation Biology*, **65**, 27-33 (1994)

[9] M. Burton, *Journal of Physical and Colloid Chemistry*, **51**, 611-625 (1947)

[10] A. O. Allen, *Journal of Physical and Colloid Chemistry*, **52**, 479-490 (1948)

[11] I.G. Kaplan and A.M. Miterev, *Adv. Chem. Phys*., **68**, 255 (1987)

[12] T. Kai, A. Yokova, M. Ukai, K. Fujii, M. Higuchi, and R Watanabe, *Radiat, Phys. Chem*., **102**, 16-22 (2014)

[13] I. G. Draganic, Z. D. Draganic, "*The Radiation Chemistry of Water"*, Vol. 26, Academic Press, New York and London, (1971)

[14] Y. Itikawa and N. Mason, *Journal of Physical and Chemical Reference Data*, **34**, 1-22 (2005)

[15] A. H. Samuel and J. L. Magee, *J. Chem. Phys*, **21**, 1080-1087 (1953)

[16] J. Meesungnoen, J. P,. Jay-Gerin, A. Filali-Mouhim, S. Mankhetkorn, *Rad. Res.*, **158,** 657-660 (2002)

[17] A. Opitz, M. Scherge, S. I. U. Ahmed, and J. A. Schaefer, *J. App. Phys.*, **101**, (2007)

[18] R.S. Smith, C. Huang, E. K. L. Wong, and B. D. Kay, *Surface Science*, **367**, (1996)

[19] J. Herring-Captain, G. A. Grieves, A. Alexandrov, M. T. Sieger, H. Chen, T. M. Orlando, *Phys. Rev.B*, **72** (2005)

[20] N. G. Petrik and G. A. Kimmel, *J. Chem. Phys.*, **121**, 3736-3744 (2004)

[21] M. A. Henderson, *Langmui*r, **21**, 3443-3450 (2005)

[22] N. G. Petrik and G. A. Kimmel, *J. Chem. Phys*, **123**, 054702 (2005)

[23] N. G. Petrik, A. G. Kavetsky, and G. A. Kimmel, *J. Phys. Chem. B*, **110**, 2723-2731 (2006)

[24] W. Zheng, D Jewitt, and R. I. Kaiser, *Astrophys. J.*, **639**, 534-548 (2006)

[25] D. R. Flower and G. Pineau-Des-Forets, *MNRAS*, **247**, 500 (1990)

[26] A. Seibert, T. Gouderm and F. Huber, *Radiochim. Acta.*, **98**, 647-654 (2010)

[27] N.G. Petrik, A.B. Alexandrov, and A. I. Vall, *J. Phys. Chem. B.*, **105**, 5935-5944 (2001)

[28] W. Zheng, D. Jewitt, and R. I. Kaiser, *The Astrophysical Journal*, **639**, 534-548 (2006)

[29] M. H. Parajon, P. Rajesh, T. Mu, S. M. Pimblott, and J. A. LaVerne, *Radiat. Phys. Chem*, **77**, 1203-1207 (2008)

[30] N.G. Petrik and G. A. Kimmel, *J. Chem. Phys.*, **121**, 3736 (2004)

[31] N.G. Petrik and G. A. Kimmel, *J. Phys. Chem. C*, **113**, 4451 (2009)

[32] G. A. Kimmel, T. M. Orlando, C. Vezina, and L. Sanche, *J. Chem. Phys*, **101**, 3282 (1994)

[33] Y. Du, N. G. Petrik, N. A. Deskins, Z. Wang, M. A. Henderson, G. A. Kimmel and I. Lyubinetsky, *PCCP*, **14**, 3066–3074 (2012)

[34] N. G. Petrik, A. G. Kavetsky, and G. A. Kimmel, *J. Chem. Phys.*, **125**, 124702 (2006)

[35] S. A. Sandford, L. J. Allamandola, A. G. G. M. Tielens, and G. J. Valero, *Astrophysical Journal*, **329**, 498-510 (1988)

[36] S. B. Charnley, M. E. Kress, A. G. G. M. Tielens, and T. J. Millar, *Astrophysical Journal*, **448**, 232 (1995)

[37] D. C. B. Whittet *et al*, *Astrophysical Journal*, **490** 729 (1997)

[38] M. J. Mumma, M. A. DiSanti, N. Dello Russo, M. Fomenkova, K. Magee-Sauer, C. D. Kaminski, D. X. Xie, *Science*, **272**, 1310 (1995)

[39] L. Šiller, M. N. Hedhili, Y. Le Coat, R. Azria, and M. Tronc, *J. Chem. Phys.*, **110**, 10554-10561 (1999)

[40] L. Šiller, M. T. Sieger, and T. M. Orlando, *J. Chem. Phys.*, **118 (19)**, 8898-8904 (2003)

[41] M. C. Akin, N. G. Petrik, and G. A. Kimmel, *J. Chem. Phys.* **130**, 104710 (2009)

[42] G. A. Kimmel and T. M. Orlando, *Surface Sci.*, **390**, 79 (1997)

[43] K. Hiraoka, T. Sato, S. Sato, N. Sogoshi, T. Yokoyama, H. Takashima, and S. Kitagawa, *The Astrophysical Journal*, **577**, 265 (2002)

[44] N. Watanabe and A. Kouchi, *The Astrophysical Journal*, **571**, 173–176 (2002)

[45] H. Hidaka, N. Watanabe, T. Shiraki, A. Nagaoka, and A. Kouchi, *The Astrophysical Journal*, **614**, 1124 (2004)

[46] G. W. Fuchs, H. M. Cuppen, S. Ioppolo, C. Romanzin, S. E. Bisschop, S. Andersson,E. F. van Dishoeck, and H. Linnartz, *A&A*, **505**, 629–639 (2009)

[47] R. L. Hudson and M. H. Moore, *Icarus*, **140**, 451-461 (1999)

[48] S. Yamamoto, A. Beniya, K. Mukai, Y. Yamashita, and J. Yoshinobu, *Chem. Phys. Lett.*, **388**, 384-388 (2004)

[49] R. I. Kaiser and K. Roessler, *Ann. Geophys.*, **10**, 222-225 (1992)

[50] P. Atkins and J de Paula, "*Atkins' Physical Chemistry*", Ch. 13, 729-730, 8th Edn., Oxford University Press, (2006)

[51] K. Kobayashi, *J. Phys. Chem.*, **87**, 4317-4321 (1983)

[52] P. H. Hahn, W.G. Schmidt, K. Seino, M. Preuss, F. Berchstedt, and J. Bernholc, *Phys. Rev. Lett.*, **94**, 37404 (2005)

[53] D.M. Bartels, P. Han and P. W. Percival, *Chem. Phys.*, **164**, 421-437 (1992)

[54] J. P. Devlin, *J. Geophys. Res*, **106**, 33,333-33,349 (2012)

[55] R. S. Smith and B. D. Kay, *Nature*,**398**, 788-791 (1999)

[56] V. F. Petrenko and R. W. Whitworth, "*Physics of ice*", Ch. 6, 126-146, OUP, Oxford (1999)

[57] S. Goursaud, M. Sizun and F. Fiquet-Fayard, *J. Chem. Phys*, **65**, 5453 (1976)

[58] P. Rawat, V. S. Prabhudesai, G. Aravind, M. A. Rahman, and E Krishnakumar, *J. Phys. B*, **40,** 4625 (2007)

[59] C. A. F. Johnson, S. D. Kelly, J. E. Parker, *Chemical Physics Letters*, **116**, 30-34 (1985)

[60] M.G. Curtis and I. C. Walker, *J. Chem. Soc. Faraday Trans*, **88(19)**, 2805-2810 (1992)

[61] W. Sailer, A. Pelc, P. Limão-Vieira, N. J. Mason, J. Limtrakul, P. Scheier, M. Probst, T. D. Märk, *Chem. Phys. Lett*, **381**, 216–222 (2003)

[62] S. Denifl, P. Scheier, T. D. Mark, M. Probst, S. E. Huber, D. Gschliesser, P. Bartl, and V. Vizcaino, *Chem. Phys. Chem*, **12 (7)**, 1272-9 (2011)

[63] S. A. Pshenichnyuk and A. Modelli, *J. Chem. Phys*, **136**, 234307 (2012)

[64] W. W. Lozier, *Phys. Rev.***, 36**, 1417 (1930)

[65] D. S. Belic, M. Landau, and R. I. Hall, *J. Phys. B* **14,** 175-190 (1981)

[66] R. N. Compton and L. G. Christophorou, *Phys. Rev.*, **154**, 110 (1967)

[67] C. E. Melton, *J. Chem. Phys*., **57**, 4218-4225 (1972)

[68] M. Jungen, J. Vogt, and V. Staemmler, Chem. Phys., **37**, 49-55 (1979)

[69] *"Linking the Gaseous and Condensed Phases of Matter"* – ed. L. G. Christophorou, E. Illenberger and W. F. Schmidt, Ch. 1-5, NATO ISI Series B: Physics Vol. 326 (1993)

[70]R. N. Compton and I. G. Christophorou, *Phys. Rev.* **154**, 110-116 (1967)

[71] C. R. Claydon, G. A. Segal, and H. S. Taylor, *J. Chem. Phys.* **54**, 3799 (1971)

[72] N. B. Ram, V. S. Prabhudesai, E. Krishnakumar, *J. Phys. B*, **42** (2009)

[73] P. Rowntree, L. Parenteau and L. Sanche, *J. Chem. Phys.*, **94**, 8570-8576 (1991)

[74] Kimmel, Orlando, Vezina, and Sanche, *J. Chem. Phys*, **101**, 3282-3286 (1994)

[75] M. Michaud and L. Sanche, *Phys. Rev. Lett.*, **59**, 645 (1987)

[76] V. Cobut, J-P. Jay-Gerin, Y. Frongillo and J. P. Patau, *Radiat. Phys. Chem.*, **47**, 247-250 (1996)

[77] W.C. Simpson, L. Parenteau, R. S. Smith, L. Sanche, and T. M. Orlando, *Surf. Sci*, **390**, 86-91 (1997)

[78] C. E. Melton and G. A. Neece, *J. Chem. Phys.*, **55**, 4665 (1971)

[79] D. J. Haxton, C. W. McCurdy and T. N. Rescigno, *Phys. Rev. A* **75**, 012710 (2007)

[80] V. S. Prabhudesai, A. H. Kelkar, D. Nandi, and E. Krishnakumar, *Phys. Rev. Lett*, **95**, 143202

[81] A. D. Bass and L. Sanche, *Radiat. Environ. Biophys*, **37**, 243–257 (1998)

[82] I. S. Buchel'nikova, *Sov. Phys. JETP*, **35** 1119 (1959)

[83] F. H. Dorman, *J. Chem. Phys.* **44** 3854 (1966)

[84] R. N. Compton and L. G. Christophorou , *Phys. Rev.* **154** 111 (1967)

[85] A. W. Weiss, M. Krauss, *J. Chem. Phys*, **52**, 4363 (1970)

[86] S. Trajmar and R. I. Hall, *J. Phys. B: At. Mol. Phys*, 7, 458 (1974)

[87] A.Chutjian , R. I. Hall, and S. Trajmar, *J. Chem. Phys.* **63(2)** (1975) 892-898

[88] D. J. Haxton, Z. Y. Zhang, H. D. Meyer, T. N. Rescigno, and C. W. McCurdy, *Phys. Rev. A.***69** (2004)

[89] N. B. Ram, V. P. Prabhudesai, and E. Krishnakumar, *J. Chem. Sci.* **124**, 271-279 (2012)

[90] H. Adaniya, B. Rudek, T. Osipov, D. J. Haxton, T. Weber, T. N. Rescigno, C. W. McCurdy, and A. Belkacem, *Phys. Rev. Lett*, **103**, 233201 (2009)

[91] R. Azria, Y. Le Coat, G. Lefevre and D. Simon, *J. Phys. B: At. Mol. Phys.* **12** 679 (1979)

[92] J. Fedor, P.Cicman, B. Coupier, S. Feil, M. Winkler, K. Gluch, J. Husarik, D. Jaksch, B. Farizon, N. J. Mason, P. Sheier, and T. D. Märk, *J. Phys. B: At. Mol. Phys,* **39**, 3935-3944 (2006)

[93] G. J. Schulz, *J. Chem. Phys,* **33,** 1661 (1960)

[94] T. Harb, W. Kedzierski, J. W. McConkey, *J. Chem. Phys*, **115**, 5507-5512 (2001)

[95] L. G. Christophorou, R. N. Compton, G. S. Hurst, and P. Reinhard, *J. Chem. Phys*, **43**, 4273 (1965)

[96] R. N. Compton, L. G. Christophorou, *Phys. Rev*, **154**, 110 (1967)

[97] D. J. Haxton, T. N. Rescigno, C. W. McCurdy, *Phys. Rev. A*, **72** (2005)

[98] C. I. M. Beenakker, F. J. Deheer, H. B. Krop, and G. R. Mohlmann, *Chem. Phys*, **6**, 445-454 (1974)

[99] M. Allan and S. F. Wong, *J. Chem. Phys*, **74**, 1687-1691 (1981)

[100] J. N. Bardsley and J. M. Wadehra, *Phys. Rev. A*, **20**, 1398-1405 (1979)

[101] D. J. Haxton, T. N. Rescigno and C. W. McCurdy, *Phys. Rev. A.* **75(1)** (2007)

[102] G. R. Mohlmann, C. I. M. Beenakker, and F. J. de Heer, *Chem. Phys.*, **13**, 375-385 (1976)

[103] M. Darrach and J. W. McConkey, *Chem. Phys. Lett.*, **184**, 141-146 (1991)

[104] H. Kawazumi and T. Ogawa, *Chem. Phys*, **114**, 149-155 (1987)

[105] A. Chutjian, R. I. Hall, and S. Trajmar, *J. Chem. Phys.*, **63**, 892 (1975)

[106] R. N. Zare, *Annual Review of Analytical Chemistry*, **5**, 1–14 (2012)

[107] L. Brewer, R. A. Berg, and G. M. Rosenblatt, *J. Chem. Phys.*, **38**, 1381-88 (1963)

[108]T. Harb, W. Kedzierski, and J. W. McConkey, *J. Chem. Phys.*, **115**, 5507-5512 (2001)

[109] G. H. Dieke and H. M. Crosswhite, *Journal of Quantitative Spectroscopy and Radiative Transfer*, **2**, 97‑199 (1962)

[110] J. Moore, C. Davis, and M. Coplan, *"Building Scientific Apparatus"*, 1st Edn, Addson-Wesley Publishing Company, Canada (1983)

[111] Pfeiffer Vacuum document 1.2.6: "*Types of flow*", available at http://www.pfeiffer-vacuum.com/know-how/introduction-to-vacuum-technology/fundamentals/types-of-flow/technology.action?chapter=tec1.2.6 (Accessed: 28th August 2014)

[112] Pfeiffer Vacuum document 2.2.1: "Rotary *Vane Pumps: Design / Operating principle*", available at http://www.pfeiffer-vacuum.com/know-how/vacuum-generation/rotary-vane-vacuum-pumps/technology.action?chapter=tec2.2 (Accessed 28th August 2014)

[113] K. J. Lesker "*Basic Out-gassing Concepts*", available at http://www.lesker.com/newweb/technical_info/vacuumtech/outgas_00_basicconcept.cfm?section=outgassing&init=skip (Accessed 28th August 2014)

[114] K. L. Nixon, A. J. Murray, O. Al-Hagan, D. H. Madison, and C. Ning, *J. Phys. B: At. Mol. Opt. Phys*. **43** (2010)

[115] G. C. King "*An Introduction to Electron Optics*", Lecture Notes, Dept. Physics and Astronomy, University of Manchester

[116] M. Harvey, "*Low Energy Electron Scattering from a Pulsed AC-MOT*", Thesis, University of Manchester (2009)

[117] "*Operation and Maintenance Manual: NarrowScan Pulsed Dye Laser*", Radiant Dyes Laser Accessories GmbH, Germany (2000)

[118] ET Enterprises "*Understanding Photomultipliers*", available at http://www.et-enterprises.com/files/file/Understanding-photomultipliers.pdf (Accessed 28th August 2014)

[119] ET Enterprises "*Technical Reprint R/P067 – test parameters and general operating rules for photomultipliers*", available at http://www.et-enterprises.com/files/file/technical-information/rp067colour.pdf (Accessed 7th August 2012)

[120] ET Enterprises "*51 mm (2") photomultiplier - 9235B series data sheet*", available at http://my.et-enterprises.com/pdf/9235B.pdf (Accessed 7th August 2012)

[121] M. A. Henderson, *Surf. Sci. Rep*., **46** , 1-308 (2002)

[122] M. A. Henderson, *Langmuir* **2005**, *21*, 3443-3450

[123] R. S. Smith, N. G. Petrik, G. A. Kimmel, and B. D. Kay, *Acc. Chem. Res*., **45**, 33–42 (2012)

[124] V. N. Ageev, *Progress in Surface Science*, **47**, 55-204 (1994)

[125] R.D. Ramsier and J.T. Yates, Jr., *Surface Science Reports*, **12,** 243 378 (1991)

[126] T. E. Madey, *Surface Science* **299/300**, 824-836 (1994)

[127] R. M. Nix, "An Introduction to Surface Chemistry", University of London, available at http://www.chem.qmul.ac.uk/surfaces/scc/scat2_6.htm (Accessed 28th August 2014)

[128] J.W. Niemantsverdriet, K. Markert, and K. Wandelt, *App. Surf. Sci*, **31**, 211–219 (1988)

[129] Y. Itikawa and N. Mason, *J. Phys. Chem. Ref. Data*, **34**, (2005)

[130] Oklahoma State University, "*Chem 1515 Databases*", available at http://intro.chem.okstate.edu/1515sp01/database/vpwater.html (Accessed 28th August 2014)

[131] N. F. Ramsay "*Thermal Beam Sources" in "Experimental Methods in the Physical Sciences"* Volume 29, Part B, Pages 1-435, Ed. F.B. Dunning and Randall G. Hulet (1996)

[132] K. R. German, *J. Chem. Phys.*, **62**, 2584 (1975)

[133] S. M. Pimblott, J. A. LaVerne and A. Mozumder, *J. Phys. Chem*, **100**, 8595-8606 (1996)

[134] Y. Oba, N. Watanabe, A. Kouchi, T. Hama, and V. Pironello, *Astrophys. J. Lett.*, **712**, L174-L178 (2010)

[135] K. Hiraoka,T. Miyagoshi, T. Takayama, K. Yamamoto and Y. Kihara, *Astrophys. J*, **498**, 715 (1998)

[136] D. E. Milligan and M.E. Jacox, *J. Chem. Phys.*, **41**, 3032 (1964)

[137] L. J. Allamandola, S. A. Sandford, and G. J. Valero, *Icarus*, **76**, 225-252 (1988)

[138]N. Watanabe, O. Mouri, A. Nagaoka, T. Chigai, A. Kouchi, and V. Pirronello,

Astrophys. J., **668**, 1001-1011 (2007)

[139] C. Prim, L. Krim, C. Laffon, Ph. Parent, F. Pauzat, J. Pilme, and Y. Ellinger, *J.*

Phys. Chem. A, **114**, 3320-3328 (2010)

[140] R. I. Kaiser, *Icarus*, **73**, 516-526 (1988)

[141] B. Nelander, *J. Chem. Phys.* **72**, 77 (1980)

[142] M. R. Line, G. Vasisht, P. Chen, D. Angerhausen, and Y. L. Yung, *The Astrophysical Journal*, **738**, 14 (2011)

[143] K. J. Zahnle and M. S. Marley, *The Astrophysical Journal*, **797,** 19 (2014)

[144] Y. Yung, W. A. Drew, J. P. Pinto, and R. Freidl, *Icarus*, **73**, 516--526 (1988)

[145] J. Fournier, J. Deson, C. Vermeil and G. C. Pimentel, *J. Chem. Phys,* **70**, 5726 (1979)

[146] L. B. D'Hendecourt, L. J. Allamandola, R. J. A. Grim, and J. M. Greenberg, *Astronom. & Astrophys*, **158**, 119-134 (1986) Roser et al, 2001

[147] J. E. Roser, G. Vidali, G. Manico and V. Pirronello, *Astrophys. J*, **555**, 61–64 (2001)

[148] T. P. M. Goumans and S. Andersson, *MNRAS*, **406**, 2213-2217 (2010)

[149] C. S. Jamieson, A. M. Mebel, and R. I. Kaiser, *Astrophys. J*, **163**, 184-206 (2006)

[150] C. J. Bennett, C. S. Jamieson, and R. I. Kaiser, *Astrophys. J. Supplement Series*, **182**, 1-11 (2009)

[151] D. P. Ruffle and E. Herbst, *MNRAS*, **324**, 1054-1062 (2001)

[152] Y. Oba, N. Watanabe, A. Kouchi, T. Hama, and V. Pirronello, *Astrophys. J. Lett.*, **713**, L174-L178 (2010)

[153] R. T. Garrod and T. Pauly, *The Astrophysical Journal*, **735**, 18 (2011)

[154] D. E. Woon, *Astrophys. J*, **569**, 541 (2002)

[155] D. E. Woon, *J. Chem. Phys*. **105**, 9921 (1996)

[156] N. Watanabe, T. Shiraki, and A. Kouchi, *Astrophys. J*, **588**, L121-L124 (2003)

[157] N. Watanabe and A. Kouchi, *Astrophys. J*, **571**, L173-L176 (2002)

[158] Z. Awab, T. Chigai, Y. Kimura, O. M. Shalabiea, and T. Yamamoto, *Astrophys. J.*, **626**, 262-271 (2005)

[159] J. Bergeld and D. Chakarov, *J. Chem. Phys*., **125**, 141103 (2006)

[160] R. S. Smith and B. D. Kay, *Nature*, **398**, 788 (1999)

[161] W. C. Simpson, M. T. Sieger,T. M. Orlando, L. Parenteau, K. Nagesha, and L. Sanche, *J. Chem. Phys*, **107**, 8668-8677 (1997)

[162] A. D. Bass, L. Parenteau, F. Weik, and L. Sanche, *J. Chem. Phys*, **115**, 4811-4818 (2001)